A measurement of D-mixing in wrong sign $D^0 \to K^+\pi^-\pi^+\pi^-$ decays to provide input to a model-independent determination of the CKM phase γ

by

Samuel T. Harnew

A thesis submitted to the University of Bristol for the degree of Doctor of Philosophy

in the
Faculty of Science
School of Physics

June 2015

Abstract

A measurement of the time dependent ratio of $D^0 \to K^+\pi^-\pi^+\pi^-$ to $D^0 \to K^-\pi^+\pi^-\pi^+$ decays is sensitive to both D-mixing and the interference between doubly Cabibbo suppressed (DCS) and Cabibbo favoured (CF) $D^0 \to K\pi\pi\pi$ amplitudes. Such a measurement is made using $1.0\,\text{fb}^{-1}$ of data collected by the LHCb experiment at a proton-proton centre of mass collision energy of $\sqrt{s} = 7\,\text{TeV}$. The ratio of DCS to CF amplitudes is measured to be,

$$r_D^{K3\pi} = 0.0548 \pm 0.0012.$$

The interference between DCS and CF amplitudes is described by the complex interference parameter $\mathcal{Z}^{K3\pi}$. A combination of results from LHCb and CLEO-c gives the following constraints:

$$\mathcal{R}e\mathcal{Z}^{K3\pi} = -0.135^{+0.095}_{-0.105} \qquad \mathcal{I}m\mathcal{Z}^{K3\pi} = -0.26^{+0.19}_{-0.16}.$$

The probability of the data being a statistical fluctuation of the no-mixing hypothesis is 2.5×10^{-6}, corresponding to a significance of 4.7σ - this is the first evidence of D-mixing in this decay mode.

A model-independent measurement of the CKM phase γ in $B \to DK, D \to f$ decays requires external input for r_D^f and $\mathcal{Z}^f$. Previously such information was only available from the charm threshold at an e^+e^- collider. Presented in this thesis is a new method that only requires input from charm mixing. The novel approach is only possible when the final state of the D decay is multi-body, and therefore the approach is demonstrated with a simulation study of the decay mode $D \to K\pi\pi\pi$. The performance of the method is evaluated with input from both charm mixing, and the charm threshold. Individually, both methods give useful constraints, but if inputs from both are combined, the method becomes highly competitive with measurements of γ in other decay modes. With assumptions about the resonant substructure of the DCS amplitude, it is estimated that γ can be measured to within 12° using existing data and 4° degrees for the LHCb-upgrade.

Declaration of authorship

I, Samuel Harnew, declare that the work in this dissertation was carried out in accordance with the requirements of the University's Regulations and Code of Practice for Research Degree Programmes and that it has not been submitted for any other academic award. Except where indicated by specific reference in the text, the work is the candidate's own work. Work done in collaboration with, or with the assistance of, others, is indicated as such. Any views expressed in the dissertation are those of the author.

Signed: _____

Date: _____

Acknowledgements

Completing this thesis would not have been possible without the help of many people. Here I would like to take the opportunity to thank those who have made this thesis what it is today.

Firstly, it has been fantastic working with my supervisor Jonas Rademacker. He has come up with a countless number of new and interesting ideas which have been the highlight of my studies. He also went through the many iterations of this thesis, which greatly improved the quality of the finished piece. I would also like to thank him for his generosity at the pub - I really hope I don't have to pay all those beers back now I'm not a 'poor student' anymore...

Thanks to Tom Hampson who helped me a great deal during the beginning of my PhD, and still helps me out from time to time with LHCb software issues. I promise you, the mixing analysis will be published eventually.

I must also thank Matt and Anatoly for getting me up to speed on the RICH alignment framework - I would genuinely have never got that running without you!

I am grateful to Tim Gershon, Guy Wilkinson and Jim Libby for providing insightful feedback on the two phenomenology studies presented in this thesis.

Thanks to all the friends I made during my time in Geneva for making it such a fun two years - there are too many to list, but special thanks must go to a few: Gary for our lasagne dinner dates and weekend ski trips; Sam Hall, Sam Cunliffe (The Samigos), Daniel, Patrick, Will and Eluned for being great office mates, our tradition of Friday afternoon whiskey/cocktails has been sorely missed back in Bristol. A special thanks must also go to Octi for providing me with delicious kebabs (and the occasional beer) most Wednesday evenings.

I would also like to thank the Bristol particle physics group, who have made my stay here so enjoyable. Thanks to my housemate and colleague Daniel for the fun times we've had over the past few years: whiskey tasting, sauna Sundays, mead brewing, just to name a few. During the first year of my PhD, particular thanks must go to Chris,

Jeson, Christian, Nik and Daniel for the many late nights spent at the Robin Hood. Also thanks to the LHCb Bristol team including Andrew, Paras, Matt and Tom who have always taken the time to help me out when I've run into difficulty.

Thanks to Charlotte for helping to make the last few months of writing as stress-free as possible, and for proofreading this thesis. The last two years have been unforgettable. Lastly, I wish to thank my family who have supported me throughout my graduate and post-graduate studies. Special thanks must go to my Mum who proofread the entire thesis, and also 'thanks' to my Dad who provided plenty of embarrassing experiences during collaboration weeks.

Author's contribution

The following list gives the Authors contributions to this thesis:

- Chapter 4 – the results presented in this chapter are the Author's own work. Some of the text and figures have already been published in a peer reviewed journal [1].
- Chapter 5 – The data used in this chapter were collected by the LHCb detector, which is managed by the LHCb collaboration. The LHCb software was used to reconstruct the data samples and generate simulated data samples. Standard tools that are used by the collaboration for correcting differences between simulated data and real data were also used. The remainder of the work presented in this chapter is the Author's own.
- Chapter 6 – the results presented in this chapter are the Author's own work. Some of the text and figures have already been published in a peer reviewed journal [2].

Contents

Chapter 1

Introduction

The Large Hadron Collider [3] (LHC) located at CERN, Geneva, is the highest energy particle accelerator ever constructed, with designed collision energy of $\sqrt{s} = 14\,\text{TeV}$. This unprecedented environment provides a unique opportunity to search for new physics beyond the Standard Model of particle physics (SM) - a theory which has stood the test of time for over 40 years[1]. The LHCb experiment [4], which is situated at one of the LHC collision points, was designed specifically to utilise the huge production cross-section of long-lived b and c hadrons. Precision measurements of these hadrons and their decays could be the first place to reveal cracks in the SM. LHCb has several distinctive features that optimise the detector for measuring such decays; the first of these is a silicon vertex tracker that is situated within 8 mm of the beam line, providing an excellent discrimination between the decay vertex of a long-lived particle and the primary interaction vertex (PV). Also essential are two Ring Imaging Cherenkov (RICH) detectors that provide a clear separation between pions, kaons and protons. Such discrimination is vital when looking for a transition between specific quark flavours.

Flavour physics is the study of quark transitions, which in the SM are described by the Cabibbo-Kobayashi-Maskawa (CKM) matrix - this is also the only source of charge-parity (CP) violation in the SM. The relationships between key parameters of the CKM matrix can be represented graphically in the unitarity triangle (Figure 2.1). Further

[1] One could argue that neutrino oscillations have fundamentally changed the SM in the last 40 years, although their treatment can be added to the SM in a completely analogous way to quark mixing.

improving the constraints of this triangle is one of the major goals in flavour physics [5]. The phase γ describing CP violation in $b \to u$ quark transitions [6, 7] is the least constrained angle of the unitarity triangle. One method to measure γ is from $B \to DK$, $D \to f$ decays where f is a final state accessible from both D^0 and $\overline{D}^0$. This provides a theoretically clean approach to constrain γ which is unlikely to be influenced by new physics beyond the SM. Such a measurement requires external input to quantify the interference between $D^0 \to f$ and $\overline{D}^0 \to f$ amplitudes [8–10]. In this thesis it is shown that this interference information can be obtained from a measurement of D-mixing where the D decays into the same final state f [1, 2]. This is demonstrated for the multi-body final state $K\pi\pi\pi$ where current constraints on the interference parameters are fairly weak [11].

This thesis is organised as follows: Chapter 2 gives a summary of the SM, with particular detail on how fundamental particles acquire their mass via the Higgs mechanism. This process is intimately linked to flavour-changing charged currents which are present at tree level in the SM, and described by the CKM matrix.

In Chapter 3, CERN and the LHCb experiment are introduced. A brief description of all detector elements is given, along with their performance during the 2009-2012 running period.

Chapter 4 introduces a new method to constrain charm interference parameters which are needed for a model-independent measurement of the CKM phase γ. Previously this input could only be obtained from e^+e^- colliders running at the charm threshold - this method obtains similar constraints using charm mixing. The method is demonstrated using simulated $D^0 \to K^+\pi^-\pi^+\pi^-$ decays.

In Chapter 5, the new method developed in Chapter 4 is applied to $1.0\,\text{fb}^{-1}$ of LHCb data collected during 2011. The results are combined with constraints from CLEO-c in order to improve the existing constraints on the $D \to K\pi\pi\pi$ charm interference parameters.

Finally, in Chapter 6, it is shown using simulation studies, how the constraints on charm interference parameters, using D-mixing, can be used to provide competitive constraints

on γ. Such a measurement can only be made if the final state f is multi-body, making its potential for the final state $K\pi\pi\pi$ exciting - this is explored using simulation studies.

Chapter 2

The Standard Model

2.1 Introduction

The SM is a theory of elementary particles and their interactions. It is widely regarded as one of the most successful theories ever developed, still agreeing with the latest experimental evidence over 40 years since its construction. Parts of the theory, quantum electrodynamics (QED), have been tested to more than one part in a trillion [12]. The SM predicts the existence of three types of fundamental particle; spin-$\frac{1}{2}$ fermions, spin-1 gauge bosons, and a spin-0 scalar known as the Higgs boson.

The fermions are divided into three generations, each of which contain two quarks and two leptons. The six quarks can be split into two groups of 'up' type and 'down' type, which have an electric charge of $\frac{2}{3}$ and $-\frac{1}{3}$ respectively. The quarks are the only fermions to carry 'colour charge' which allows them to couple to the strong force. The two leptons differ by their electric charge; the 'electron type' lepton has a charge of +1, while the 'neutrino' is electrically neutral. Each successive generation of fermions can be thought of as a heavier 'copy' of the previous one. For example, the first generation has the electron, whereas the second generation has the muon - these have masses of 0.510 MeV[1] and 105.7 MeV respectively [13].

[1] Throughout this thesis natural units are used $c = \hbar = 1$

The bosons can be split into three fundamental force carriers. The electromagnetic force is carried by the massless photon which couples to electric charge. The weak force is carried by the massive $W^{\pm}$ and Z^0 bosons which couple to 'weak isospin' and 'weak hypercharge'. The strong force is carried by 8 massless gluons which couple to 'colour charge'.

The final piece of the SM is a scalar boson known as the Higgs boson. This is responsible for giving both the fermions and gauge bosons their mass, and couples to all massive particles. Since the discovery of the Higgs boson in 2013 [14, 15], all particles in the SM have been observed experimentally.

2.2 Continuous Symmetries in the Standard Model

Symmetries are of huge importance in all fields of physics. As described by Noether's theorem [16], any continuous symmetry of a physical system will have an associated conserved quantity. An example of this is the conservation of momentum, which is a result of translational invariance.

The SM is a gauge theory, which is built by taking the Lagrangian of free particles (no interactions) and requiring that specific symmetries hold. The following subsections will demonstrate how these symmetries manifest themselves as the interactions that we observe in nature.

2.2.1 Quantum Electrodynamics

QED is the theory of electromagnetism - the interaction of charged fermions with photons. In this section it is shown that one can produce the laws of electromagnetism by ensuring the Lagrangian is locally gauge-invariant under U(1) transformations - this means it is *symmetric* under a phase rotation at any point in space-time. To illustrate this, the free Dirac Lagrangian is first considered,

$$\mathcal{L} = i\overline{\psi}\gamma^{\mu}\partial_{\mu}\psi - m\overline{\psi}\psi, \tag{2.1}$$

where ψ is a Dirac spinor that represents a fermionic field with mass m, and γ^μ are the four Dirac matrices. A Lagrangian is said to be locally gauge-invariant (under the U(1) group) if one can make the substitution $\psi \to \psi e^{-iq\lambda(x)}$ without altering the Lagrangian. Here x is a point in space-time, which makes it 'local', and q is a constant that will later turn out to be the charge of the fermion. Making this substitution in the free Dirac Lagrangian,

$$\mathcal{L} \to \mathcal{L} + q\overline{\psi}\gamma^\mu\psi\partial_\mu\lambda(x), \tag{2.2}$$

one can see that it is *not* locally gauge-invariant. To remedy this problem one can add a new field A_μ that transforms so that $A_\mu \to A_\mu + \partial_\mu\lambda$. The additional term $q\overline{\psi}\gamma^\mu\psi\partial_\mu\lambda(x)$ that appears in the Lagrangian can then be absorbed into A_μ giving the locally gauge-invariant Lagrangian:

$$\mathcal{L} = i\overline{\psi}\gamma^\mu\partial_\mu\psi - m\overline{\psi}\psi - q\overline{\psi}\gamma^\mu\psi A_\mu. \tag{2.3}$$

It can be shown that the new vector field A_μ has exactly the same properties as the electromagnetic field. To complete the Lagrangian, a free photon term is also necessary,

$$\mathcal{L} = i\overline{\psi}\gamma^\mu\partial_\mu\psi - m\overline{\psi}\psi - q\overline{\psi}\gamma^\mu\psi A_\mu - \frac{1}{16\pi}A^{\mu\nu}A_{\mu\nu}, \tag{2.4}$$

where $A_{\mu\nu} = \partial_\mu A_\nu - \partial_\nu A_\mu$ is the electromagnetic field strength tensor that encompasses Maxwell's equations. One can also try to add a mass term to the field A_μ, but this ruins gauge invariance.

2.2.2 Quantum Chromodynamics

Quantum Chromodynamics (QCD) is the theory of the strong interaction. The theory begins by postulating a new charge carried by a fermion that comes in three types. To describe such a fermion, a triplet of Dirac spinors is required,

$$\psi = \begin{pmatrix} \psi_r \\ \psi_g \\ \psi_b \end{pmatrix}, \tag{2.5}$$

where the subscripts r, g and b represent the three types of charge, known as red, green, and blue respectively. Any particle that carries this charge is said to be coloured. The Lagrangian for a free coloured fermion can then be written as

$$\mathcal{L} = i\overline{\psi}\gamma^{\mu}\partial_{\mu}\psi - m\overline{\psi}\psi. \tag{2.6}$$

In Section 2.2.1, invariance under the transformation $\psi \rightarrow \psi e^{-iq\lambda(x)}$ was considered - also known as a U(1) transformation. In QCD there is a three-component field, and so instead consider a local transformation of the form,

$$\psi \rightarrow U(x)\psi, \tag{2.7}$$

where $U(x)$ is a 3×3 unitary matrix. This is known as an SU(3) transformation, where S stands for 'special' ($\det(U) = +1$) and where U stands for 'unitary' ($UU^{\dagger} = \mathbf{I}$ where $\mathbf{I}$ is the identity matrix). One can also write the SU(3) transformation in exponential form:

$$U(x) = e^{i\lambda_i a_i(x)}. \tag{2.8}$$

Such a transformation allows for local rotations in colour space, where λ_i are the 8 Gell-Mann matrices, the generators of the SU(3) group, and $a_i(x)$ are the real constants which define the local transformation.

To make the Lagrangian invariant under such a transformation, the following modification is made,

$$\partial_{\mu} \rightarrow D_{\mu} = \partial_{\mu} - iq\lambda_i G_{\mu,i}, \tag{2.9}$$

where $G_{\mu,i}$ are the 8 gluon fields, which have transformation properties to ensure gauge invariance. D_{μ} is the covariant derivative, which when substituted into Equation 2.6 introduces a coupling between coloured fermions and 8 gluon fields. A kinetic term for free gluons must also be added,

$$\mathcal{L} = i\overline{\psi}\gamma^{\mu}D_{\mu}\psi - m\overline{\psi}\psi - G_i^{\mu\nu}G_{\mu\nu,i}, \tag{2.10}$$

where $G_{\mu\nu,i}$ are the gluon field strength tensors. These are defined as,

$$G_i^{\mu\nu} = \partial^\mu G_i^\nu - \partial^\nu G_i^\mu - q f_{ijk} G_j^\mu G_k^\nu, \tag{2.11}$$

where f_{ijk} are the SU(3) structure constants. Comparing this to the electromagnetic field strength tensor in Section 2.2.1, there is an additional term, $-q f_{ijk} G_j^\mu G_k^\nu$, that is required to conserve gauge invariance - a result of the SU(3) group being non-abelian ($AB \neq BA$). This term has important implications for the theory because it results in 3 and 4 point self interactions of the gluons, meaning that the gluons *themselves* carry colour charge.

In electromagnetism, the force between two oppositely charged particles is proportional to $1/r^2$, where r is their separation. The potential energy will therefore asymptotically reach a maximum as $r \to \infty$. In contrast to this, the strong interaction gives approximately the same force at all distances. This is due to the gluon self-interaction which cause the gluons to form a 'colour string' between two coloured objects. Therefore, as separation increases, there will be a point at which there is sufficient energy to create a new quark anti-quark pair, which snaps the colour string in two - a process known as hadronisation. The distance required is incredibly small due to the large coupling constant of the strong force, and for this reason, only colourless objects have ever been observed. This phenomenon is known as 'colour confinement'.

Another interesting property of the strong interaction is 'asymptotic freedom'. This is due to the apparent coupling constant being dependent on the energy scale of the interaction. At low energies the coupling constant is large, making perturbative calculations, and therefore phenomenological predictions, extremely difficult. At high energies the coupling constant is smaller, taking us to a regime where the usual Feynman rules are applicable.

2.2.3 Electroweak Interaction

The electroweak interaction, the marriage between the electromagnetic and weak interactions, is a result of a broken $\mathrm{U}(1)_Y \times \mathrm{SU}(2)_I$ symmetry. Here the subscript on each

group identifies the conserved quantity associated with that gauge transformation. The hypercharge, not to be confused with electric charge, is given by Y, and weak isospin is given by I. Symmetry breaking, which is required to give the gauge bosons their mass, will be considered in Section 2.2.4. In this section, only the unbroken symmetry is considered.

The weak interaction is a chiral theory, meaning that its Lagrangian is not invariant under a change of chirality i.e. not parity invariant. In the limit of massless particles, chirality is the same as helicity (the spin vector projected onto the momentum vector). For massive particles helicity and chirality are no longer the same; chirality is a frame independent quantum number under proper Lorentz transformations, whereas helicity is not. Experimental evidence [17] has shown that the weak interaction only couples to chirally left-handed particles. For this reason the doublets are defined using only left-handed fields,

$$L^i = \left\{ \begin{pmatrix} \nu_{eL} \\ e_L \end{pmatrix}, \begin{pmatrix} \nu_{\mu L} \\ \mu_L \end{pmatrix}, \begin{pmatrix} \nu_{\tau L} \\ \tau_L \end{pmatrix} \right\}, \quad Q^i = \left\{ \begin{pmatrix} u_L \\ d_L \end{pmatrix}, \begin{pmatrix} c_L \\ s_L \end{pmatrix}, \begin{pmatrix} t_L \\ b_L \end{pmatrix} \right\}, \tag{2.12}$$

which will later couple to the SU(2) gauge bosons. The right-handed fields are then defined as singlets,

$$e_R^i = \{e_R, \mu_R, \tau_R\}, \qquad \nu_R^i = \{\nu_{eR}, \nu_{\mu R}, \nu_{\tau R}\}, \tag{2.13}$$

$$u_R^i = \{u_R, c_R, t_R\}, \qquad d_R^i = \{d_R, s_R, b_R\}, \tag{2.14}$$

which will only couple to the U(1) gauge boson. The Lagrangian for free, massless, quarks is defined:

$$\mathcal{L} = i\overline{Q}\gamma^\mu \partial_\mu Q + i\overline{u_R}\gamma^\mu \partial_\mu u_R + i\overline{d_R}\gamma^\mu \partial_\mu d_R. \tag{2.15}$$

The Lagrangian can trivially be extended to include leptons and the other generations of quarks. For now we have not included mass terms because these are intimately linked to the Higgs mechanism, an important topic that will be discussed in Section 2.3.1. Following the same procedure as Section 2.2.1 and Section 2.2.2 one can make the

Lagrangian gauge-invariant by using the covariant derivatives:

$$\partial_\mu \rightarrow D_\mu^{\mathrm{U}(1)} = \partial_\mu - ig'YB_\mu, \tag{2.16}$$

$$\partial_\mu \rightarrow D_\mu^{\mathrm{U}(1)\times\mathrm{SU}(2)} = \partial_\mu - ig\tau_a W_{\mu,a} - ig'YB_\mu. \tag{2.17}$$

Here B_μ and $W_{\mu,i}$ are the U(1) and SU(2) gauge fields respectively, with couplings of g' and g. The constant Y gives the hypercharge of the field. The 3 generators of SU(2) are given by τ_a, which are linked to the well known 2×2 Pauli matrices, σ_a, through $\tau_a = \frac{1}{2}\sigma_a$. The left-handed particles form doublets so use the $D_\mu^{\mathrm{U}(1)\times\mathrm{SU}(2)}$ covariant derivative, whereas the right-handed singlets use $D_\mu^{\mathrm{U}(1)}$. Making this substitution, and using the field strength tenors $W_{\mu\nu}$ and $B_{\mu\nu}$ for the kinetic terms [2], one arrives at the gauge-invariant Lagrangian,

$$\begin{aligned}\mathcal{L} = {} & i\overline{Q}\gamma^\mu D_\mu^{\mathrm{U}(1)\times\mathrm{SU}(2)} Q \\ & + i\overline{u_R}\gamma^\mu D_\mu^{\mathrm{U}(1)} u_R + i\overline{d_R}\gamma^\mu D_\mu^{\mathrm{U}(1)} d_R \\ & - W_{\mu\nu,a}W_a^{\mu\nu} - B_{\mu\nu}B^{\mu\nu}.\end{aligned} \tag{2.18}$$

Although this Lagrangian predicts four gauge bosons, enough to represent the physical $W^\pm$ Z^0 and γ bosons, there is a big problem because one cannot give the bosons mass in a gauge-invariant way. Section 2.2.4 will show how three of the gauge bosons acquire mass, and the physical fields form from a superposition of the gauge fields.

2.2.4 The Higgs Field

The Higgs field is defined as a doublet of complex scalar fields, $\phi^T = (\phi^+, \phi^0)$, which is used to construct the following Lagrangian,

$$\mathcal{L} = \partial_\mu\phi^\dagger\partial^\mu\phi + m^2\phi^\dagger\phi - \frac{\lambda}{4}(\phi^\dagger\phi)^2. \tag{2.19}$$

This includes a kinetic term, and importantly a potential term which is 4^{th} order in ϕ. To achieve spontaneous symmetry breaking, that is required for the Higgs mechanism,

[2] $W_{\mu\nu}$ is defined in the same way as the SU(3) field strength tensor in Equation 2.11, but using the SU(2) structure constant. B_μ is the U(1) field strength tensor described in Section 2.2.1.

one needs $m^2 > 0$ and $\lambda > 0$ - this gives a potential with the classic 'wine bottle' shape that has a local maximum at $\phi^T = (\ 0 \ \ 0\ )$, and a degenerate global minimum. Because of this degeneracy the system has no preference for any of the minima, and it therefore has to 'spontaneously' choose one at random.

Following the same approach used in Equation 2.19, the Lagrangian is required to be invariant under $\mathrm{U}(1)_Y \times \mathrm{SU}(2)_I$ transformations,

$$\mathcal{L} = -\frac{1}{4}W_{\mu\nu,a}W_a^{\mu\nu} - \frac{1}{4}B_{\mu\nu}B^{\mu\nu} + D_\mu\phi^\dagger D^\mu\phi + m^2\phi^\dagger\phi - \frac{\lambda}{4}(\phi^\dagger\phi)^2, \tag{2.20}$$

where $D_\mu = \partial_\mu - ig\tau_a W_{\mu,a} - \frac{i}{2}g^{'}B_\mu$ is the covariant derivative introduced in Equation 2.17. The factor of $\frac{1}{2}$ arises in the B^μ term because the Higgs doublet has a hypercharge of $\frac{1}{2}$.

To evaluate the physical fields, the Lagrangian is expanded about one of its minima. One is free to choose any of the degenerate minima, but for convenience the minimum at $\phi^T = (\ 0 \ \ \frac{v}{\sqrt{2}}\ )$ is chosen, where $v = \frac{2m}{\sqrt{\lambda}}$ is the expectation value of ϕ in the ground state (VEV). The expansion is performed using the following substitution,

$$\phi = e^{2i\frac{\pi^a\tau^a}{v}}\begin{pmatrix} 0 \\ \frac{v}{\sqrt{2}} + \frac{h}{2} \end{pmatrix}, \tag{2.21}$$

where τ^a are the three SU(2) generators, and π^a and h are the 4 degrees of freedom in the Higgs field. Changes in the field associated with π^a result in the same potential i.e. rotate to another degenerate minimum. Changes in the field associated with h will increase the potential.

In Equation 2.20 the Lagrangian was forced to be gauge-invariant in U(1) × SU(2) transformations - there is now the freedom to choose any gauge i.e. one can pick a specific U(1) × SU(2) transformation, because the Physics must remain unchanged. In particular it is possible to choose a gauge which will counteract a Higgs field that is defined by a non zero π^a. This is called the 'unitary gauge' [18], and is defined as,

$$\phi \to \phi' = \phi e^{-2i\frac{\pi^a\tau^a}{v}}. \tag{2.22}$$

Using the unitary gauge allows π^a to be set to zero, simplifying the transformation in Equation 2.21 considerably. One may ask where these three degrees of freedom have gone? If a different choice of gauge was used, they would have resulted in three massless gauge bosons, or 'Goldstone bosons' [19], but after fixing the gauge, these bosons no longer exist. The answer is that the gauge will also transform the SU(2) field $W_i^\mu \rightarrow W_{i'}^\mu$. This transformation adds a longitudinal polarisation to the three gauge bosons, and accounts for the three degrees of freedom lost from the Goldstone bosons. It is often said that the gauge boson 'eats' the Goldstone boson and gains a longitudinal component.

Equation 2.21 is now substituted into the kinetic term of the Lagrangian, restricting the expansion to terms which generate the gauge bosons masses:

$$\begin{aligned} |D_\mu \phi|^2 &= \frac{1}{4} \begin{pmatrix} 0 & \frac{v}{\sqrt{2}} + \frac{h}{2} \end{pmatrix} \begin{pmatrix} g' B_\mu + g W_\mu^3 + 2\partial_\mu & g W_\mu^1 - i g W_\mu^2 \\ g W_\mu^1 + i g W_\mu^2 & \frac{g'}{g} g' B_\mu - g W_\mu^3 + 2\partial_\mu \end{pmatrix}^2 \begin{pmatrix} 0 \\ \frac{v}{\sqrt{2}} + \frac{h}{2} \end{pmatrix} \\ &= \frac{v^2}{8} \left[g^2 (W_\mu^1)^2 + g^2 (W_\mu^2)^2 + \left(g' B_\mu - g W_\mu^3 \right)^2 \right] + f(h). \end{aligned} \tag{2.23}$$

It is seen that there is mixing between the B_μ and W_μ^3 fields, so these must be diagonalised to find the physical states,

$$\begin{aligned} Z_\mu &\equiv \cos\theta_w W_\mu^3 - \sin\theta_w B_\mu, \\ A_\mu &\equiv \sin\theta_w W_\mu^3 + \cos\theta_w B_\mu, \\ W_\mu^\pm &\equiv \frac{1}{\sqrt{2}} (W_\mu^1 \mp i W_\mu^2), \end{aligned} \tag{2.24}$$

where θ_w is the Weinberg angle. Making the substitution one arrives at,

$$|D_\mu \phi|^2 = \frac{g^2 v^2}{4} W_\mu^- W^{+\mu} + \frac{g^2 v^2}{8 \cos^2\theta_w} Z_\mu Z^\mu + 0 A_\mu A^\mu + f(h), \tag{2.25}$$

from which the masses of the gauge bosons can easily be determined. The massive $W_\mu^\pm$ bosons are a superposition of the original W_μ^1 and W_μ^2 gauge bosons, and therefore couple to weak isospin. The bosons Z_μ and A_μ are a superposition of the W_μ^3 and B_μ gauge bosons, so couple to a combination of weak isospin and weak hypercharge. The

Z_μ field is massive, whereas the A_μ field is massless.

As discussed in Section 2.2.2, the standard model also contains an unbroken SU(3) symmetry in order to generate the strong force. This can trivially be added into the broken $\mathrm{U}(1)_Y \times \mathrm{SU}(2)_I$ symmetry. To summarise, before spontaneous symmetry breaking the standard model Lagrangian obeys a $\mathrm{U}(1)_Y \times \mathrm{SU}(2)_I \times \mathrm{SU}(3)_C$ symmetry. After spontaneous symmetry breaking, it becomes a $\mathrm{U}(1)_Q \times \mathrm{SU}(3)_C$ symmetry, where $Q = Y + I_3$ is the electric charge, and I_3 is the third component of weak isospin. The properties of the SM fermions are summarised in Table 2.1.

	ν_L	e_L	u_L	d_L	ν_R	e_R	u_R	d_R
I_3	$+\frac{1}{2}$	$-\frac{1}{2}$	$+\frac{1}{2}$	$-\frac{1}{2}$	-	-	-	-
Y	$-\frac{1}{2}$	$-\frac{1}{2}$	$+\frac{1}{6}$	$+\frac{1}{6}$	0	-1	$+\frac{2}{3}$	$-\frac{1}{3}$
Q	0	-1	$+\frac{2}{3}$	$-\frac{1}{3}$	0	-1	$+\frac{2}{3}$	$-\frac{1}{3}$

Table 2.1: This table summaries the weak hypercharge and weak isospin of the SM fermions. The electric charge $Q = Y + I_3$ is also given.

2.3 CKM Matrix

2.3.1 Yukawa Couplings

In order to add mass terms to the fermions it is not possible to add a simple Dirac mass to the Lagrangian such as,

$$\mathcal{L}_{\text{dirac}} = -m_d d\overline{d} = -m_d(d_L + d_R)(\overline{d_L} + \overline{d_R}), \tag{2.26}$$

$$= -m_d d_L \overline{d_R} - m_d d_R \overline{d_L}, \tag{2.27}$$

where m_d is the mass of down quark, and d is its Dirac spinor. Splitting the expression into a sum of its left and hight handed parts, it becomes clear that this is not gauge-invariant under SU(2) because the left and right-handed parts of the field have different transformation properties.

To remedy this problem one can add a Yukawa type coupling to the Lagrangian,

$$\mathcal{L}_{\text{yukawa}} = -Y_d \overline{Q} \phi d_R + \text{h.c.} \tag{2.28}$$

where Q is a left-handed quark doublet (Equation 2.12), ϕ is the Higgs doublet, Y_d is the Yukawa coupling strength, and 'h.c.' is the hermitian conjugate. This term is gauge-invariant because any SU(2) gauge transformation will cancel in $\overline{Q}\phi$. After spontaneous symmetry breaking, the Higgs doublet becomes $\phi^T = (0, \frac{v}{\sqrt{2}} + \frac{h}{2})$. Substituting this into the Yukawa coupling results in the mass term,

$$\mathcal{L}_{\text{yukawa}} = -\frac{Y_d v}{\sqrt{2}} d\overline{d} + f(h). \tag{2.29}$$

In a similar way, one can also generate mass terms for the up quark by adding the term,

$$\mathcal{L}_{\text{yukawa}} = -Y_u \overline{Q} \epsilon \phi^* u_R + \text{h.c.}\ , \tag{2.30}$$

where ϵ is the anti-symmetric tensor. The same process can also be repeated for the leptons.

2.3.2 Additional Generations

Following the procedure in Section 2.3.1, it is easy to add additional Yukawa couplings for each flavour of quark. When doing so, it is also possible to add cross terms, making the couplings for down type quarks become,

$$\mathcal{L}_{\text{yukawa}} = -Y_{d,ij} \overline{Q^i} \phi d_R^j + h.c.\ , \tag{2.31}$$

where $Y_{d,ij}$ are the 9 Yukawa couplings. A similar principle can also be applied to the up type quarks. After spontaneous symmetry breaking the following mass terms emerge,

$$\mathcal{L}_{\text{yukawa}} = -\frac{v}{\sqrt{2}} \left(\overline{\mathbf{d}} Y_d \mathbf{d} - \overline{\mathbf{u}} Y_u \mathbf{u} \right), \tag{2.32}$$

where $\mathbf{u}$ and $\mathbf{d}$ are three-component vectors containing the three generations of up and down type quark fields respectively. Y_d and Y_u are 3×3 matrices containing all the Yukawa couplings. To find the masses of the physical particles one must diagonalise the matrices Y_d and Y_u,

$$Y_d = U_d M_d U_d^\dagger, \qquad\qquad Y_u = U_u M_u U_u^\dagger, \tag{2.33}$$

where U_d and U_u are unitary matrices, and M_d and M_u give the masses of the physical quarks. This allows one to rotate to the mass eigenstates,

$$\mathbf{u}' = U_u^\dagger \mathbf{u}, \qquad\qquad \mathbf{d}' = U_d^\dagger \mathbf{d}, \tag{2.34}$$

where the prime indicates a mass eigenstate, as opposed to a flavour eigenstate (which diagonalises the coupling to the weak interaction). A rotation of both up and down type quarks by the same unitary matrix would leave the physics unchanged, so one is free to do the following,

$$\mathbf{u}' \to \mathbf{u}, \qquad\qquad \mathbf{d}' \to U_u U_d^\dagger \mathbf{d} = V_{\mathrm{CKM}}^\dagger \mathbf{d}. \tag{2.35}$$

The matrix V_{CKM} is known as the CKM matrix, which is named after the physicists Cabibbo, Kobayashi, and Maskawa who introduced it [6, 7]. This has no physical consequences to interactions with the Z^0 and γ because they couple to up or down type quarks, and never to a mixture. It does however have important consequences for interactions with the $W^\pm$ bosons, whose interaction term becomes:

$$\mathcal{L} \propto W_\mu^- \overline{\mathbf{u}'} \gamma^\mu V_{\mathrm{CKM}} \mathbf{d}' + W_\mu^+ \overline{\mathbf{d}'} \gamma^\mu V_{\mathrm{CKM}}^\dagger \mathbf{u}' \tag{2.36}$$

This implies that an up type quark interacting with a W^+ boson can couple to any of the down type quarks, with probabilities given by the CKM matrix.

2.3.3 Unitarity Triangle

For clarity, all components of the CKM matrix, defined in Equation 2.35, are labeled:

$$V_{CKM} = \begin{pmatrix} V_{ud} & V_{cd} & V_{td} \\ V_{us} & V_{cs} & V_{ts} \\ V_{ub} & V_{cb} & V_{tb} \end{pmatrix} \tag{2.37}$$

Where the elements V_{ij} are complex numbers. It was shown in Section 2.3.1 that the CKM matrix is unitary i.e. $V_{\text{CKM}} V_{\text{CKM}}^{\dagger} = \mathbf{I}$. This property restricts the total number of free parameters from $2N^2 \rightarrow N^2$, where N is the number of quark generations. This number is then further reduced by absorbing $2N - 1$ phases into the quark fields. In the case of a 3×3 matrix, this results in 4 free parameters; 3 magnitudes, and one phase. It is this phase which allows *CP* violation in the SM.

To highlight that the CKM matrix can be parameterised by 4 parameters it can be written in the following form [20]:

$$V_{CKM} = \begin{pmatrix} 1 & 0 & 0 \\ 0 & c_{23} & s_{23} \\ 0 & -s_{23} & c_{23} \end{pmatrix} \begin{pmatrix} c_{13} & 0 & s_{13}e^{-\delta_{13}} \\ 0 & 1 & 0 \\ -s_{13}e^{\delta_{13}} & 0 & c_{13} \end{pmatrix} \begin{pmatrix} c_{12} & s_{12} & 0 \\ -s_{12} & c_{12} & 0 \\ 0 & 0 & 1 \end{pmatrix}, \tag{2.38}$$

where c_{ij} and s_{ij} give the sine and cosine of the 3 Euler angles θ_{12}, θ_{13} and θ_{23} - the single complex phase is given by δ_{13}. A popular way to expand this is by defining the following parameters,

$$s_{12} = \lambda, \tag{2.39}$$

$$s_{23} = A\lambda^2, \tag{2.40}$$

$$s_{13}e^{-i\delta_{13}} = A\lambda^3(\rho - i\eta), \tag{2.41}$$

then expanding in powers of $\lambda \sim 0.22$. This is known as the Wolfenstein parameterisation [21], which is shown to 3$^{\text{rd}}$ order,

$$V_{CKM} = \begin{pmatrix} 1 - \frac{\lambda^2}{2} & \lambda & A\lambda^3(\rho - i\eta) \\ -\lambda & 1 - \frac{\lambda^2}{2} & A\lambda^2 \\ A\lambda^3(1 - \rho - i\eta) & -A\lambda^2 & 1 \end{pmatrix}. \tag{2.42}$$

The parameters A, ρ and η are $\mathcal{O}(1)$, making this parameterisation particularly informative. It allows one to quickly estimate the magnitude of different quark transitions and their *CP* violating phase.

A graphical way to visualise the CKM matrix is the 'unitarity triangles'. These come from the unitarity condition, $V_{\text{CKM}}V_{\text{CKM}}^{\dagger} = \mathbf{I}$, which results in 6 equations that sum to zero:

$$\begin{aligned} &V_{ud}V_{us}^* + V_{cd}V_{cs}^* + V_{td}V_{ts}^* = 0, && V_{ud}V_{ub}^* + V_{cd}V_{cb}^* + V_{td}V_{tb}^* = 0, \\ &V_{us}V_{ud}^* + V_{cs}V_{cd}^* + V_{ts}V_{td}^* = 0, && V_{us}V_{ub}^* + V_{cs}V_{cb}^* + V_{ts}V_{tb}^* = 0, \\ &\underline{V_{ub}V_{ud}^* + V_{cb}V_{cd}^* + V_{tb}V_{td}^* = 0,} && V_{ub}V_{us}^* + V_{cb}V_{cs}^* + V_{tb}V_{ts}^* = 0. \end{aligned} \tag{2.43}$$

All 6 equations can be represented as a triangle in the complex plane, although of particular interest is the underlined equation, which is known as 'the unitarity triangle'. This triangle has terms which are all of the order λ^3, and include large *CP* violating phases. These two conditions make this unitarity triangle particularly triangular i.e. 3 similar angles and sides of similar lengths. Figure 2.1 shows the graphical representation of the unitary triangle - the commonly used angles α, β and γ are superimposed and defined.

Constraining all parameters of the unitarity triangle is one of the major goals in flavour physics [5]. If it is shown that the measured parameters do not form a triangle (i.e. the CKM matrix is *not* unitary) this will be a clear sign of new physics beyond the SM. Another interesting test is to measure the unitarity triangle using decays that are dominated by either 'loop' or 'tree' amplitudes. A loop amplitude can be drawn as a Feynman diagram containing a loop of virtual particles - this makes them very sensitive

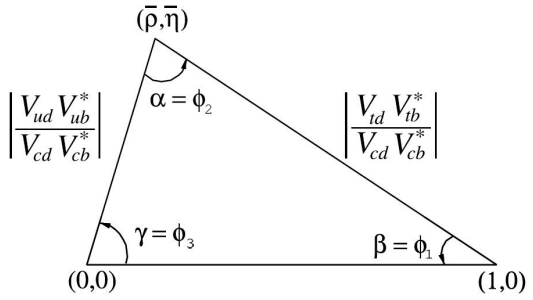

$$\alpha = \arg\left(-\frac{V_{td}V_{tb}^*}{V_{ud}V_{ub}^*}\right) \tag{2.44}$$

$$\beta = \arg\left(-\frac{V_{cd}V_{cb}^*}{V_{td}V_{tb}^*}\right) \tag{2.45}$$

$$\gamma = \arg\left(-\frac{V_{ud}V_{ub}^*}{V_{cd}V_{cb}^*}\right) \tag{2.46}$$

Figure 2.1: A graphical representation of the unitarity triangle, with the angles α, β and γ defined on the RHS. The real parameters $\overline{\rho}$ and $\overline{\eta}$ are defined as $\overline{\rho} + i\overline{\eta} = \frac{V_{ud}V_{ub}^*}{V_{cd}V_{cb}^*}$. These are approximately equal to ρ and η from the Wolfenstein parameterisation (Equation 2.41).

to new physics, particularly to new particles that are beyond the energy frontier. A tree amplitude is far less sensitive to new physics. If there is a significant difference between measurements dominated by tree and loop amplitudes, this will be a clear sign of new physics.

Several groups combine experimental measurements to produce global constraints on the unitarity triangle. Shown in Figure 2.2 are the constraints from the CKM fitter group [22] who have produced separate fits for both loop and tree measurements. Currently the constraints from tree processes are much weaker than those from loop processes.

2.3.3.1 The CKM phase γ

The least constrained angle of the unitarity triangle is γ, making its measurement a priority for the LHCb experiment (Chapter 3). The family of $B^{\pm} \to Dh^{\pm}$ decays, where h represents either a kaon or a pion, are particularly sensitive to γ, and are copiously produced within the LHCb detector [23]. These decays are dominated by tree level Feynman diagrams, meaning that any influence from new physics is unlikely. This makes them perfect for a benchmark measurement of the SM, which can be compared to measurements of γ in loop processes. Such decays will be discussed in detail in Chapter 4.

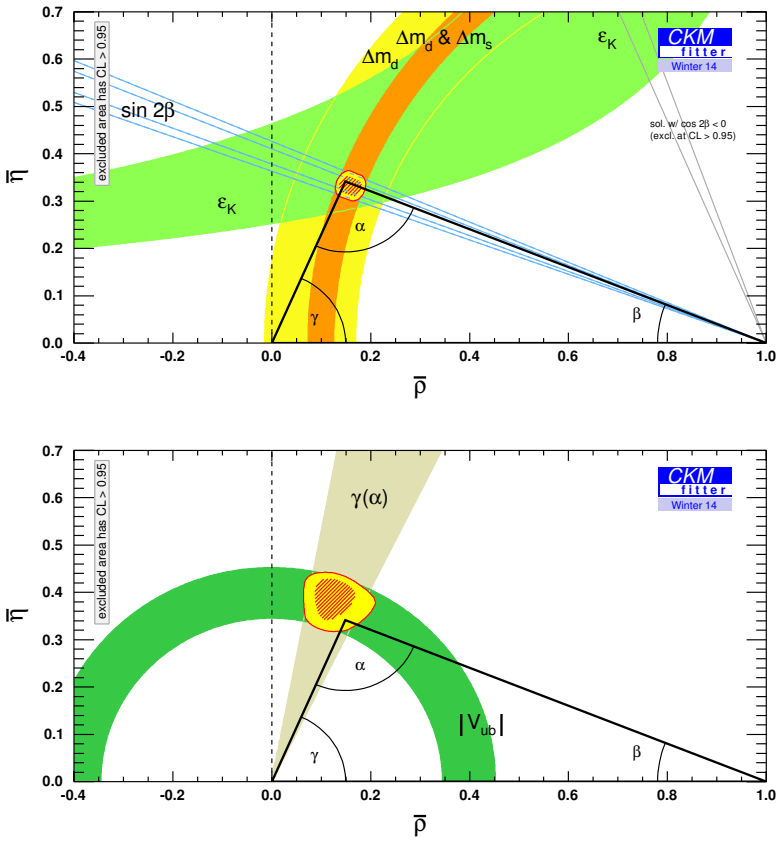

Figure 2.2: (top) Current constraints from loop measurements (bottom) current constraints from tree measurements. Both figures are taken from the CKMfitter group [22]. The parameters $\alpha, \beta, \gamma, \overline{\rho}$ and $\overline{\eta}$ are defined in Figure 2.1.

Chapter 3

The LHCb detector

3.1 Large Hadron Collider

The Large Hadron Collider (LHC) [3] is a proton-proton collider based at CERN, Geneva. The collider tunnel, which previously housed LEP, crosses the French-Swiss border, and is $\sim 100\,\mathrm{m}$ underground. It is both the largest, and highest energy particle collider ever built, with a circumference of 27 km and a design collision energy of $\sqrt{s}$ =14 TeV. To achieve the design energy, a complex of particle accelerators is needed to progressively ramp up the energy before injecting the beam of protons into the LHC. At the beginning of the accelerator chain, hydrogen gas is ionised to give the source of protons which are then accelerated to 50 MeV by LINAC2. The protons are then further accelerated by the Proton Synchrotron Booster, the Proton Synchrotron, and the Super Proton Synchrotron, taking the beam energy to 1.4 GeV, 25 GeV, and 450 GeV respectively. Finally the particles are transferred to two counter-rotating beams in the LHC each with a design energy of 7 TeV.

The LHC has 1232 dipole magnets to steer and focus the beam, and 392 quadropole magnets to focus the beam. The magnets are made from niobium-titanium and cooled to less than 2 K using superfluid helium, giving a maximum flux density of 8.3 T. Each beam has a maximum of 2808 bunches, allowing a maximum collision rate of 25 ns. The design luminosity of the LHC is $\sim 10^{34}\,\mathrm{cm}^{-2}\,\mathrm{s}^{-1}$.

The LHC is made of 8 sections, each of which has a straight segment, a bending segment, and an interaction point. At present only 4 of the 8 interaction points house operational detectors - these are ATLAS, CMS, ALICE, and LHCb [4, 24–26]. ATLAS and CMS are general purpose detectors, primarily designed to look for the Higgs boson and heavy particles beyond the SM. ALICE is designed to look at quark-gluon plasma in heavy ion collisions - which can also be provided by the LHC.

3.2 LHCb

LHCb is a specialised detector designed for precision measurements in flavour physics. With the high collision energy provided by the LHC, the detector is in a unique environment to collect vast samples of heavy flavour decays, such as those from B and D mesons. Precision measurements of these flavour-changing decays could reveal new physics beyond the SM.

In the upcoming sections, the LHCb detector is described in the following coordinate system: the z-axis is defined to be parallel to the beam pipe, with the origin located at the LHCb interaction point. A point in the coordinate system at A is said to be downstream of a point B if $z_A > z_B$. If the opposite is true, point A is said to be 'upstream' of B. The y-axis is defined to be in the vertical direction, and the x-axis in the horizontal direction. The x-y axes define the 'transverse plane', which is used to define quantities such as transverse momentum, p_{T}, and transverse energy, E_{T}.

The LHCb detector is a forward arm spectrometer which has an angular acceptance of 10-300 mrad in the y-z plane, and 10-250 mrad in the x-z plane. This geometry is due to the b meson cross-section being predominately in the forward and backward directions, as indicated in Figure 3.1. At 8 TeV, the LHCb geometry covers 27% of the total b or $\overline{b}$ cross-section.

The detector is made-up of several sub-detectors that perform well-defined tasks. Starting from the interaction point and moving downstream there are the following detector elements: the vertex locator (VELO), a ring imaging Cherenkov detector (RICH1), the tracker turicensis (TT), the dipole magnet, further tracking stations (T1-3), a second

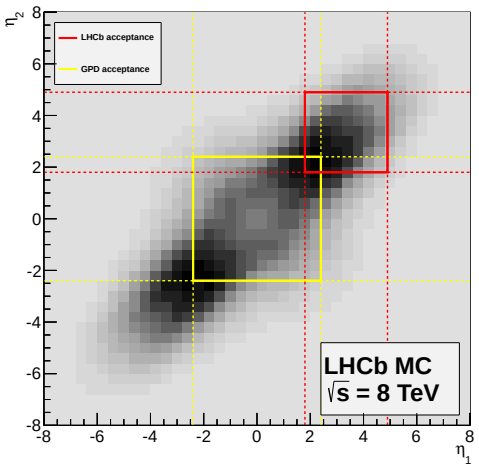

Figure 3.1: Correlation plot showing the pseudo-rapidity of $b\bar{b}$ quark pairs in proton-proton collisions at $\sqrt{s} = 8\,\text{TeV}$. Overlaid is the acceptance of both LHCb and the general purpose detectors (GPDs).

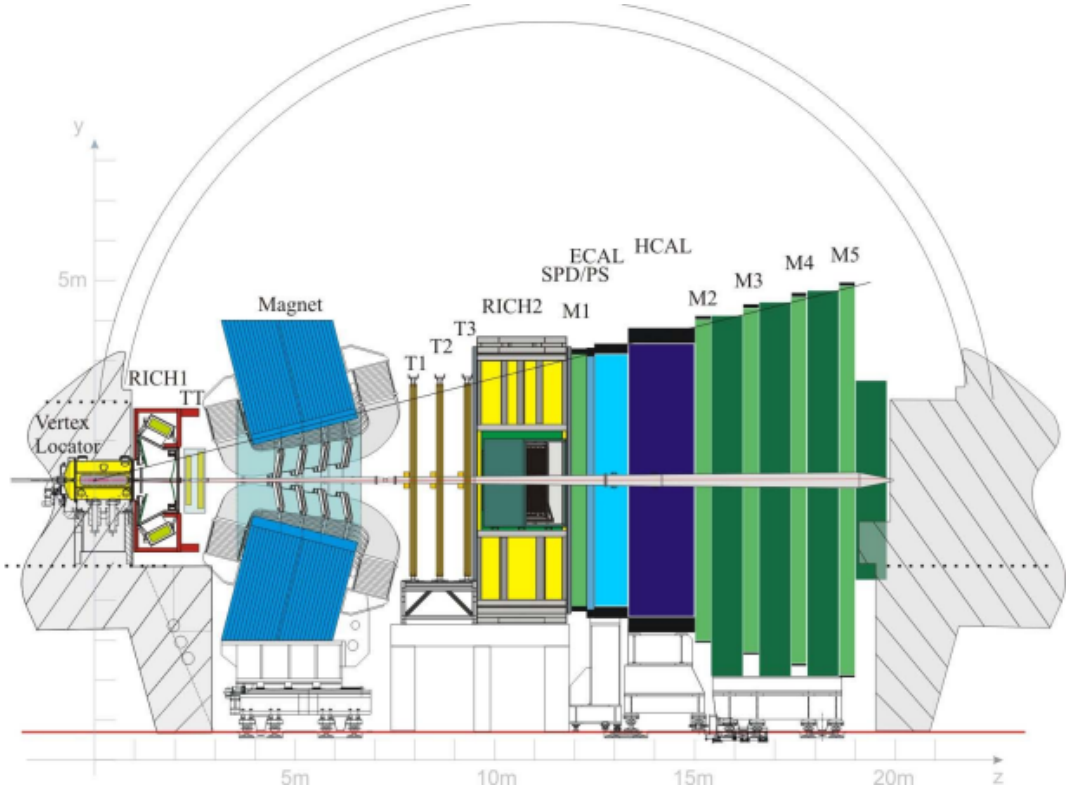

Figure 3.2: Schematic of the LHCb detector, with all sub-detectors labeled [4].

ring imaging Cherenkov detector (RICH2), a muon station (M1), the scintillating pad detector (SPD), the pre-shower detector (PS), the electromagnetic calorimeter (ECAL), the hadronic calorimeter (HCAL), and the remaining muon stations (M2-M5). A diagram of these sub-detectors is taken from [4] and shown in Figure 3.2.

The following sections give a detailed description for each of the sub-detectors, and their role in the LHCb detector. Section 3.3 describes the tracking system which includes the VELO, TT, T1-3, and the dipole magnet. Section 3.4 explains how particle identification at LHCb works with input from the RICH detectors, the calorimeters, and the muon stations. Section 3.5 describes the LHCb trigger system, and finally Section 3.6 describes the LHCb software that is used by an analyst.

3.3 Tracking

Tracking in the LHCb detector is performed by several sub-detectors: the VELO, the TT, and T1-3 [27–29]. Tracks are classified according to which of these sub-detectors they pass through:

Long tracks: These pass through all of the three sub-detectors, and therefore have momentum information and good vertexing. Long tracks are typically required in a physics analysis.

Upstream tracks: These are seen in the VELO and the TT but not after the magnet, so momentum information is limited.

Downstream tracks: These are detected in the TT and the T1-3. This track category is common for K^0_S decay products, since the former usually decay outside the VELO.

T tracks: These tracks are only detected in the T1-3 stations.

VELO tracks: These tracks are only detected in the VELO so have no momentum information. They are useful for finding the primary vertex position.

Figure 3.3 shows a diagram of all track types discussed.

3.3.1 VELO

The VELO is a silicon microstrip detector that surrounds the interaction region. Its primary function is to locate primary vertices in an event, and identify any tracks which

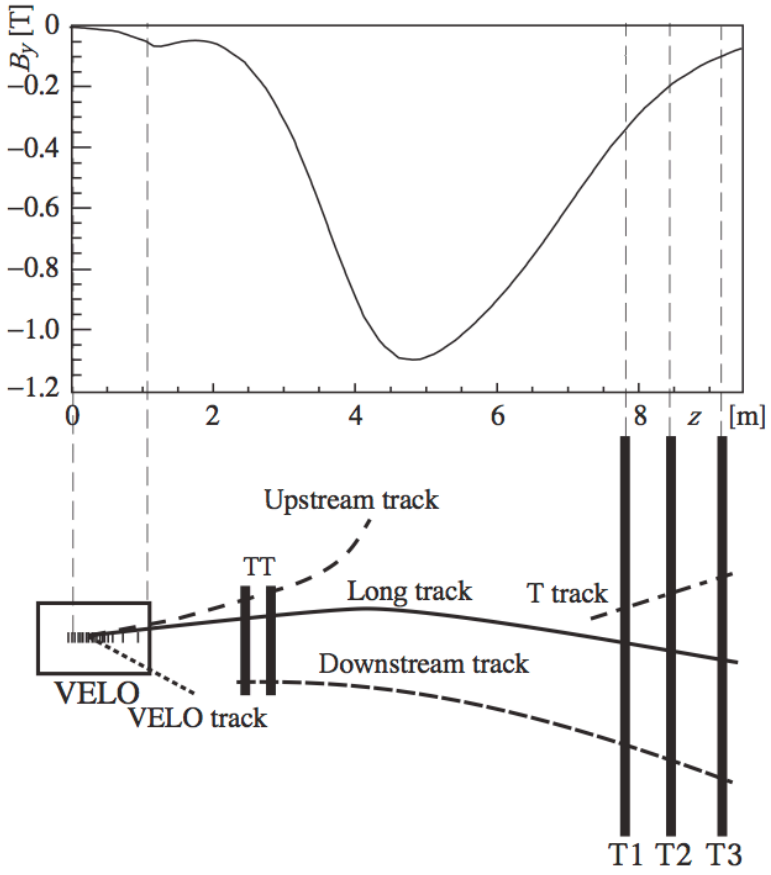

Figure 3.3: (top) The variation of the magnetic field along the y-direction (bottom) A diagram of the five different track types used at LHCb [30].

are significantly displaced from them. This allows long-lived particles such as B and D mesons to be identified. Measuring the separation of a primary and secondary vertex also allows particle lifetime to be determined. The angular coverage of the VELO is 15-300 mrad, where a track is defined to be in the 'coverage' if it passes through at least 3 detector modules.

The VELO has two halves, which each contain 21 modules positioned perpendicular to the beam. During beam injection the two halves are separated horizontally by a distance of approximately 6 cm. This is a safety measure to protect the silicon sensors from radiation damage. Once stable beams have been achieved, the two halves are moved back together, now with a small overlap between the modules - this ensures complete coverage, and helps to align the modules in reconstruction software. Each module is 300 µm thick and has an 8 mm hole for the focused beam to pass through. The z-position of the sensors is staggered between the two halves, and the spacing between

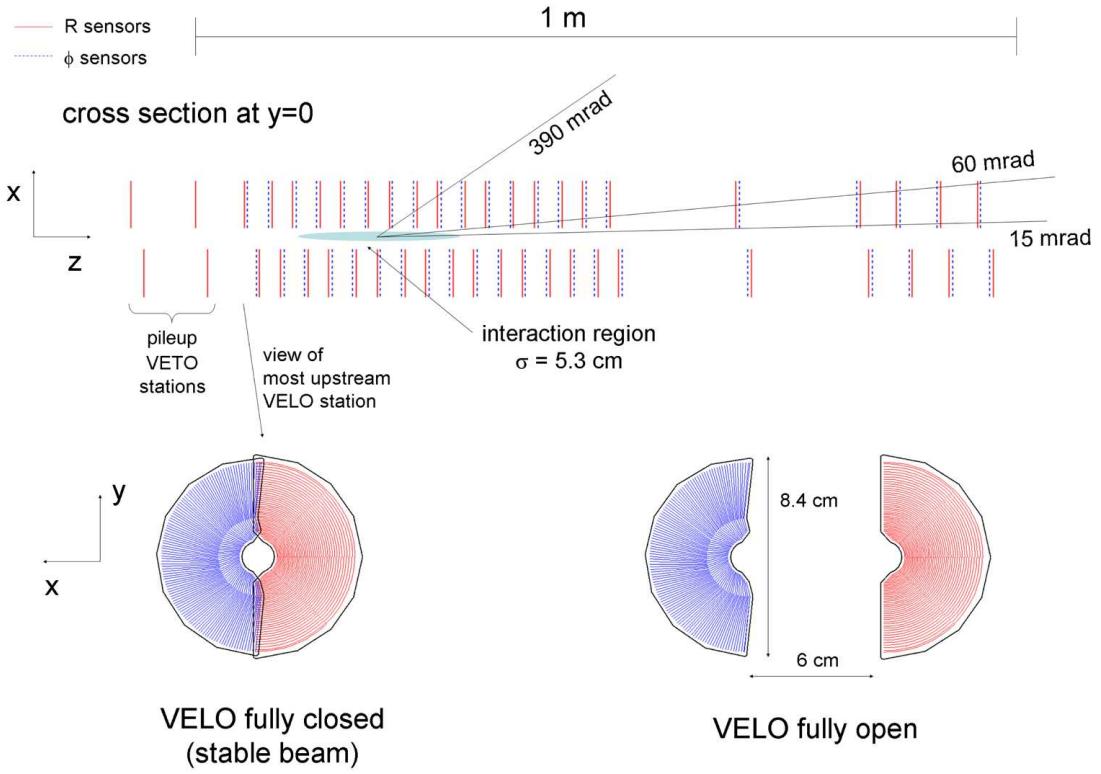

Figure 3.4: The layout of the VELO modules [4].

adjacent sensors gets larger with distance from the interaction point. The layout of the modules is pictured in Figure 3.4.

Each module has an r and a ϕ sensor, both of which are approximately semicircular with a radius of 42 mm. The r sensors have strips in 512 concentric circles - at the centre the strips have a pitch of 38 µm, increasing to 102 µm at the edge. The ϕ sensors have 683 inner strips, and 1365 outer strips, which run from the centre to the circumference of the sensor. These have a pitch which increases from 38 µm in the centre to 97 µm at the edge. A diagram of both sensor types in shown in Figure 3.5.

To determine the position of a pp collision, known as the primary vertex (PV), some modules are positioned at $z < 0$ behind the interaction point. The spread in the z-position of PVs is 5.3 cm.

Each half of the detector is kept in a vacuum which is separated from the beam vacuum by a corrugated radio frequency (RF) foil. This is made of 0.3 mm thick aluminium which prevents RF pickup from the beam, and protects the beam vacuum from detector gases.

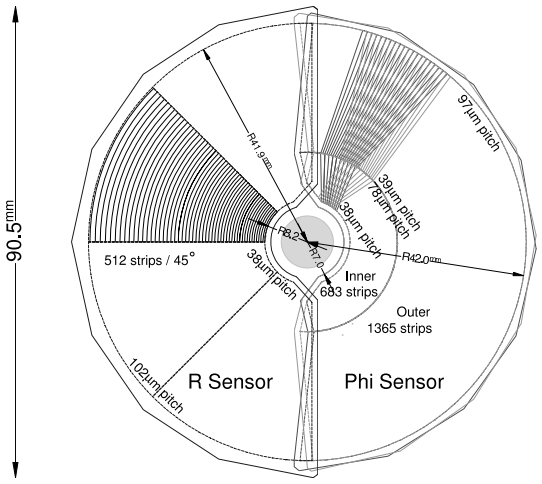

Figure 3.5: A schematic showing the strip layout in the ϕ and r sensors [4].

3.3.2 Magnet

To provide the LHCb tracking system with momentum information, a water-cooled dipole magnet is placed between the TT and T1 detectors [31]. This consists of two, 27 tonne, saddle-shape coils contained within a 1500 tonne yoke, with dimensions 11 m $\times$ 8 m$\times$5 m (x m$\times y$ m$\times z$ m). The coils are a reflection of each other in the horizontal plane, covering the full angular acceptance of 250 mrad in the vertical direction, and 300 mrad in the horizontal direction. The magnetic field is in the z-direction, so tracks are bent in the horizontal direction. The polarity of the magnet can be flipped to either 'magnet up' or 'magnet down' configuration - this allows one to make detailed systematic checks when comparing CP-conjugate processes. The magnet is designed to provide a large magnetic field in the region between the TT and T1 whilst minimising it in the RICH and VELO sub-detectors. Upstream of the TT region there is an integrated magnetic field of 0.1159 Tm, opposed to 3.616 Tm downstream. Both the VELO and RICH sub-detectors have additional magnetic shielding to stop the magnetic field degrading the quality of the apparatus in these regions. A diagram of the magnet is shown in Figure 3.6.

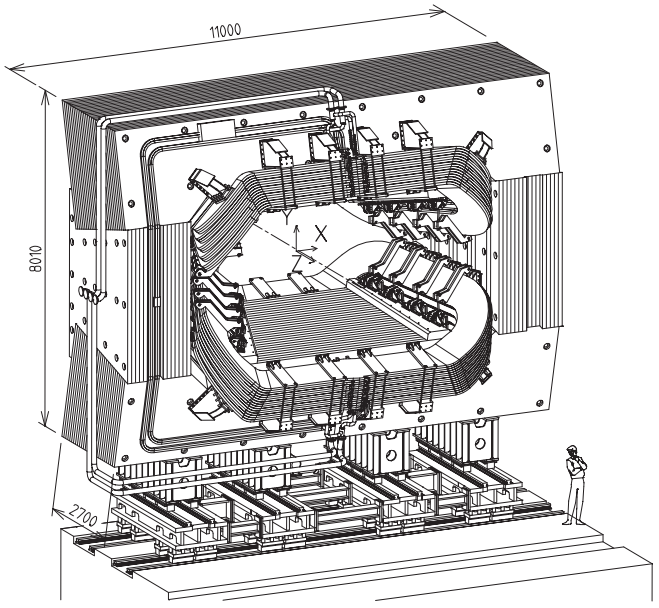

Figure 3.6: The LHCb dipole magnet [4].

3.3.3 Tracking Stations

3.3.3.1 Tracker Turicensis

The Tracker Turicensis (TT) is a silicon microstrip detector located between RICH1 and the dipole magnet. It consists of 4 layers which are 150 cm wide and 130 cm high - an area which covers the entire LHCb acceptance. The outer layers have the strips oriented vertically, whereas the two centre layers have a rotation of $+5°$ and $-5°$. The first two layers are separated from the second by 27 cm. The relative orientation of layers gives additional information on the vertical position of a track.

Each TT layer is made-up from 30 or 34 'half modules' which each have 7 silicon sensors. The sensors are 9.64 cm wide, 9.44 cm long and 500 μm thick, with a pitch of 183 μm. The readout electronics are placed outside the acceptance to reduce the material traversed by tracks within the acceptance, and thus reducing multiple scattering. The layout of a TT layer is shown in Figure 3.7. The TT has a total of 143360 readout strips, and an active area of 8.4 m^2.

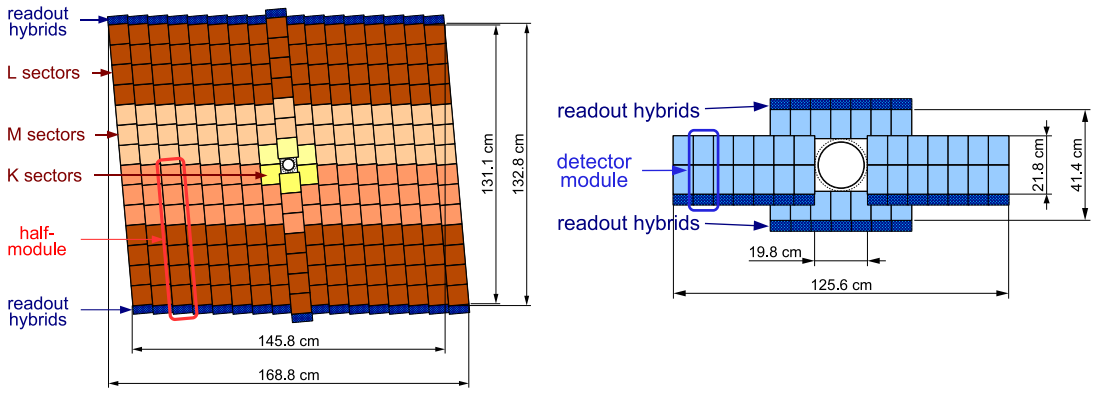

Figure 3.7: A schematic showing the arrangement of silicon sensors in the (left) tracker Turicensis (right) inner tracker [4].

3.3.3.2 Tracking Stations T1-T3

The three tracking stations T1-T3 are located downstream of the dipole magnet, and are used in conjunction with the VELO and TT to provide accurate momentum measurements.

Each tracking station has 4 layers which follow the same $(0^\circ, +5^\circ, -5^\circ, 0^\circ)$ orientation as the TT. The centre of the tracking station, the inner tracker (IT), uses the same silicon technology as the TT. The remainder of the tracking station, the outer tracker (OT), completes the LHCb acceptance, and uses straw drift tubes.

Each IT layer consists of 28 modules, each with 1 or 2 silicon sensors. The modules are arranged in a cross shape, chosen to cover the area with the largest flux of particles. Although the IT only covers 2% of the acceptance, it contains $\sim 20\%$ of the cross section. Each sensor is 7.6 cm wide, 11.0 cm long and 320-410 µm thick, with a pitch of 198 µm. The IT has a total of 129024 readout strips and an active area of $4\,\mathrm{m}^2$. The layout of the IT is displayed in Figure 3.7.

The OT layers are each made of 22 gas drift tube modules, each containing two staggered layers of 64 tubes. The tubes have an inner diameter of 4.9 mm, and contain a mixture of 70% argon, 28.5% CO_2 and 1.5% O_2. The maximum drift time is 50 ns. The OT is 6.0 m wide and 4.9 m high, giving an active area of $\sim 29\,\mathrm{m}^2$ per layer. The OT has ~ 55000 readout channels.

3.4 PID

The particle identification (PID) system of the LHCb detector allows the discrimination of different species of final state particle. Although thousands of different particle species can be produced at the LHCb collision point, there are only a limited number of stable particles that live long enough to traverse active regions of the detector. These particles are pions, kaons, protons, neutrons, electrons, muons and photons. Distinguishing these particles is vital for any analysis that wishes to separate decays which are topologically similar but have a different final state. An important example to this thesis are the decays $D^0 \to K^-\pi^+\pi^-\pi^+$ and $D^0 \to K^+\pi^-\pi^+\pi^-$- the former decay is approximately 300 times more copious, and a background to the second.

The PID system uses the following sub-detectors: two ring imaging Cherenkov (RICH) detectors, the scintillating pad detector (SPD), the pre-shower detector (PS), the electromagnetic calorimeter (ECAL), the hadronic calorimeter (HCAL), and 5 muon chambers [32, 33]. The SPD, PS, ECAL and HCAL can be grouped together and called the calorimeter system (CALO).

When looking at charged tracks, information from each of the sub-detectors gives a likelihood for the track to be a specific particle species. The likelihoods from each sub-detector can then be multiplied together to give the total likelihood:

$$\mathcal{L}(e) = \mathcal{L}^{\mathrm{RICH}}(e)\mathcal{L}^{\mathrm{CALO}}(e)\mathcal{L}^{\mathrm{MUON}}(\text{non } \mu) \tag{3.1}$$

$$\mathcal{L}(h) = \mathcal{L}^{\mathrm{RICH}}(h)\mathcal{L}^{\mathrm{CALO}}(\text{non } e)\mathcal{L}^{\mathrm{MUON}}(\text{non } \mu) \tag{3.2}$$

$$\mathcal{L}(\mu) = \mathcal{L}^{\mathrm{RICH}}(\mu)\mathcal{L}^{\mathrm{CALO}}(\text{non } e)\mathcal{L}^{\mathrm{MUON}}(\mu). \tag{3.3}$$

A likelihood alone does not provide any information - in order to discriminate between particle species one looks at likelihood ratios, or equivalently differences in log likelihoods (DLL). Of particular interest to this thesis is π/K separation, which has a DLL defined as:

$$\mathrm{DLL}_{\mathrm{K}\pi} = \log \mathcal{L}(K) - \log \mathcal{L}(\pi). \tag{3.4}$$

3.4.1 RICH Detectors

The RICH detectors provide a way to discriminate between different species of charged particles - particularly hadrons, which cannot be easily separated in the calorimeters. They work on the principle of Cherenkov radiation - when a charged particle travelling faster than the local speed of light radiates photons i.e. the particle velocity is larger than $1/n$ where n is the refractive index of the medium.

A charged particle traversing a medium with speed $\beta > 1/n$ will radiate spherical wavefronts travelling at a speed $1/n$. As the particle traverses, these spherical wavefronts interfere to give a wave that only propagates at an angle θ to the particle momentum. θ is given by the following formula:

$$\cos\theta = \frac{1}{n\beta} \tag{3.5}$$

Therefore, if one can measure θ, in a medium of known n, it is possible to determine the velocity of the particle. The particle momentum is already known from the tracking system, so the mass of the particle can be calculated. In practice there are Cherenkov photons coming from many particles, so one does not know which photons are associated with each track. To solve this, one builds a PDF for the distribution of Cherenkov photons assuming that the tracks have a specific mass hypothesis. By evaluating this PDF at the positions of photons seen in data, one obtains the likelihood $\mathcal{L}^{\mathrm{RICH}}$.

If a particle is travelling too slowly ($< 1/n$) it will not cross the threshold necessary to radiate Cherenkov light. If a particle is moving too quickly $\cos\theta \to 1/n$, so the system no longer has any power to discriminate different mass hypotheses. For this reason, LHCb has three different radiators with different refractive indices. RICH1 uses both aerogel (1.03) and C_4F_{10} (1.0014), while RICH2 uses CF_4 (1.0005) - the refractive index of each radiator for 400 nm light is indicated in parenthesis. This makes the RICH1 suitable for

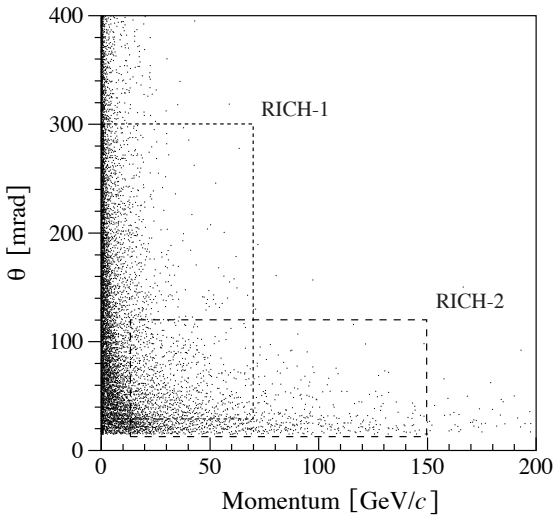

Figure 3.8: 2D histogram showing track momentum against polar angle for simulated $B^0 \to \pi^+\pi^-$ events. The superimposed boxes show the regions in which RICH1 and RICH2 are able to discriminate between different particle species [4].

particles in the momentum range 1-60 GeV, and RICH2 for higher momentum particles in the range 15-100 GeV.

The RICH1 detector covers the full LHCb acceptance, while RICH2 only has a partial acceptance of ± 15 to ± 120 mrad in the horizontal direction and ± 15 to ± 100 in the vertical direction. It is unnecessary for RICH2 to cover the full acceptance because high momentum tracks are predominantly in the more forward direction, as displayed in Figure 3.8

In both RICH detectors, Cherenkov light produced in the radiators is reflected by spherical (primary) mirrors onto two planes of flat (secondary) mirrors. Each plane of secondary mirrors then reflects the photons onto an array of hybrid photon detectors (HPDs) where their position in the HPD plane is determined.

3.4.1.1 RICH1

The RICH1 detector is located at $990\,\text{mm} < z < 2165\,\text{mm}$, between the VELO and TT. The optical layout consists of 4 spherical primary mirrors, two planes of flat secondary mirrors, and two arrays of HPDs, one located above the beam pipe, and one below.

The C_4F_{10} gas is enclosed in a sealed aluminium box which also houses the aerogel and mirror assembly. The upstream side of the box has an aperture which seals to the VELO exit window, and the downstream side has an exit window designed to minimise the material budget. The top and bottom of the gas enclosure have a window for the focussed Cherenkov photons to pass through - these are made from 8 mm quartz, and coated in magnesium fluoride for lower reflectivity. The aerogel is arranged in tiles which measure $200 \times 200 \times 51$ mm and are located at the upstream side of the gas enclosure, symmetrically around the beam pipe. The total gas volume is $3.5\,\mathrm{m}^3$.

The 4 primary mirrors have a radius of curvature measuring 2.7 m, and have dimensions of 830 mm $\times$ 630 mm when projected onto the x-y plane. The mirrors are positioned symmetrically around the beam pipe such that their edges meet along the $x = 0$ and $y = 0$ planes. Each primary mirror has one quarter of a 62.5 mm radius circle removed to allow the beam pipe to pass. The mirrors are made of a carbon fibre reinforced polymer, which is coated with Al and MgF_2.

The secondary mirrors are in two planes of 8 mirrors located above and below the beam pipe, outside of the LHCb acceptance. Each 380 mm $\times$ 347.5 mm mirror is made of simax glass, and coated with Al, SiO_2, and HfO_2.

The HPDs are located in two boxes positioned above and below the beam pipe. Each box contains 7×14 HPDs and has shielding to protect against the magnetic field of the dipole magnet. A schematic of RICH1 is shown in Figure 3.9.

The RICH1 detector weighs a total of 16 tonnes and has a low material budget of 0.08 radiation lengths ($0.08X_0$).

3.4.1.2 RICH2

The RICH2 detector is located between the tracking station T3 and the first muon detector M1, 9.5 m from the interaction point.

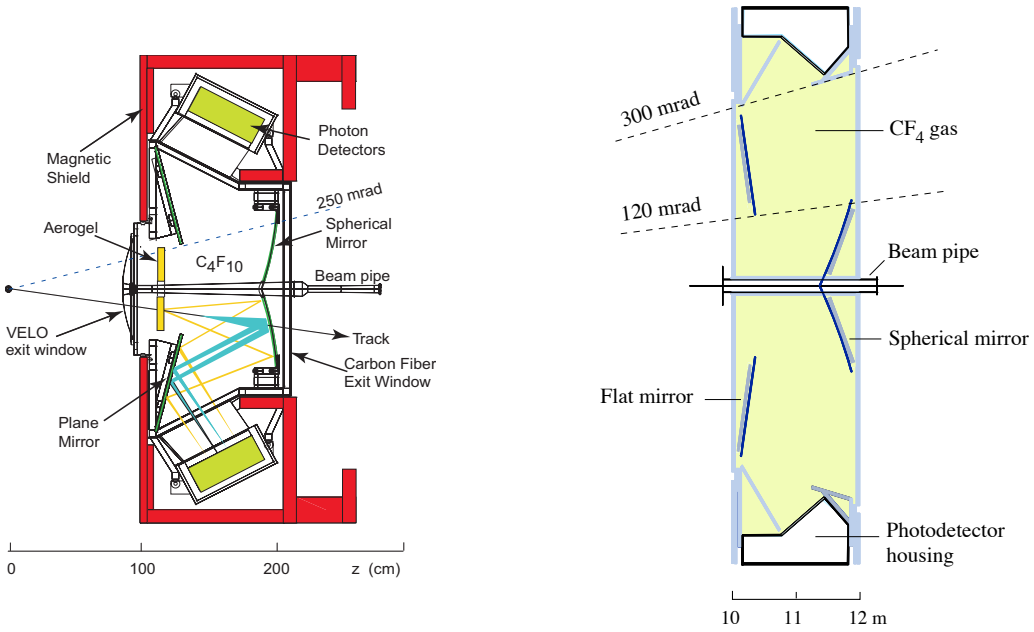

Figure 3.9: A cross-section of (left) the RICH1 detector in the y-z plane (right) the RICH2 detector in the x-z plane [32].

The optical layout consists of 52 spherical primary mirrors (or half mirrors), two planes of secondary mirrors and two arrays of HPDs, one located to the left of the beam pipe, and one to the right.

The primary mirrors have a radius of curvature measuring 8.6 m and are hexagonal in shape. The mirrors are split into two arrays located on the left and right-hand sides of the beam pipe, and meet at the $y = 0$ plane. Each primary mirror array reflects Cherenkov light onto a plane of 20 secondary mirrors, which is then reflected onto an array of 9×16 HPDs, outside the LHCb acceptance. Both the primary and secondary mirrors have a simax glass substrate, which is coated with Al, SiO_2, and HfO_2.

The CF_4 gas radiator is kept in a sealed box which also houses the mirror assembly. As for RICH1, the exit windows to the left and right of the beampipe are sealed with 5 mm thick quartz. The total gas volume is 95 m^3. A schematic of RICH2 is shown in Figure 3.9.

The RICH2 detector weighs a total of 30 tonnes and has a material budget of $\sim 0.15X_0$.

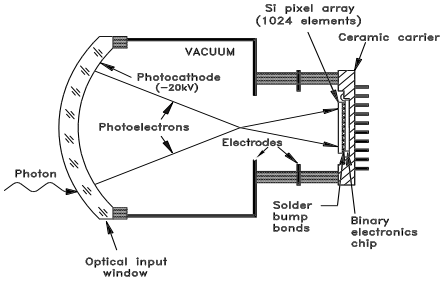

Figure 3.10: The schematic of a HPD used for detecting Cherenkov photons in the RICH detectors [32].

3.4.1.3 HPDs

The HPDs are used for detecting Cherenkov photons in both RICH1 and RICH2. At the front of the HPD is a spherical quartz window with a radius of curvature measuring 55 mm, and a thickness of approximately 7 mm. On the inner surface of the quartz is a photocathode which emits a photo-electron from an incident photon. Such a photo-electron is then accelerated through a vacuum in a 16-18 keV electric field on to a silicon pixel detector. This sensor size is 500 µm × 500 µm with 32 × 32 pixels. The schematic of a HPD is shown in Figure 3.10.

The HPDs are packed into hexagonal arrays with their centres separated by 89.5 mm. A total of 484 HPDs are used in both RICH detectors.

3.4.2 CALO

The calorimeter system at LHCb consists of the SPD, PS, ECAL and HCAL, which are located downstream of the first muon station, M1, and upstream of the remaining muon stations, M2-M5.

The goal of the calorimeter system is to identify the location and energy of hadrons, electrons and photons. The presence or absence of an energy deposit in any of these sub-detectors can also help to identify the species of a particle.

All parts of the calorimeter system are segmented to have a finer granularity near the beam line where the flux of particles is larger.

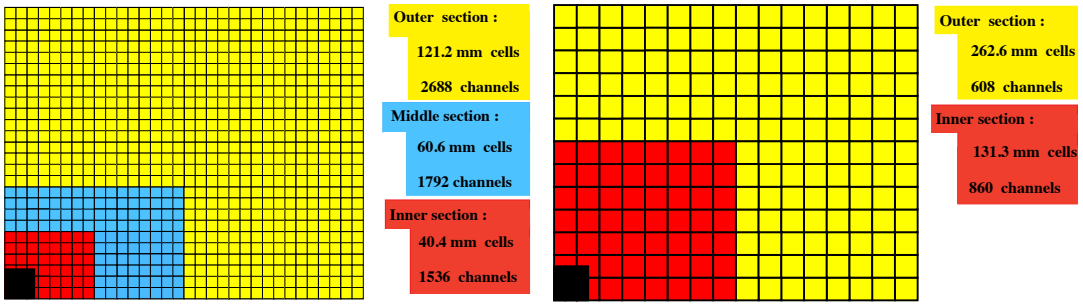

Figure 3.11: A schematic showing the division of the (left) ECAL (right) HCAL into sub-modules. The colour coding indicates different granularity of cells within the sub-module [33].

3.4.2.1 SPD + PS

The SPD and PS are located between M1 and the ECAL. Together they consist of two arrays of scintillator pads, separated by a 15 mm lead convertor, equating to 2.5 X_0. The scintillator light is carried to multi-anode photo-multiplier tubes (PMTs) via wavelength shifting fibres.

The SPD identifies charged particles, allowing the separation of photons (either prompt or from $\pi^0 \to \gamma\gamma$) from electrons. The PS then provides discrimination between $\pi^{\pm}$ and electrons, where the latter are more likely to shower in the upstream absorber.

The active area of the sub-detectors is 7.6 m $\times$ 6.2 m in the x-y plane, with the dimensions of the SPD being 0.45% smaller than the PS to maintain the same angular acceptance. The segmentation of the scintillator pads follows the same segmentation as the ECAL, which is pictured in Figure 3.11.

3.4.2.2 ECAL

The ECAL is a shashlik calorimeter designed to completely contain electron and photon showers with 25 X_0 of material. It is located downstream of the PS, approximately 12.5 m from the interaction point. The calorimeter is made-up from modules which each contain 66 layers of 2 mm lead absorber, spaced with 4 mm polystyrene scintillator. The segmentation of the modules varies across the detector, and matches the segmentation seen in the SPD and PS detectors. The scintillator light is carried to PMTs via wavelength shifting fibres.

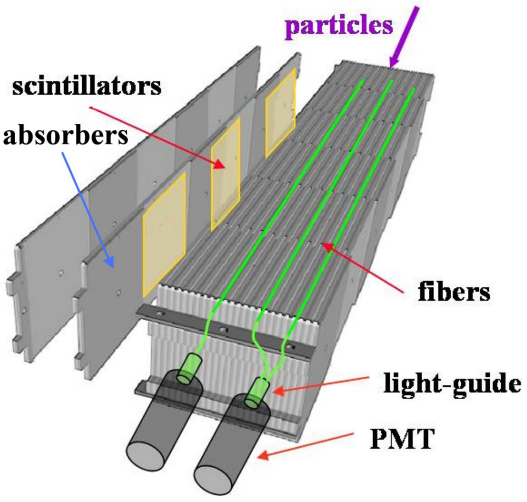

Figure 3.12: A 3D diagram of a HCAL sub-module [33].

3.4.2.3 HCAL

The HCAL is a sampling calorimeter designed to measure the energy and location of hadronic showers. The basic building block in the HCAL is a sub-module, which is built up from alternating layers of 6 mm steel and 5 mm spacers/scintillator tiles. The total size of a sub-module measures 525.2 mm wide, 262 mm tall, and 1286 mm deep, with the scintillator tiles oriented in the y-z plane - therefore, unlike the ECAL, the scintillator tiles are oriented parallel to the beam. Wavelength shifting fibres from scintillator pads are grouped together to make cells, whose segmentation is shown in Figure 3.11. The groups of fibres are read out using PMTs.

The total size of the HCAL is 8.5 m wide, 6.8 m tall, and 1.64 m deep, corresponding to 5.6 interaction lengths. The sub-detector weighs 500 tonnes.

3.4.3 Muon Stations

The muon stations have an acceptance of 20-306 mrad in the horizontal direction, and 16-258 mrad in the vertical direction. To keep this acceptance over all stations, the size in the x-y plane scales with distance from the interaction point z.

The stations M2-M5 are positioned downstream of the HCAL and are each separated by 80 cm of iron absorbers. This equates to 20 interaction lengths including the calorimeters.

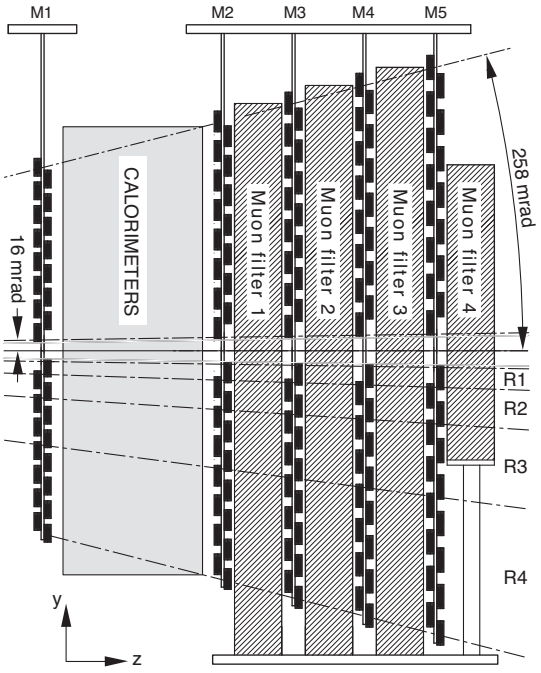

Figure 3.13: Schematic showing the layout of the 5 muon stations M1-M5 within the LHCb detector [34].

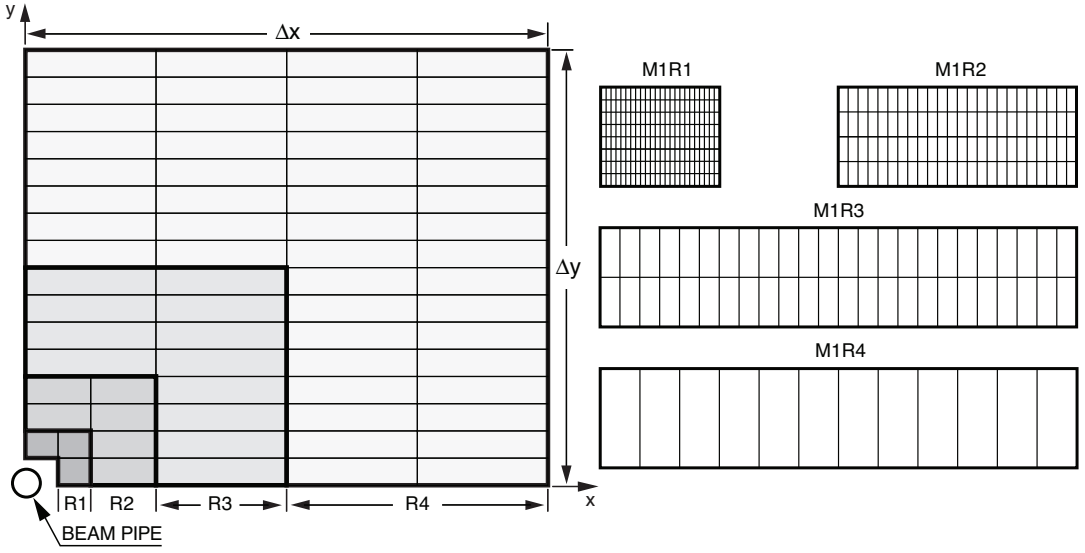

Figure 3.14: (left) A schematic showing one quarter of M1 segmented into chambers, which are organised into four different regions. (right) The division of each chamber category into logical pads in M1. In the stations M2-M3 the number of columns doubles, while in M4-M5 it halves. The number of rows remains the same in all stations [34].

A muon must have a momentum larger than 6 GeV to penetrate all layers of the detector. The station M1 is located directly upstream of the calorimeter system in order to get a better p_{T} estimate for muons. The layout of the muon stations within LHCb is pictured in Figure 3.13.

The stations M1-M3 have a good resolution in the horizontal plane, whereas M4-5 are mainly just to identify that a particle has penetrated the remaining iron absorbers. Each muon station is divided into chambers, which are then divided into 'logical pads'. The relative size of the logical pads increases with distance from the beam pipe in the ratio 1:2:4:8 - this ensures that the occupancy is approximately the same across the detector. The layout of chambers and logicals pads is pictured in Figure 3.14.

With the exception of the inner region of M1, which uses triple gas electron multipliers (GEMs), all muon chambers use multi-wire proportional chambers (MWPC). The GEMs have a higher radiation tolerance which is necessary due to the high flux of particles in this region. The MWPCs in M2-M5 have 4 gas gaps in the z-direction, whereas those in M1 only have 2 in order to reduce the amount of material before the calorimeter. The gas gaps are 5 mm deep, and filled with a mixture of Ar, CO_2 and CF_4 in the ratio 40:55:5. The anode wires run vertically through the chambers with a spacing of 2 mm in the x-direction. The readout for the MWPCs depends on the muon station, and its proximity to the beam pipe. In the outer region, R4, the y-resolution is limited to the height of the chamber - therefore wire anode readouts are sufficient. For the inner regions of M2 and M3, the highest resolution regions of the muon stations, mixed wire cathode pads are used. Finally, the remaining chambers use a cathode pad readout. The inner region of M1 has two superimposed layers of triple GEMs with an anode pad readout.

The output of a logical pad is a boolean yes/no response, which is the result of a logical OR from its 2 or 4 layers. A muon candidate is required to have hits in all 5 muon stations. The complete muon system has 1380 chambers with an active area of 435 m^2.

3.5 Trigger

The LHCb trigger is used to select interesting events in the 10 MHz of visible interactions [35]. This is done in two stages: first the hardware trigger (L0 trigger) brings the event rate to 1 MHz, then the software trigger (HLT) reduces the event rate further to 3 kHz. The basic principle is to select events which contain tracks with large p_T, E_T, and

IP, which are all properties of tracks which come from c or b hadron decays. The impact parameter (IP) is defined as the shortest distance between a track and its primary vertex - this variable is commonly used to distinguish tracks coming from secondary vertices. The HLT also has more flexible trigger options to select a specific decay, or a group of decays i.e. exclusive or inclusive triggers.

The L0 trigger uses information from the calorimeter and muon system to build four types of candidate; `L0Electron`, `L0Hadron`, `L0Photon`, and `L0Muon`. Each of these candidates is then required to pass a threshold in order to be accepted by the L0 decision unit (L0DU). The trigger is synchronised with the bunch crossings, and therefore a decision is made for each event.

`L0Hadron`, `L0Electron` and `L0Photon` look at clusters defined by 2×2 blocks of calorimeter cells. The cluster with the largest E_{T} from the ECAL and HCAL is kept as the `L0Hadron` candidate. The `L0Electron` candidate is the cluster with the largest E_{T} in the ECAL which also has 1 or 2 PS hits. The `L0Photon` candidate is the cluster with the largest E_{T} in the ECAL which also has 1 or more SPD hits.

Two `L0Muon` candidates are picked in each detector quadrant by finding the two highest p_{T} muons. The p_{T} is computed by looking at the position of the track in M1 and M2, giving a momentum resolution of $\sim 20\%$. From these 8 candidates, two quantities $p_{\mathrm{T}}^{\mathrm{max}}$ and $p_{\mathrm{T}}^{\mathrm{max}} \times p_{\mathrm{T}}^{\mathrm{2nd\ max}}$ are computed. If either of these quantities pass a certain threshold, the event is kept. The L0 trigger also has a global event cut on the total number of hits in the SPD. This is because events with a high particle multiplicity have a very long processing time in the HLT.

The HLT is a two-stage C++ application which can be easily reprogrammed to be flexible to changes in running conditions and physics goals. Both HLT stages have access to data from all sub-detectors (although they do not necessarily use it all) so are able to make more informed decisions on each event. To speed-up decision time in the HLT a simplified tracking algorithm is used - this has a tracking uncertainty of $\sim 1\%$, which can be compared to the offline uncertainty of 0.35%.

The first stage (HLT1) has a single track trigger line, requiring a track with high p_{T}, good track χ^2 and a large IP. The second stage (HLT2) is divided into many different trigger lines, each targeted towards a different physics goal. HLT2 is able to combine tracks in order to reconstruct the momentum and invariant mass of composite particles.

The trigger options at any given time are encoded into a Trigger Configuration Key (TCK), which is an 8 digit hexadecimal. This is given to the event filter farm, where 29500 copies of the HLT are run simultaneously over an array of micro-processors.

To look for a specific decay chain in LHCb data, one uses DaVinci (see Section 3.6) to build a ROOT nTuple containing potential candidates for the decay. It is often useful to see how these candidates interacted with the trigger lines; and for this some terminology is introduced; if a candidate is TOS (Trigger On Signal) with respect to a trigger line, this means that the candidate alone was sufficient to fire the trigger i.e. if everything was removed from the event except the candidate, the trigger would still fire. If a candidate is TIS (Trigger Independent of Signal) with respect to a trigger line, this indicates that the trigger would still have fired even if the candidate was removed from the event.

3.6 Software

The LHCb software is based on the C++ Gaudi framework. Built on top of this is a selection of projects that are used for tasks such as Monte Carlo (MC) generation, event reconstruction, and physics analysis.

The Gauss project is used for generating MC samples. This includes event generation, event decay, and interactions with the detector material. The event generation is usually handled by Pythia [36, 37], then event decay by EvtGen [38] or Mint. Final-state radiation is performed using Photos. Geant4 [39] is used to describe interactions with the detector material i.e. multiple scattering in the tracking stations, showering in the calorimeters. This stage requires a detector description database (DDDB) which describes the layout of all detector elements. The output of Gauss is 'hits' in the areas of active material.

BOOLE takes the hits from GAUSS and digitises the detector response. This includes the effects from detector resolution and imperfections. The output of BOOLE is the same as real data, although it also contains the MC truth.

BRUNEL is used for event reconstruction. This includes reconstructing tracks, Cherenkov photons, and calorimeter clusters. These tasks require a conditions database (CondDB) which describes the alignment and calibration of the detector. When reconstructing MC data, BRUNEL is also used to associate reconstructed tracks with the particles generated in GAUSS - this process is known a 'truth matching'. Occasionally a track reconstructed in BRUNEL cannot be matched to a generated particle - this is known as a 'ghost' track.

MOORE is the software used by the HLT, which is run online in the event filter farm. It can also be run offline for applying the HLT to MC data.

DAVINCI is used for offline analysis. This involves finding candidates for a particular decay chain in reconstructed data. From these candidates, one can then calculate all the quantities needed for offline analysis - examples being particle momentum, lifetime or PID information. All this information can then be saved to ROOT nTuples. When using DAVINCI on MC, it is also used to assign a background category to each event. Background category 0, for instance, is the signal category - this means that the reconstructed decay chain is completely matched to the same decay chain in the generated MC (from GAUSS).

3.7 Running Conditions

Although the design luminosity of the LHC is $\sim 10^{34}\,\mathrm{cm}^{-2}\,\mathrm{s}^{-1}$ [3], the LHCb detector is designed to run at a lower luminosity of $\sim 2 \times 10^{32}\,\mathrm{cm}^{-2}\,\mathrm{s}^{-1}$. This reduces the average number of visible interactions, μ_{vis}, also known as pile-up, in each event. Lower pile-up makes events easier to reconstruct and analyse, improving resolution and systematic uncertainties. It also gives lower detector occupancy, resulting in less radiation damage to the detector.

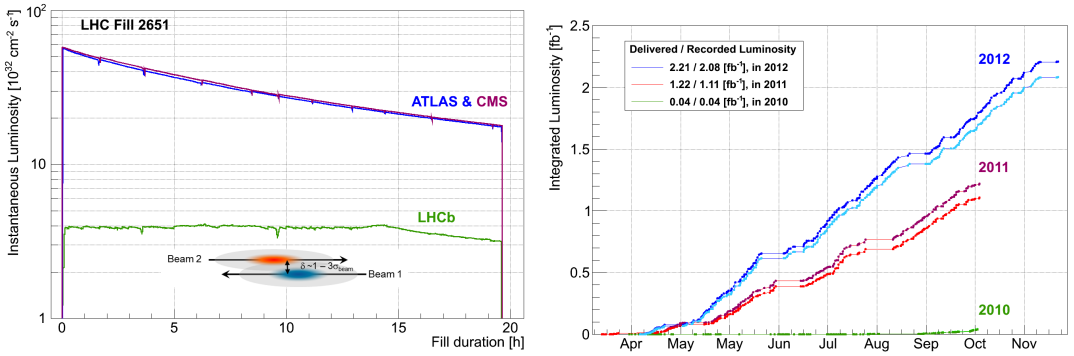

Figure 3.15: (left) The instantaneous luminosity of ATLAS, CMS, and LHCb during LHC fill 2651 (right) The cumulative integrated luminosity collected by LHCb during Run I data-taking. Also shown is the total delivered luminosity, indicating the excellent detector performance.

LHCb started collecting data in 2009, when the LHC was running at a centre of mass collision energy of 0.9 TeV. This data was used for commissioning the detector, and calibrating the sub-detectors.

At the beginning of 2010, the beam energy was increased to 3.5 TeV, with an instantaneous luminosity of $10^{28}\,\mathrm{cm}^{-2}\,\mathrm{s}^{-1}$. The luminosity was quickly increased over the year to reach $10^{32}\,\mathrm{cm}^{-2}\,\mathrm{s}^{-1}$ with a pile-up of $\sim 2.5\mu_{\mathrm{vis}}$. Although the luminosity was roughly in line with the designed value, the pile-up was much higher due to a lower number of bunches circulating in the beam. The total amount of data collected in 2010 was $38\,\mathrm{pb}^{-1}$.

In 2011 the bunch spacing was decreased to 50 ns, giving a total of 1300 bunches per beam. This allowed a higher instantaneous luminosity of $3.5 \times 10^{32}\,\mathrm{cm}^{-2}\,\mathrm{s}^{-1}$ with a lower pile-up. Luminosity levelling was also introduced - this is the process where the overlap between beams is adjusted during a fill to achieve a constant luminosity to within 5%. The effect of the luminosity levelling procedure is shown in Figure 3.15. This process gives the same detector occupancy throughout running, reducing systematic uncertainties. The total amount of data collected in 2011 was $1.11\,\mathrm{fb}^{-1}$.

In 2012 the the beam energy was increased to 4 TeV, with the luminosity also increased to $4.0 \times 10^{32}\,\mathrm{cm}^{-2}\,\mathrm{s}^{-1}$. The total amount of data collected in 2011 was $2.08\,\mathrm{fb}^{-1}$. The total luminosity collected by LHCb during 2010, 2011, and 2012 is pictured in Figure 3.15 - this period of running is defined as Run I.

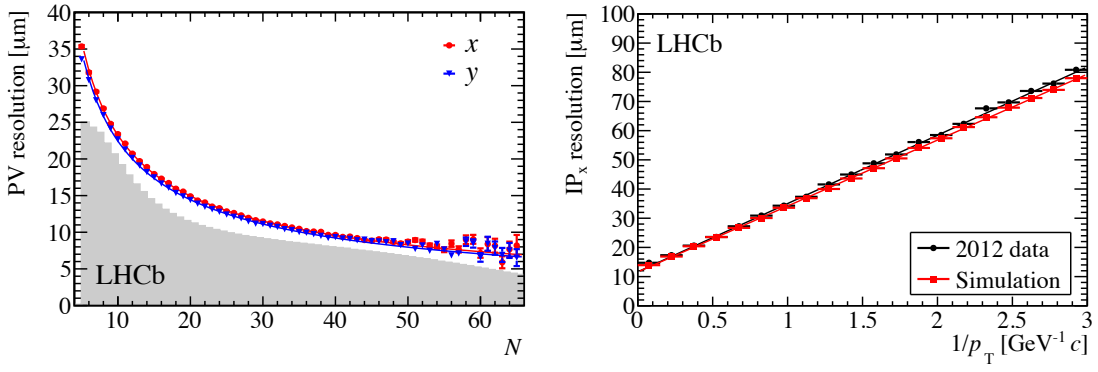

Figure 3.16: (left) The primary vertex resolution against track multiplicity for events with only one primary vertex. Both the x (blue) and y (red) resolution is shown. The shaded histogram shows the number of tracks in each primary vertex for events passing HLT2. (right) The x resolution of the impact parameter with respect to $1/p_T$ in 2012 data [30].

3.8 Performance

This section gives a short review of LHCb performance during Run I data taking. Important to this thesis is a time-dependent measurement of $D^0 \to K^+\pi^-\pi^+\pi^-$ decays, therefore focus is directed to the areas of performance that are important for this decay mode. Further details can be found in [30, 40–43].

The D^0 mesons produced within the LHCb acceptance will usually have a large boost in the z-direction, and therefore have measurable flight distance before decaying. In order to distinguish the D^0 decay vertex from the PV, one requires precise tracking near the interaction point. Figure 3.16 illustrates the PV resolution in 2012 as a function of the number of tracks, or 'track multiplicity'. Figure 3.16 also shows the IP resolution as a function $1/p_T$ during 2012 data taking. This demonstrates an excellent resolution of $< 35\,\mu\text{m}$ for tracks with $p_T > 1\,\text{GeV}$.

Measuring D-mixing in $D^0 \to K^+\pi^-\pi^+\pi^-$ decays (as will be discussed in Chapter 5) requires excellent lifetime resolution. Figure 3.17 shows the decay time resolution for $B_s^0 \to J/\psi\,\phi$ as a function of B_s^0 momentum.

The tracking efficiency can be defined as the probability to reconstruct a charged track that traverses the entire detector. Shown in Figure 3.17 is the reconstruction of a typical

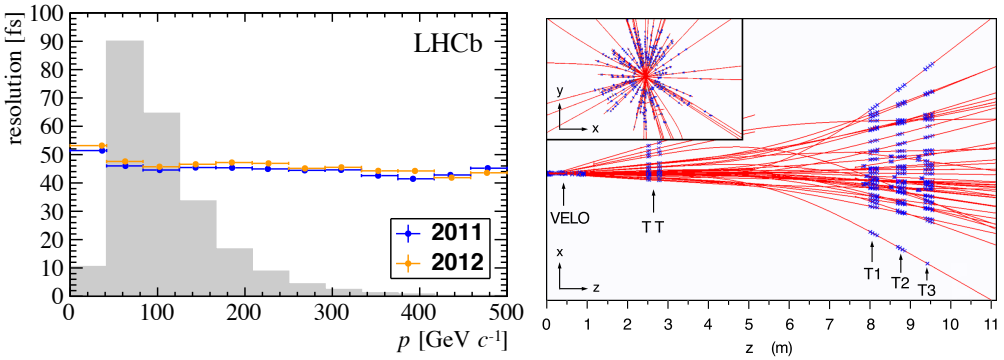

Figure 3.17: (left) The decay time resolution for $B_s^0 \to J/\psi\,\phi$ decays as a function of B_s^0 momentum in 2011 and 2012 data. Only events with one primary vertex are used. The shaded histogram shows the distribution of momentum in the same decay mode. (right) A typical reconstructed event in the LHCb detector [30].

event in the LHCb detector, highlighting the different sub-detectors. The tracking efficiency at LHCb is shown in Figure 3.18 as a function of several variables. This efficiency is determined using a data driven 'tag and probe' technique which uses $J/\psi \to \mu^+\mu^-$ decays. The first muon, 'the tag', is fully reconstructed, while the second, 'the probe', is reconstructed using only a subset of sub-detectors. One can then look in the remaining sub-detectors to see if the entire track was reconstructed. The excellent performance demonstrated in Figure 3.18 is particularly important for multi-body final states such as $D^0 \to K^-\pi^+\pi^-\pi^+$, where a large number of charged tracks have to be reconstructed.

For final states containing hadrons, input from the RICH detectors is essential for distinguishing the different hadron species. This is very important for the suppressed decay $D^0 \to K^+\pi^-\pi^+\pi^-$, because a simultaneous misidentification of $K \to \pi$ and $\pi \to K$ in the favoured $D^0 \to K^-\pi^+\pi^-\pi^+$ decay results in a peaking background. Figure 3.19 shows the clear separation between muons, protons, pions, and kaons that is possible using the gas radiator in RICH1. The Cherenkov angle resolution for the two gas radiators is as follows: 1.618 ± 0.002 mrad for RICH1 (C_4F_{10}) and 0.68 ± 0.02 mrad for RICH2 (CF_4). This can be compared to the MC resolutions of 1.52 ± 0.02 mrad and 0.68 ± 0.01 mrad respectively. The determination of the RICH1 resolution is illustrated in Figure 3.19.

To select a particle of a particular species, the DLL variables defined in Equation 3.4 are used. One can cut at different values to get the purity required, at the expense

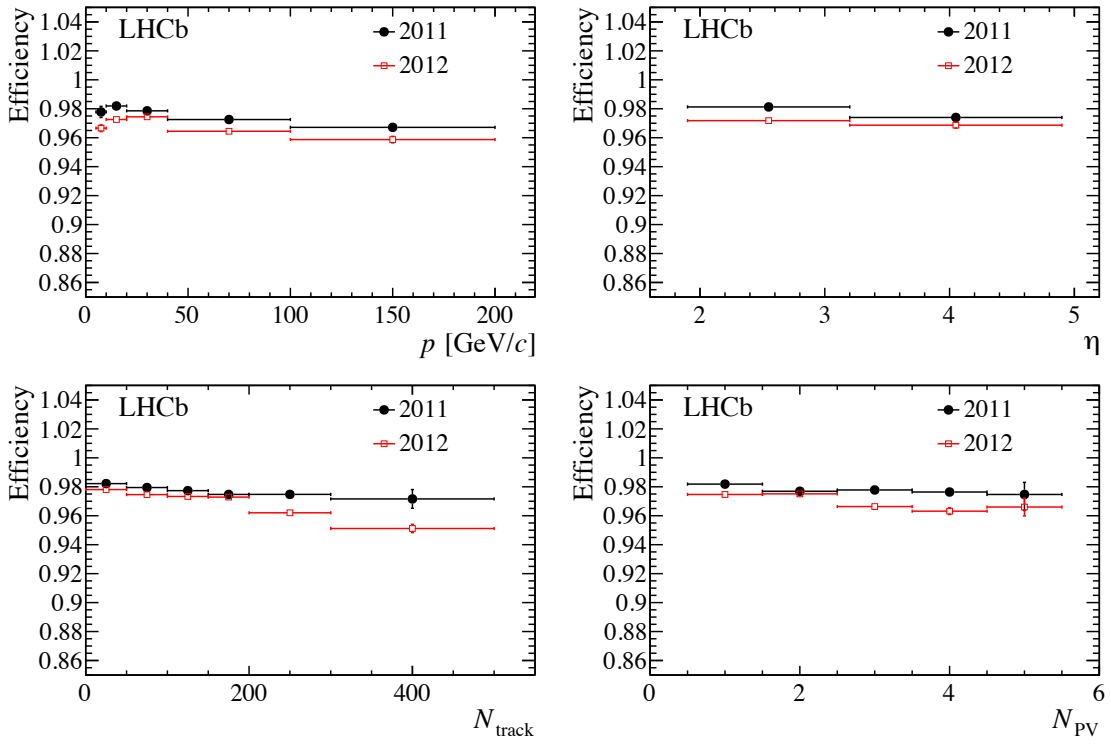

Figure 3.18: The track reconstruction efficiency as a function of track momentum, p, pseudo-rapidity, η, track multiplicity, N_{tracks}, and number of primary verticies N_{PV}. This is shown for both 2011 (black) and 2012 (red) data [30].

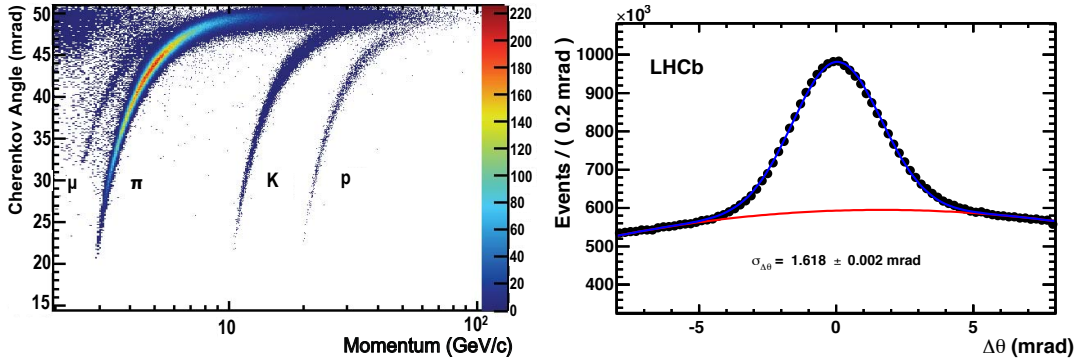

Figure 3.19: (left) The measured Cherenkov angle in the C_4F_{10} radiator against track momentum. Only tracks with non overlapping Cherenkov rings have been used. (right) The Cherenkov angle resolution of the C_4F_{10} radiator, where $\delta\theta$ is the difference between the measured and expected Cherenkov angle. This uses high momentum tracks from 2011 data, such that all particle species have similar Cherenkov angles (see left figure) [41].

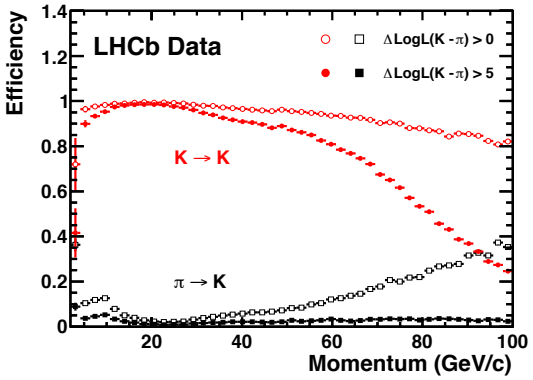

Figure 3.20: Efficiency of selecting kaons, and the misidentification rate of $\pi \to K$, both shown against track momentum. The distributions are shown for both $\mathrm{DLL}_{\mathrm{K}\pi} > 0$ and $\mathrm{DLL}_{\mathrm{K}\pi} > 5$. These efficiencies are determined using a sample of $D^{*+} \to D^0(K^-\pi^+)\pi^+$ decays [41].

of efficiency. Figure 3.20 shows the kaon selection efficiency, and pion misidentification rate for two different $\mathrm{DLL}_{\mathrm{K}\pi}$ cuts; one targeted at high efficiency, and the other at high purity. With a loose cut on $\mathrm{DLL}_{\mathrm{K}\pi} > 0$, and averaged over the momentum range 2-100 GeV, the kaon efficiency is $\sim 95\%$, while the pion misidentification rate is $\sim 10\%$. With a tighter cut on $\mathrm{DLL}_{\mathrm{K}\pi} > 5$, the pion misidentification rate is reduced to only $\sim 3\%$.

Chapter 4

Constraining charm interference parameters using D-mixing

4.1 Introduction

The measurement of the CKM phase γ (Section 2.3.3.1) from $B^- \to DK^-$, $D \to f$ [9, 10, 23, 44–46] (where f represents a multi-body final state accessible to both D^0 and $\overline{D}^0$) depends on the correct description of the interference between the $D^0 \to f$ and $\overline{D}^0 \to f$ decay amplitudes.[1] This can be obtained from an amplitude model (Section 4.2.2) of the D decay. However, this model dependence can lead to significant systematic uncertainties. Alternative model-independent methods use experimental input [8, 47] to remove this source of systematic uncertainty. This input can be summarised in the complex interference parameter $\mathcal{Z}^f = R_D^f e^{-i\delta_D^f}$, where R_D^f and δ_D^f are the coherence factor and average strong phase-difference introduced in [8]. $\mathcal{Z}^f$ can be measured exploiting quantum-correlated $D\overline{D}$ pairs available at experiments operating at the charm threshold, such as CLEO-c or BES III [8, 11, 47–52]. In this chapter it is demonstrated that the same input can also be provided by charm mixing.

Although the simulation studies in this chapter could, in principle, be applied to several decay modes, it was chosen to focus on $D \to K\pi\pi\pi$ decays. As pictured in Figure 4.1,

[1] Charged conjugate modes are implied throughout the chapter unless stated otherwise. The symbol D is used to represent any superposition of D^0 and $\overline{D}^0$.

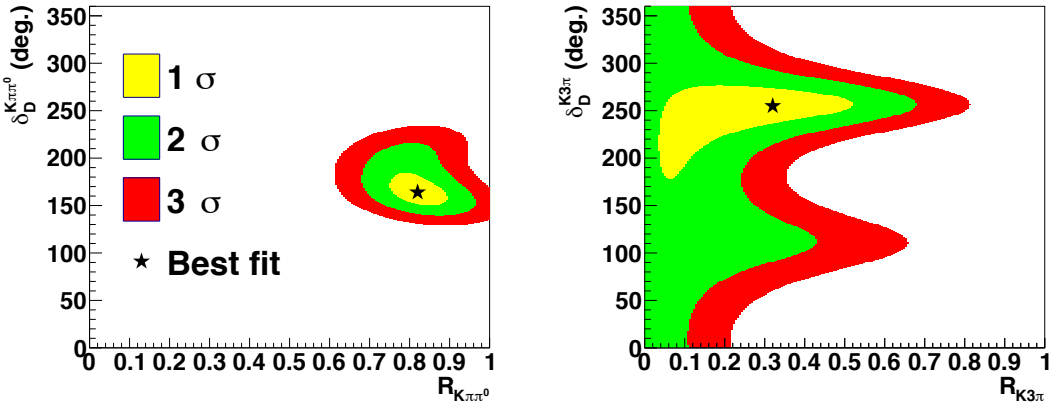

Figure 4.1: Constraints on $\mathcal{Z}^{K\pi\pi^0}$ (left) and $\mathcal{Z}^{K3\pi}$ (right) obtained by CLEO-c [11, 48] from the charm threshold. The results are shown in polar coordinates $\mathcal{Z}^f = R_D^f e^{-i\delta_D^f}$. The black star indicates the location with the smallest χ^2.

the constraints on $\mathcal{Z}^{K3\pi}$ are fairly weak when compared to others such as $\mathcal{Z}^{K\pi\pi^0}$. The potential benefits in this decay mode are therefore much larger.

The chapter is organised as follows: Section 4.2 gives an introduction to multi-body D^0 decays, discussing the dimensionality and parameterisation of phase space for N-body decays, and reviewing phase space dependent decay amplitudes. Section 4.3 reviews the mixing formalism for multi-body D decays, building on and extending the treatment presented in [53, 54]. A unified description of the mixing-induced interference effects is presented for decays to self-conjugate and non-self-conjugate final states. Section 4.4 introduces a new method to constrain the complex interference parameter $\mathcal{Z}^f$, which requires measuring the time-dependent rate of multi-body D^0 decays (charm mixing).

4.2 Multi-body D^0 decays to N pseudo-scalars

This section gives a brief description of the formalism for a D^0 meson decaying to N pseudo-scalar daughters.

4.2.1 Phase space dimensionality and parameterisation

The daughters of a multi-body D decay ($N > 2$) can decay into many different topological configurations that are not interchangeable under rotation. The abstract space

describing these configurations is known as the phase space of the decay. The dimensionality of the phase space is dependent on N.

Without loss of generality one can assume that the D^0 is at rest, $p_{D^0} = (\mathbf{0}, m_{D^0})$. The D^0 daughters are described by N 4-vectors, p_i, giving $4N$ degrees of freedom. When dealing with a specific final state f the mass of the daughters, m_i, is known, adding N constraints of the form $p_i^2 = m_i^2$. The sum of 4-vectors in the initial and final state must also be equal, $p_{D^0} = \sum p_i$, giving a further 4 constraints. Finally, the topology of the decay does not depend on the overall orientation, therefore one can define that daughter 1 points along the z-axis and daughter 2 is in the x-z plane. This adds a further 3 constraints[2]. Therefore the total degrees of freedom in a $D^0 \to N$-body decay is $3N - 7$.

For a two-body decay, there no degrees of freedom, meaning the phase space of the decay is fixed i.e. in the D^0 rest frame, the daughters are always back to back with momenta determined by the particle masses.

For a three-body decay, there are 2 degrees of freedom, or a 2D phase space. A popular way to describe 2D phase space is the Dalitz plot [55] - this uses the squared invariant mass of two daughter pairs to fully describe the system[3]. Figure 4.2 shows the Dalitz plot for $D^+ \to K^+K^-\pi^+$ decays, with the intermediate resonances $\overline{K}^*(892)^0$ and $\phi(1020)^0$ clearly visible [56].

For four-body decays, the phase space is 5D. This makes experimental measurements of 4-body decays particularly challenging because detection efficiencies and the underlying physics regularly have to be described over the full dimensionality of phase space. Often used to parameterise 4-body phase space is the squared invariant mass of different daughter combinations e.g. in the decay $0 \to 1234$ one might use $m^2(12)$, $m^2(23)$, $m^2(34)$, $m^2(123)$, $m^2(234)$. An example of this is seen in Figure 4.3 for the decay $D^0 \to K^+K^-\pi^+\pi^-$, where the authors [57] have used 1D projections of these variables to visualise the phase space. Although this appears a natural extension to the Dalitz plot, which would fully describe the 4-body phase space, this is not quite the case. A

[2]For two-body decays, the second daughter is automatically in the $x - z$ plane because daughters 1 and 2 are back to back. Therefore, for two-body decays there are only 2 additional constraints.

[3]The 'original' Dalitz plot used different variables, although these variables are now the most common in the literature.

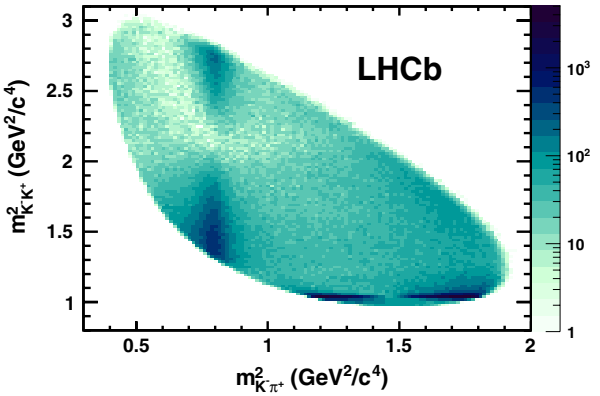

Figure 4.2: The Dalitz plot for $D^+ \to K^+K^-\pi^+$ decays collected by LHCb and published in [56]. Clearly visible as bands in the horizontal and vertical directions are the intermediate resonances $\overline{K}^*(892)^0$ and $\phi(1020)^0$, decaying to $K^-\pi^+$ and K^-K^+ respectively.

phase space point described by invariant masses is insensitive to changes in parity i.e. $m_{12} = (\mathbf{p_1}, E_1).(\mathbf{p_2}, E_2) \equiv (-\mathbf{p_1}, E_1).(-\mathbf{p_2}, E_2)$. This is not an issue in 3-body decays because they are parity-invariant. This invariance is due to the three daughters always decaying in a plane - in this case, the operation of parity can equally be achieved by a rotation out of the plane. A 4-body decay, however, is not constrained to a plane, and is therefore not inherently parity-invariant. Although using invariant masses does not give a complete description of the 4-body phase space it is still useful in many scenarios - an example being the description of phase space dependent detection efficiencies, which are often assumed parity-invariant.

4.2.2 Decay amplitudes

The way in which a multi-body decay is distributed over phase space (examples shown in Figure 4.2 and Figure 4.3) is dependent on the underlying physics. One can summarise this underlying physics in a phase space dependent amplitude such as,

$$\mathcal{A}(\mathbf{p}) \equiv \langle f_{\mathbf{p}}|\hat{H}|D^0\rangle \equiv A(\mathbf{p})e^{i\delta(\mathbf{p})}, \tag{4.1}$$

where f is the final state, $A(\mathbf{p})$ is the magnitude of the amplitude, $\delta(\mathbf{p})$ is its phase, and $\mathbf{p}$ parameterises a point in the multi-body phase space. $\hat{H}$ is the interaction Hamiltonian

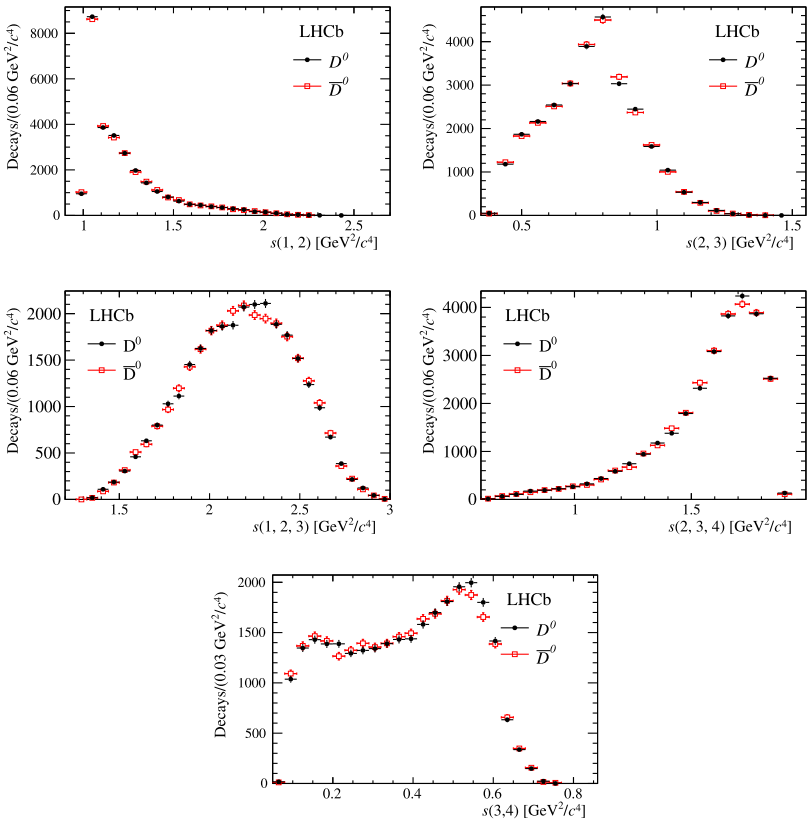

Figure 4.3: Squared invariant mass projections for the decay $D \to KK\pi\pi$, where $s(i,j) = (p_i + p_j)^2$ and $s(i,j,k) = (p_i + p_j + p_k)^2$. The data were collected by LHCb and published in [57]. The black markers show $D^0 \to K_1^+ K_2^- \pi_3^+ \pi_4^-$ and the red markers show $\overline{D}^0 \to K_1^- K_2^+ \pi_3^- \pi_4^+$. The subscripts on the decay daughters indicate the numbering scheme for $s(i,j)$ and $s(i,j,k)$.

relevant for the decay. The probability density for a particle to decay to a point $\mathbf{p}$ is given by

$$|\mathcal{A}(\mathbf{p})|^2 \frac{d\Phi}{d\mathbf{p}}, \tag{4.2}$$

where $\frac{d\Phi}{d\mathbf{p}}$ gives the density of states at $\mathbf{p}$.

A current hot-topic in multi-body decays is finding an analytic expression for $\mathcal{A}(\mathbf{p})$ by fitting experimental data with an *amplitude model*. To make such a model, one has to make an educated guess about the resonant substructure of the decay, then allow parameters describing these resonances to float in the fit. For example the decay $D^0 \to K^+\pi^-\pi^+\pi^-$ can decay by both $K^*(892)\rho(770)$ and $a_1(1260)^+K^-$ – each of these

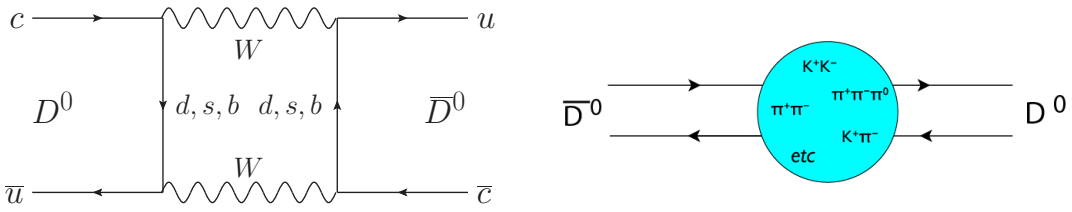

Figure 4.4: (Left) Feynman diagram for short range D-mixing. (Right) long range contributions to D-mixing that proceed via intermediate resonances.

resonances will interfere with one another and sculpt the shape and phase of the amplitude $\mathcal{A}(\mathbf{p})$. Because this thesis will use existing amplitude models, it is not concerned with their construction - here it is only important to know that the amplitude model gives a magnitude and phase at each point in phase space.

4.3 D-mixing phenomenology

Mixing is the process where a neutral meson oscillates to its own anti-particle. This process is well established in the s and b quark sectors, where mixing has been observed in K^0, B^0, and B_s^0 mesons [58–60]. Here mixing is dominated by short distance box diagrams, making theoretical predictions relatively simple.

In the charm sector, short distance interactions are highly suppressed in the SM ($< 10^{-5}$) [61], although mixing has been observed at $\sim 10^{-2}$. This is due to contributions from long-distance interactions which cannot be calculated using perturbative expansions, making theoretical predictions difficult. A long-distance interaction is when the mixing proceeds by an intermediate resonance that is accessible to both D^0 and $\overline{D}^0$ such as $K^+\pi^-$, $K^+\pi^-\pi^0$ or $K^+\pi^-\pi^+\pi^-$. Figure 4.4 shows diagrams for both short and long range D-mixing contributions.

4.3.1 Mixing Formalism

The mass eigenstates $|D_1^0\rangle$ and $|D_2^0\rangle$, with masses M_1, M_2 and widths $\Gamma_{D,1}, \Gamma_{D,2}$, are related to the flavour eigenstates $|D^0\rangle$ and $|\overline{D}^0\rangle$ through

$$\begin{aligned} |D_1^0\rangle &= p|D^0\rangle + q|\overline{D}^0\rangle, \\ |D_2^0\rangle &= p|D^0\rangle - q|\overline{D}^0\rangle, \end{aligned} \tag{4.3}$$

where p and q are complex numbers that satisfy $|q|^2 + |p|^2 = 1$. Also defined are,

$$M \equiv \frac{M_1 + M_2}{2}, \quad \Gamma_D \equiv \frac{\Gamma_{D,1} + \Gamma_{D,2}}{2}, \quad \Delta M \equiv M_2 - M_1, \quad \Delta\Gamma_D \equiv \Gamma_{D,2} - \Gamma_{D,1} \tag{4.4}$$

and the usual dimensionless mixing parameters

$$x \equiv \frac{\Delta M}{\Gamma_D}, \qquad\qquad y \equiv \frac{\Delta\Gamma_D}{2\Gamma_D}. \tag{4.5}$$

The mixing parameters x and y are properly defined in terms of the approximate *CP* eigenstates $|D_+\rangle \approx |D_2\rangle$ and $|D_-\rangle \approx |D_1\rangle$ (*CP* even and *CP* odd respectively) which assumes the convention $CP|D^0\rangle = -|\bar{D}^0\rangle$. The impact of different conventions for the *CP* operator on this formalism is further discussed in Appendix A. The deviation of $|q/p|$ from 1 is a measure of *CP* violation (CPV) in D-mixing. The phase $\phi_{mix} \equiv \arg(q/p)$ is a convention-dependent quantity that is sensitive to CPV in the interference between mixing and decay - usually, a phase convention is chosen where $\phi_{mix} = 0$ in the absence of CPV.

In practice, only D mesons created with a definite flavour are considered. These evolve over time t to the following superpositions of D^0 and $\overline{D}^0$:

$$\begin{aligned} |D^0(t)\rangle &= g_+(t)|D^0\rangle + \frac{q}{p} g_-(t)|\overline{D}^0\rangle, \\ |\overline{D}^0(t)\rangle &= g_+(t)|\overline{D}^0\rangle + \frac{p}{q} g_-(t)|D^0\rangle, \end{aligned} \tag{4.6}$$

where $|D^0(t)\rangle$ refers to a state that was pure D^0 at time $t = 0$, while $|\bar{D}^0(t)\rangle$ refers to a state that was purely $\overline{D}^0$ at $t = 0$. The time-dependent functions $g_-(t)$ and $g_+(t)$ are

given by

$$g_+(t) = e^{-iMt-\frac{1}{2}\Gamma_D t}\ \cos\left(\frac{1}{2}\Delta M t - \frac{i}{4}\Delta\Gamma_D t\right),$$
$$g_-(t) = e^{-iMt-\frac{1}{2}\Gamma_D t}\ i\sin\left(\frac{1}{2}\Delta M t - \frac{i}{4}\Delta\Gamma_D t\right). \tag{4.7}$$

4.3.2 The complex interference parameter $\mathcal{Z}^f$

For the decay amplitudes of a D flavour eigenstate to a particular final state f, or its *CP*-conjugate $\bar{f}$, the following notation is used:

$$\mathcal{A}(\mathbf{p}) \equiv \langle f_{\mathbf{p}}|\hat{H}|D^0\rangle, \qquad \bar{\mathcal{A}}(\bar{\mathbf{p}}) \equiv \langle \bar{f}_{\bar{\mathbf{p}}}|\hat{H}|\overline{D}^0\rangle,$$
$$\mathcal{B}(\mathbf{p}) \equiv \langle f_{\mathbf{p}}|\hat{H}|\overline{D}^0\rangle, \qquad \bar{\mathcal{B}}(\bar{\mathbf{p}}) \equiv \langle \bar{f}_{\bar{\mathbf{p}}}|\hat{H}|D^0\rangle. \tag{4.8}$$

Here $\mathbf{p}$ identifies a point in phase space for the multi-body final state f, and $\bar{\mathbf{p}}$ identifies the corresponding point for the *CP*-conjugate final state, where all final state momenta and charges are reversed. In practice, any measurement will be made over an integrated region of phase space. Following [8] one can therefore define[4]

$$\int_\Omega \mathcal{A}(\mathbf{p})\mathcal{A}^*(\mathbf{p})\frac{d\Phi}{d\mathbf{p}}\mathrm{d}\mathbf{p} \equiv \mathcal{A}_\Omega^2, \qquad \int_{\bar{\Omega}} \bar{\mathcal{A}}(\bar{\mathbf{p}})\bar{\mathcal{A}}^*(\bar{\mathbf{p}})\frac{d\bar{\Phi}}{d\bar{\mathbf{p}}}\mathrm{d}\bar{\mathbf{p}} \equiv \bar{\mathcal{A}}_{\bar{\Omega}}^2,$$
$$\int_\Omega \mathcal{B}(\mathbf{p})\mathcal{B}^*(\mathbf{p})\frac{d\Phi}{d\mathbf{p}}\mathrm{d}\mathbf{p} \equiv \mathcal{B}_\Omega^2, \qquad \int_{\bar{\Omega}} \bar{\mathcal{B}}(\bar{\mathbf{p}})\bar{\mathcal{B}}^*(\bar{\mathbf{p}})\frac{d\bar{\Phi}}{d\bar{\mathbf{p}}}\mathrm{d}\bar{\mathbf{p}} \equiv \bar{\mathcal{B}}_{\bar{\Omega}}^2. \tag{4.9}$$

The symbols $\frac{d\Phi}{d\mathbf{p}}$ and $\frac{d\bar{\Phi}}{d\bar{\mathbf{p}}}$ are used to represent the density of states at $\mathbf{p}$ and $\bar{\mathbf{p}}$ respectively. The integrals containing $\mathcal{A}(\mathbf{p})$ and $\mathcal{B}(\mathbf{p})$ run over the phase space volume Ω, and the ones containing $\bar{\mathcal{A}}(\bar{\mathbf{p}})$ and $\bar{\mathcal{B}}(\bar{\mathbf{p}})$ run over the *CP*-conjugate volume $\bar{\Omega}$. These volumes can encompass all of phase space or any part thereof. The interference effects are described by the integrals over the cross terms:

$$\frac{\int_\Omega \mathcal{A}(\mathbf{p})\mathcal{B}^*(\mathbf{p})\frac{d\Phi}{d\mathbf{p}}\mathrm{d}\mathbf{p}}{\mathcal{A}_\Omega\mathcal{B}_\Omega} \equiv \mathcal{Z}_\Omega^f\ , \qquad \frac{\int_{\bar{\Omega}} \bar{\mathcal{A}}(\bar{\mathbf{p}})\bar{\mathcal{B}}^*(\bar{\mathbf{p}})\frac{d\bar{\Phi}}{d\bar{\mathbf{p}}}\mathrm{d}\bar{\mathbf{p}}}{\bar{\mathcal{A}}_{\bar{\Omega}}\bar{\mathcal{B}}_{\bar{\Omega}}} \equiv \mathcal{Z}_{\bar{\Omega}}^{\bar{f}}. \tag{4.10}$$

[4] Throughout this chapter * is used to denote the complex conjugate, whereas $^-$ is used to denote the *CP*-conjugate

This defines the complex interference parameter $\mathcal{Z}_\Omega^f$ for the final state f over the phase space region Ω, and $\mathcal{Z}_{\bar{\Omega}}^{\bar{f}}$, its *CP*-conjugate. For integrals over all phase space $\mathcal{Z}^f$ is used, omitting the subscript. The magnitude of $\mathcal{Z}_\Omega^f$ is between 0 and 1. The phase of $\mathcal{Z}_\Omega^f$ represents a weighted average of the phase difference between the two amplitudes over Ω. The parameter $\mathcal{Z}^f$ is directly related to the coherence factor R_D^f and average phase difference δ_D^f introduced in [8],

$$\mathcal{Z}^f \equiv R_D^f e^{-i\delta_D^f}. \tag{4.11}$$

For binned analyses in decays to self-conjugate final states such as $K_S^0\pi\pi$, these interference effects are usually parameterised instead by c_i and s_i. These are weighted averages of the cosine and the sine of the phase difference between D^0 and $\overline{D}^0$ decay amplitudes, taken over a phase space bin i covering the volume Ω_i. This formalism was originally introduced in [47]; this thesis follows the definition of c_i and s_i used in most subsequent articles [49, 50, 54, 62, 63]. The c_i and s_i parameters are related to the complex interference parameter through

$$\mathcal{Z}_{\Omega_i}^f \equiv c_i + i\, s_i \tag{4.12}$$

In the following, $\mathcal{Z}^f$ is used as it unifies the formalism for decays to self-conjugate and non-self-conjugate states. In terms of the parameters defined above, the time-dependent decay rates are given by

$$\begin{aligned}\Gamma\big(D^0(t)\to f\big)_\Omega = \frac{1}{2}\Bigg[&\mathcal{A}_\Omega^2\left(\cosh y\Gamma_D t + \cos x\Gamma_D t\right) + \mathcal{B}_\Omega^2\left(\cosh y\Gamma_D t - \cos x\Gamma_D t\right)\left|\frac{q}{p}\right|^2 \\ &+ 2\mathcal{A}_\Omega\mathcal{B}_\Omega\left[\mathcal{R}e\left(\mathcal{Z}_\Omega^f\,\frac{q}{p}\right)\sinh(y\Gamma_D t) + \mathcal{I}m\left(\mathcal{Z}_\Omega^f\,\frac{q}{p}\right)\sin(x\Gamma_D t)\right]\Bigg]e^{-\Gamma_D t},\end{aligned} \tag{4.13}$$

$$\begin{aligned}\Gamma\big(D^0(t)\to \bar{f}\big)_{\bar{\Omega}} = \frac{1}{2}\Bigg[&\bar{\mathcal{B}}_{\bar{\Omega}}^2\left(\cosh y\Gamma_D t + \cos x\Gamma_D t\right) + \bar{\mathcal{A}}_{\bar{\Omega}}^2\left(\cosh y\Gamma_D t - \cos x\Gamma_D t\right)\left|\frac{q}{p}\right|^2 \\ &+ 2\bar{\mathcal{A}}_{\bar{\Omega}}\bar{\mathcal{B}}_{\bar{\Omega}}\left[\mathcal{R}e\left(\mathcal{Z}_{\bar{\Omega}}^{\bar{f}*}\,\frac{q}{p}\right)\sinh(y\Gamma_D t) + \mathcal{I}m\left(\mathcal{Z}_{\bar{\Omega}}^{\bar{f}*}\,\frac{q}{p}\right)\sin(x\Gamma_D t)\right]\Bigg]e^{-\Gamma_D t},\end{aligned} \tag{4.14}$$

$$\Gamma\big(\overline{D}^0(t)\to \bar{f}\big)_{\bar{\Omega}} = \frac{1}{2}\Bigg[\bar{\mathcal{A}}^2_{\bar{\Omega}}\left(\cosh y\Gamma_D t + \cos x\Gamma_D t\right) + \bar{\mathcal{B}}^2_{\bar{\Omega}}\left(\cosh y\Gamma_D t - \cos x\Gamma_D t\right)\left|\frac{p}{q}\right|^2 + 2\bar{\mathcal{A}}_{\bar{\Omega}}\bar{\mathcal{B}}_{\bar{\Omega}}\left[\mathcal{R}e\left(\mathcal{Z}^{\bar{f}}_{\bar{\Omega}}\frac{p}{q}\right)\sinh(y\Gamma_D t) + \mathcal{I}m\left(\mathcal{Z}^{\bar{f}}_{\bar{\Omega}}\frac{p}{q}\right)\sin(x\Gamma_D t)\right]\Bigg]e^{-\Gamma_D t}, \tag{4.15}$$

$$\Gamma\big(\overline{D}^0(t)\to f\big)_{\Omega} = \frac{1}{2}\Bigg[\mathcal{B}^2_{\Omega}\left(\cosh y\Gamma_D t + \cos x\Gamma_D t\right) + \mathcal{A}^2_{\Omega}\left(\cosh y\Gamma_D t - \cos x\Gamma_D t\right)\left|\frac{p}{q}\right|^2 + 2\mathcal{A}_{\Omega}\mathcal{B}_{\Omega}\left[\mathcal{R}e\left(\mathcal{Z}^{f*}_{\Omega}\frac{p}{q}\right)\sinh(y\Gamma_D t) + \mathcal{I}m\left(\mathcal{Z}^{f*}_{\Omega}\frac{p}{q}\right)\sin(x\Gamma_D t)\right]\Bigg]e^{-\Gamma_D t}. \tag{4.16}$$

Assuming that terms of order 3 and higher in the mixing parameters x and y are negligible leads to the following expressions:

$$\Gamma\big(D^0(t)\to f\big)_{\Omega} \simeq \Bigg[\mathcal{A}^2_{\Omega}\left(1+\frac{y^2-x^2}{4}(\Gamma_D t)^2\right) + \mathcal{B}^2_{\Omega}\left(\left|\frac{q}{p}\right|^2\frac{x^2+y^2}{4}(\Gamma_D t)^2\right) + \mathcal{A}_{\Omega}\mathcal{B}_{\Omega}\left(y\mathcal{R}e\left(\mathcal{Z}^{f}_{\Omega}\frac{q}{p}\right) + x\mathcal{I}m\left(\mathcal{Z}^{f}_{\Omega}\frac{q}{p}\right)\right)(\Gamma_D t)\Bigg]e^{-\Gamma_D t} \tag{4.17}$$

$$\Gamma\big(D^0(t)\to \bar{f}\big)_{\bar{\Omega}} \simeq \Bigg[\bar{\mathcal{B}}^2_{\bar{\Omega}}\left(1+\frac{y^2-x^2}{4}(\Gamma_D t)^2\right) + \bar{\mathcal{A}}^2_{\bar{\Omega}}\left(\left|\frac{q}{p}\right|^2\frac{x^2+y^2}{4}(\Gamma_D t)^2\right) + \bar{\mathcal{A}}_{\bar{\Omega}}\bar{\mathcal{B}}_{\bar{\Omega}}\left(y\mathcal{R}e\left(\mathcal{Z}^{\bar{f}*}_{\bar{\Omega}}\frac{q}{p}\right) + x\mathcal{I}m\left(\mathcal{Z}^{\bar{f}*}_{\bar{\Omega}}\frac{q}{p}\right)\right)(\Gamma_D t)\Bigg]e^{-\Gamma_D t} \tag{4.18}$$

$$\Gamma\big(\overline{D}^0(t)\to \bar{f}\big)_{\bar{\Omega}} \simeq \Bigg[\bar{\mathcal{A}}^2_{\bar{\Omega}}\left(1+\frac{y^2-x^2}{4}(\Gamma_D t)^2\right) + \bar{\mathcal{B}}^2_{\bar{\Omega}}\left(\left|\frac{p}{q}\right|^2\frac{x^2+y^2}{4}(\Gamma_D t)^2\right) + \bar{\mathcal{A}}_{\bar{\Omega}}\bar{\mathcal{B}}_{\bar{\Omega}}\left(y\mathcal{R}e\left(\mathcal{Z}^{\bar{f}}_{\bar{\Omega}}\frac{p}{q}\right) + x\mathcal{I}m\left(\mathcal{Z}^{\bar{f}}_{\bar{\Omega}}\frac{p}{q}\right)\right)(\Gamma_D t)\Bigg]e^{-\Gamma_D t} \tag{4.19}$$

$$\Gamma\big(\overline{D}^0(t)\to f\big)_{\Omega} \simeq \Bigg[\mathcal{B}^2_{\Omega}\left(1+\frac{y^2-x^2}{4}(\Gamma_D t)^2\right) + \mathcal{A}^2_{\Omega}\left(\left|\frac{p}{q}\right|^2\frac{x^2+y^2}{4}(\Gamma_D t)^2\right) + \mathcal{A}_{\Omega}\mathcal{B}_{\Omega}\left(y\mathcal{R}e\left(\mathcal{Z}^{f*}_{\Omega}\frac{p}{q}\right) + x\mathcal{I}m\left(\mathcal{Z}^{f*}_{\Omega}\frac{p}{q}\right)\right)(\Gamma_D t)\Bigg]e^{-\Gamma_D t}. \tag{4.20}$$

For the remainder of this chapter it is assumed, for simplicity, that CPV in charm is negligible, leading to: $|\mathcal{Z}^{f}_{\Omega}| = |\mathcal{Z}^{\bar{f}}_{\bar{\Omega}}|$, $\mathcal{A} = \bar{\mathcal{A}}$ and $\mathcal{B} = \bar{\mathcal{B}}$ (no direct CPV); $|q/p| = 1.0$ (no CPV in mixing); and $\arg(\mathcal{Z}^{f}_{\Omega}\frac{q}{p}) = \arg(\mathcal{Z}^{\bar{f}}_{\bar{\Omega}}\frac{p}{q})$ (no CPV in the interference between mixing and decay). Following the usual phase convention, ϕ_{mix} is set to zero in the absence of

CPV in the interference between mixing and decay, leading to $q/p = 1$ and $\mathcal{Z}^f_\Omega = \mathcal{Z}^{\bar{f}}_{\bar{\Omega}}$. With this, the expressions in Equations 4.17 - 4.20 simplify to

$$\Gamma\big(D^0(t)\to f\big)_\Omega \simeq \left[\mathcal{A}^2_\Omega\left(1+\frac{y^2-x^2}{4}(\Gamma_D t)^2\right)+\mathcal{B}^2_\Omega\left(\frac{x^2+y^2}{4}(\Gamma_D t)^2\right)+ \mathcal{A}_\Omega\mathcal{B}_\Omega\left(y\mathcal{R}e(\mathcal{Z}^f_\Omega)+x\mathcal{I}m(\mathcal{Z}^f_\Omega)\right)(\Gamma_D t)\right]e^{-\Gamma_D t}, \tag{4.21}$$

$$\Gamma\big(\overline{D}^0(t)\to f\big)_\Omega \simeq \left[\mathcal{B}^2_\Omega\left(1+\frac{y^2-x^2}{4}(\Gamma_D t)^2\right)+\mathcal{A}^2_\Omega\left(\frac{x^2+y^2}{4}(\Gamma_D t)^2\right)+ \mathcal{A}_\Omega\mathcal{B}_\Omega\left(y\mathcal{R}e(\mathcal{Z}^f_\Omega)-x\mathcal{I}m(\mathcal{Z}^f_\Omega)\right)(\Gamma_D t)\right]e^{-\Gamma_D t}, \tag{4.22}$$

with identical expressions for the *CP*-conjugate processes. Since all weak phases have been removed, $\arg(\mathcal{Z}^f) = -\delta^f_D$ now represents the average *strong* phase difference.

4.4 Simulation studies of D-mixing in $D^0\to K^+\pi^-\pi^+\pi^-$ decays

The dependence of Equations 4.21 - 4.22 on $\mathcal{Z}^f_\Omega$ has usually been taken to imply that external input on $\mathcal{Z}^f_\Omega$ is required to extract charm mixing parameters from multi-body D decays [53, 54, 64]. Instead, in this study, existing measurements of charm mixing parameters [65–71] are used as input to constrain $\mathcal{Z}^f_\Omega$ from charm mixing in multi-body decays [64]. This in turn provides important input to the amplitude model-unbiased measurement of γ [8, 47–50, 52]. So far, this type of input has only been accessible at the charm threshold [48–52].

In this section it is shown how D-mixing can be used to constrain $\mathcal{Z}^f$. Simulated $D\to K\pi\pi\pi$ decays are used to demonstrate that a substantial improvement in the precision of $\mathcal{Z}^{K3\pi}$ is possible using existing data; here expected signal yields are motivated by LHCb's Run I data-taking period.

4.4.1 Method

In Equation 4.21, the term linear in t (the "interference term") is sensitive to $y\mathcal{R}e(\mathcal{Z}^f_\Omega) + x\mathcal{I}m(\mathcal{Z}^f_\Omega)$, while in Equation 4.22 it is sensitive to $y\mathcal{R}e(\mathcal{Z}^f_\Omega) - x\mathcal{I}m(\mathcal{Z}^f_\Omega)$, so both $\mathcal{R}e\mathcal{Z}^f_\Omega$ and $\mathcal{I}m\mathcal{Z}^f_\Omega$ can be extracted. However, previous studies [64] indicate that datasets much larger than those currently available are required to provide useful constraints on $\mathcal{Z}^f_{\Omega_i}$ (or c_i and s_i) from mixing using self-conjugate decays such as $D^0 \to K^0_S\pi\pi$ and $D^0 \to K^0_S KK$.

It is demonstrated here that significant improvements on $\mathcal{Z}^f$ can be achieved with existing data for the case where $D^0(t) \to f$ is a "wrong-sign" (WS) decay and $\overline{D}^0(t) \to f$ is the corresponding "right-sign" (RS) decay. This is the case when $\mathcal{A}$ is a doubly Cabibbo-suppressed (DCS) amplitude, such as $D^0 \to K^+\pi^-\pi^+\pi^-$ or $D^0 \to K^+\pi^-$, and $\mathcal{B}$ is Cabibbo-favoured (CF) amplitude such as $D^0 \to K^-\pi^+\pi^-\pi^+$ or $D^0 \to K^-\pi^+$. The Feynman diagrams for the $D^0 \to K^+\pi^-$ and $D^0 \to K^-\pi^+$ amplitudes is pictured in Figure 4.5. In this case $\mathcal{A}^{DCS}_\Omega \ll \mathcal{B}^{CF}_\Omega$, where the superscripts have been added for clarity. Neglecting terms of order 4 or higher in the small quantities $\mathcal{A}_\Omega, x, y$, Equation 4.21 becomes,

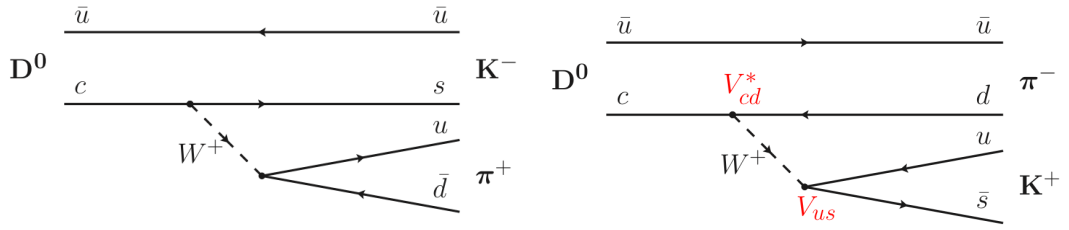

Figure 4.5: Feynman diagrams for the amplitudes $D^0 \to K^+\pi^-$ (left) and $D^0 \to K^-\pi^+$ (right). The $D^0 \to K^+\pi^-$ diagram is known as Cabibbo Favoured (CF) because all $W^\pm$ interaction vertices are between quarks of the same generation. The $D^0 \to K^-\pi^+$ diagram is known as Doubly Cabibbo Suppressed (DCS) due to both $W^\pm$ interaction vertices having off-diagonal CKM elements V_{cd} and V_{ub}.

$$\Gamma\big(D^0(t) \to f\big)_\Omega \simeq \left[\mathcal{A}^2_\Omega + \mathcal{A}_\Omega\mathcal{B}_\Omega\left(y\mathcal{R}e(\mathcal{Z}^f_\Omega) + x\mathcal{I}m(\mathcal{Z}^f_\Omega)\right)(\Gamma_D t) + \mathcal{B}^2_\Omega\frac{x^2+y^2}{4}(\Gamma_D t)^2\right]e^{-\Gamma_D t}. \tag{4.23}$$

In this simplified expression, which will now be referred to as the WS rate, one can interpret the three terms as follows: $\mathcal{A}^2_\Omega$ is the DCS amplitude, $\mathcal{B}^2_\Omega\frac{x^2+y^2}{4}(\Gamma_D t)^2$ is from a D^0 oscillating to a $\overline{D}^0$ followed by the CF amplitude, and finally $\mathcal{A}_\Omega\mathcal{B}_\Omega\left(y\mathcal{R}e(\mathcal{Z}^f_\Omega) + x\mathcal{I}m(\mathcal{Z}^f_\Omega)\right)(\Gamma_D t)$

is the interference between the two - this interpretation is pictured in Figure 4.6. For typical decay times t, the interference term is of a similar order to the DCS amplitude, providing enhanced sensitivity to $\mathcal{Z}_\Omega^f$.

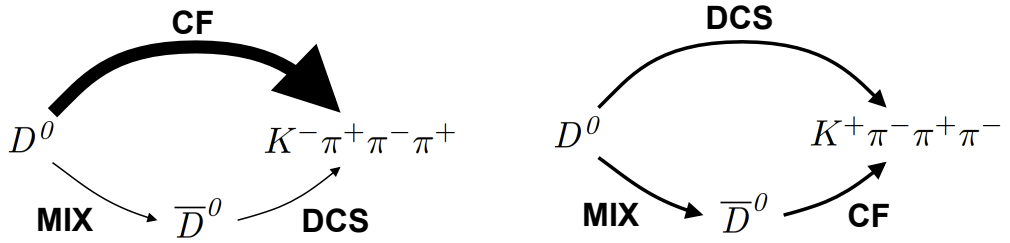

Figure 4.6: Amplitudes contributing to (left) "Right Sign" (RS) $D^0 \to K^-\pi^+\pi^-\pi^+$ decays (right) "Wrong Sign" (WS) $D^0 \to K^+\pi^-\pi^+\pi^-$ decays. The thickness of the arrows represents the relative size of the different amplitudes.

Again neglecting terms of order 4 or higher in $\mathcal{A}_\Omega, x, y$, Equation 4.22 becomes

$$\Gamma\left(\overline{D}^0(t) \to f\right)_\Omega \simeq \mathcal{B}_\Omega^2 e^{-\Gamma_D t}. \tag{4.24}$$

From this expression, which will now be referred to as the RS rate, one can see the decay is completely dominated by the CF amplitude, and has negligible contributions from D-mixing. Therefore there is effectively no sensitivity to $\mathcal{Z}_\Omega^f$. In practice the RS rate will be used to normalise the WS rate, as this cancels many experimental uncertainties.

4.4.2 $\mathcal{Z}^f$ from the mixing-induced interference of DCS and CF amplitudes

In this scenario it is useful to define the ratio of the DCS amplitude to the CF amplitude:

$$r_{D,\Omega} \equiv \frac{\mathcal{A}^{DCS}}{\mathcal{B}^{CF}}. \tag{4.25}$$

Dividing the WS rate by the RS rate (Equation 4.23 and Equation 4.24 respectively) results in the following expression:

$$R_\Omega(t) = r_{D,\Omega}^2 + r_{D,\Omega}\left(y\mathcal{R}e\mathcal{Z}_\Omega^f + x\mathcal{I}m\mathcal{Z}_\Omega^f\right)\Gamma_D t + \frac{x^2+y^2}{4}(\Gamma_D t)^2. \tag{4.26}$$

An analysis of the time-dependent decay rate ratio will, through the linear term of Equation 4.26, provide a measurement of

$$b_\Omega \equiv \left(y\mathcal{R}e\mathcal{Z}^f_\Omega + x\mathcal{I}m\mathcal{Z}^f_\Omega \right). \tag{4.27}$$

The factor $r_{D,\Omega}$, which also features in the linear term, can be obtained in the same analysis from the 0^{th} order term of Equation 4.26, and Γ_D has been measured very precisely [13]. Taking the D-mixing parameters x and y as input, a measurement of b_Ω can be translated into constraints in the $\mathcal{R}e\mathcal{Z}^f_\Omega - \mathcal{I}m\mathcal{Z}^f_\Omega$ plane. A given value of b_Ω corresponds to a line of slope y/x in the $\mathcal{R}e\mathcal{Z}^f_\Omega - \mathcal{I}m\mathcal{Z}^f_\Omega$ plane defined by:

$$\mathcal{I}m\mathcal{Z}^f_\Omega = -\frac{y}{x}\mathcal{R}e\mathcal{Z}^f_\Omega + \frac{b_\Omega}{x}. \tag{4.28}$$

To show the effect of the current uncertainties in x and y on the measurement of $\mathcal{Z}^f$ from

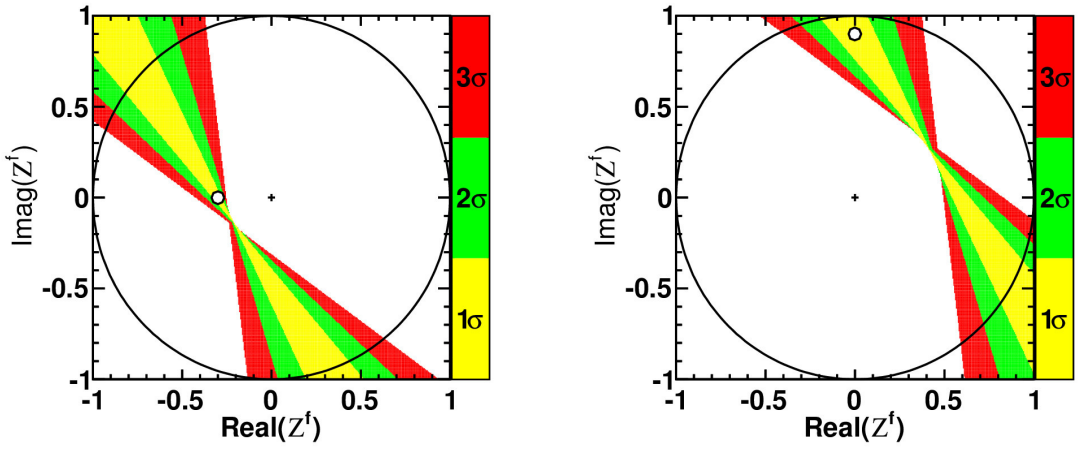

Figure 4.7: Constraints on $\mathcal{Z}^f$ for $\mathcal{Z}^f = -0.3$ (left) and $\mathcal{Z}^f = 0.9i$ (right), taking into account current uncertainties on the mixing parameters x, y [13], but ignoring, in this illustration, other measurement uncertainties. The white filled circle indicates the central values of $\mathcal{Z}^{K3\pi}$ used.

D-mixing, the limiting case of negligible uncertainties on any other parameter is first considered - in particular the parameter b_Ω, as defined in Equation 4.27. The following values and uncertainties for x, y, and their correlation coefficient $\rho_{x,y}$ [71] are used:

$$x = (0.53 \pm 0.16)\,\%, \quad y = (0.67 \pm 0.09)\,\%, \quad \rho_{x,y} = 0.19\,. \tag{4.29}$$

Figure 4.7 shows $1, 2$ and 3σ confidence limits in the $\mathcal{R}e\mathcal{Z}_\Omega^f - \mathcal{I}m\mathcal{Z}_\Omega^f$ plane using these inputs for two illustrative example values for the complex interference paramter, $\mathcal{Z}_\Omega^f = -0.3$ and $\mathcal{Z}_\Omega^f = 0.9i$. The $1, 2$ and 3σ regions are calculated using standard techniques based on χ^2 differences.

4.4.3 Sensitivity with existing LHCb datasets

To estimate the precision on $\mathcal{Z}^{K3\pi}$ achievable with current data, a simulation study is performed based on plausible $D^0 \to K\pi\pi\pi$ event yields in LHCb's $3\,\text{fb}^{-1}$ Run I data sample. The mixing parameters are set to values given in Equation 4.29, and r_D is set to 0.058 based on the WS/RS branching ratio reported in [13]. Simulated events are generated according to the full expressions for the decay rates given in Equations 4.13 - 4.16. To take into account the effect of LHCb's trigger and event selection process, which preferentially selects decays with long D decay times, a decay-time dependent efficiency function, $\epsilon(t)$, is applied, based on that seen in [72]. For this feasibility study other detector effects and background contamination are ignored. Based on the RS yields reported in [57], and taking into account that for the WS mode tighter selection criteria might be necessary to control backgrounds, about 8 million RS+WS events in LHCb's Run I dataset are estimated. The exact fraction of WS events depends on the input parameters, in particular on $R^{K3\pi}$; typically, 8 million RS+WS events correspond to about $30,000$ WS events.

To constrain $\mathcal{Z}^{K3\pi}$ a χ^2 fit is performed to the WS/RS ratio in 10 bins of proper decay time. The bins have variable widths, chosen such that each bin contains a sufficient number of events. Using the same approximations that led to Equation 4.26 the expected WS/RS ratio $R_i^{WS/RS}$ in bin i that covers the proper decay time interval $[t_i^{min}, t_i^{max}]$ is calculated as:

$$R_i^{WS/RS} = \frac{\int_{t_i^{min}}^{t_i^{max}} \epsilon(t)\, e^{-\Gamma_D t} \left(r_{D,\Omega}^2 + r_{D,\Omega} \left(y\mathcal{R}e\mathcal{Z}_\Omega^f + x\mathcal{I}m\mathcal{Z}_\Omega^f \right) \Gamma_D t + \frac{x^2+y^2}{4} (\Gamma_D t)^2 \right) dt}{\int_{t_i^{min}}^{t_i^{max}} \epsilon(t)\, e^{-\Gamma_D t}\, dt}. \tag{4.30}$$

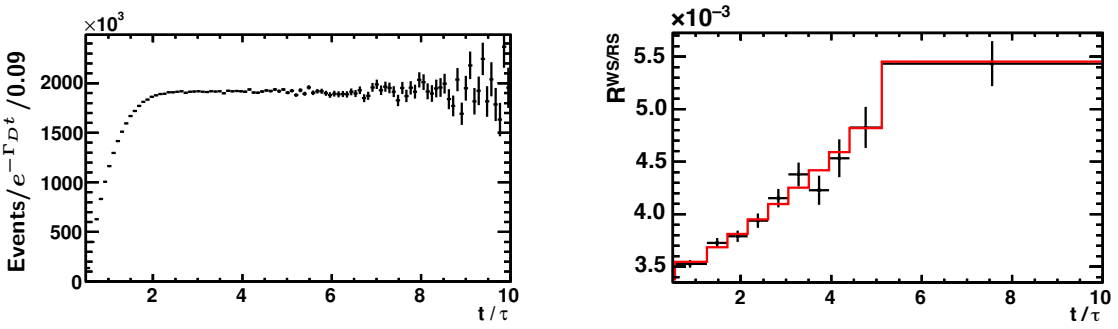

Figure 4.8: (left) Simulated RS data divided by $e^{-\Gamma_D t}$, representing the shape of $\epsilon(t)$ (right) Simulated data (black crosses) and fit (red line) in bins of proper decay time, expressed in units of $\tau = 1/\Gamma_D$. The discontinuous shape of the line representing the fit reflects the way the expected WS/RS ratio is calculated for each bin, described in the text.

The fit parameters are r_D, $b = y\mathcal{R}e(Z^0) + x\mathcal{I}m(Z^0)$, x, and y, where x and y are constrained according to Equation 4.29.

In a real experiment, the time-dependent efficiency $\epsilon(t)$ would not necessarily be known beforehand, but it is reasonable to assume that $\epsilon(t)$ would be the same for WS and RS decays. Its shape is therefore extracted from the (here simulated) data by dividing the RS decay time distribution (histogrammed in 100 bins) by $e^{-\Gamma_D t}$, as shown in Figure 4.8; the overall normalisation cancels when using $\epsilon(t)$ in Equation 4.30.

A pull study based on generating and fitting 200 simulated data samples, each containing 8 million RS+WS events, shows no evidence of fit biases, and confirms the correct coverage of the confidence intervals obtained from the fit χ^2.

An example of such a fit is shown in Figure 4.8. The 8M events have been generated using CLEO-c's central value $\mathcal{Z}^{K3\pi} = -0.09{+}0.32i$ [48] and include 30.5k WS events. Figure 4.9 shows $1, 2$ and 3σ confidence regions based on 8 million simulated events that have been generated with the illustrative values $\mathcal{Z}^{K3\pi} = -0.3$ and $\mathcal{Z}^{K3\pi} = 0.9i$ used also to obtain Figure 4.7. Figure 4.10 shows the constraints for events generated using the CLEO-c central value for $\mathcal{Z}^{K3\pi}$, in both polar coordinates (i.e. the coherence factor $R^{K3\pi} = \left|\mathcal{Z}^{K3\pi}\right|$ and strong phase difference $\delta^{K3\pi} = -\arg\left(\mathcal{Z}^{K3\pi}\right)$) and cartesian coordinates ($\mathcal{R}e\ \mathcal{Z}^{K3\pi}$ and $\mathcal{I}m\ \mathcal{Z}^{K3\pi}$).

To evaluate the potential impact of input from charm mixing on the precision of $\mathcal{Z}^{K3\pi}$, the χ^2 function used to obtain Figure 4.10 is combined with CLEO-c's measurement of

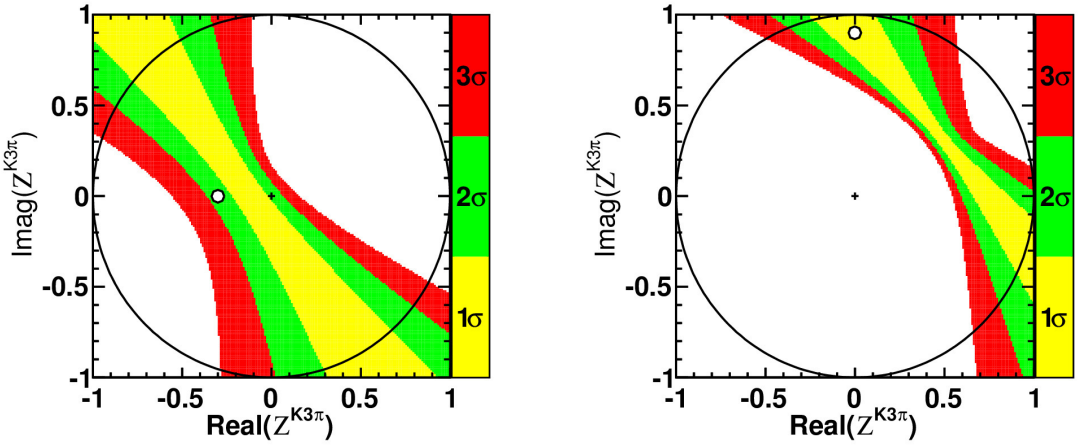

Figure 4.9: Examples for constraints on $\mathcal{Z}^{K3\pi}$ obtained from 8 million simulated events, generated with $\mathcal{Z}^{K3\pi} = -0.3$ (left) and $\mathcal{Z}^{K3\pi} = 0.9i$ (right), with current uncertainties on x, y. The white filled circle indicates the value of $\mathcal{Z}^{K3\pi}$ used to generate the events.

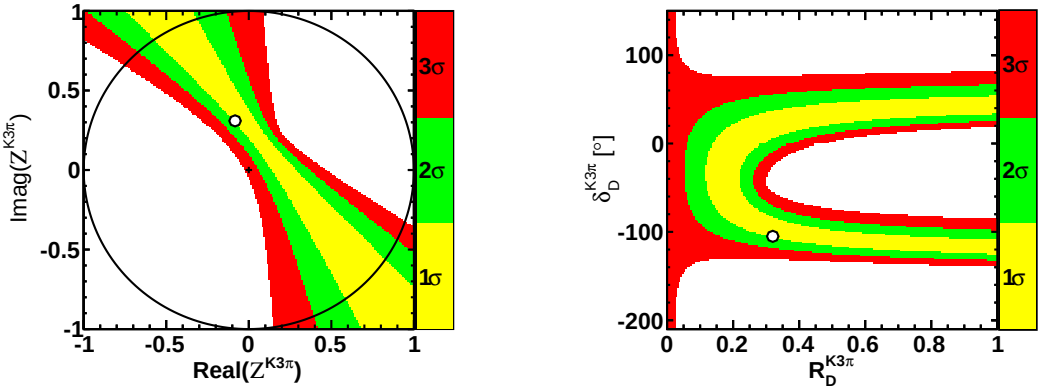

Figure 4.10: Constraints on $\mathcal{Z}^{K3\pi}$ for $8M$ RS and $30k$ WS simulated events generated with CLEO-c's central value for the complex interference parameter, $\mathcal{Z}^{K3\pi} = -0.09{+}0.32i = 0.31e^{-255^\circ i}$ [48]. The constraints are shown both in Cartesian (left) and polar coordinates (right). The white filled circle indicates the values used to generate the events.

$\mathcal{Z}^{K3\pi}$ [48]. The CLEO-c results, and their combination with this simulated data, are shown in Figure 4.11. The input from charm mixing improves the constraints considerably. The effect is particularly striking at the $\geq 2\sigma$ level where there were previously no constraints on δ_D^f. To quantify these improvements, one-dimensional 68% and 95% confidence intervals for $R^{K3\pi}$ and $\delta^{K3\pi}$ are calculated, following the same procedures as used by CLEO-c [48] to ensure comparable results. The 68% confidence limits are based on a standard χ^2 difference calculation. The same process would lead to 95% confidence limits reaching the edge of the R_D^f-δ_D^f parameter space in the CLEO-c measurement.

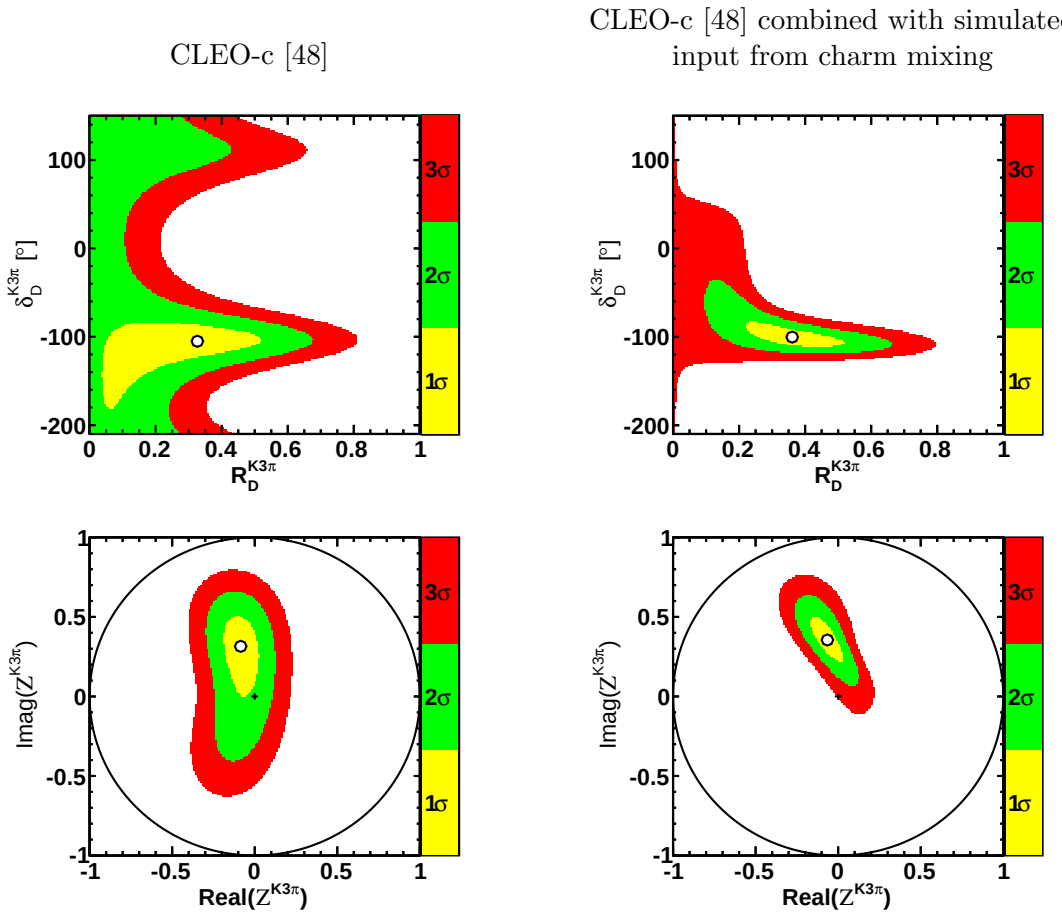

Figure 4.11: Constraints on $\mathcal{Z}^{K3\pi}$ obtained by CLEO-c [48] are shown on the left. Constraints obtained by combining the CLEO-c results with the input from simulated $D^0 \to K\pi\pi\pi$ charm mixing data are shown on the right. The simulated signal sample is similar in size to that expected from $3\,\text{fb}^{-1}$ of data taken by LHCb in 2011 and 2012. The same results are shown in polar coordinates $R^{K3\pi}$, $\delta^{K3\pi}$ (top row) and in cartesian coordinates $\mathcal{R}e\mathcal{Z}^{K3\pi}$, $\mathcal{I}m\mathcal{Z}^{K3\pi}$ (bottom row). The white filled circle indicates the location with the smallest χ^2.

These are therefore obtained using a Bayesian approach with a uniform prior in the physically allowed region of the parameter of interest. The procedure is demonstrated in Figure 4.12.

The results are summarised in Table 4.1. The constraints from 8M simulated charm events (with 30k WS events) shrink the existing uncertainties on $\mathcal{I}m\mathcal{Z}^{K3\pi}$ by a factor of ~ 1.5, and the 95% CL on $\mathcal{I}m\mathcal{Z}^{K3\pi}$ by a factor ~ 2. In terms of polar coordinates, the simulated input improves the uncertainty on $R^{K3\pi}$ by a factor of ~ 1.5, and significantly reduces the uncertainty on $\delta^{K3\pi}$. There is currently no constraint on $\delta^{K3\pi}$ at the 2σ level, and only a one-sided upper limit for $R^{K3\pi}$. From the combination of simulated data with the CLEO-c result, the constraints $\delta^{K3\pi} \in [-126°, 58°]$, and $R^{K3\pi} \in [0.11, 0.65]$

Fit result (where available) with 68% confidence intervals ($\Delta\chi^2$)

	Simulation $8M$ evts	CLEO-c [48]	Combination
$R^{K3\pi}$	$[0.12, 1.00]$	$0.31^{+0.21}_{-0.27}$	$0.36^{+0.16}_{-0.14}$
$\delta^{K3\pi}$	$[-124°, 54°]$	$-105°^{+21}_{-77}$	$-100°^{+17}_{-12}$
$\mathcal{R}e\mathcal{Z}^{K3\pi}$	–	$-0.09^{+0.11}_{-0.11}$	$-0.07^{+0.10}_{-0.11}$
$\mathcal{I}m\mathcal{Z}^{K3\pi}$	–	$0.32^{+0.20}_{-0.32}$	$0.36^{+0.15}_{-0.14}$

Bayesian 95% confidence intervals

$R^{K3\pi}$	$[0.14, 1.00]$	$[0.00, 0.60]$	$[0.11, 0.65]$
$\delta^{K3\pi}$	$[-126°, 58°]$	–	$[-126°, 38°]$
$\mathcal{R}e\mathcal{Z}^{K3\pi}$	$[-0.58, 0.82]$	$[-0.30, 0.13]$	$[-0.27, 0.13]$
$\mathcal{I}m\mathcal{Z}^{K3\pi}$	$[-0.94, 0.78]$	$[-0.36, 0.65]$	$[0.07, 0.65]$

Table 4.1: Constraints on $R^{K3\pi}$ and $\delta^{K3\pi}$ as well as $\mathcal{R}e\mathcal{Z}^{K3\pi}$ and $\mathcal{I}m\mathcal{Z}^{K3\pi}$ from simulation, CLEO-c [48], and their combination, at 68% and 95% CL, obtained with two different techniques following [48], as described in the text. The $\Delta\chi^2$ method is not suitable for obtaining separate constraints on $\mathcal{R}e\mathcal{Z}^{K3\pi}$ and $\mathcal{I}m\mathcal{Z}^{K3\pi}$ from the simulated mixing data alone.

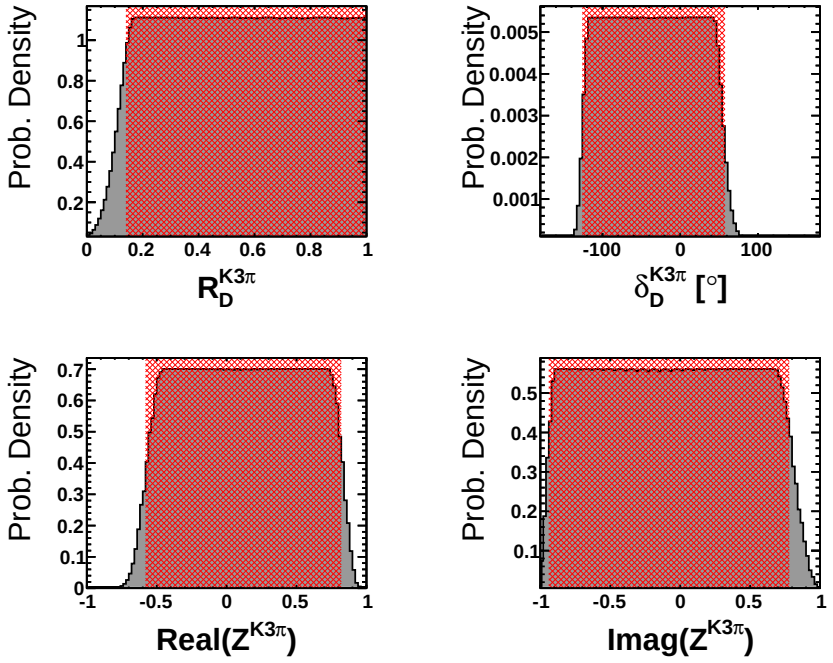

Figure 4.12: These plots illustrate the calculation of 95% Bayesian intervals for $R^{K3\pi}$, $\delta^{K3\pi}$, $\mathcal{R}e\mathcal{Z}^{K3\pi}$ and $\mathcal{I}m\mathcal{Z}^{K3\pi}$. The shaded histograms show the probability density function, $p(x)$, found from the 1D χ^2 scan and a flat prior i.e. $p(x) = e^{-0.5(\chi^2(x)-\chi^2_{min})}/\mathcal{N}$. The normalisation constant, $\mathcal{N}$, is the integral of $p(x)$ in the physically allowed region. In principle, any interval that integrates to 95% could be chosen, although here the smallest possible interval has been chosen (region with the largest $p(x)$). This interval is indicated by the red cross-hatching.

are obtained at 95% confidence.

4.5 Conclusions

Charm mixing is sensitive to the same charm interference parameters that are relevant to the measurement of γ in $B \to DK$ and related decay modes [8, 47, 53, 54, 63, 64, 73]. So far, these have only been accessible at the charm threshold [48–52]. The increased precision with which the charm mixing parameters x and y have been measured [51, 65–71] opens up the possibility of constraining charm interference parameters using charm mixing. However, previous studies indicate that for decays to self-conjugate final states, such as $D^0 \to K^0_S\pi\pi$ and $D^0 \to K^0_S KK$, datasets much larger than those currently available are required to significantly improve constraints on the binned complex interference parameters $\mathcal{Z}^f_{\Omega_i} = c_i + is_i$ from charm mixing [64]. On the other hand, in wrong-sign decay modes such as $D^0 \to K^+\pi^-\pi^+\pi^-$ and $D^0 \to K^+\pi^-$, the mixing-induced interference effects are significantly enhanced compared to self-conjugate decays. This provides greater sensitivity to the complex interference parameter $\mathcal{Z}^f$, or, equivalently, the coherence factor $R^f_D = |\mathcal{Z}^f|$ and average strong phase difference $\delta^f_D = -\arg(\mathcal{Z}^f)$ introduced in [8]. While it is interesting to note that useful information can be obtained in this way without additional input, the true power of the method lies in the combination with threshold data. The potential of this approach was evaluated with a simulation study based on estimated $D^0 \to K\pi\pi\pi$ signal yields expected in LHCb's Run I dataset. For these studies, unlike the binned studies in Chapter 6, no improvements on external inputs (x and y) are assumed. These results indicate that charm mixing input from existing LHCb data, when combined with CLEO-c's measurement [48], could substantially reduce the current uncertainty on the coherence factor and average strong phase difference in $D^0 \to K\pi\pi\pi$. Such a measurement is presented in Chapter 5, and is expected to have a significant impact on the precision with which the CKM parameter γ can be measured at LHCb, BELLE II, and the LHCb upgrade.

Chapter 5

Measurement of the $D \to K^+\pi^-\pi^+\pi^-$ complex interference parameter

5.1 Introduction

In Chapter 4 it was shown using simulation studies that charm mixing in WS $D^0 \to K^+\pi^-\pi^+\pi^-$ decays can be used to improve constraints on the complex interference parameter $\mathcal{Z}^f$. In this chapter the same method is applied to $1\,\text{fb}^{-1}$ of LHCb data collected during 2011.

The chapter is organised as follows: Section 5.2 gives an overview of the analysis technique. Section 5.3 describes the data sample used for the analysis, and the selection applied in order to optimise sensitivity to D-mixing. Section 5.4 describes the fitting procedure applied to signal candidates used to estimate the WS and RS $D^0 \to K\pi\pi\pi$ signal yields. Section 5.5 gives a discussion of the peaking backgrounds or systematic effects that can bias the measured WS/RS ratio (and therefore the constraints on $\mathcal{Z}^f$). Due to WS and RS decays having different decay amplitudes, the phase space integrated detection and selection efficiencies can differ between the two decay modes. This difference is described, and corrected for in Section 5.6. The lifetime-dependent fit to the

WS/RS ratio, used to constrain $\mathcal{Z}^f$, is described in Section 5.7. This builds on the WS/RS fitter presented in Chapter 4, with additional features to account for the difficulties associated with experimental data. Section 5.8 shows the results of a simulation study used to validate the analysis procedure. In Section 5.9 the results are presented, followed by the conclusions in Section 5.10.

5.2 Analysis Overview

In order to distinguish WS ($D^0 \to K^+\pi^-\pi^+\pi^-$) from RS ($D^0 \to K^-\pi^+\pi^-\pi^+$) decays, the flavour of the D^0 at production must be determined. This is achieved using a sample of D mesons that comes from $D^*(2010)^+ \to D^0\pi^+$ and $D^*(2010)^- \to \overline{D}^0\pi^-$ decays, where the charge of the bachelor pion tags the flavour of the D meson. Because the mass difference between the $D^*(2010)^+$ and the $D^0\pi^+$ is small, the bachelor pion is nearly at rest in the $D^*(2010)^\pm$ rest frame - for this reason it is known as the 'slow pion', or π_s.

In this analysis four categories of decays are studied; WS and RS decays from D^0 and $\overline{D}^0$. The symbol 'CAT' is used to represent one of these categories. The expected number of events in each category, $N_{\rm CAT}$, is given by:

$$N_{{\rm WS}D^0} = \Gamma[D^0 \to K^+\pi^-\pi^+\pi^-] \times \epsilon^{\rm WS}_{K^+\pi^-\pi^+\pi^-} \times \epsilon_{\pi_s^+} \times P_{D^{*+}}, \tag{5.1}$$

$$N_{{\rm RS}D^0} = \Gamma[D^0 \to K^-\pi^+\pi^-\pi^+] \times \epsilon^{\rm RS}_{K^-\pi^+\pi^-\pi^+} \times \epsilon_{\pi_s^+} \times P_{D^{*+}}, \tag{5.2}$$

$$N_{{\rm WS}\overline{D}^0} = \Gamma[\overline{D}^0 \to K^-\pi^+\pi^-\pi^+] \times \epsilon^{\rm WS}_{K^-\pi^+\pi^-\pi^+} \times \epsilon_{\pi_s^-}, \times P_{D^{*-}} \tag{5.3}$$

$$N_{{\rm RS}\overline{D}^0} = \Gamma[\overline{D}^0 \to K^+\pi^-\pi^+\pi^-] \times \epsilon^{\rm RS}_{K^+\pi^-\pi^+\pi^-} \times \epsilon_{\pi_s^-} \times P_{D^{*-}}. \tag{5.4}$$

Here $\Gamma[D \to f]$ are the theoretical decay rates listed in Equations 4.13 - 4.16. The phase space-integrated detection efficiency for the final state f is given by $\epsilon_f^{\rm WS}$ ($\epsilon_f^{\rm RS}$) for WS (RS) decays. The detection efficiency of the slow pion is given by $\epsilon_{\pi_s^\pm}$, and the $D^{*\pm}$ production rates by $P_{D^{*\pm}}$. In this formalism it is assumed that the total detection efficiency , $\epsilon_{\rm TOT}$, factorizes e.g. $\epsilon^{{\rm WS}\overline{D}^0}_{\rm TOT} = \epsilon^{\rm WS}_{K^-\pi^+\pi^-\pi^+} \times \epsilon_{\pi_s^-}$.

From the above the measured WS/RS ratio, R^M, can be written,

$$\begin{aligned}(R^M)^2 &= \frac{N_{\mathrm{WS}D^0} N_{\mathrm{WS}\bar{D}^0}}{N_{\mathrm{RS}D^0} N_{\mathrm{RS}\bar{D}^0}} \\ &= \frac{\Gamma[D^0 \to K^+\pi^-\pi^+\pi^-]\ \Gamma[\bar{D}^0 \to K^-\pi^+\pi^-\pi^+]}{\Gamma[D^0 \to K^-\pi^+\pi^-\pi^+]\ \Gamma[\bar{D}^0 \to K^+\pi^-\pi^+\pi^-]} \times \frac{\epsilon^{\mathrm{WS}}_{K^+\pi^-\pi^+\pi^-}\epsilon^{\mathrm{WS}}_{K^-\pi^+\pi^-\pi^+}}{\epsilon^{\mathrm{RS}}_{K^-\pi^+\pi^-\pi^+}\epsilon^{\mathrm{RS}}_{K^+\pi^-\pi^+\pi^-}} \\ &= R^2 \frac{1}{\epsilon^2_{\mathrm{COR}}}, \end{aligned} \tag{5.5}$$

where,

$$R = \sqrt{\frac{\Gamma[D^0 \to K^+\pi^-\pi^+\pi^-]\ \Gamma[\bar{D}^0 \to K^-\pi^+\pi^-\pi^+]}{\Gamma[D^0 \to K^-\pi^+\pi^-\pi^+]\ \Gamma[\bar{D}^0 \to K^+\pi^-\pi^+\pi^-]}}, \tag{5.6}$$

is the WS/RS ratio that will ultimately be measured, and

$$\epsilon_{\mathrm{COR}} = \sqrt{\frac{\epsilon^{\mathrm{RS}}_{K^+\pi^-\pi^+\pi^-}\epsilon^{\mathrm{RS}}_{K^-\pi^+\pi^-\pi^+}}{\epsilon^{\mathrm{WS}}_{K^-\pi^+\pi^-\pi^+}\epsilon^{\mathrm{WS}}_{K^+\pi^-\pi^+\pi^-}}}, \tag{5.7}$$

is the efficiency correction. ϵ_{COR} is expected to be close to 1, so is neglected until Section 5.6.

In the following sections R^M will be measured in several independent lifetime bins. A χ^2 fit is then applied to the results in order to constrain the parameters of interest.

5.3 Selection

The analysis uses the full data sample collected by LHCb in 2011 at a centre of mass collision energy of $\sqrt{s} = 7\,\mathrm{TeV}$ - this corresponds to an integrated luminosity of $1.0\,\mathrm{fb}^{-1}$.

Before describing the selection cuts used in the analysis, the list of variables that are used is first defined:

- Track χ^2/ndf – the χ^2 of the track fit.
- χ^2_{IP} – the χ^2 difference between the PV reconstruction with and without the particle in question.

- DoCA (Distance of Closest Approach) – the shortest distance between the reconstructed tracks of the daughters of the particle.
- FD – reconstructed flight distance of a long-lived particle.
- LT – reconstructed proper lifetime of a long-lived particle.
- DIRA (cosine DIRection Angle) – a particle with an origin vertex $\mathbf{x_O}$, decay vertex $\mathbf{x_D}$, and momentum $\mathbf{p}$, has its DIRA defined by $((\mathbf{x_D} - \mathbf{x_O}) \cdot \mathbf{p}) / |\mathbf{p}| \; |\mathbf{x_D} - \mathbf{x_O}|$. This is the cosine of the angle between the reconstructed momentum and the direction vector (calculated from origin and decay vertex).
- Vertex χ^2/ndf – the χ^2 per degree of freedom of a particle's vertex fit i.e. D^0 Vertex χ^2/ndf is the χ^2/ndf of the vertex formed from $K\pi\pi\pi$ candidates.
- GhostProb – probability of a particle being a ghost (see Section 5.5.3).
- χ^2_{DTF} – the χ^2 calculated by the Decay Tree Fitter (DTF) algorithm (see Section 5.3.3).
- $\mathrm{DLL_{K\pi}}$ – the log-likelihood difference between K and π hypotheses (see Equation 3.4).
- $\mathrm{DLL_{e\pi}}$ – the log-likelihood difference between e and π hypotheses (see Equation 3.4).
- m_{D^0}– the reconstructed invariant mass of the $K\pi\pi\pi$ candidates used to form the D^0 candidate.
- m_{D^*} – the reconstructed invariant mass of the $K\pi\pi\pi\pi_s$ candidates used to form the D^* candidate.
- Δm (or 'delta mass') – the mass difference between the D^0 and the D^* candidate i.e. $\Delta m = m_{D^*} - m_{D^0}$.
- $m^{\mathrm{PDG}}_{D^0}$– the well-measured D^0 mass taken from PDG [13].
- τ_{D^0}– the well-measured D^0 lifetime taken from PDG [13].

5.3.1 Trigger

When the data are collected, only events that fire one or more trigger lines (as described in Section 3.5) are stored to disk. In this analysis, the signal candidates are additionally required to pass a specific subset of those trigger lines.

For the L0 trigger it is required that the D^* candidate is TOS with respect to the `L0Hadron` trigger or TIS[1] with respect to all L0 triggers. For the HLT1 trigger it is required that the D^* candidate is TOS with respect to the signal track trigger line. For the HLT2 trigger it is required that the D^* candidate is TOS with respect to a dedicated $D \to hhhh$ trigger line.

The dedicated $D \to hhhh$ trigger line's algorithm first loops over pairs of hadrons and requires that they satisfy loose requirements on variables such as χ^2_{IP}, Track χ^2/ndf, and p_{T}. A second loop is then performed where two more hadrons are added - at this stage the invariant mass of the $hhhh$ candidates is calculated, allowing cuts on the D^0 candidate mass, m_{D^0}, to be applied. Finally the D^0 is combined with π_s candidates with $p_{\text{T}} > 300\,\text{MeV}$ and $p > 3\,\text{GeV}$ - it is required that the mass difference between the D^* and the D^0 candidate, $m(hhhh\pi_s) - m(hhhh)$, is less than 180 MeV. This quantity is called the 'delta mass' or Δm.

5.3.2 Stripping

When using DaVinci to find signal candidates in the LHCb dataset (Section 3.6), it would take too long, and be too inefficient, to run over the entire LHCb dataset. For this reason the LHCb dataset is 'stripped' several times a year to reduce the dataset down to a more manageable size. In order to study a particular decay chain, a 'stripping line' can be written to ensure candidates for that decay chain are present in the stripped dataset. For this analysis a dedicated $D^0 \to hhhh$ stripping line is used - the cuts imposed by this stripping line are listed at the end of the section (Table 5.3).

[1] Definitions of TIS and TOS are given in Section 3.5

5.3.3 Decay Chain Reconstruction

Decay chain reconstruction is the way in which reconstructed tracks are combined to form a decay chain e.g. in this analysis $K\pi\pi\pi\pi_s$ candidates are put together to form the decay chain $D^* \to D^0\pi_s, D^0 \to K\pi\pi\pi$.

The usual way to reconstruct a decay chain, known as the 'leaf by leaf' approach, is to start from the bottom of the decay chain and work upwards i.e. combine the $K\pi\pi\pi$ candidates to form a D^0 candidate, then combine this with a π_s candidate to form a D^* candidate. Another way to do this is using the Decay Tree Fitter (DTF) algorithm [74] - this takes all final state particles at once and fits the entire decay tree simultaneously. DTF also allows additional constraints to be added to the system - for instance forcing the D^0 and π_s candidates to come from a common vertex located at the PV. This constraint has large resolution benefits for the Δm distribution, as demonstrated in Figure 5.1, where DTF has been applied to MC signal events (the simulated data sample, known as the MC sample, is described in Section 5.6.1).

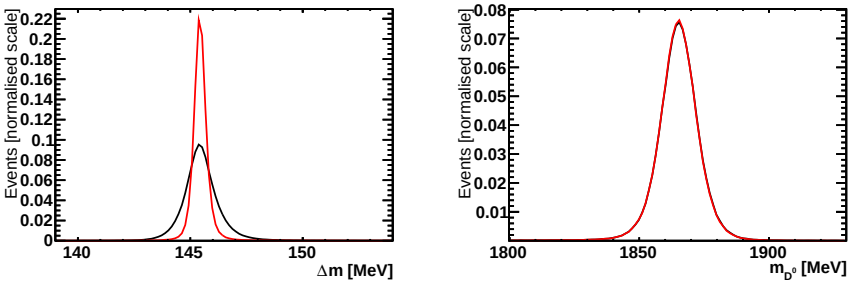

Figure 5.1: The Δm and m_{D^0} distribution of MC signal events using (black) no DTF (red) DTF

Although DTF brings a large benefit in terms of resolution, it can also cause strange behaviour when applied to backgrounds. For secondary D decays (i.e. a D meson created in the decay of a B meson) that are reconstructed as a prompt D (i.e. created at the PV) the Δm distribution is shifted to a lower mass with respect to signal (Figure 5.2). This is because it forces the D^0 and the π_s to point back to the PV, narrowing the opening angle, and lowering the D^* mass (and therefore Δm). The effect is dependent on the B flight distance, and therefore the D^0 lifetime (calculated with respect to to the PV), as illustrated in Figure 5.2. For the stripping and trigger cuts described in

Section 5.3.1 and Section 5.3.2, all variables are calculated using 'leaf by leaf' decay chain reconstruction. From this section onwards, all variables are calculated using DTF. One exception is the D^0 $\chi^2_{\rm IP}$ (and D^0 $\log_{10}\chi^2_{\rm IP}$) variable which is later used to discriminate prompt from secondary D^0 decays (Section 5.5.1). The DTF algorithm is not used for this variable because it forces the D^0 to point to the PV, meaning the variable will always be identically 0 i.e. it forces all decays to look like they were produced at the PV.

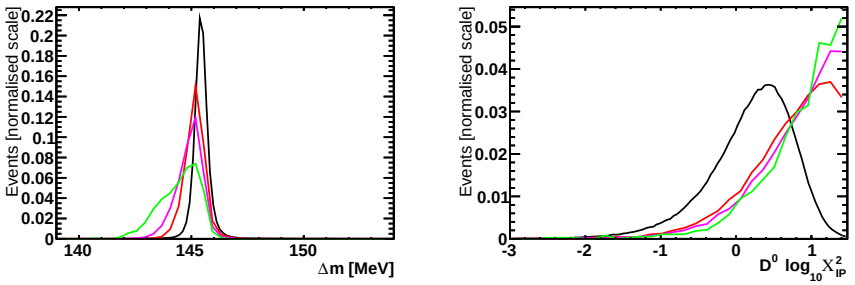

Figure 5.2: Histograms showing (left) the Δm distribution (right) the D^0 $\log_{10}\chi^2_{\rm IP}$ distribution. MC signal events are shown in black, the coloured lines show MC secondary events with (red) $D^0\,{\rm LT} < 2\,\tau_{D^0}$ (pink) $2\,\tau_{D^0} < D^0\,{\rm LT} < 5\,\tau_{D^0}$ (green) $D^0\,{\rm LT} > 5\,\tau_{D^0}$.

5.3.4 Preselection

Before optimising offline selection cuts, preselection cuts are applied to reduce the number of peaking background events in the sample - the exact values for these cuts are motivated in subsequent sections. The preselection cuts are listed in Table 5.1.

Preselection Cut	**Reason**
$D^0 \log_{10}\chi^2_{\rm IP} < 1.0$	Reduce secondary background (Section 5.5.1)
π_sGhostProb < 0.05	Reduce ghost background (Section 5.5.2)
$\lvert m_{D^0} - m^{\rm PDG}_{D^0}\rvert < 24.0\,{\rm MeV}$	Reduce double mis-ID background (Section 5.5.3)

Table 5.1: List of preselection cuts.

5.3.5 Offline Selection

The offline selection cuts are optimised using 1% of the total dataset, which will be referred to as the 'training sample'. This sample is discarded for the remainder of

the analysis. From the training sample a 'signal training sample' and a 'background training sample' are created. The signal training sample is taken from the RS candidates, selecting a elliptical region around the measured m_{D^0} and Δm:

$$\left(\frac{\Delta m - 145.45}{0.65}\right)^2 + \left(\frac{m_{D^0} - 1866.0}{13.0}\right)^2 < 2.0.$$

The background training sample is taken from WS candidates, selecting events in the Δm sidebands:

$$\left|\frac{\Delta m - 145.45}{0.65}\right| > 4.0.$$

The background training sample mainly consists of 'random slow pion' background, where a true D^0 candidate is combined with a fake slow pion. Both signal and background regions are shown in the 2D m_{D^0}-Δm plane in Figure 5.3.

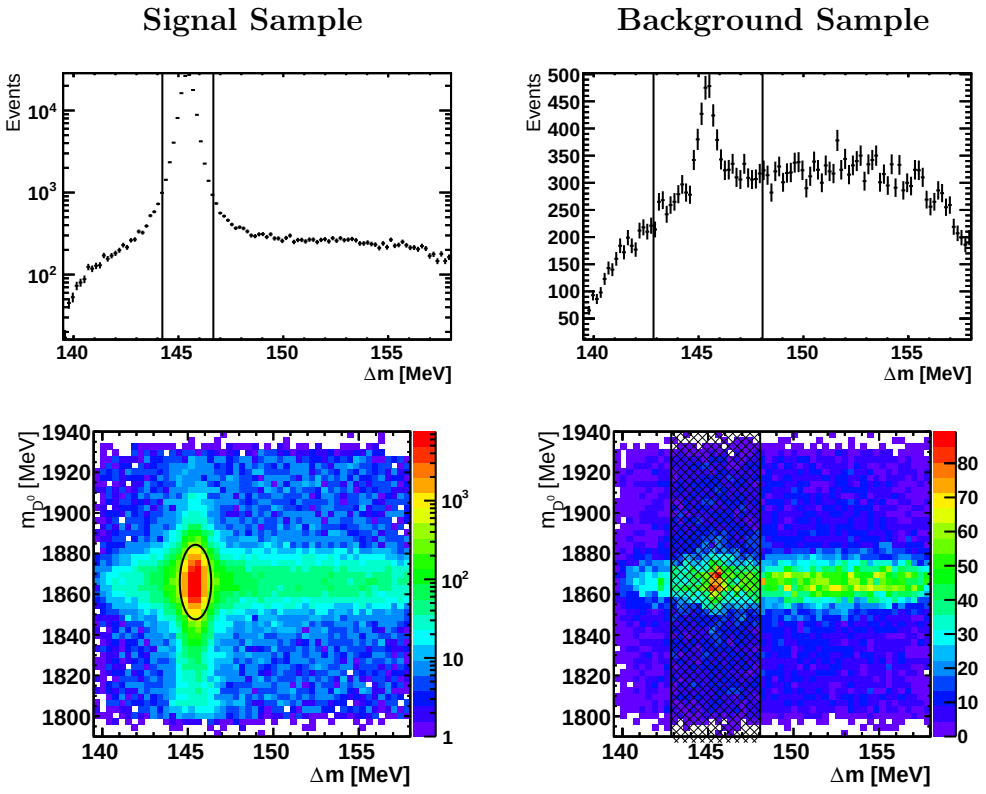

Figure 5.3: Candidates that pass preselection and trigger cuts (left) The 'signal training sample' are RS decays that fall within the superimposed ellipse (right) The 'background training sample' are WS decays that fall outside the superimposed hashed region.

To optimise the offline selection cuts a genetic algorithm was used. It was found that only four variables were necessary to give the optimal selection, these being π_s p_{T}, π_s $\mathrm{DLL}_{e\pi}$, D^0 p_{T} and $(D^*\chi^2_{\mathrm{DTF}} - D^0\chi^2_{\mathrm{IP}})$. The reason $(D^*\chi^2_{\mathrm{DTF}} - D^0\chi^2_{\mathrm{IP}})$ is used (as opposed to

$D^*\chi^2_{\rm DTF}$ alone) is because $D^*\chi^2_{\rm DTF}$ is correlated to $D^0\chi^2_{\rm IP}$ - this is not desirable because this variable is used for determining the fraction of candidates that comes from the decay of a b-hadron (Section 5.5.1).

The figure of merit (FoM) used to optimise the selection cuts is the signal significance, $\frac{s}{\sqrt{s+b}}$, where s is the number of signal, and b is the number of background in the region $\Delta m \in [145.4-1.3, 145.4+1.3]$. The FoM is optimised for WS candidates in the highest lifetime bins, where it is estimated there will be $\sim$ 150 signal events prior to offline selection. The number of events in the signal training sample was therefore scaled to 150. The number of events in the background training sample was scaled to $150/f_{\rm s/b}$, where $f_{\rm s/b}$ is the signal/background fraction of WS candidates in the training sample prior to offline selection. The quantity $f_{\rm s/b}$ was measured to be ~ 0.22 by fitting the Δm distribution of candidates - the training sample with the superimposed Δm fit is shown in Figure 5.4. The distribution of the training variables, prior to offline selection,

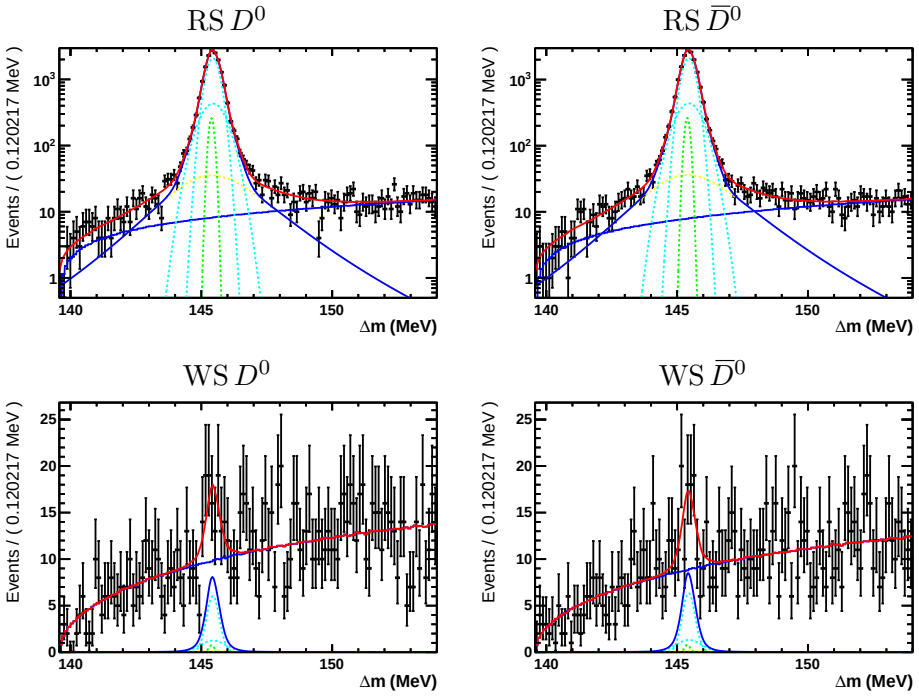

Figure 5.4: The Δm distribution of the training sample for all event categories with the fit result superimposed. This is used to estimate the WS signal to background ratio, $f_{\rm s/b}$, prior to any preselection cuts. The fit procedure is detailed in Section 5.4.

for signal and background samples is shown in Figure 5.5. The optimal cut values are also superimposed in the figure. On an independent test sample, the offline selection

cuts were found to retain 86% of signal, while rejecting 37% of background, for events passing the stripping, trigger and preselection cuts.

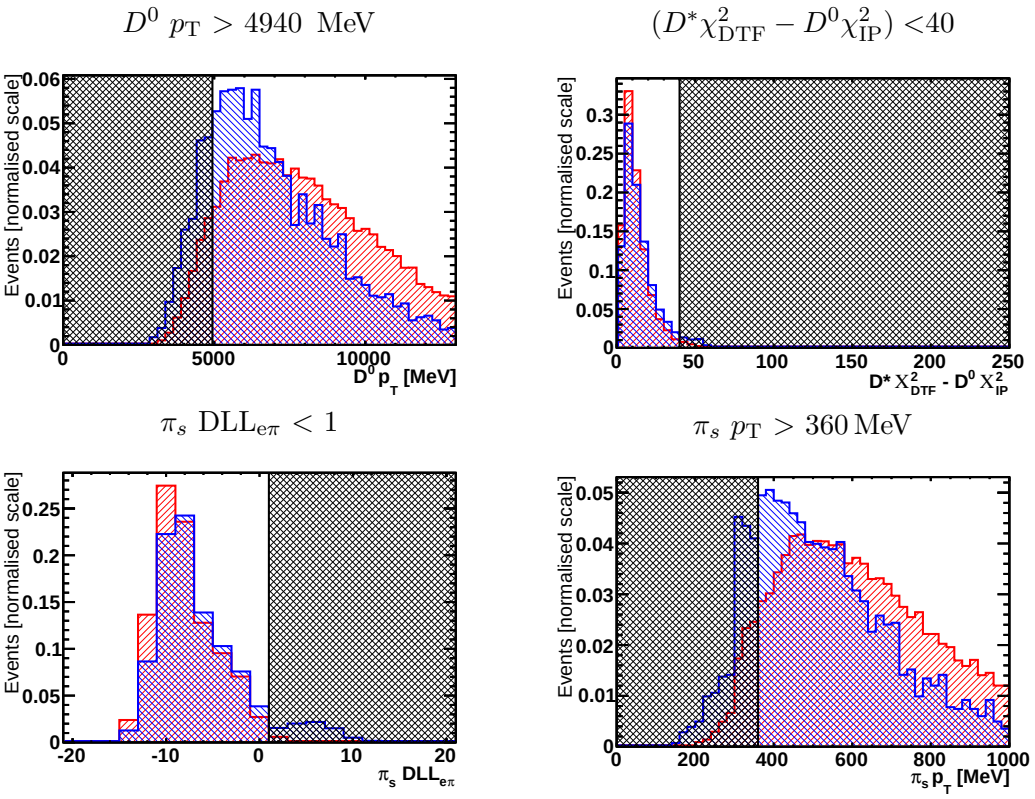

Figure 5.5: The signal training sample (red) and the background training sample (blue) used to optimise the offline selection cuts. The black hashed area shows the region excluded by the optimised offline selection cuts. The limits and binning of the histograms demonstrate the cut values that were available to the genetic algorithm.

5.3.6 PID Selection

A large peaking background in the sample of WS candidates is caused by the double misidentification of two D daughters, which can make a RS decay ($D^0 \to K^-\pi^+\pi^-\pi^+$) look like a WS decay ($D^0 \to \pi^-K^+\pi^-\pi^+$) i.e. both a kaon misidentified as a pion and a pion misidentified as a kaon. Such events are called double mis-ID background.

To demonstrate the nature of this background, a sample of MC signal has been reconstructed with the incorrect mass hypotheses. Projections of m_{D^0} and Δm are plotted in Figure 5.6 for both the correct and incorrect mass hypotheses - it is seen that double mis-ID events peak in Δm but are very broad in m_{D^0}.

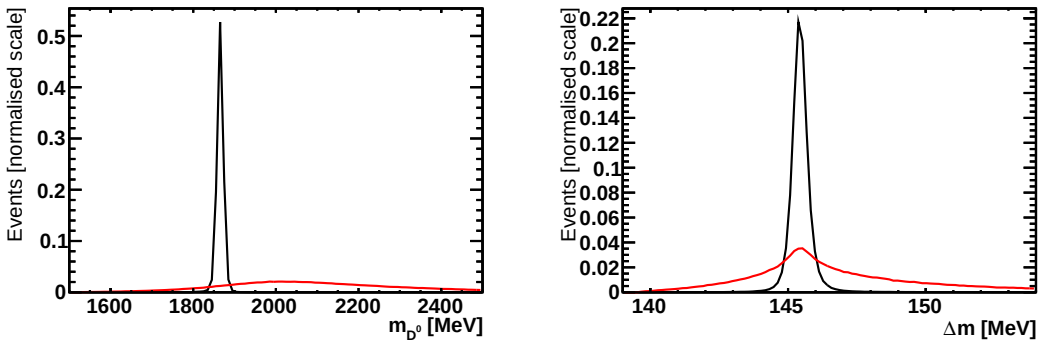

Figure 5.6: Projections of both m_{D^0} and Δm for the correct mass hypothesis (black) and when the mass hypotheses of a π and a K are swapped (red).

To suppress double mis-ID background a signal window in m_{D^0} is defined $|m_{D^0} - m_{D^0}^{\mathrm{PDG}}| < 24.0$ (see Table 5.1). This is defined symmetrically around $m_{D^0}^{\mathrm{PDG}}$, containing approximately $\pm 3\sigma$ of the observed signal width.

When later fitting the Δm distribution to obtain signal yields, only double mis-ID events that are within the m_{D^0} signal window remain - Figure 5.7 shows the Δm shape of double mis-ID events within this window. It is clear that within the m_{D^0} signal window, the Δm shape is very similar for both signal and double mis-ID events. Therefore, to a good approximation, it is possible to use the same Δm PDF to describe both shapes i.e. the signal yield will encompass both true signal and double mis-ID events.

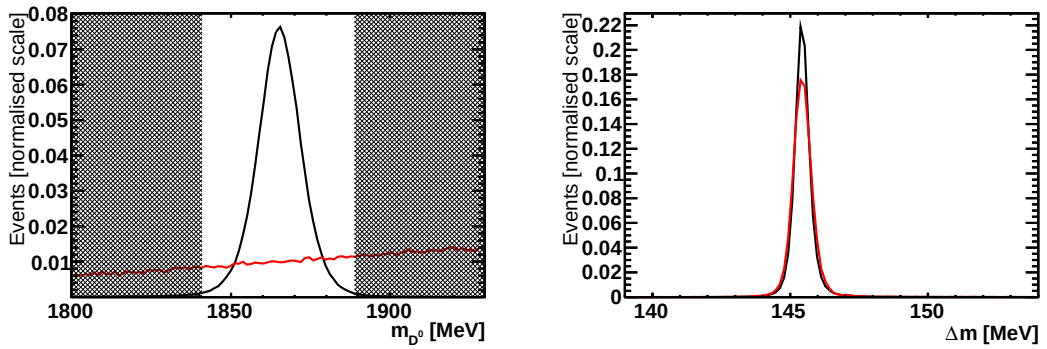

Figure 5.7: Projections of both m_{D^0} and Δm for (black) the correct mass hypothesis (red) the mass hypotheses of a π and a K are swapped. The m_{D^0} signal window is highlighted in the left figure. Only events that fall within this window are used in the right figure.

To estimate the number of double mis-ID events in the WS signal region (region R1) the number in the m_{D^0} sidebands (region R2) is determined, then extrapolated into R1. The two regions are defined:

- R1: $139.0 < \Delta m < 154.0$ && $|m_{D^0} - m_{D^0}^{\rm PDG}| < 24.0$.
- R2: $139.0 < \Delta m < 154.0$ && $|m_{D^0} - m_{D^0}^{\rm PDG}| > 40.0$.

These regions are also shown in the 2D m_{D^0}–Δm plane in Figure 5.8.

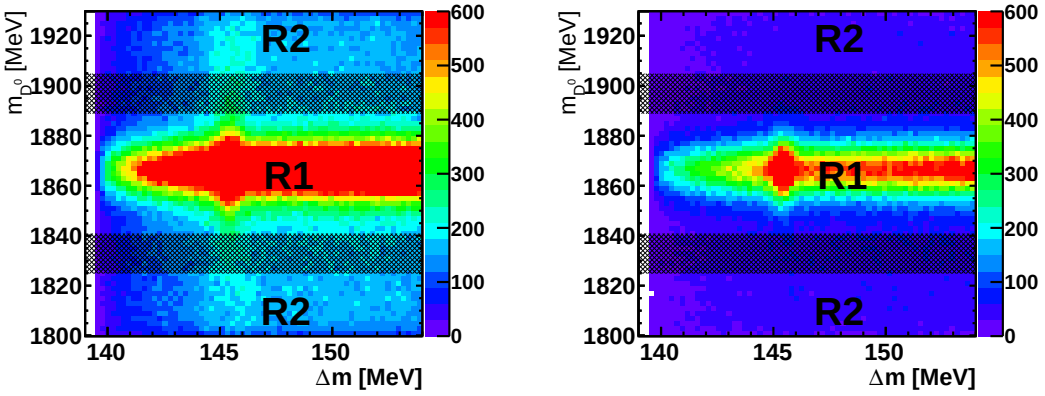

Figure 5.8: 2D histogram of m_{D^0} – Δm for WS candidates that pass (left) trigger requirements and offline selection (right) trigger requirements, offline and PID selection. R1 is the signal region used to determine the signal yields. R2 is the sideband region used to estimate the number of double mis-ID events that contaminate the signal region.

The number of double mis-ID events in R2 is found from a fit to the Δm distribution (see Figure 5.9). The shape of double mis-ID background is hard to parameterise, and

therefore the Δm sidebands are fitted using only a background PDF. The background shape is then integrated into the signal region, allowing the number of double mis-ID events to be calculated. Once the number of double mis-ID events in R2 is determined, this is scaled (assuming a linear shape in m_{D^0}) to determine the number in R1.

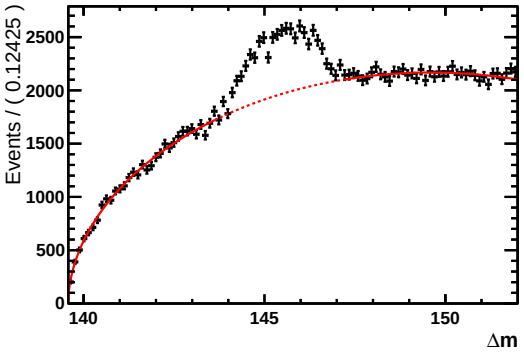

Figure 5.9: Black data points show Δm for WS candidates in the sidebands of m_{D^0} (as highlighted as R2 in Figure 5.8). Superimposed with a red line is a fit to this distribution, only performed in the region with a solid line. The PDF is then integrated in the dashed region to calculate the number of double mis-ID events.

In order to suppress double mis-ID background, the $\mathrm{DLL}_{\mathrm{K}\pi}$ cuts on the D^0 daughters are optimised. The optimisation is performed by scanning over the $\mathrm{DLL}_{\mathrm{K}\pi}$ cuts K PIDK and π PIDK which, for the final state $K^-\pi_1^+\pi^-\pi_2^+$, are defined[2]:

- K PIDK $= x$: K^- $\mathrm{DLL}_{\mathrm{K}\pi} > x$
- π PIDK $= x$: π_1^+ $\mathrm{DLL}_{\mathrm{K}\pi} < x$ && π_2^+ $\mathrm{DLL}_{\mathrm{K}\pi} < x$

Notice that cuts are only applied to the opposite sign pions ($Q(K) \neq Q(\pi)$) because only these will change the event type from RS to WS (and therefore bias the WS/RS ratio). To find the optimum point in K PIDK – π PIDK parameter space, a figure of merit (FoM) is evaluated at points in a 2D grid. The chosen FoM is $s/\sqrt{s+2b}$, where s is the number of WS events, and b is the number of double mis-ID events. This is similar to the 'signal significance' FoM used in Section 5.3.5, but accounts for the limited m_{D^0} sidebands available to determine the number of double mis-ID events[3]. The FoM is optimised for WS events in the highest lifetime bins, and for this reason the signal

[2]where ':' should be interpreted as 'is defined by'

[3]regions R1 and R2 are approximately the same width in m_{D^0} so there is an error of $\sim\sqrt{b}$ on the *expected number* of background in R1, which itself fluctuates according to a Poisson distribution, giving $\sigma_B^2 = 2b$

and background yields are scaled to give 150 signal events before the $\mathrm{DLL}_{\mathrm{K}\pi}$ cuts are applied. The results of the study are shown in Figure 5.10.

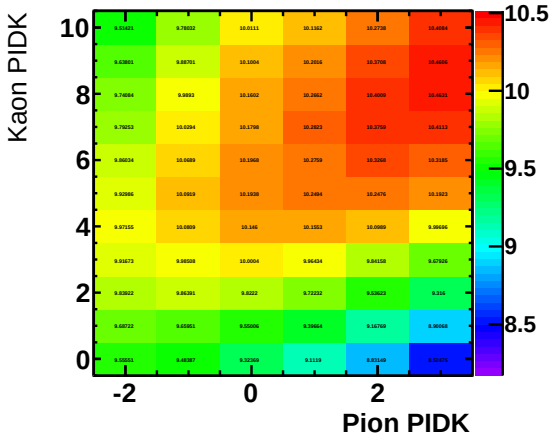

Figure 5.10: The FoM (described in the text) evaluated at a grid of points in K PIDK – π PIDK plane.

From the results of the optimisation study in Figure 5.10, the best strategy is to have a tight $\mathrm{DLL}_{\mathrm{K}\pi}$ cut on the K candidate (K $\mathrm{DLL}_{\mathrm{K}\pi} > 8.0$) and no $\mathrm{DLL}_{\mathrm{K}\pi}$ cut on the π candidates (limited by the cut in the stripping of π $\mathrm{DLL}_{\mathrm{K}\pi} < 3.0$). The 2D m_{D^0} -Δm distribution before and after PID cuts is shown in Figure 5.8. The vertical band, seen before PID cuts, is a result of double mis-ID events. This is seen to be significantly reduced after PID cuts. Any remaining double mis-ID events are considered in Section 5.5.2.

5.3.7 Multiple Candidates

A small fraction of events contain multiple candidates. Most of these have the same D^0 candidate combined with a different π_s, meaning that the vast majority of these are random slow pion background. For any event containing multiple candidates, one candidate is picked at random and the rest are discarded - this criterion removes $\sim 4\%$ of candidates.

The multiple candidates are removed after all selection cuts, except those used to reduce peaking backgrounds (Table 5.1). These cuts are later relaxed (Sections 5.5.1 - 5.5.3) in

order to quantify peaking backgrounds, so it is convenient to remove multiple candidates before these cuts are made.

5.3.8 Selection Overview

Table 5.2 gives a summary of the number of candidates remaining after different stages of selection. After all cuts, there is a total of 3,617,461 WS+RS candidates remaining. This number includes the 1% of events that were removed to train the offline selection cuts. Table 5.3 gives a summary of all selection cuts.

	Magnet Up	Magnet Down	Total
Stripping	13,738,418	19,826,553	33,564,971
Trigger	4,504,505	6,361,998	10,866,503
Preselection	4,025,399	5,711,654	9,737,053
Selection	3,098,624	4,427,155	7,525,779
PID	2,516,132	3,607,714	6,123,846
Multiple Cands	2,401,095	3,446,084	5,847,179
π_s GhostProb	1,875,959	2,700,020	4,575,979
D^0 $\log_{10}\chi^2_{\rm IP}$	2,053,868	2,957,486	5,011,354
m_{D^0}	2,220,272	3,190,438	5,410,710
Final	1,480,418	2,137,043	3,617,461

Table 5.2: Candidate yields after each stage of selection. Separate numbers are given for data taken with 'magnet up' and 'magnet down' polarity. The indented rows indicates the three selection cuts used to suppress peaking backgrounds (Table 5.1) - the candidate yields given in these rows are all with respect to the 'Multiple Cands' row. The bottom row shows the candidate yields when all three cuts are applied.

	Variable name	Stripping	Offline Selection
$h^\pm$	Track χ^2/ndf	< 4	—
	$\chi^2_{\rm IP}$	> 3.0, —, —, 30^a	—
	$p_{\rm T}$	$> 350\,$MeV	—
	$\lvert\vec{p}\rvert$	$> 3\,$GeV	—
K^-	$\rm DLL_{K\pi}$	> 0	> 8
$\pi^\pm$	$\rm DLL_{K\pi}$	< 3	—
D^*	Vertex χ^2/ndf	< 20	—
	DoCA	$< 0.22\,$mm	—
	$p_{\rm T}$	$> 3\,$GeV	—
π_s	$p_{\rm T}$	$> 120\,$MeV	$> 360\,$MeV
	$\lvert\vec{p}\rvert$	$> 3\,$GeV	—
	$\rm DLL_{e\pi}$	$> 120\,$MeV	< 1
	GhostProb	—	< 0.05
D^0	Vertex χ^2/ndf	< 10	—
h_ih_j pair	DoCA	$< 0.12\,$mm	—
	$p_{\rm T}$	$> 3000\,$MeV	$> 4940\,$MeV
	FD χ^2	> 48	—
	$\chi^2_{\rm IP}$	< 30	< 10
	DIRA	> 0.99980	—
	$\lvert m - m_{\rm PDG}\rvert$	$< 65\,$MeV	$< 24\,$MeV
	DTFχ^2- D^0 $\chi^2_{\rm IP}$	—	< 40.0

Table 5.3: Selection criteria used in the stripping selection and offline selection. This does not include the trigger criteria described in Section 5.3.1 or the removal of multiple candidates detailed in Section 5.3.7. The symbol h represents any D^0 daughter i.e. both π and K.

[a]The $\chi^2_{\rm IP}$ of the D^0 daughters are sorted in ascending order, then the cuts are applied in the order listed.

5.4 Measuring RS and WS yields

To determine the RS and WS yields the Δm distribution of selected signal candidates is modelled using a signal and a background shape. As well as true signal decays, the signal shape is also designed to encompass peaking backgrounds (Section 5.5) from double mis-ID and secondary background (a D meson that is the decay product of a B meson) - a correction is later applied to account for the presence of these backgrounds.

5.4.1 Shape components

This section describes the shape components used to create the signal and background parameterisations.

5.4.1.1 Gaussian shape

The Gaussian shape is defined as:

$$\mathscr{G}\left(\Delta m; \mu, \sigma\right) = \frac{1}{N_{\mathscr{G}}} e^{-\frac{1}{2}\left(\frac{\Delta m - \mu}{\sigma}\right)^2} \tag{5.8}$$

The parameters μ and σ describe the mean and width of the distribution. The parameter $N_{\mathscr{G}}$ gives the normalisation integral of the Gaussian, which is calculated analytically.

5.4.1.2 Johnson shape

The Johnson shape [75] is defined as:

$$\mathscr{J}\left(\Delta m; \mu, \sigma, \delta, \gamma\right) = \frac{1}{N_{\mathscr{J}}} \frac{e^{-\frac{1}{2}\left[\gamma + \delta \mathrm{arcsinh}\left(\frac{\Delta m - \mu}{\sigma}\right)\right]}}{\sqrt{1 + \left(\frac{\Delta m - \mu}{\sigma}\right)^2}} \tag{5.9}$$

The parameters μ and σ describe the mean and width of the distribution, whereas γ and δ describe the asymmetric tails. The parameter $N_{\mathscr{J}}$ gives the normalisation integral of the Johnson, which is calculated analytically.

5.4.1.3 Chebyshev polynomial

A third order Chebyshev polynomial is defined in Equation 5.10 with coefficients p_1, p_2 and p_3. The set of Chebyshev polynomials are orthogonal over the range $[-1, 1]$, so the data are mapped (via a linear transformation) into this range.

$$\begin{aligned} \text{Chebyshev}\,(\Delta m; p_1, p_2, p_3) &= 1.0 + p_1 x + p_2(2x^2 - 1) + p_3(4x^3 - 3x), \\ \text{where} \quad x &= 2\frac{\Delta m - \min(\Delta m)}{\max(\Delta m) - \min(\Delta m)} - 1. \end{aligned} \tag{5.10}$$

5.4.1.4 HistPoly shape

The HistPoly Shape, defined in Equation 5.11, is a histogram $h(\Delta m)$ multiplied by a Chebyshev polynomial. The Chebyshev polynomial is evaluated at the bin centre of the nearest bin. This ensures that the HistPoly Shape stays constant over the bin width.

$$\text{HistPoly}\,(\Delta m; p_1, p_2, p_3) = \frac{1}{N_{\text{HistPoly}}} h(\Delta m)\text{Chebyshev}\,(\text{binCenter}(\Delta m); p_1, p_2, p_3) \tag{5.11}$$

The parameter N_{HistPoly} gives the normalisation integral of the HistPoly shape, which is calculated numerically.

The histogram, $h(\Delta m)$, is made from a large sample of 'random slow pion' events. These are generated by combining a D^0 candidate with a π_s candidate from another event. The Δm of the 'random slow pion' combination is then added to $h(\Delta m)$ - the resulting histogram is seen in Figure 5.11.

5.4.2 Signal PDF

The parameterisation used to model the signal shape is the sum of a Johnson and 3 Gaussians. The Johnson has fit parameters μ, σ, δ and γ, as defined in Equation 5.9. The 3 Gaussians are described by the fit parameters $\Delta_{\mu,i}$ and $s_{\sigma,i}$, where i labels the Gaussian number. The mean and width of each Gaussian is then given by $\mu + \Delta_{\mu,i}$ and $\sigma \cdot s_{\sigma,i}$ respectively i.e. $\Delta_{\mu,i}$ gives the offset between the Johnson mean and the

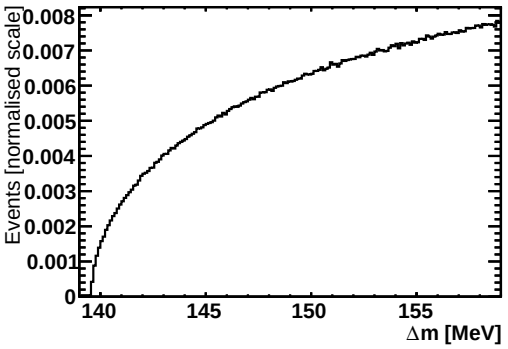

Figure 5.11: Δm distribution of D^0 candidates combined with slow pion candidates from different events.

ith Gaussian mean, whereas $s_{\sigma,i}$ gives the scale between the Johnson width and the ith Gaussian width. The parameters f_1, f_2 and f_3 describe the relative fraction of events in each signal component. The full signal PDF is defined:

$$\begin{aligned}\mathcal{S}(\Delta m; \mathbf{\Theta}_{\text{sig}}) =& f_3 \Bigg(f_2 \Big(f_1 \mathscr{G}\left(\Delta m; \mu + \Delta_{\mu,1}, \sigma \cdot s_{\sigma,1}\right) \\ &+ (1-f_1)\mathscr{G}\left(\Delta m; \mu + \Delta_{\mu,2}, \sigma \cdot s_{\sigma,2}\right) \Big) \\ &+ (1-f_2)\mathscr{G}\left(\Delta m; \mu + \Delta_{\mu,3}, \sigma \cdot s_{\sigma,3}\right) \Bigg) \\ &+ (1-f_3)\,\mathscr{J}\left(\Delta m; \mu, \sigma, \delta, \gamma\right),\end{aligned} \tag{5.12}$$

where the parameter $\mathbf{\Theta}_{\text{sig}}$ is a vector containing all fit parameters in the signal PDF.

5.4.3 Background PDF

To model the background shape the HistPoly Shape is used from Equation 5.11. It was found sufficient to use only a first order polynomial i.e. $p_2 = p_3 = 0$. The full background PDF is defined:

$$\mathcal{B}(\Delta m; \mathbf{\Theta}_{\text{back}}) = \text{HistPolyShape}\left(\Delta m; p_1, 0, 0\right), \tag{5.13}$$

where the parameter $\mathbf{\Theta}_{\text{back}}$ is a vector containing all fit parameters in the background PDF.

5.4.4 Full PDF

To extract the RS D^0, RS $\overline{D}^0$, WS D^0 and WS $\overline{D}^0$ yields from data, a simultaneous binned maximum likelihood fit is performed to all four event categories. The signal shape of each category is expected to be the same, therefore all signal shape parameters, $\mathbf{\Theta}_{\rm sig}$, are shared. This allows the signal shape to be constrained from the much higher statistics in the RS category, giving a smaller uncertainty on the WS yields. All categories have the same background parameterisation but use independent parameters, $\mathbf{\Theta}^{\rm CAT}_{\rm back}$. The signal and background yields in each category are given by $\mathcal{N}^{\rm CAT}_{\rm sig}$ and $\mathcal{N}^{\rm CAT}_{\rm back}$ respectively. The total PDF, $\mathcal{T}_{\rm CAT}$, for each category, is given by:

$$
\begin{aligned}
\mathcal{T}_{\mathrm{RS}\,D^0}\left(\Delta m; \mathbf{\Theta}^{\mathrm{RS}\,D^0}_{\rm back}, \mathbf{\Theta}_{\rm sig}\right) &= \mathcal{N}^{\mathrm{RS}\,D^0}_{\rm sig}\mathcal{S}(\Delta m; \mathbf{\Theta}_{\rm sig}) + \mathcal{N}^{\mathrm{RS}\,D^0}_{\rm back}\mathcal{B}(\Delta m; \mathbf{\Theta}^{\mathrm{RS}\,D^0}_{\rm back}) \\
\mathcal{T}_{\mathrm{RS}\,\overline{D}^0}\left(\Delta m; \mathbf{\Theta}^{\mathrm{RS}\,\overline{D}^0}_{\rm back}, \mathbf{\Theta}_{\rm sig}\right) &= \mathcal{N}^{\mathrm{RS}\,\overline{D}^0}_{\rm sig}\mathcal{S}(\Delta m; \mathbf{\Theta}_{\rm sig}) + \mathcal{N}^{\mathrm{RS}\,\overline{D}^0}_{\rm back}\mathcal{B}(\Delta m; \mathbf{\Theta}^{\mathrm{RS}\,\overline{D}^0}_{\rm back}) \\
\mathcal{T}_{\mathrm{WS}\,D^0}\left(\Delta m; \mathbf{\Theta}^{\mathrm{WS}\,D^0}_{\rm back}, \mathbf{\Theta}_{\rm sig}\right) &= \mathcal{N}^{\mathrm{WS}\,D^0}_{\rm sig}\mathcal{S}(\Delta m; \mathbf{\Theta}_{\rm sig}) + \mathcal{N}^{\mathrm{WS}\,D^0}_{\rm back}\mathcal{B}(\Delta m; \mathbf{\Theta}^{\mathrm{WS}\,D^0}_{\rm back}) \\
\mathcal{T}_{\mathrm{WS}\,\overline{D}^0}\left(\Delta m; \mathbf{\Theta}^{\mathrm{WS}\,\overline{D}^0}_{\rm back}, \mathbf{\Theta}_{\rm sig}\right) &= \mathcal{N}^{\mathrm{WS}\,\overline{D}^0}_{\rm sig}\mathcal{S}(\Delta m; \mathbf{\Theta}_{\rm sig}) + \mathcal{N}^{\mathrm{WS}\,\overline{D}^0}_{\rm back}\mathcal{B}(\Delta m; \mathbf{\Theta}^{\mathrm{WS}\,\overline{D}^0}_{\rm back})
\end{aligned}
\quad (5.14)
$$

5.4.5 Fit to Lifetime-Integrated Sample

To test the validity of the PDF in Equation 5.14, the fit is performed on the full sample of selected signal candidates, using the entire lifetime range $[0.5\,\tau_{D^0}, 20\,\tau_{D^0}]$. The signal candidates in all four categories are shown in Figure 5.12 with the fit result superimposed. Also shown are the pull distributions, which indicate a good fit quality. The signal yields for each category are $\mathcal{N}^{\mathrm{RS}\,D^0}_{\rm sig} = 1,614,900 \pm 1500$, $\mathcal{N}^{\mathrm{RS}\,\overline{D}^0}_{\rm sig} = 1,678,300 \pm 1600$, $\mathcal{N}^{\mathrm{WS}\,D^0}_{\rm sig} = 6050 \pm 120$ and $\mathcal{N}^{\mathrm{WS}\,\overline{D}^0}_{\rm sig} = 6242 \pm 120$.

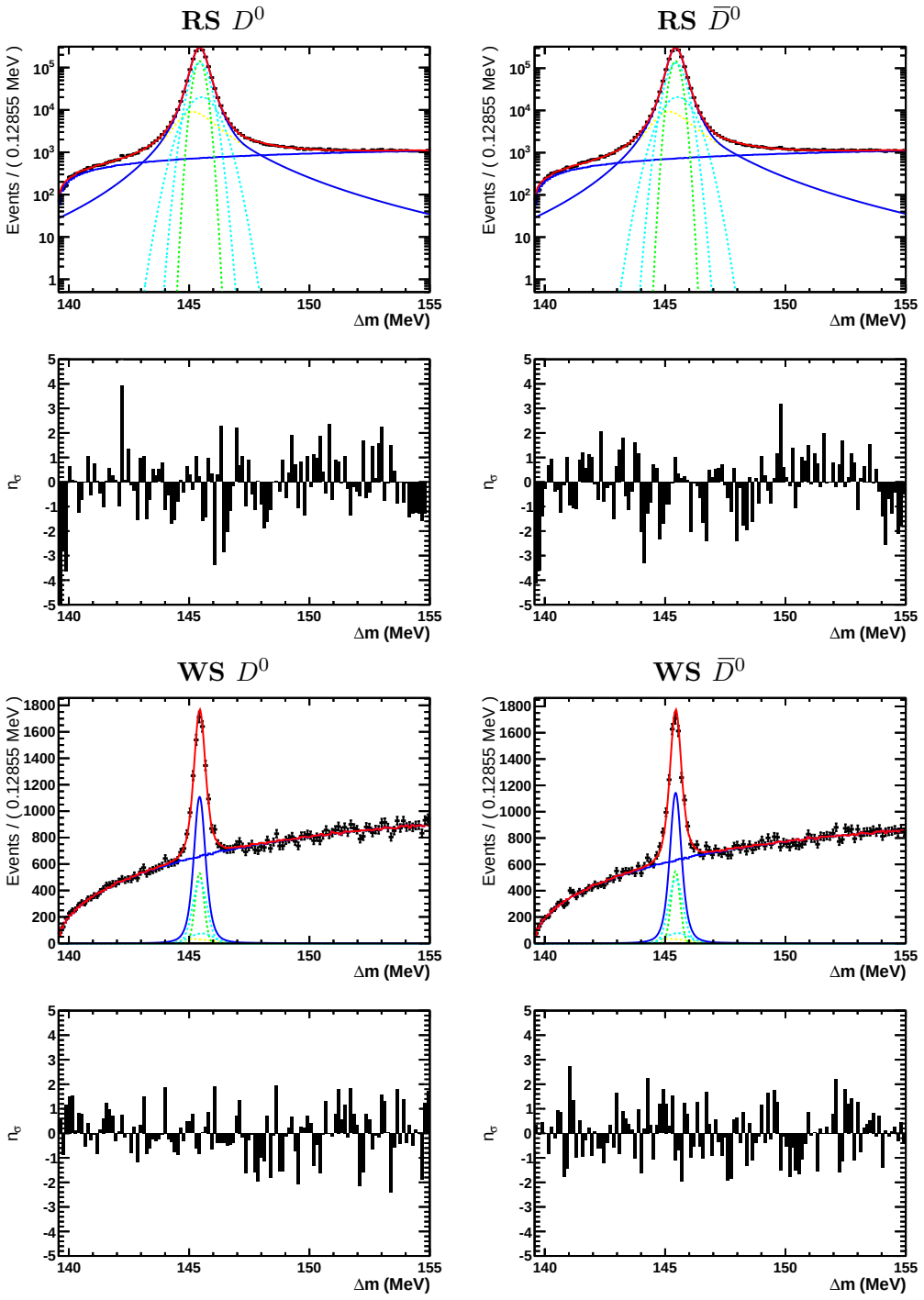

Figure 5.12: Δm distribution of selected signal candidates for all four event categories. In all figures, the result of the simultaneous fit is superimposed. The signal and background PDFs (peaking and not-peaking respectively) are drawn using a solid blue line. The individual components of the signal PDF are drawn using dashed lines (the Johnson function is coloured green, and the remaining colours are the Gaussian components). The total PDF (signal + background) is drawn using a solid red line.

5.4.6 Determination of the time-dependent WS/RS ratio

To measure the time-dependent WS/RS ratio, the fit method presented in Section 5.4.5 is applied in 10 independent lifetime bins. The lifetime bins are defined in the range $[0.5\,\tau_{D^0}, 20\,\tau_{D^0}]$ so that no bin contains fewer that 150 WS signal events. The resulting yields are summarised in Table 5.4. The time-dependent WS/RS ratio is shown in Figure 5.13 - this displays a clear time-dependent variation, indicating contributions from D-mixing.

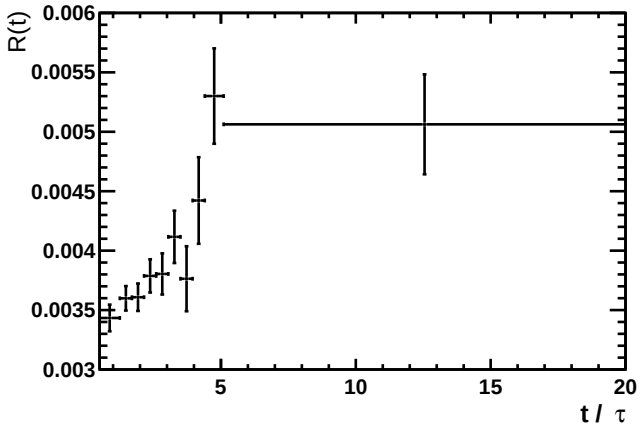

Figure 5.13: The WS/RS ratio measured in bins of D^0 LT (defined in Table 5.4)

Bin	t_i^-/τ_{D^0}	t_i^+/τ_{D^0}	$\mathcal{N}_{\rm sig}^{\rm RS}{}^{D^0}$	$\mathcal{N}_{\rm sig}^{\rm RS}{}^{\bar{D}^0}$	$\mathcal{N}_{\rm sig}^{\rm WS}{}^{D^0}$	$\mathcal{N}_{\rm sig}^{\rm WS}{}^{\bar{D}^0}$	$\mathcal{N}_{\rm sig}^{tot}$	$\mathcal{N}_{\rm back}^{\rm RS}{}^{D^0}$	$\mathcal{N}_{\rm back}^{\rm RS}{}^{\bar{D}^0}$	$\mathcal{N}_{\rm back}^{\rm WS}{}^{D^0}$	$\mathcal{N}_{\rm back}^{\rm WS}{}^{\bar{D}^0}$	$\mathcal{N}_{\rm back}^{tot}$	WS/RS
0	0.50	1.25	302924 ± 1468	314729 ± 1519	1058 ± 49	1062 ± 49	619773 ± 2114	17271 ± 1364	17097 ± 1414	13580 ± 122	13148 ± 120	61096 ± 1972	0.00343 ± 0.00011
1	1.25	1.70	383589 ± 751	399338 ± 771	1383 ± 57	1434 ± 57	785745 ± 1079	21660 ± 451	22033 ± 467	18916 ± 144	18074 ± 140	80683 ± 680	0.00360 ± 0.00010
2	1.70	2.15	312542 ± 1715	323620 ± 1779	1142 ± 52	1153 ± 52	638457 ± 2472	17127 ± 1622	17483 ± 1686	15782 ± 132	15118 ± 129	65510 ± 2346	0.00361 ± 0.00012
3	2.15	2.60	217714 ± 658	226223 ± 676	829 ± 44	853 ± 44	445618 ± 945	12289 ± 477	12381 ± 493	11187 ± 111	10515 ± 108	46373 ± 703	0.00379 ± 0.00014
4	2.60	3.05	144123 ± 427	150393 ± 435	533 ± 36	589 ± 36	295638 ± 612	8274 ± 216	8404 ± 219	7515 ± 91	7231 ± 89	31424 ± 333	0.00380 ± 0.00017
5	3.05	3.50	93038 ± 363	97144 ± 373	396 ± 30	387 ± 29	190965 ± 522	5404 ± 210	5681 ± 218	4920 ± 73	4696 ± 72	20701 ± 320	0.00412 ± 0.00022
6	3.50	3.95	60018 ± 274	61817 ± 279	214 ± 23	245 ± 24	122295 ± 393	3415 ± 138	3515 ± 141	3190 ± 59	3103 ± 58	13222 ± 214	0.00376 ± 0.00027
7	3.95	4.40	37230 ± 226	39168 ± 233	150 ± 19	190 ± 20	76738 ± 326	2313 ± 127	2370 ± 133	2043 ± 48	1889 ± 46	8615 ± 195	0.00442 ± 0.00036
8	4.40	5.10	32961 ± 246	33853 ± 252	183 ± 19	171 ± 19	67169 ± 353	1967 ± 171	1988 ± 177	1744 ± 44	1646 ± 43	7345 ± 254	0.00530 ± 0.00040
9	5.10	20.00	30675 ± 204	31869 ± 208	159 ± 18	157 ± 19	62861 ± 293	2007 ± 114	1886 ± 115	1691 ± 43	1779 ± 44	7362 ± 174	0.00506 ± 0.00042
10	0.50	20.00	1614902 ± 1525	1678263 ± 1562	6050 ± 118	6242 ± 118	3305457 ± 2189	91642 ± 899	92735 ± 927	80566 ± 297	77198 ± 291	342140 ± 1356	0.00373 ± 0.00005

Table 5.4: Signal and background yields found from fitting the Δm distribution of selected signal candidates in independent lifetime bins. The upper and lower boundary of each lifetime bin is given in the second and third columns respectively.

5.5 Peaking Backgrounds and Systematics

5.5.1 Secondary Decays

One source of peaking background is from D^* mesons that originate from the decay of b-hadrons. This 'background' is actually real signal, but because the D^0 lifetime is calculated with respect to the primary vertex, there is a bias in the measured lifetime. The measured WS/RS ratio, including this background, can be expressed as:

$$\begin{aligned} R^M(t) &= \frac{N^{WS}(t) + N_B^{WS}(t)}{N^{RS}(t) + N_B^{RS}(t)} && (5.15)\\ &= R(t)\left[1 - f_B^{RS}(t)\left(1 - \frac{R_B(t)}{R(t)}\right)\right] && (5.16)\\ &= R(t)\left[1 - \Delta_B(t)\right] && (5.17) \end{aligned}$$

where $N^{WS}(t)$ and $N^{RS}(t)$ are the number of promptly produced WS and RS decays, and $N_B^{WS}(t)$ and $N_B^{RS}(t)$ are the number of WS and RS decays produced in the decay of b-hadrons. $R(t)$ and $R_B(t)$ give the WS/RS ratio of promptly produced and not-promptly produced decays respectively. The fraction of secondary decays in the RS sample is defined as,

$$f_B^{RS}(t) = \frac{N_B^{RS}(t)}{N^{RS}(t) + N_B^{RS}(t)}, \tag{5.18}$$

and the secondary correction is defined as,

$$\Delta_B(t) = f_B^{RS}(t)\left(1 - \frac{R_B(t)}{R(t)}\right). \tag{5.19}$$

For correctly measured D decay times $R_B(t) \equiv R(t)$. However the measured lifetime of a D^0 produced at a secondary vertex will always be an overestimation, and therefore $R_B(t)$ must be bounded on both sides by the minimum and maximum of $R(t)$ in the lifetime range $[0, t]$ (given by $R_{\min}(t)$ and $R_{\max}(t)$ respectively),

$$R_{\min}(t) \leq R_B(t) \leq R_{\max}(t). \tag{5.20}$$

After some simple algebraic manipulation, one can show that the secondary correction, $\Delta_B(t)$, must also be bounded on both sides:

$$f_B^{RS}(t)\left[1-\frac{R_{\max}(t)}{R(t)}\right] \leq \Delta_B(t) \leq f_B^{RS}(t)\left[1-\frac{R_{\min}(t)}{R(t)}\right], \tag{5.21}$$

$$\Delta_B^{\min}(t) \leq \Delta_B(t) \leq \Delta_B^{\max}(t), \tag{5.22}$$

where $\Delta_B^{\min}(t)$ and $\Delta_B^{\max}(t)$ are defined:

$$\Delta_B^{\min}(t) = f_B^{RS}(t)\left[1-\frac{R_{\max}(t)}{R(t)}\right], \tag{5.23}$$

$$\Delta_B^{\max}(t) = f_B^{RS}(t)\left[1-\frac{R_{\min}(t)}{R(t)}\right]. \tag{5.24}$$

To correct the measured WS/RS ratio for the presence of secondary decays, the mid-point, $\Delta_B^{\mathrm{COR}}(t)$, of $\Delta_B^{\min}(t)$ and $\Delta_B^{\max}(t)$ is used. One also needs to allow for fluctuations between these limits, and so an uncertainty, $\sigma_B^{\mathrm{COR}}(t)$, is assigned to the correction. This is chosen to be the half distance between $\Delta_B^{\min}(t)$ and $\Delta_B^{\max}(t)$. The two quantities are defined:

$$\Delta_B^{\mathrm{COR}}(t) = \frac{\Delta_B^{\max}(t)+\Delta_B^{\min}(t)}{2} \tag{5.25}$$

$$\sigma_B^{\mathrm{COR}}(t) = \frac{\Delta_B^{\max}(t)-\Delta_B^{\min}(t)}{2} \tag{5.26}$$

To compute these quantities, one needs to find $R_{\min}(t)$ and $R_{\max}(t)$ which depend on the quantities being measured (x, y, r_D, R_D^f, δ_D^f). For this reason, the calculation and application of $\Delta_B^{\mathrm{COR}}(t)$ and $\sigma_B^{\mathrm{COR}}(t)$ must be performed in time-dependent WS/RS fitter, so that their values can be updated from the current parameterisation of the WS/RS ratio that is described in the fitter. This procedure is described in Section 5.7.

5.5.1.1 Determination of the Secondary Fraction

In order to calculate the secondary correction, the secondary fraction in RS decays, $f_{B,i}^{RS}$, first has to be determined - the i subscript indicates the secondary fraction in lifetime bin i. To determine $f_{B,i}^{RS}$ a fit is performed to the D^0 $\log_{10}\chi^2_{\mathrm{IP}}$ distribution in each lifetime bin, where the fitted PDF has both a prompt and a secondary component.

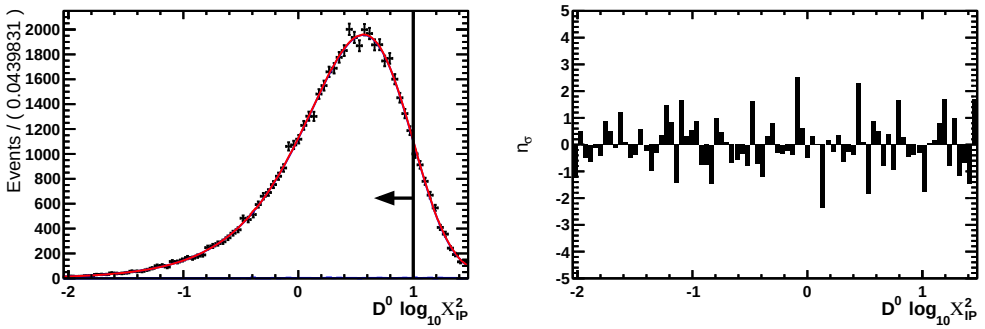

Figure 5.14: Fit to the *sWeighted* D^0 $\log_{10}\chi^2_{\rm IP}$ distribution of candidates with D^0 lifetime below $0.7\,\tau_{D^0}$. The distribution is fitted using only the prompt component described in the text. The arrow superimposed in the figure indicates the candidates that pass the event selection (D^0 $\log_{10}\chi^2_{\rm IP} < 1.0$).

The background is first subtracted from the D^0 $\log_{10}\chi^2_{\rm IP}$ distribution using the *sPlot* technique [76]. The *sPlot* technique uses a fit to a discriminating variable, Δm in this example, to calculate event by event weights called *sWeights* - these weights can then be used to subtract background from any distribution uncorrelated to Δm. The *sWeights* are generated independently in each lifetime bin from a fit to the Δm distribution. Unlike the Δm fits described in Section 5.4.6, the cut of $D^0 \log_{10}\chi^2_{\rm IP} < 1.0$ is now relaxed to < 1.48 - this cannot be relaxed further due to a cut in the HLT2 trigger line. Using this looser cut increases the secondary component, which in turn improves the reliability of the fit - this is evident from a reduced correlation between prompt and secondary yields, giving a better determination of $f^{RS}_{B,i}$. The prompt and secondary yields returned by the fitter are for candidates passing the looser D^0 $\log_{10}\chi^2_{\rm IP}$ cut - in order to determine the yields with the cut reapplied, the prompt and secondary shapes are integrated in the region $D^0 \log_{10}\chi^2_{\rm IP} < 1.0$. From these the secondary fraction is determined.

The prompt component is modelled with the sum of a Johnson and a Gaussian (Equation 5.9 and Equation 5.8 respectively). Because a promptly produced D meson should always point back to the primary vertex (independent of its lifetime), the shape of the prompt component is expected to be the same in all lifetime bins. For this reason the shape is fixed from a fit to candidates with a D^0 lifetime below $0.7\,\tau_{D^0}$ where the fraction of secondary decays is expected to be negligible. Although the parameters describing the shape of the prompt distribution are fixed, the mean of the distribution is allowed to float. The determination of the prompt shape is shown in Figure 5.14.

Due to the characteristically large flight distance of the b-hadron, a D^0 produced in the decay of b-hadron is not expected to point back to the PV. Because the D^0 LT is correlated to the b-hadron flight distance (the D^0 LT is calculated with respect to to the PV) the D^0 $\log_{10}\chi^2_{\rm IP}$ shape of secondary decays is not expected to be the same in different lifetime bins. To obtain the secondary D^0 $\log_{10}\chi^2_{\rm IP}$ shape, signal candidates which can also be reconstructed as the decay $B \to D^*\mu X$ are used. This involves looking for a μ candidate that forms a common vertex with the D^* candidate. A sample of these candidates is created for each lifetime bin then used as a template for the secondary shape.

The *sWeighted* D^0 $\log_{10}\chi^2_{\rm IP}$ distribution of candidates (with the loosened D^0 $\log_{10}\chi^2_{\rm IP}$ cut) are shown in Figure 5.15 for each lifetime bin with the results of a binned χ^2 fit superimposed. Beneath each figure are the pulls which indicate a rather good fit quality - one would not expect the distribution of pulls to be perfectly Gaussian due to limited (and correlated) statistics in the secondary template. Figure 5.16 shows the $f^{RS}_{B,i}$ distribution determined from the D^0 $\log_{10}\chi^2_{\rm IP}$ fits. As one would expect, the secondary fraction has a strong time dependence that increases with D^0 LT.

The secondary fraction was found to be sensitive to the choice of prompt and secondary shape chosen. Therefore a systematic uncertainty is assigned to the secondary fractions reported in Figure 5.16 - this is estimated by re-calculating the $f^{RS}_{B,i}$ with several different prompt and secondary parameterisations. The standard deviation of the different fractions is taken as the systematic uncertainty, which is added in quadrature to the statistical uncertainty. As an alternate prompt shape a Johnson (without a Gaussian) is used. For an alternate secondary shape a smoothed out version of the template (used as the nominal model) is used. The secondary fraction is determined using all four combinations of prompt/secondary shape with the results shown in Figure 5.17. The final result, with the systematic uncertainty included, is also presented in Figure 5.17. The statistical uncertainty associated with $f^{RS}_{B,i}$ is typically $\sim 0.25\%$, compared to a systematic uncertainty of $\sim 0.5\%$.

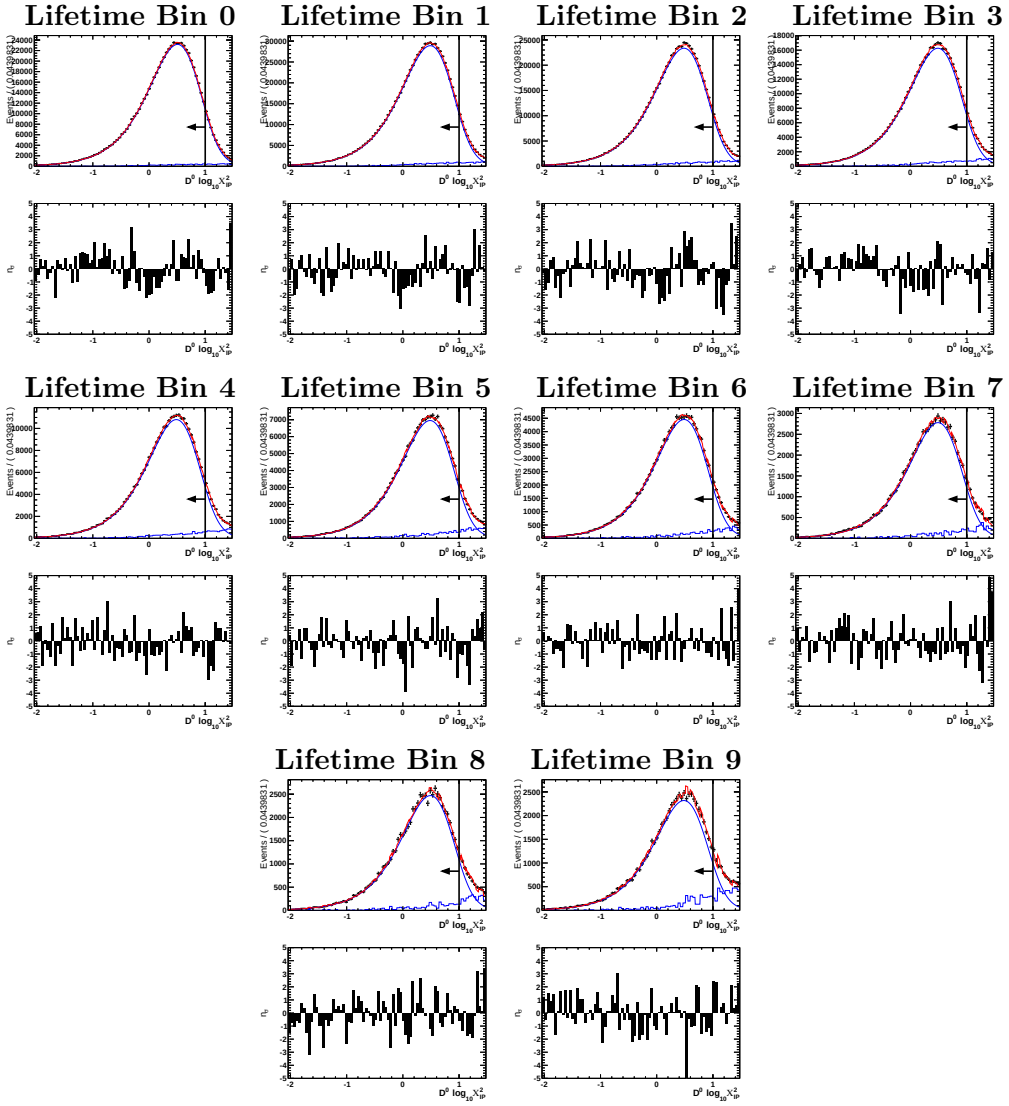

Figure 5.15: Fits to the *sWeighted* D^0 $\log_{10}\chi^2_{\rm IP}$ distribution of candidates with the loosened cut of $D^0 \log_{10}\chi^2_{\rm IP} < 1.48$. The distribution is shown in each lifetime bin. The arrow in each figure indicates which candidates pass the selection cut of D^0 $\log_{10}\chi^2_{\rm IP} < 1$ (the region in which the secondary fraction ultimately needs to be determined). The total PDF is superimposed using a solid red line, whereas the individual prompt and secondary components are drawn using a solid blue line.

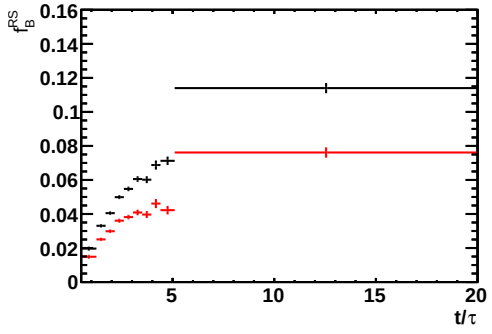

Figure 5.16: The secondary fraction in each lifetime bin before (red) and after (black) the $D^0 \log_{10}\chi^2_{\rm IP} < 1.0$ cut.

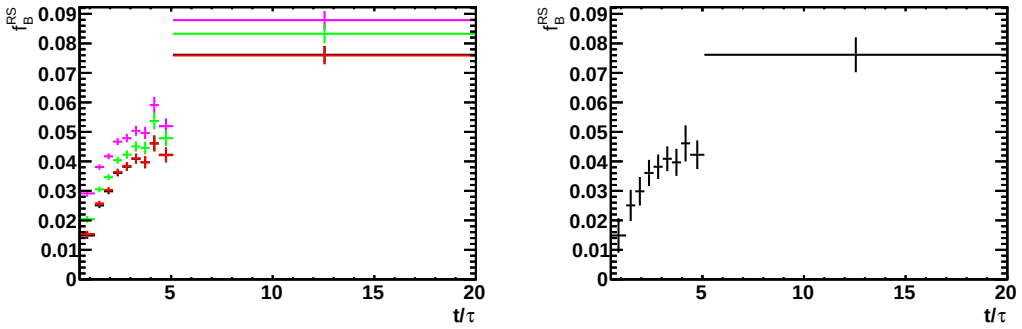

Figure 5.17: The secondary fraction once the $D^0 \log_{10} \chi^2_{\rm IP} < 1.0$ cut is applied. The figure on the left shows the results from 4 different prompt/secondary parameterisations (black) Johnson+Gaussian / template (black) Johnson / template (pink) Johnson+Gaussian / smoothed template (green) Johnson / smoothed template. The figure on the right shows the secondary fraction of the nominal model (Johnson+Gaussian / template) with the systematic error included.

5.5.2 Double mis-ID events

As described in Section 5.3.6, a large peaking background in the sample of WS candidates is caused by the double misidentification of two D daughters. The tight $\mathrm{DLL}_{\mathrm{K}\pi}$ requirements defined in Table 5.3 remove the majority of these events, but some are still present.

To determine the number of double mis-ID events remaining in the WS signal region, the procedure described in Section 5.3.6 is repeated. In summary, it requires finding the number of mis-ID events in the D^0 sidebands (not otherwise used in the analysis), and extrapolating this number into the signal region. Figure 5.18 shows, in each lifetime bin, the Δm distribution of candidates in the D^0 sidebands. Superimposed in each figure is the fit used to determine the number of double mis-ID events in this region.

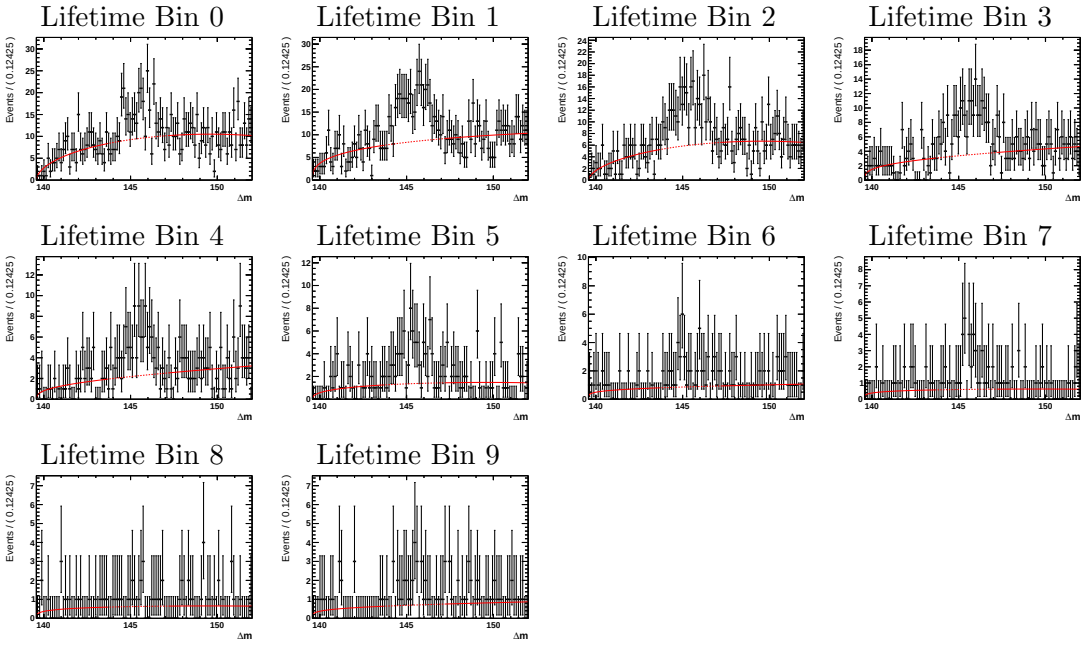

Figure 5.18: Fits to Δm in the sideband region $|m_{D^0}^{\mathrm{PDG}} - m_{D^0}| > 40\,\mathrm{MeV}$. The different figures correspond to different D^0 lifetime ranges. The fit results are used to determine the number of double mis-ID events that peak in the signal region.

From the Δm fits in the m_{D^0} sideband region, the number of double mis-ID events that fall in the signal window, $|m_{D^0} - m_{D^0}^{\mathrm{PDG}}| < 24.0$, is estimated. To do so, the number of events counted in the sideband region is divided by the total width of the sidebands (50 MeV) and then multiplied by the width of the signal window (48 MeV). Such a

scaling assumes the background has a linear shape in m_{D^0}, which is justified looking at Figure 5.7 (shown previously in Section 5.3.5). The expected number of double mis-ID events peaking under the WS signal is displayed in Figure 5.19.

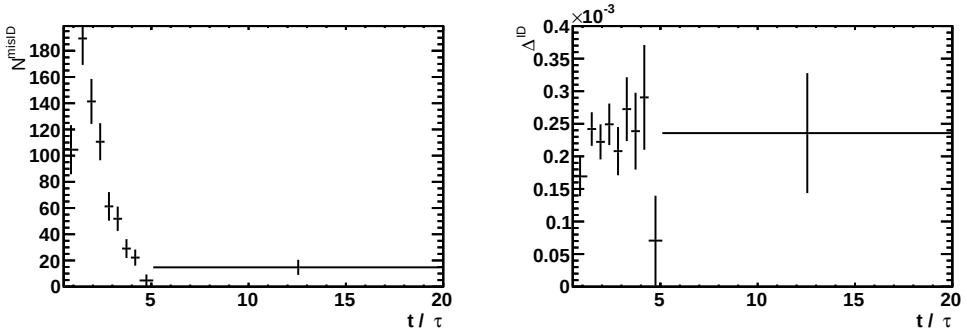

Figure 5.19: (left) The expected number of double mis-ID events peaking under the WS signal determined from Figure 5.18 (right) The double mis-ID correction $\mathbf{\Delta}_{ID,i}$, with calculation detailed in Equation 5.28.

The measured WS yield, $N^M_{\rm WS}$, will differ from the true WS yield, $N_{\rm WS}$, by the number of mis-ID events, $N^{\rm misID}$, leading to the following relation,

$$\frac{N^M_{\rm WS}}{N^M_{\rm RS}} = \frac{N_{\rm WS} + N^{\rm misID}}{N^M_{\rm RS}}, \tag{5.27}$$

where $N^M_{\rm RS}$ is the measured number of RS events (that has a negligible contamination from double mis-ID background). From this expression it is clear that the difference between the measured WS/RS ratio and the true WS/RS ratio, also known as the double mis-ID correction, is

$$\mathbf{\Delta}^{\rm ID}_i = \frac{N^{\rm misID}_i}{N^M_{{\rm RS},i}}, \tag{5.28}$$

were i labels the ith lifetime bin. The uncertainty associated with $\mathbf{\Delta}^{\rm ID}_i$ is given by $\sigma^{\rm ID}_i$. The double mis-ID correction and its uncertainty are shown in Figure 5.19 - as one would expect, it displays a flat time dependence. In order to combine $\sigma^{\rm ID}_i$ with other systematic uncertainties it is convenient to express it in the following covariance matrix:

$$\Sigma^{\rm ID}_{ij} = (\sigma^{\rm ID}_i)^2 \quad [i = j] \tag{5.29}$$

$$\Sigma^{\rm ID}_{ij} = 0 \quad [i \neq j]. \tag{5.30}$$

5.5.3 Ghost Events

When reconstructing an event, it is possible to falsely reconstruct tracks that do not correspond to a true particle - such tracks are called 'ghosts'. There are many sources of ghosts, although the one important to this section is known as 'inconsistent parts' [77]. This is when a track is formed from clusters that originate from two or more particles.

One particularly difficult peaking background is from π_s ghosts, or 'slow pion ghosts'. In particular, the problem arises from ghosts where one correctly identifies the slow pion clusters in the VELO and TT, but then pairs these with clusters from a different particle in T1-T3. An illustration of this is seen in Figure 5.20. In these events the determination of the π_s direction is correct, but its momentum is wrong. The charge of these tracks will also be wrong $\sim 50\%$ of the time, making a RS decay look like a WS decay (and therefore causing a bias to the WS/RS ratio).

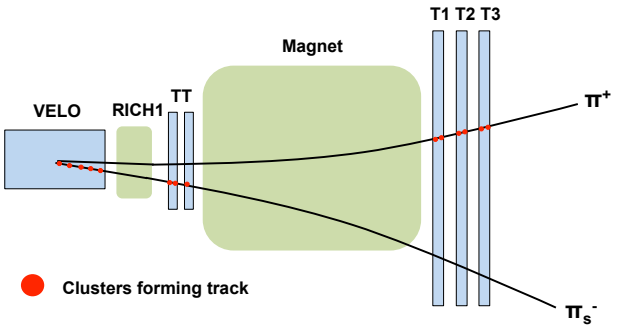

Figure 5.20: An example of a 'slow pion ghost' event. The red dots indicate the clusters that form the track.

As a toy experiment to simulate π_s ghosts, a sample of MC signal has had the momentum of the slow pion randomised, but its direction remains unchanged. The randomisation is performed in two ways; the first is to generate a random momentum uniformly between 0 and 80 GeV, while the second is to generate the momentum according to the slow pion momentum distribution in MC. The Δm shape obtained using the randomised momenta is shown in Figure 5.21 - for both randomisation methods there is clearly a peak in Δm.

For further study, 3 independent MC samples have been isolated: 'slow pion ghost', 'random slow pion' and 'signal'. All candidates are required to be true D^0 candidates that are from a promptly produced D^*. The signal sample has a slow pion candidate

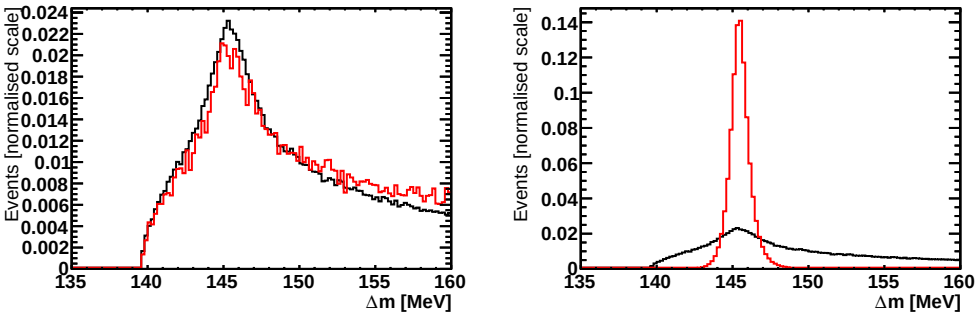

Figure 5.21: (left) The Δm distribution of MC signal candidates with a randomised slow pion momentum - the two colours represent the two different randomisation methods described in the text (right) The Δm distribution of MC signal candidates with a randomised slow pion momentum (black) and MC signal (red).

that is correctly matched to the true slow pion[4]. The random slow pion sample has a slow pion candidate which is successfully matched to a true pion, although this is not the true *slow* pion. Finally, the ghost sample has a slow pion candidate that cannot be matched to any truth particle. Figure 5.22 shows the Δm distribution of these 3 samples, which demonstrate the expected behaviour.

To further investigate the origin of the π_s ghosts, the following definitions are useful: $\vec{\mathbf{p}}_{\text{truth}}$ is the 3-momentum of the true π_s generated in PYTHIA, and $\vec{\mathbf{p}}_{\text{reco}}$ is the 3-momentum of the reconstructed π_s candidate. The angle between $\vec{\mathbf{p}}_{\text{truth}}$ and $\vec{\mathbf{p}}_{\text{reco}}$ is defined $\theta_{\text{truth}-\text{reco}}$, and the asymmetry between $|\vec{\mathbf{p}}_{\text{truth}}|$ and $|\vec{\mathbf{p}}_{\text{reco}}|$ is defined $A_{\text{truth}-\text{reco}} = (|\vec{\mathbf{p}}_{\text{truth}}| - |\vec{\mathbf{p}}_{\text{reco}}|) \,/\, (|\vec{\mathbf{p}}_{\text{truth}}| + |\vec{\mathbf{p}}_{\text{reco}}|)$. True signal should peak in both $\theta_{\text{truth}-\text{reco}}$ and $A_{\text{truth}-\text{reco}}$ whereas random slow pion background should not peak in either. Slow pion ghost background is correctly identified in the VELO, so should peak in $\theta_{\text{truth}-\text{reco}}$, but is incorrectly identified downstream of the magnet, and therefore shouldn't peak in $A_{\text{truth}-\text{reco}}$. Distributions of $\theta_{\text{truth}-\text{reco}}$ and $A_{\text{truth}-\text{reco}}$ are shown in Figure 5.22 for each sample of MC - everything demonstrates the expected behaviour.

To investigate how the slow pion ghost background influences the WS/RS ratio, the data sample is split into 30 independent bins of π_s GhostProb, and a Δm fit is performed in each. π_s GhostProb is used because it is seen to give a good discrimination between the signal and slow pion ghost samples in MC (see Figure 5.23). The results presented in Figure 5.24 show that the WS/RS ratio measured in data is indeed highly correlated

[4]The π_s generated by PYTHIA.

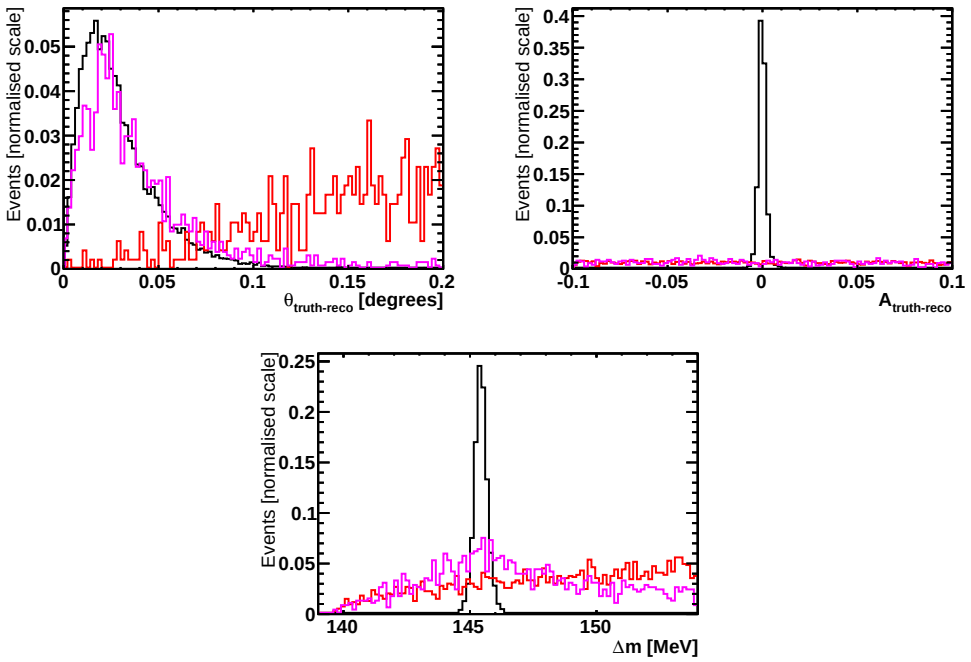

Figure 5.22: (top left) the angle, $\theta_{\text{truth}-\text{reco}}$, between the true slow pion and the reconstructed track (top right) the absolute momentum asymmetry, $A_{\text{truth}-\text{reco}}$, between the true slow pion and the reconstructed track (bottom) the Δm distribution. In all figures black is 'signal', red is 'random slow pion', and pink is 'slow pion ghost'.

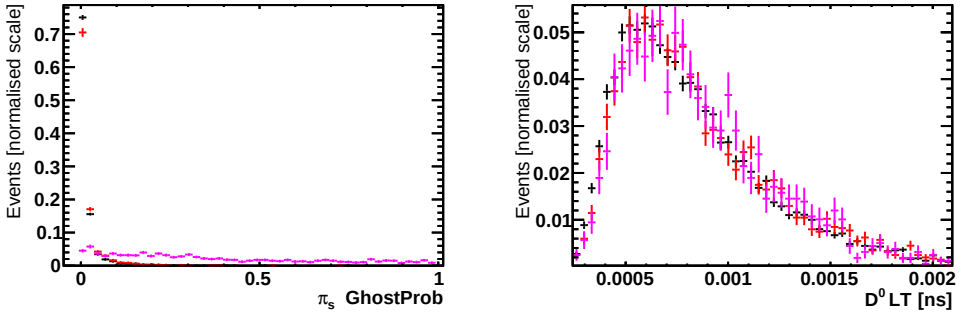

Figure 5.23: Projections of the 'signal' sample (black) the 'random slow pion' sample (red), and the 'slow pion ghost' sample (pink) for π_s GhostProb (left) and D^0 LT (right).

to π_s GhostProb - for candidates with π_s GhostProb > 0.5 the WS/RS ratio increases by almost an order of magnitude. In order to remove the majority of slow pion ghost background, the event selection includes a tight cut of π_s GhostProb < 0.05. The WS/RS ratio below this cut does not show any correlation to π_s GhostProb.

The slow pion ghost background can also cause a difference in yields when using, or not using, DTF for decay tree reconstruction (this is in fact how the background was discovered). As previously shown in Section 5.3.3, the Δm resolution of signal events

greatly improves when using DTF. The shape of the ghost background however remains approximately the same. This means that fewer slow pion ghost events get absorbed into the signal yield when using DTF. This effect can clearly be seen in the highest π_s GhostProb bins of Figure 5.24. Below the cut at π_s GhostProb < 0.05 the WS/RS is consistent when using or not using DTF.

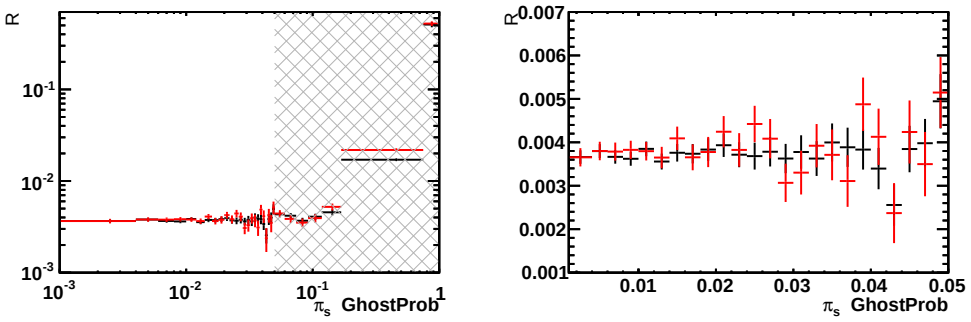

Figure 5.24: The WS/RS ratio in bins of π_s GhostProb - these numbers were obtained from a fit to (red) Δm distribution without DTF (black) Δm distribution with DTF. The left figure shows the WS/RS ratio over the entire range of π_s GhostProb, while the right figure only shows the range π_s GhostProb < 0.05 (the candidates which pass the selection cuts).

To assign a systematic uncertainty to any ghost background that may be remaining, the WS/RS ratio vs. π_s GhostProb distribution is fit with 3 polynomials of increasing order. The fits are shown in Figure 5.25, and the results in Table 5.5. The range of y-intercepts ($P0$) reported in Table 5.5 is used as a systematic uncertainty, σ_{Ghost}, on the WS/RS ratio.

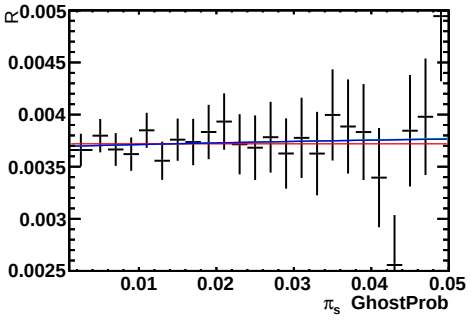

Figure 5.25: The WS/RS ratio in bins of π_s GhostProb - these numbers were obtained from a fit to Δm. Superimposed are 3 fits using a 0th (red) 1st (green) and 2nd (blue) order polynomial.

The systematic uncertainty from ghost background is expected to be highly correlated between lifetime bins - Figure 5.23 shows that in MC the lifetime distribution of ghost

Polynomial Order	P0[%]	P1[%]	P2[%]
0th	0.372 ± 0.005107	-	-
1st	0.3697 ± 0.008606	0.1484 ± 0.4598	-
2nd	0.3695 ± 0.01361	0.1874 ± 1.602	-0.9106 ± 35.91
Systematic	0.002503	-	-

Table 5.5: The results from the 3 fits pictured in (Figure 5.25). The bottom row shows the systematic calculated from the range of y-intercepts ($P0$)

events is in good agreement with signal. The correlation between all lifetime bins is therefore set, somewhat arbitrarily, to 0.9. The covariance matrix for the ghost systematic is defined:

$$\Sigma_{ij}^{\mathrm{GHOST}} = (\sigma^{\mathrm{GHOST}})^2 \qquad [i = j] \tag{5.31}$$

$$\Sigma_{ij}^{\mathrm{GHOST}} = 0.9(\sigma^{\mathrm{GHOST}})^2 \ [i \neq j] \tag{5.32}$$

The total systematic uncertainty on the parameters of interest (later reported in Table 5.7 and Table 5.8) were also calculated assuming no correlation of the ghost systematic uncertainty between lifetime bins i.e. $\Sigma_{ij}^{\mathrm{GHOST}} = 0.0$ for $i \neq j$. The change in the total systematic uncertainty was at most $\sim 5\%$ on any parameter, the majority of which resulted in a smaller uncertainty. Including this correlation is therefore the more conservative approach.

5.5.4 Signal shape systematic

To determine the systematic uncertainty associated with the choice of signal and background parameterisation (used in Section 5.4) the Δm fit is repeated with a selection of different models. A systematic uncertainty, $\sigma_i^{\rm SHAPE}$, is calculated independently for each lifetime bin i, and is taken to be the standard deviation of the measured WS/RS ratios found using the different models. The correlation of this systematic uncertainty, $\rho_{ij}^{\rm SHAPE}$, between lifetime bins i and j is also calculated. The results are summarised in Figure 5.26. The systematic uncertainty is $\sim 10\%$ of the statistical uncertainty in the lower lifetime bins, increasing to $\sim 20\%$ in the higher lifetime bins. The systematic uncertainty is highly correlated between lifetime bins.

Lifetime Bin	Stat. [%]	Sys. [%]	Sys/Stat
1	0.011	0.00087	0.078
2	0.01	0.00069	0.068
3	0.012	0.00088	0.077
4	0.014	0.0011	0.076
5	0.017	0.0018	0.1
6	0.022	0.0043	0.19
7	0.027	0.0014	0.051
8	0.036	0.0039	0.11
9	0.04	0.0033	0.081
10	0.042	0.0093	0.22

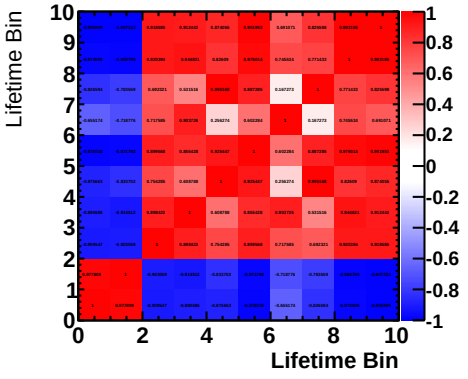

Figure 5.26: (left) The shape systematic in each lifetime bin compared to the statistical uncertainty (right) the correlation coefficients between the systematic uncertainties in different lifetime bins.

The systematic uncertainty can conveniently be summarised by the covariance matrix:

$$\Sigma_{ij}^{\rm SHAPE} = \sigma_i^{\rm SHAPE}\,\sigma_j^{\rm SHAPE}\,\rho_{ij}^{\rm SHAPE}, \tag{5.33}$$

The procedure to find the systematic uncertainty associated with the choice of Δm shape was repeated, but this time only considering changes to the signal shape parameterisation (and not the background parameterisation). From the results shown in Table 5.6 it is

clear that the systematic uncertainty reported in Figure 5.26 is dominated by variations in the background parameterisation.

Lifetime Bin	Stat. [%]	Sys. [%]	Sys/Stat
1	0.011	0.00017	0.015
2	0.01	0.0001	0.01
3	0.012	0.00011	0.0099
4	0.014	6.4e-05	0.0046
5	0.017	5e-05	0.0029
6	0.022	8.6e-05	0.0039
7	0.027	0.00015	0.0055
8	0.036	8.1e-05	0.0022
9	0.04	0.0002	0.0051
10	0.042	0.00016	0.0038

Table 5.6: The shape systematic in each lifetime bin compared to the statistical uncertainty - this is calculated using variations of the signal parameterisation only.

5.6 Efficiency Correction

5.6.1 Monte Carlo Sample

To determine the phase space dependent efficiency, a dedicated MC sample of $D^{*+} \to D^0(K^-\pi^+\pi^-\pi^+)\pi^+$ decays is used. Half of the simulated events are generated using Pythia 6 and half using Pythia 8.

The kinematics of the D^0 decay are generated using MINT[5] - this is used in conjunction with a preliminary amplitude model of the RS $D^0 \to K^-\pi^+\pi^-\pi^+$ decay, which is currently being developed in another LHCb analysis. Although the amplitude model is preliminary, this will not cause any bias in this analysis because efficiencies are determined at points in the 4-body phase space. Having an amplitude model that reproduces something similar to data will increase the 'usefulness' of the MC i.e. the uncertainty associated with finite MC statistics will be lower for the same number of MC events generated.

[5]MINT (Minuit INTerface) is piece of software used for building and fitting amplitude models of 3 and 4 body decays. It can also be used to generate toy MC samples according to such a model.

The MC sample is passed through exactly the same trigger and selection requirements as the data. Additional corrections are also applied to correct for known discrepancies between MC and data. The first of these corrections is needed for the DLL variables (Section 3.4) which are known to be badly modelled in MC. The efficiency of applying DLL cuts is therefore modelled using a data driven approach. This is done using a calibration sample of $D^0 \to K^-\pi^+$ candidates where the particle type of the daughters is confirmed using a kinematic veto i.e. a selection process that doesn't involve the DLL variables. Using the calibration sample, the efficiency of a pion or kaon passing a particular DLL cut is evaluated - this is found to be highly dependent on track $|\vec{p}|$, track η and N_{tracks}, where η is the peusdo-rapidity of the track and N_{tracks} is the total number of charged tracks reconstructed in the event. The efficiency is therefore determined at points in the 3D parameter space i.e. the efficiency of a kaon to pass a cut of $\text{DLL}_{\text{K}\pi} > 7$ is given by $\epsilon^{K}_{\text{DLL}_{\text{K}\pi}>7}(|\vec{p}|, \eta, N_{\text{tracks}})$. For the final state $K\pi_1\pi_2\pi_3$ the total PID efficiency is given by:

$$\begin{aligned}\epsilon^{K\pi\pi\pi}_{\text{DLL}} =& \epsilon^{K}_{\text{DLL}_{\text{K}\pi}>7}(K\ |\vec{p}|, K\,\eta, N_{\text{tracks}}) \\ &\times \epsilon^{\pi}_{\text{DLL}_{\text{K}\pi}<3}(\pi_1\ |\vec{p}|, \pi_1\,\eta, N_{\text{tracks}}) \\ &\times \epsilon^{\pi}_{\text{DLL}_{\text{K}\pi}<3}(\pi_2\ |\vec{p}|, \pi_2\,\eta, N_{\text{tracks}}) \\ &\times \epsilon^{\pi}_{\text{DLL}_{\text{K}\pi}<3}(\pi_3\ |\vec{p}|, \pi_3\,\eta, N_{\text{tracks}}). \end{aligned} \tag{5.34}$$

The MC sample with no DLL cuts is weighted by $\epsilon^{K\pi\pi\pi}_{\text{DLL}}$ in order to simulate the application of DLL cuts.

A small difference ($\sim 2\%$) is also present between the tracking efficiency determined from MC and data. The tracking efficiency in data is evaluated using the 'tag and probe' technique described in Section 3.8. The efficiency difference is dependent on track $|\vec{p}|$ and track η so corrections are applied to the MC sample on a track by track basis using a 2D lookup table in these variables.

The MC is also reweighted in the variables $D^0\ |\vec{p}|$, $D^0\,\eta$, D^* `L0_TIS` and N_{tracks} to match the distributions in data. Here D^* `L0_TIS` is a boolean describing whether the D^* candidate was TIS with respect to all L0 trigger lines. The correlation between the

reweighting variables is displayed in Figure 5.27 for both data and MC signal samples. The data sample is taken from RS candidates that are background-subtracted using the *sPlot* technique. The correlation matrix shows that the variables (D^0 $|\vec{p}|$, D^0 η) are almost uncorrelated to (D^* `L0_TIS`, N_{tracks}) and therefore two 2D reweightings are carried out independently.

1D distributions of data and MC are shown in Figure 5.28 both before reweighting and after reweighting. These demonstrate a good agreement between MC and data, justifying the decision to factorise the reweighting procedure into two independent steps.

The weights used for the reweighting procedure are determined by dividing a 2D histogram filled with *sWeighted* data, by a 2D histogram filled with MC signal. The binning of the histograms is automatically selected using an adaptive binning technique - the algorithm iteratively splits bins until either a minimum bin content or a minimum bin width is reached. The bins are split so that each of the resulting bins contains approximately the same number of events. The minimum bin width for the variables D^0 $|\vec{p}|$ (2500 MeV), D^0 η (0.05) D^* `L0_TIS` (0.5), N_{tracks} (5) is given in parenthesis. The minimum bin content is 50 events. The 2D histograms of MC, *sWeighted* data, and their ratio, are shown in Figure 5.29. Although in this scenario the binning algorithm is demonstrated in 2D, it is capable of binning in any dimensionality (a 5D example will be described in Section 5.6.3).

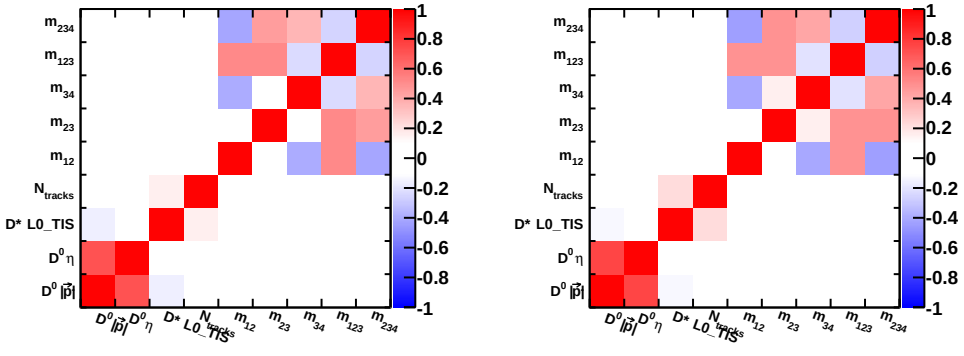

Figure 5.27: Correlation coefficients between the reweighting variables D^0 $|\vec{p}|$, D^0 η, D^* `L0_TIS` and N_{tracks}, and the variables that parameterise phase space, m_{12}, m_{23}, m_{34}, m_{123} and m_{234} (defined in Equation 5.40). The left histogram shows the correlation coefficients in the *sWeighted* RS data sample, while the right shows the correlation coefficients in the MC sample.

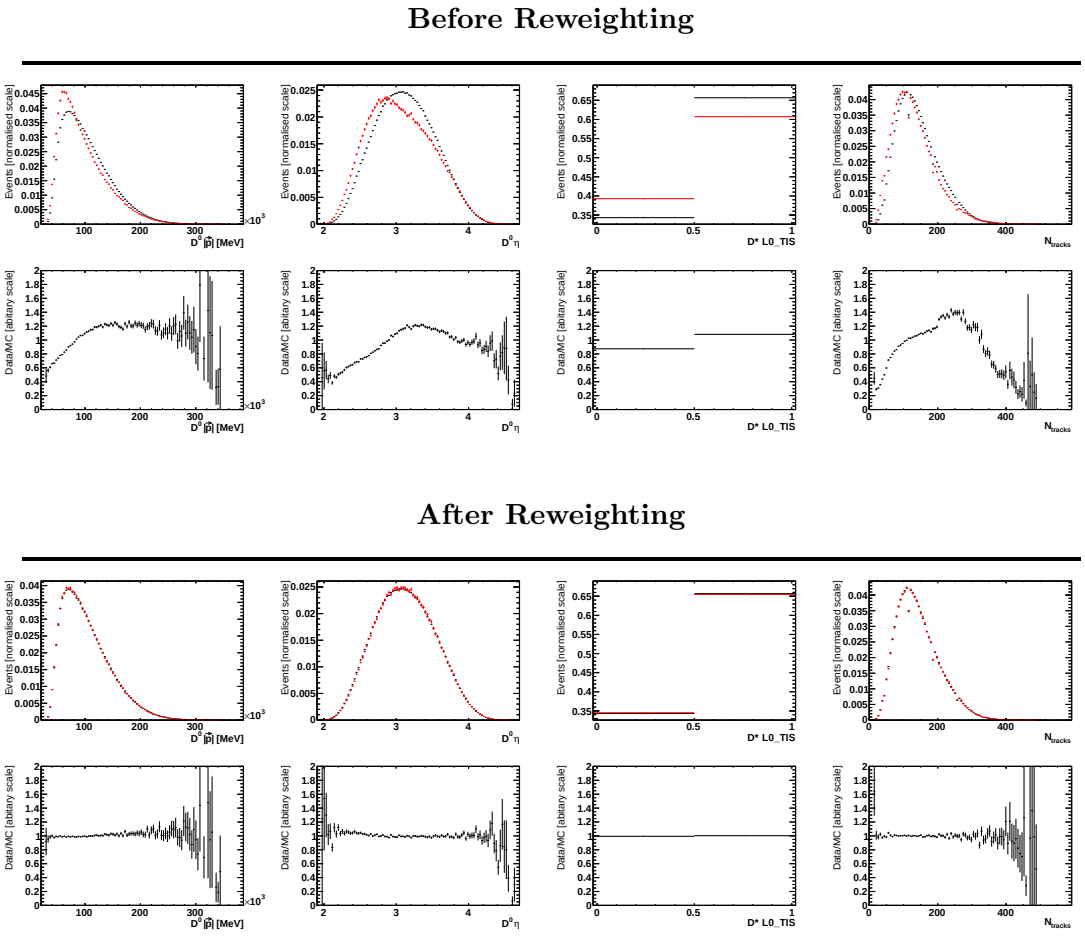

Figure 5.28: Histograms, from left to right, of D^0 $|\vec{p}|$, $D^0\,\eta$, D^* `L0_TIS` and N_{tracks}. The top row shows MC (red) and data (black) before the reweighting procedure. The second row shows the division of MC and data distributions before reweighting. The third and fourth rows follow the same format of rows one and two, although now with the reweighting applied.

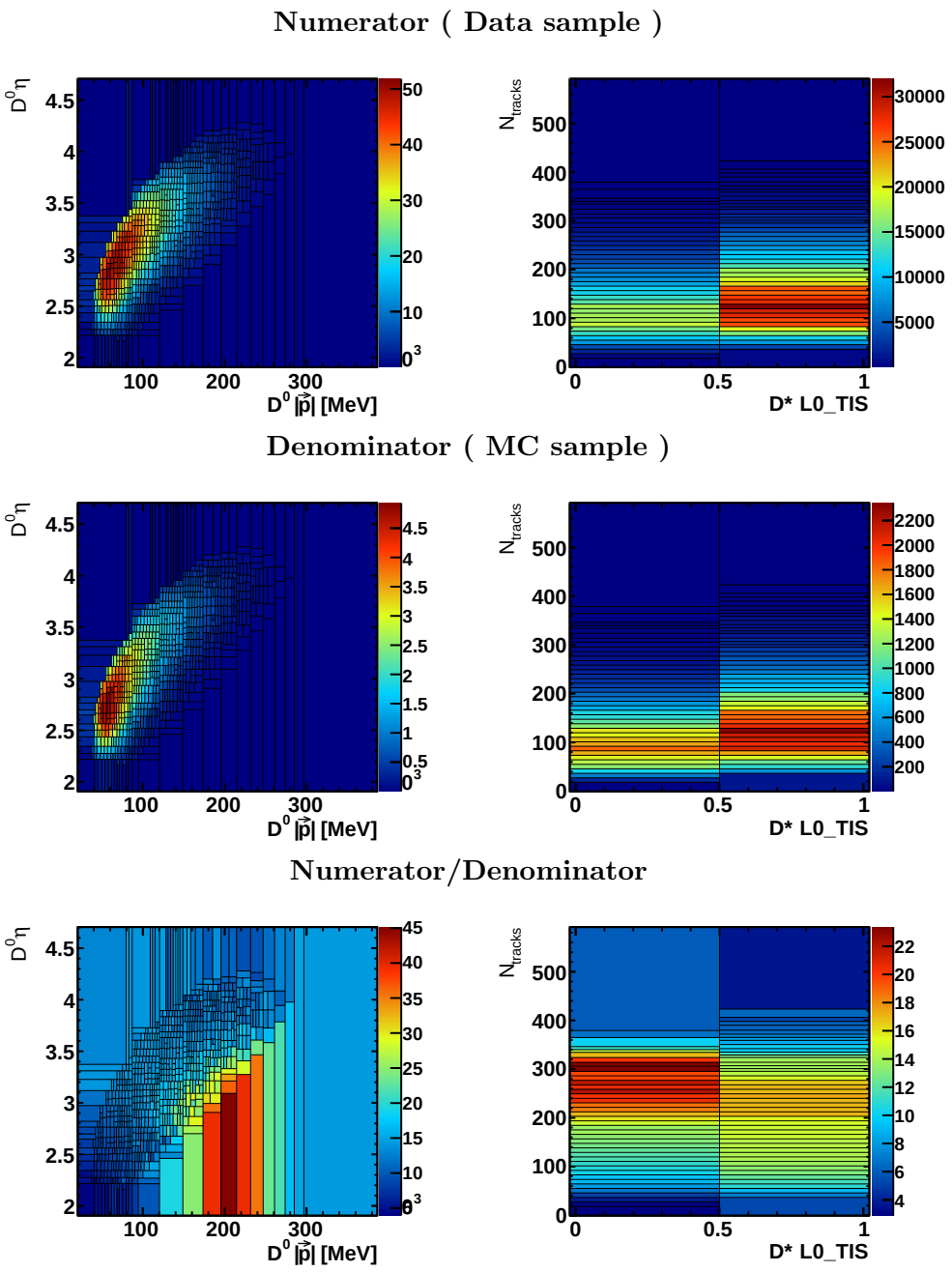

Figure 5.29: 2D histogram of (left) $D^0\,\eta$ against D^0 $|\vec{p}|$ (right) D^* `L0_TIS` against N_{tracks}. The top row shows the *sWeighted* RS data sample, the middle row shows the MC sample, and the bottom row shows the division of the two. The division histograms are used to reweight the MC to look like data.

5.6.2 Formalism

In order to describe the efficiency correction, Equation 5.5 is first repeated in a rearranged form:

$$R^2 = (R^M)^2\epsilon^2_{\rm COR} \quad \text{where} \quad \epsilon^2_{\rm COR} = \frac{\epsilon^{\rm RS}_{K^+\pi^-\pi^+\pi^-}\epsilon^{\rm RS}_{K^-\pi^+\pi^-\pi^+}}{\epsilon^{\rm WS}_{K^-\pi^+\pi^-\pi^+}\epsilon^{\rm WS}_{K^+\pi^-\pi^+\pi^-}}. \tag{5.35}$$

Therefore, the correction factor $\epsilon_{\rm COR}$ is needed to correct the measured ratio to the true ratio. The quantities $\epsilon^{\rm CAT}_{K\pi\pi\pi}$ are the phase space-integrated efficiencies which are defined:

$$\epsilon^{\rm WS}_{K^-\pi^+\pi^-\pi^+} = \frac{\int\int WS(\mathbf{p},t)\exp(-\Gamma t)\epsilon_{K^-\pi^+\pi^-\pi^+}(\mathbf{p},t)\mathrm{d}\mathbf{p}\mathrm{d}t}{\int\int WS(\mathbf{p},t)\exp(-\Gamma t)\mathrm{d}\mathbf{p}\mathrm{d}t} \tag{5.36}$$

$$\epsilon^{\rm WS}_{K^+\pi^-\pi^+\pi^-} = \frac{\int\int WS(\overline{\mathbf{p}},t)\exp(-\Gamma t)\epsilon_{K^+\pi^-\pi^+\pi^-}(\overline{\mathbf{p}},t)\mathrm{d}\overline{\mathbf{p}}\mathrm{d}t}{\int\int WS(\overline{\mathbf{p}},t)\exp(-\Gamma t)\mathrm{d}\overline{\mathbf{p}}\mathrm{d}t} \tag{5.37}$$

$$\epsilon^{\rm RS}_{K^-\pi^+\pi^-\pi^+} = \frac{\int\int RS(\mathbf{p})\exp(-\Gamma t)\epsilon_{K^-\pi^+\pi^-\pi^+}(\mathbf{p},t)\mathrm{d}\mathbf{p}\mathrm{d}t}{\int\int RS(\mathbf{p})\exp(-\Gamma t)\mathrm{d}\mathbf{p}\mathrm{d}t} \tag{5.38}$$

$$\epsilon^{\rm RS}_{K^+\pi^-\pi^+\pi^-} = \frac{\int\int RS(\overline{\mathbf{p}})\exp(-\Gamma t)\epsilon_{K^+\pi^-\pi^+\pi^-}(\overline{\mathbf{p}},t)\mathrm{d}\overline{\mathbf{p}}\mathrm{d}t}{\int\int RS(\overline{\mathbf{p}})\exp(-\Gamma t)\mathrm{d}\overline{\mathbf{p}}\mathrm{d}t} \tag{5.39}$$

where $WS(\mathbf{p},t)$ is the time and phase space dependent WS rate, and $RS(\mathbf{p})$ is the phase space dependent RS rate. Here $\mathbf{p}$ parameterises a point in the multi-body phase space, and $\bar{\mathbf{p}}$ is the equivalent point in *CP* conjugate space. The expression $\epsilon_{K^-\pi^+\pi^-\pi^+}(\mathbf{p},t)$ gives the combined detection and selection efficiency for the final state $D \to K^-\pi^+\pi^-\pi^+$ at a point $\mathbf{p}$ in phase space, and with a D^0 lifetime t. The quantity $\varepsilon_{K^+\pi^-\pi^+\pi^-}(\overline{\mathbf{p}},t)$ is the equivalent for the charge conjugate final state $D \to K^+\pi^-\pi^+\pi^-$.

To parameterise a point in 4 body phase space the 5 variables m_{12}, m_{23}, m_{34}, m_{123}, m_{234} are used, which for the final state $\pi^+_1\pi^-\pi^+_2K^-$ are defined:

$$m_{12} = m(\pi^+_1\pi^-) \quad m_{23} = m(\pi^-\pi^+_2) \quad m_{34} = m(\pi^+_2K^-)$$
$$m_{123} = m(\pi^+_1\pi^-\pi^+_2) \quad m_{234} = m(\pi^-\pi^+_2K^-) \tag{5.40}$$

The phase space projections of *sWeighted* RS candidates decaying to $K^-\pi^+\pi^-\pi^+$ and $K^+\pi^-\pi^+\pi^-$ are compared in Figure 5.30 - from these projections the two distributions appear to be compatible. To confirm this observation, both datasets are binned

in 5D $(m_{12}, m_{23}, m_{34}, m_{123}, m_{234})$ using the adaptive binning algorithm described in Section 5.6.1. The χ^2 between the samples is 3.22×10^4 using 32232 bins - this is equivalent to a p-value of 0.59. This compatibility between the phase space projections of

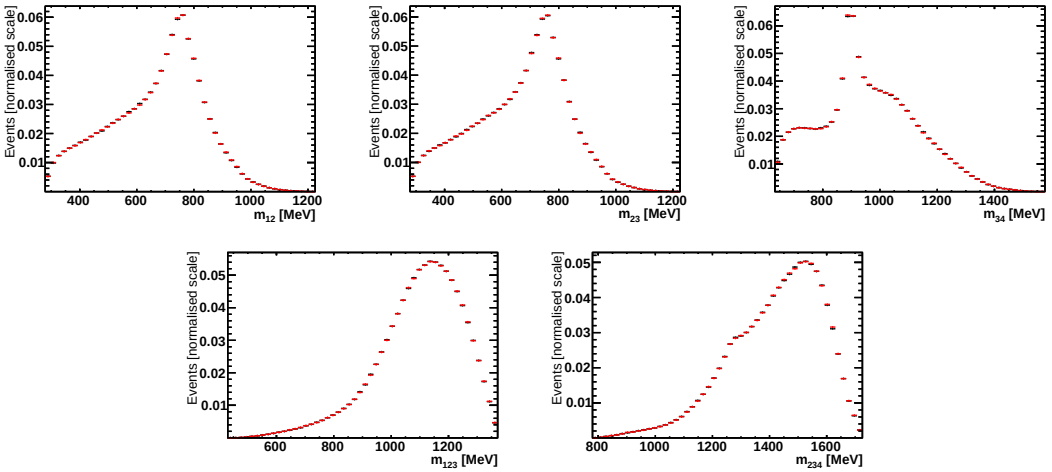

Figure 5.30: Projections of *sWeighted* RS candidates (black) $D^0 \to K^-\pi^+\pi^-\pi^+$ (red) $\overline{D}^0 \to K^+\pi^-\pi^+\pi^-$ in the 5 variables used to parameterise phase space $(m_{12}, m_{23}, m_{34}, m_{123}, m_{234})$.

$D^0 \to K^-\pi^+\pi^-\pi^+$ and $\overline{D}^0 \to K^+\pi^-\pi^+\pi^-$ suggests that the efficiency for both final states must also be equivalent. The charge-averaged efficiency is therefore defined as,

$$\varepsilon_{K\pi\pi\pi}(\mathbf{p}, t) \equiv \frac{\varepsilon_{K^-\pi^+\pi^-\pi^+}(\mathbf{p}, t) + \varepsilon_{K^+\pi^-\pi^+\pi^-}(\overline{\mathbf{p}}, t)}{2}, \tag{5.41}$$

and substituted into the expression for ϵ_{COR}, simplifying it to:

$$\epsilon_{\text{COR}} = \frac{\varepsilon^{RS}_{K\pi\pi\pi}}{\varepsilon^{WS}_{K\pi\pi\pi}}. \tag{5.42}$$

In order to calculate the correction, ϵ_{COR}, the expression $\varepsilon_{K\pi\pi\pi}(\mathbf{p}, t)$ needs to be determined from MC - this is discussed in the following section.

5.6.3 Efficiency Parameterisation

Instead of trying to parameterise the efficiency in 6D (5 phase space variables and time) the 5D efficiency is evaluated independently in each lifetime bin. The lifetime-integrated efficiency is denoted as $\varepsilon_{K\pi\pi\pi}(\mathbf{p}; i)$, where the i represents integration over

the ith lifetime bin. This is then modelled using the following expression,

$$\varepsilon_{K\pi\pi\pi}(\mathbf{p};i) = h^i_{12}(m_{12}) \cdot h^i_{23}(m_{23}) \cdot h^i_{34}(m_{34}) \cdot h^i_{123}(m_{123}) \cdot h^i_{234}(m_{234}) \cdot h^i(\mathbf{m}) \quad (5.43)$$

The group of functions labeled h represent histograms i.e.

$$h(x) = h.\text{GetBinContent}(h.\text{FindBin}(x)). \quad (5.44)$$

Each histogram has a dimensionality indicated by the number of arguments. The vector $\mathbf{m}$ is defined $\mathbf{m} = (m_{12}, m_{23}, m_{34}, m_{123}, m_{234})$ i.e. $h^i(\mathbf{m})$ is a 5D histogram. This approach means that large efficiency fluctuations at the edge of phase space can be described by narrow binning in the 1D histograms. The correlation between the variables can then be described by the 5D histogram.

To describe how each of these histograms is created, the algorithm HIST$\{$DATA$; w(\mathbf{y}); \mathbf{x}\}$ is first defined. This algorithm makes a histogram of the dataset 'DATA' weighted by the function $w(\mathbf{y})$, where $\mathbf{y}$ is a vector of variables contained within the dataset. The histogram is created in the variables $\mathbf{x}$ i.e. if $\mathbf{x}$ only has one element, HIST will produce a 1D histogram of x_0. The binning of the histogram is determined using the adaptive binning algorithm that was described in Section 5.6.1.

The histograms in Equation 5.43 are now defined:

$$h^i_{12}(m_{12}) = \frac{\text{HIST}\{\text{MC}^\text{i}; 1.0; \text{m}_{12}\}}{\text{HIST}\{\text{GEN}; 1.0; \text{m}_{12}\}} \quad (5.45)$$

$$h^i_{23}(m_{23}) = \frac{\text{HIST}\{\text{MC}^\text{i}; 1.0; \text{m}_{23}\}}{\text{HIST}\{\text{GEN}; \text{h}^\text{i}_{12}(\text{m}_{12}); \text{m}_{23}\}} \quad (5.46)$$

$$h^i_{34}(m_{34}) = \frac{\text{HIST}\{\text{MC}^\text{i}; 1.0; \text{m}_{34}\}}{\text{HIST}\{\text{GEN}; \text{h}^\text{i}_{12}(\text{m}_{12})\text{h}^\text{i}_{23}(\text{m}_{23}); \text{m}_{34}\}} \quad (5.47)$$

$$h^i_{123}(m_{123}) = \frac{\text{HIST}\{\text{MC}^\text{i}; 1.0; \text{m}_{123}\}}{\text{HIST}\{\text{GEN}; \text{h}^\text{i}_{12}(\text{m}_{12})\text{h}^\text{i}_{23}(\text{m}_{23})\text{h}^\text{i}_{34}(\text{m}_{34}); \text{m}_{123}\}} \quad (5.48)$$

$$h^i_{234}(m_{234}) = \frac{\text{HIST}\{\text{MC}^\text{i}; 1.0; \text{m}_{234}\}}{\text{HIST}\{\text{GEN}; \text{h}^\text{i}_{12}(\text{m}_{12})\text{h}^\text{i}_{23}(\text{m}_{23})\text{h}^\text{i}_{34}(\text{m}_{34})\text{h}^\text{i}_{123}(\text{m}_{123}); \text{m}_{234}\}} \quad (5.49)$$

$$h^i(\mathbf{m}) = \frac{\text{HIST}\{\text{MC}^\text{i}; 1.0; \mathbf{m}\}}{\text{HIST}\{\text{GEN}; \text{h}^\text{i}_{12}(\text{m}_{12})\text{h}^\text{i}_{23}(\text{m}_{23})\text{h}^\text{i}_{34}(\text{m}_{34})\text{h}^\text{i}_{123}(\text{m}_{123})\text{h}^\text{i}_{234}(\text{m}_{234}); \mathbf{m}\}} \quad (5.50)$$

where the data sample labeled 'MC$^\text{i}$' is the simulated data (described in Section 5.6.1)

that is within lifetime bin i. The data sample labeled 'GEN' is the generator level MC created by MINT - this is not generated with any lifetime dependence, so it is unnecessary to split the sample into lifetime bins.

This technique is now demonstrated on the lifetime-integrated sample of MC (labeled MC^{ALL}). Figure 5.31 shows projections of the phase space variables for both MC^{ALL} and GEN. In this figure there is clearly a difference between the two samples due to the phase space dependent acceptance effects. In Figure 5.32 the same projections are repeated, but now with the GEN sample weighted by $\varepsilon_{K\pi\pi\pi}(\mathbf{p}; \text{ALL})$. In this figure the two distributions appear consistent, validating the efficiency parameterisation method. Further checks are made in Appendix C by comparing slices of the 5D phase space.

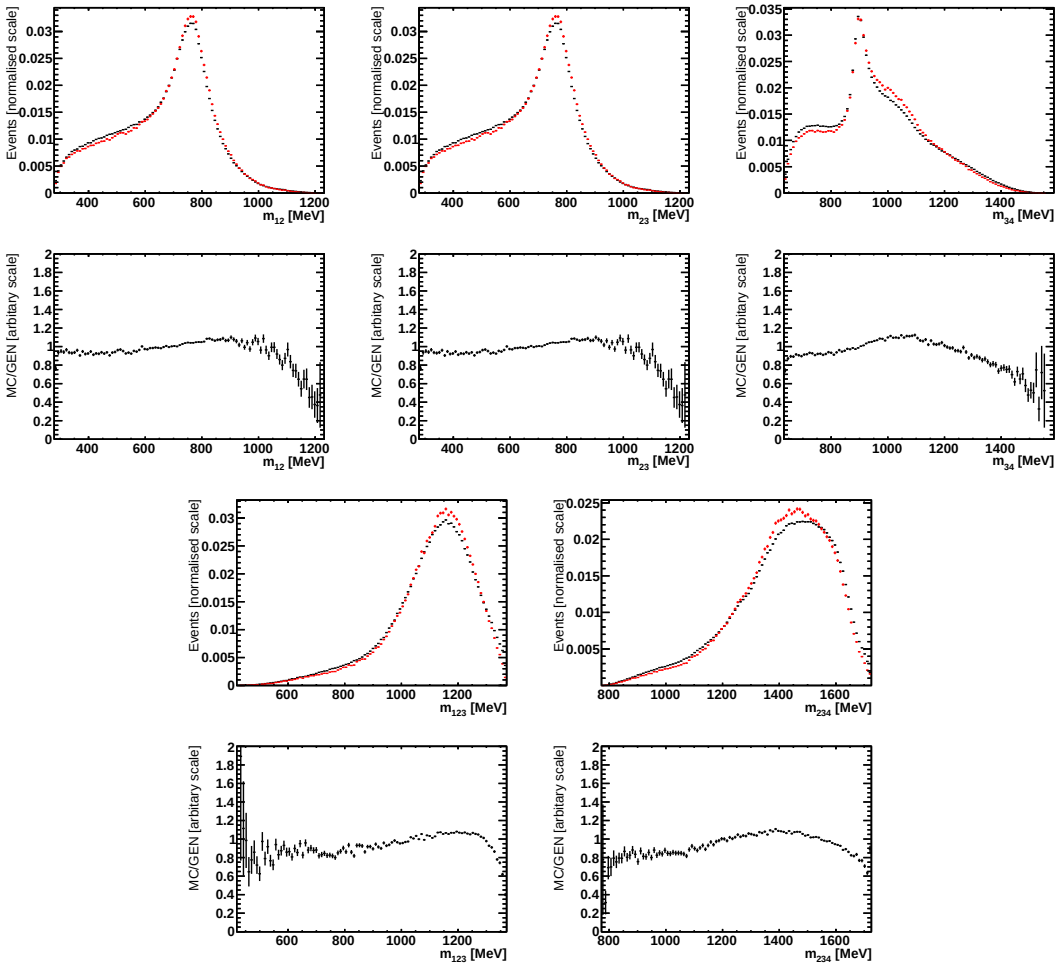

Figure 5.31: Projections of MC (black) and GEN (red) in the 5 variables chosen to parameterise phase space ($m_{12}, m_{23}, m_{34}, m_{123}, m_{234}$). The ratio plots show the ratio of the MC to GEN projections.

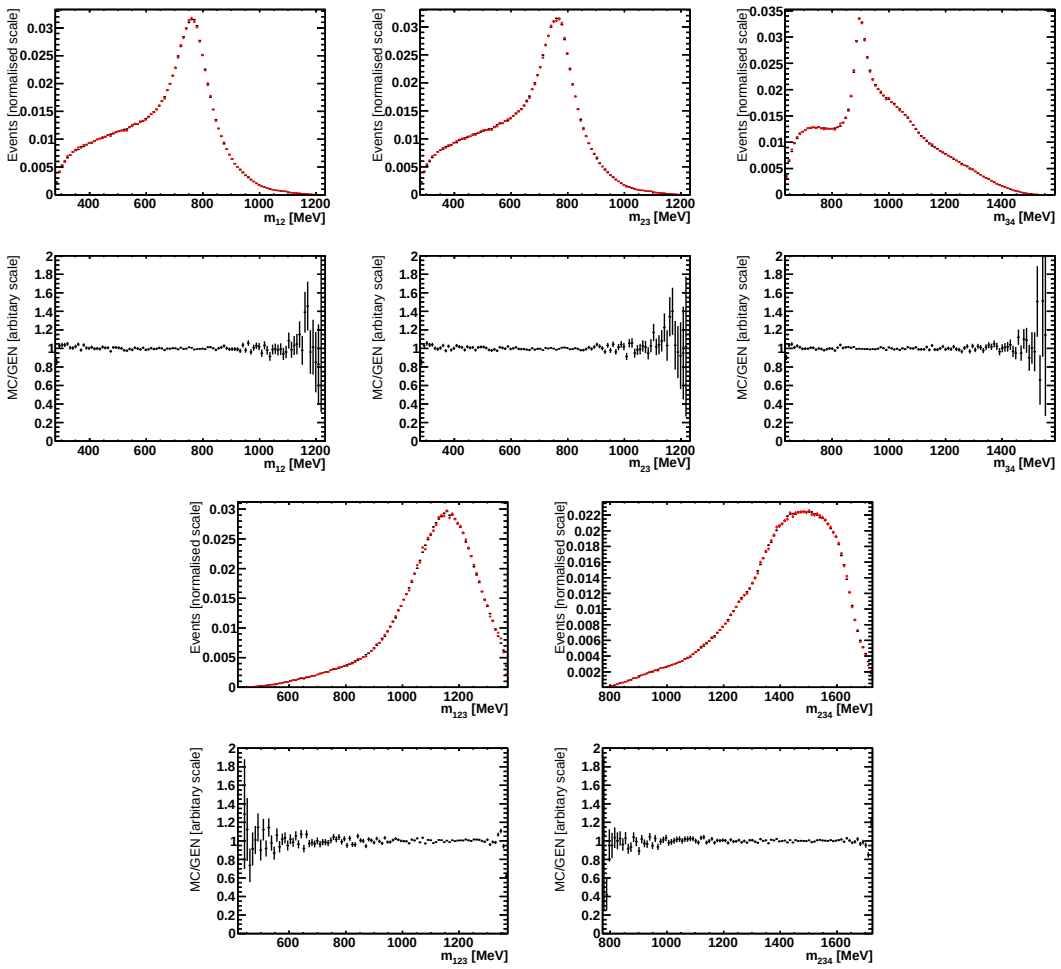

Figure 5.32: Projections of MC (black) and GEN weighted by $\varepsilon_{K\pi\pi\pi}(\mathbf{p})$ (red) in the 5 variables chosen to parameterise phase space $(m_{12}, m_{23}, m_{34}, m_{123}, m_{234})$. The ratio plots show the ratio of the MC to GEN projections.

5.6.4 Determination of the Correction

From the efficiency parameterisations, $\varepsilon_{K\pi\pi\pi}(\mathbf{p}; i)$, determined in the previous section, one can use *sWeights* to calculate the integrated efficiencies:

$$\varepsilon^{\mathrm{WS(RS)}}_{K\pi\pi\pi,i} = \frac{\sum w_j^{\mathrm{WS(RS)}}}{\sum \frac{w_j^{\mathrm{WS(RS)}}}{\varepsilon_{K\pi\pi\pi}(\mathbf{p}_j;i)}}. \tag{5.51}$$

where $w_j^{\mathrm{WS(RS)}}$ is the *sWeight* of the jth WS (RS) candidate in lifetime bin i found from the Δm fit, and $\mathbf{p}_j$ is the candidate's phase space location. The efficiency correction,

$\epsilon_{\mathrm{COR},i}$, in each lifetime bin, i, is then determined from:

$$\epsilon_{\mathrm{COR},i} = \frac{\sum w_j^{\mathrm{WS}}}{\sum \frac{w_j^{\mathrm{WS}}}{\varepsilon_{K\pi\pi\pi}(\mathbf{p}_j;i)}} \frac{\sum \frac{w_j^{\mathrm{RS}}}{\varepsilon_{K\pi\pi\pi}(\mathbf{p}_j;i)}}{\sum w_j^{\mathrm{RS}}}. \tag{5.52}$$

The efficiency corrections, $\epsilon_{\mathrm{COR},i}$, obtained from this technique are displayed in Figure 5.33. The errors in the figure, $\sigma_{\mathrm{COR},i}$, are found by varying the efficiency histograms (defined in Equation 5.50) within their errors, then recalculating the efficiency correction. This is done 50 times, taking the standard deviation of the results as the uncertainty.

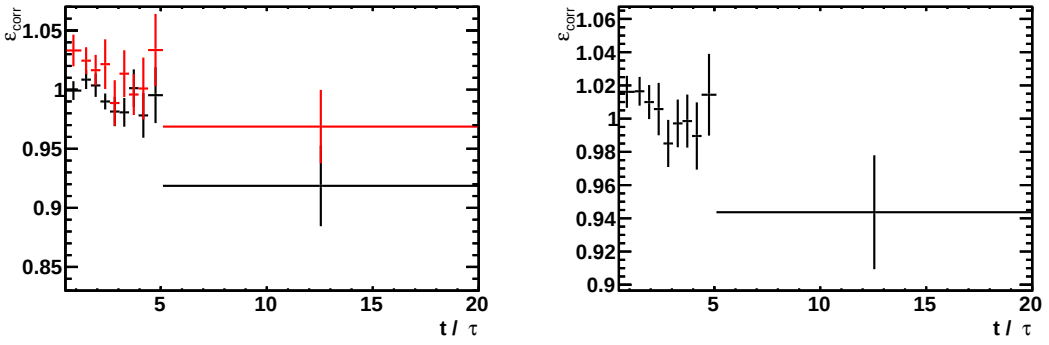

Figure 5.33: (left) The efficiency correction for the WS/RS ratio using (black) the default technique (red) the alternate technique (right) The final efficiency correction, Λ_i^{EFF}, described in the text.

Also shown in Figure 5.33 is the results of an alternative method to calculate ϵ_{COR} ($\varepsilon_{\mathrm{COR}}^{\mathrm{ALT}}$). This uses MC to find the lifetime-integrated efficiency, then uses *sWeighted* RS data (which importantly has an amplitude that is *not* lifetime-dependent) to find the 'efficiency difference', $\delta_{K\pi\pi\pi}(\mathbf{p};i)$, between the lifetime-integrated dataset, and the dataset in lifetime bin i. This approach is written,

$$\varepsilon_{K\pi\pi\pi}^{\mathrm{ALT}}(\mathbf{p};i) = \varepsilon_{K\pi\pi\pi}(\mathbf{p};\mathrm{ALL})\delta_{K\pi\pi\pi}(\mathbf{p};i). \tag{5.53}$$

The efficiency difference, $\delta_{K\pi\pi\pi}(\mathbf{p};i)$, is determined using the same procedure that was used to determine $\varepsilon_{K\pi\pi\pi}(\mathbf{p};i)$.

The final efficiency correction used, $\Lambda_i^{\rm EFF}$, is the average of the two methods. The uncertainty associated with $\Lambda_i^{\rm EFF}$ is the combination of a statistical and systematic component. The statistical uncertainty is taken directly from the uncertainty on $\epsilon_{\rm COR}$, whereas the systematic is the difference between $\epsilon_{\rm COR}$ and $\varepsilon_{\rm COR}^{\rm ALT}$. The combination of these uncertainties is presented in Figure 5.33, and can be conveniently written in the covariance matrix $\Sigma^{\rm EFF}$:

$$\Sigma_{ii}^{\rm EFF} = \sigma_{{\rm COR},i}^2 + (\epsilon_{{\rm COR},i} - \epsilon_{{\rm COR},i}^{\rm ALT})^2, \tag{5.54}$$

$$\Sigma_{ij}^{\rm EFF} = 0. \tag{5.55}$$

5.7 Fitting the lifetime distribution

This section describes the procedure used to fit the WS/RS ratio measured in Section 5.4. The expression for this ratio (Equation 4.26) is repeated here for convenience:

$$R_\Omega(t) = r^2_{D,\Omega} + r_{D,\Omega}\left(y\mathcal{R}e\mathcal{Z}^f_\Omega + x\mathcal{I}m\mathcal{Z}^f_\Omega\right)\Gamma_D t + \frac{x^2+y^2}{4}(\Gamma_D t)^2. \tag{5.56}$$

In this analysis only the 'global $\mathcal{Z}^f_\Omega$' is considered (where the phase space volume Ω represents the entire kinematically allowed region). For the remainder of the chapter the Ω subscript will be therefore be dropped.

5.7.1 Fit parameterisations

To fit the WS/RS ratio, four different parameterisations are used:

- `'No Mixing'`

$$R(t) = a \tag{5.57}$$

- `'Mixing Unconstrained'`

$$R(t) = r^2_D + r_D b\Gamma_D t + c(\Gamma_D t)^2 \tag{5.58}$$

- `'Mixing Constrained'`

$$R(t) = r^2_D + r_D b\Gamma_D t + \frac{x^2+y^2}{4}(\Gamma_D t)^2 \tag{5.59}$$

(with x, y constrained to HFAG averages)

- `'Mixing Constrained Scan'` (Cartesian and Polar)

$$R(t) = r^2_D + r_D\left(y\mathcal{R}e\mathcal{Z}^f + x\mathcal{I}m\mathcal{Z}^f\right)\Gamma_D t + \frac{x^2+y^2}{4}(\Gamma_D t)^2 \tag{5.60}$$

$$= r^2_D + r_D R^f_D\left(y\cos\delta^f_D - x\sin\delta^f_D\right)\Gamma_D t + \frac{x^2+y^2}{4}(\Gamma_D t)^2 \tag{5.61}$$

(with x, y constrained to HFAG averages)

The `'No Mixing'` and `'Mixing Unconstrained'` fits are used to calculate the probability of the data being a statistical fluctuation of the no mixing hypothesis - also referred to as the 'mixing significance'. The `'Mixing Unconstrained'` fit is also used for a standalone measurement of r_D, b and c that has no external input. The `'Mixing Constrained'` fit is used for a measurement of r_D and b that includes external input on x and y. Finally, the `'Mixing Constrained Scan'` fit is used to create a 2D χ^2 scan in the complex $\mathcal{Z}^f$ plane - this is also done in the polar coordinates R_D^f and δ_D^f.

5.7.2 Chi2 calculation

The fit to the WS/RS ratio is done using a binned χ^2 technique - in this subsection the formulation of the χ^2 is detailed.

From the WS and RS yields measured in section Section 5.4 the vector of the measured ratios $\mathbf{R}^M$ is defined:

$$R_i^M = \sqrt{\frac{N^i_{WSD^0} N^i_{WS\bar{D}^0}}{N^i_{RSD^0} N^i_{RS\bar{D}^0}}}, \tag{5.62}$$

where i labels the lifetime bin. From this, the vector of corrected ratios, $\mathbf{R}_i^{\rm COR}$, is defined:

$$R_i^{\rm COR} = \left(R_i^M + \Delta_i^{\rm SHAPE} - \Delta_i^{\rm ID} - \Delta_i^{GHOST}\right) \Lambda_i^{\rm EFF} \tag{5.63}$$

The vector $\mathbf{\Delta}^{\rm SHAPE}$ is determined in Section 5.5.4 and introduces a systematic for the choice of parameterisation used in the Δm fit. The vector $\mathbf{\Delta}^{\rm ID}$ is determined in Section 5.5.2 and corrects for double mis-ID background. The vector $\mathbf{\Delta}^{\rm GHOST}$ is determined in Section 5.5.3 and introduces a systematic for ghost background. The vector $\mathbf{\Lambda}^{\rm EFF}$ is determined in Section 5.6.2 and corrects for phase-space-integrated efficiency differences between WS and RS decays. The values of $\mathbf{\Delta}^{\rm SHAPE}$ and $\mathbf{\Delta}^{\rm GHOST}$ are zero, although they are included in this expression for the purposes of error propagation.

Some of the corrections described above are correlated between lifetime bins, and therefore the full covariance matrix $\Sigma^{\rm COR}$ is used in the lifetime fitter. This is found using standard error combination techniques,

$$\Sigma^{\mathrm{COR}} = \mathbf{\Lambda}_{\mathbf{I}}^{\mathrm{EFF}} \left(\Sigma^{m} + \Sigma^{\mathrm{SHAPE}} + \Sigma^{\mathrm{ID}} + \Sigma^{\mathrm{GHOST}}\right) \mathbf{\Lambda}_{\mathbf{I}}^{\mathrm{EFF}} \tag{5.64}$$
$$+ \left(\mathbf{R}^{m} + \mathbf{\Delta}^{\mathrm{SHAPE}} - \mathbf{\Delta}^{\mathrm{ID}} - \mathbf{\Delta}^{\mathrm{GHOST}}\right)_{\mathbf{I}} \Sigma^{\mathrm{EFF}} \left(\mathbf{R}^{m} + \mathbf{\Delta}^{\mathrm{SHAPE}} - \mathbf{\Delta}^{\mathrm{ID}} - \mathbf{\Delta}^{\mathrm{GHOST}}\right)_{\mathbf{I}},$$

where the **I** subscript indicates a vector that has been put into diagonal matrix form i.e. $(\mathbf{R_I})_{ii} = \mathbf{R}_i$ and $(\mathbf{R_I})_{ij} = 0$ (where $i \neq j$).

The vector of WS/RS ratios that results from a particular set of fit parameters (as listed in Equations 5.57 - 5.61) is defined:

$$R_i^{\mathrm{MOD}}(\boldsymbol{\nu}) = \frac{\int_{t^i_{\mathrm{min}}}^{t^i_{\mathrm{max}}} \mathrm{acc}(t) R(t;\boldsymbol{\nu}) \exp(-\Gamma t)\mathrm{d}t}{\int_{t^i_{\mathrm{min}}}^{t^i_{\mathrm{max}}} \mathrm{acc}(t) \exp(-\Gamma t)\mathrm{d}t} \tag{5.65}$$

where $R(t;\boldsymbol{\nu})$ is the time-dependent WS/RS ratio that depends on a set of fit parameters $\boldsymbol{\nu}$ (which will later be varied to minimise the χ^2). The lifetime acceptance is given by $\mathrm{acc}(t)$, which is discussed in Section 5.7.3. This is then adjusted to account for the presence of secondary D decays:

$$R_i^{\mathrm{MOD}}(\boldsymbol{\nu}, \nu_{\Delta_{B,i}}) = \frac{\int_{t^i_{\mathrm{min}}}^{t^i_{\mathrm{max}}} \mathrm{acc}(t) R(t;\boldsymbol{\nu}) \exp(-\Gamma t)\mathrm{d}t}{\int_{t^i_{\mathrm{min}}}^{t^i_{\mathrm{max}}} \mathrm{acc}(t) \exp(-\Gamma t)\mathrm{d}t} \cdot \left(1 - \nu_{\Delta_{B,i}}\right) \tag{5.66}$$

The parameter $\nu_{\Delta_{B,i}}$ is the correction needed for secondary decays in lifetime bin i, as described in Section 5.5.1. The parameter floats in the fit, although its value is constrained (as shown later in Equation 5.69).

Using the definitions above the χ^2 between $\mathbf{R}^{\mathrm{COR}}$ and $\mathbf{R}^{\mathrm{MOD}}(\boldsymbol{\nu}, \boldsymbol{\nu}_{\Delta_B})$ is defined:

$$\chi^2_{\mathrm{WS/RS}} = [\mathbf{R}^{\mathrm{COR}} - \mathbf{R}^{\mathrm{MOD}}(\boldsymbol{\nu}, \boldsymbol{\nu}_{\Delta_B})][\Sigma^{\mathrm{COR}}]^{-1}[\mathbf{R}^{\mathrm{COR}} - \mathbf{R}^{\mathrm{MOD}}(\boldsymbol{\nu}, \boldsymbol{\nu}_{\Delta_B})]^T, \tag{5.67}$$

This is one term in the total χ^2:

$$\chi^2_{\mathrm{tot}} = \chi^2_{\mathrm{WS/RS}} + \chi^2_{\Delta_B} + \chi^2_{f_B^{\mathrm{RS}}} + [\chi^2_{x,y}] \tag{5.68}$$

The first of the additional χ^2 terms, $\chi^2_{\Delta_B}$, is used to constrain the secondary correction $\nu_{\Delta_{B,i}}$:

$$\chi^2_{\Delta_B} = \sum \left(\frac{\nu_{\Delta_{B,i}} - \Delta_{B,i}}{\sigma_{\Delta_{B,i}}} \right)^2 \tag{5.69}$$

where $\Delta_{B,i}$ and $\sigma_{\Delta_{B,i}}$ are determined from,

$$\Delta_{B,i} = \frac{\Delta^{\min}_{B,i} + \Delta^{\max}_{B,i}}{2}, \qquad \sigma_{\Delta_{B,i}} = \frac{\Delta^{\max}_{B,i} - \Delta^{\min}_{B,i}}{2}, \tag{5.70}$$

which themselves are determined from,

$$\Delta^{\min}_{B,i} = \nu_{f^{\rm RS}_{B,i}} \left[1 - \frac{R_{\max}(t^i_{\rm ave};\boldsymbol{\nu})}{R(t^i_{\rm ave};\boldsymbol{\nu})} \right], \qquad \Delta^{\max}_{B,i} = \nu_{f^{\rm RS}_{B,i}} \left[1 - \frac{R_{\min}(t^i_{\rm ave};\boldsymbol{\nu})}{R(t^i_{\rm ave};\boldsymbol{\nu})} \right]. \tag{5.71}$$

As described in Section 5.5.1, $R_{\max}(t^i_{\rm ave};\boldsymbol{\nu})$ and $R_{\min}(t^i_{\rm ave};\boldsymbol{\nu})$ are the maximum and minimum of $R(t;\boldsymbol{\nu})$ in the lifetime range $[0, t^i_{\rm ave}]$. Here $t^i_{\rm ave}$ is the time at which the lifetime dependent ratio, $R(t;\boldsymbol{\nu})$, is equal to the lifetime-integrated ratio in bin i, $R^{\rm MOD}_i(\boldsymbol{\nu})$ i.e. $R(t^i_{\rm ave};\boldsymbol{\nu}) = R^{\rm MOD}_i(\boldsymbol{\nu})$.

Both of the expressions in Equation 5.71 depend on the fit parameter $\nu_{f^{\rm RS}_{B,i}}$ which describes the fraction of secondary decays in the RS sample of lifetime bin i. This fraction is constrained to $f^{\rm RS}_{B,i}$ measured in data (Section 5.5.1):

$$\chi^2_{f^{\rm RS}_B} = \sum \left(\frac{\nu_{f^{\rm RS}_{B,i}} - f^{\rm RS}_{B,i}}{\sigma_{f^{\rm RS}_{B,i}}} \right)^2. \tag{5.72}$$

The final term, $\chi^2_{x,y}$, is used to constrain the mixing parameters x and y in the '`Mixing Constrained`' and '`Mixing Constrained Scan`' fits. This is defined as:

$$\chi^2_{x,y} = \begin{pmatrix} \Delta x & \Delta y \end{pmatrix} \begin{pmatrix} \sigma_x^2 & \rho_{x,y}\sigma_x\sigma_y \\ \rho_{x,y}\sigma_x\sigma_y & \sigma_y^2 \end{pmatrix}^{-1} \begin{pmatrix} \Delta x \\ \Delta y \end{pmatrix} \tag{5.73}$$

where,

$$\Delta x = x - x_{\rm HFAG}\,, \;\; \Delta y = y - y_{\rm HFAG}. \tag{5.74}$$

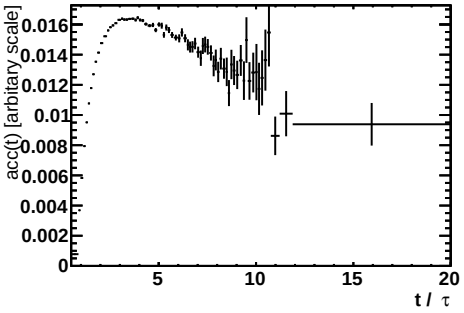

Figure 5.34: Lifetime acceptance, found from the *sWeighted* RS sample, and assuming a D^0 lifetime of 0.4101 ps.

The central values, uncertainties and correlations ($x_{\rm HFAG}$, $y_{\rm HFAG}$, σ_x, σ_y, and $\rho_{x,y}$) are taken from the Heavy Flavour Averaging Group (HFAG) [71]:

$$x_{\rm HFAG} = 0.526 \pm 0.161\% \qquad y_{\rm HFAG} = 0.668 \pm 0.088\% \qquad \rho = 0.188 \tag{5.75}$$

5.7.3 Lifetime Acceptance

The lifetime distribution of RS signal events is found using the *sPlot* technique, where *sWeights* are determined from the Δm fit. The lifetime acceptance acc(t), featured in Equation 5.65, is then determined by weighting the *sWeighted* RS data sample by $\exp(\Gamma_D t)$ - this is presented in Figure 5.34. For Γ_D the inverse of the well-measured D^0 lifetime is taken from PDG (0.4101 ps). Instead of trying to parameterise the efficiency shape, the fitter is provided with the histogram directly. The same procedure was used for the toy studies in Section 5.8, and no bias was observed.

5.8 Simulation Studies

To check for any biases in the yield extraction and time-dependent fitting procedure (Section 5.4 and Section 5.7 respectively) a toy simulation study is performed. This is done by taking real data and replacing the measured D^0 lifetimes with new lifetimes determined from toy simulation. The yield extraction and the lifetime-dependent fitting procedure is then performed on the toy dataset in an identical fashion to which it would be done on real data.

The expected total number of WS and RS decays is determined from,

$$N_{\rm WS}^{\rm SIG} = \alpha \int_{t_{\rm min}}^{t_{\rm max}} R(t){\rm acc}(t)\exp(-\Gamma t){\rm d}t \qquad (5.76)$$
$$N_{\rm RS}^{\rm SIG} = \alpha \int_{t_{\rm min}}^{t_{\rm max}} {\rm acc}(t)\exp(-\Gamma t){\rm d}t$$

where $t_{\rm min}$ and $t_{\rm max}$ give the upper and lower lifetime limits used in the analysis (0.5 τ_{D^0} and 20 τ_{D^0} respectively). The factor α is used to scale the absolute number of RS and WS decays.

To determine the expected number background events, the signal to background fraction, $f_{\rm CAT}$, is taken from the lifetime-integrated Δm fit (Section 5.4):

$$N_{\rm CAT}^{\rm BG} = \left(\frac{1}{f_{\rm CAT}}\right) N_{\rm CAT}^{\rm SIG} \qquad (5.77)$$

For each simulated dataset, the number of events in each category is randomly selected by sampling from a Poisson distribution with random seed i, with the expected number of events taken from Equation 5.76 and Equation 5.77:

$$N_{\rm CAT,i} = {\rm Poisson}_i\left(N_{\rm SIG}^{\rm BG} + N_{\rm CAT}^{\rm BG}\right) \qquad (5.78)$$

The scaling factor α is chosen so that $N_{\rm CAT,i}$ will not exceed the number of candidates in the real dataset (although is as close to this as possible). To create a simulated dataset, $N_{\rm CAT,i}$ candidates from each category are copied from the real dataset, removing all D^0

lifetime information. To assign a new D^0 lifetime to each candidate the acceptance-corrected RS and WS rates (seen in the integrand of Equation 5.76) are randomly sampled using an accept-reject technique.

The toy studies were carried out for 3 different sets of input parameters:

- `CleoNew`: R_D^f and δ_D^f are taken from the latest CLEO-c measurement [11]. Mixing parameters x and y are taken from the latest HFAG average. For each toy study, the mixing parameters are randomly sampled according to the HFAG covariance matrix - this is necessary because constraints are applied to these parameters.
- `CleoOld`: This is identical to `CleoNew` but with the R_D^f and δ_D^f taken from a previous CLEO-c result [48]. These input values better reproduce the LHCb result.
- `NoMixing`: The mixing parameters x and y are set to zero. R_D^f and δ_D^f do not feature in the WS/RS rate in this scenario, so their input values are irrelevant.

In addition to the input values listed above, the parameter r_D is set to $\frac{1}{\sqrt{300}}$ in all simulated datasets. Figure 5.35 shows, for each set of input values, an example of the WS/RS ratio obtained. The results of the toy studies are presented in Section 5.8.1, Section 5.8.2 and Section 5.8.3. No bias is observed for any scenario.

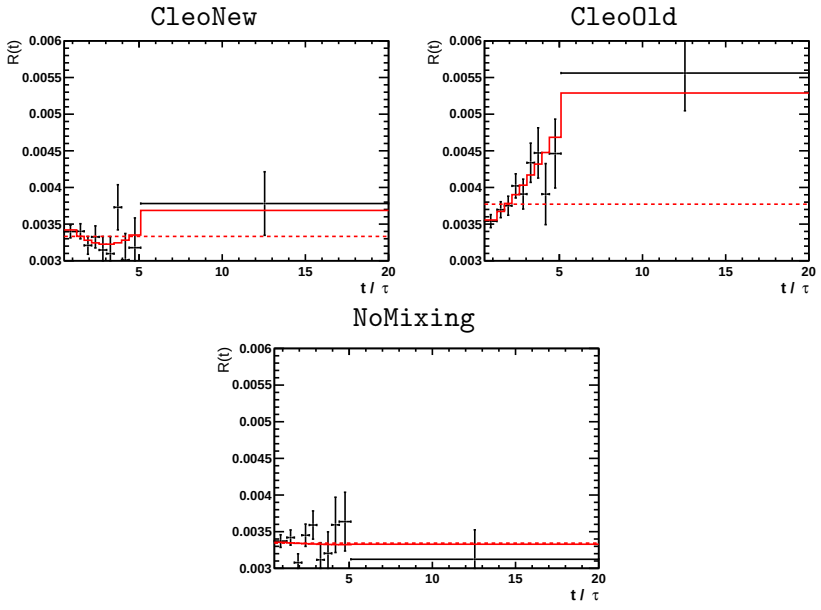

Figure 5.35: The WS/RS ratio obtained from toy data, where the three figures use different input values for the physical parameters R_D^f, δ_D^f, x and y.

5.8.1 Cleo New

When using the `CleoNew` input values two different fit procedures are tested, '`Mixing Unconstrained`', and '`Mixing Constrained`'. Both fit procedures are described in Section 5.7. The results of a pull study using 300 simulated datasets is shown in Figure 5.36 and Figure 5.37. No bias is observed.

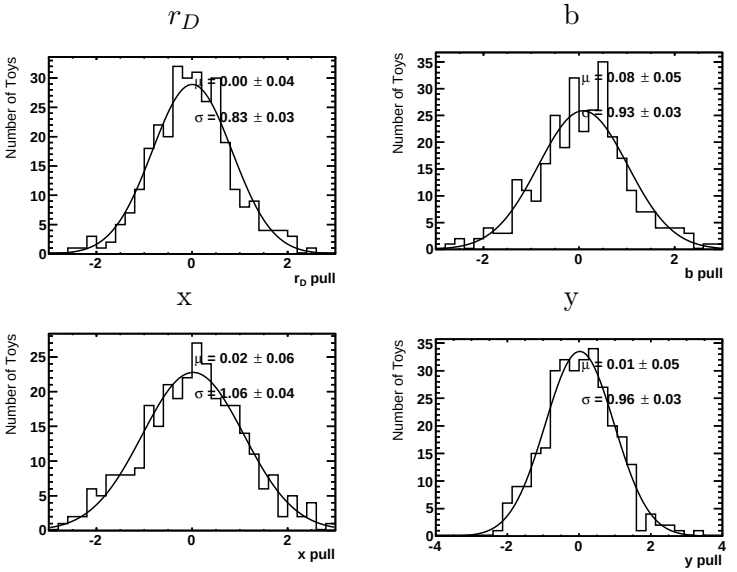

Figure 5.36: Results of the '`Mixing Constrained`' pull study for simulated data generated with `CleoNew` input values. The fit parameters are defined in Section 5.7.

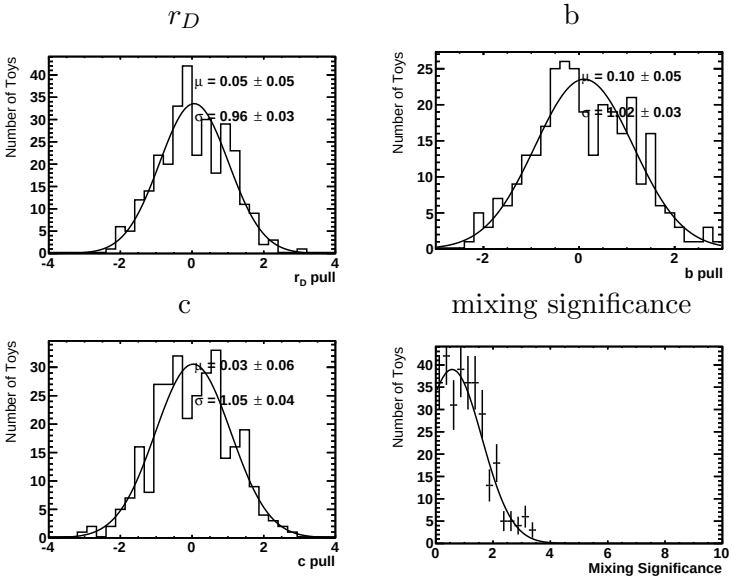

Figure 5.37: Results of the '`Mixing Unconstrained`' pull study for simulated data generated with `CleoNew` input values. The fit parameters are defined in Section 5.7. The bottom right plot shows the mixing significance obtained from the simulated data samples.

5.8.2 Cleo Old

When using the `CleoOld` input values two different fit procedures are tested, '`Mixing Unconstrained`', and '`Mixing Constrained`'. Both fit procedures are described in Section 5.7. The results of a pull study using 300 simulated datasets is shown in Figure 5.38 and Figure 5.39. No bias is observed.

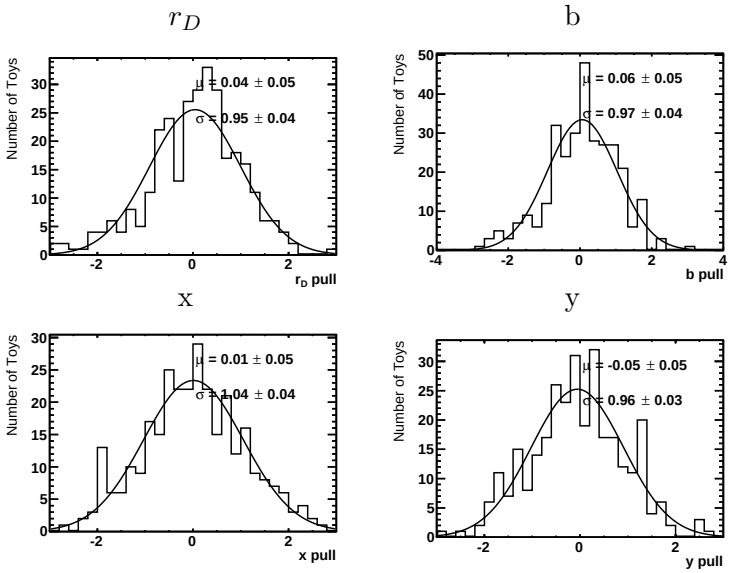

Figure 5.38: Results of the '`Mixing Constrained`' pull study for simulated data generated with `CleoNew` input values. The fit parameters are defined in Section 5.7.

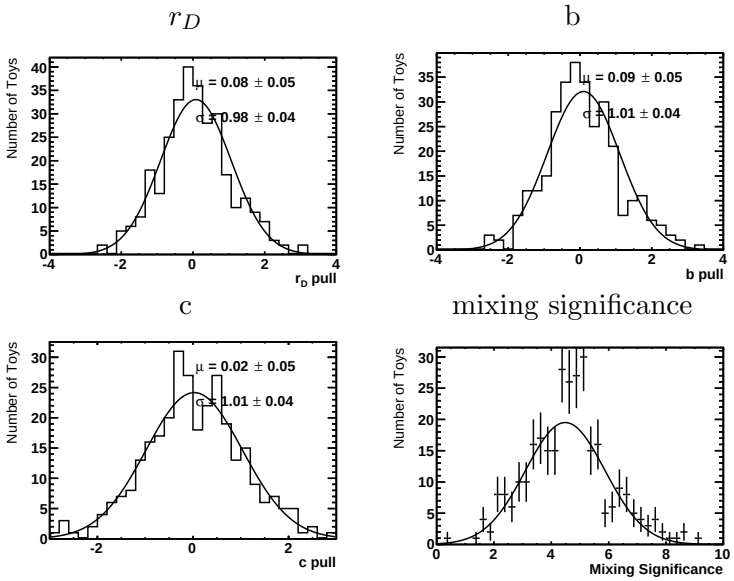

Figure 5.39: Results of the '`Mixing Unconstrained`' pull study for simulated data generated with `CleoOld` input values. The fit parameters are defined in Section 5.7. The bottom right plot shows the mixing significance obtained from the simulated data samples.

5.8.3 No Mixing

When using the `MoMixing` input values the `'Mixing Constrained'` fit no longer makes sense, so only the `'Mixing Unconstrained'` fit is tested. The results of a pull study using 300 toy datasets is shown in Figure 5.40. Also shown in Figure 5.40 is the mixing significance obtained from fits to toy data. As one would expect, this nicely agrees with a Gaussian of mean 0 and width 1 (as superimposed on the figure).

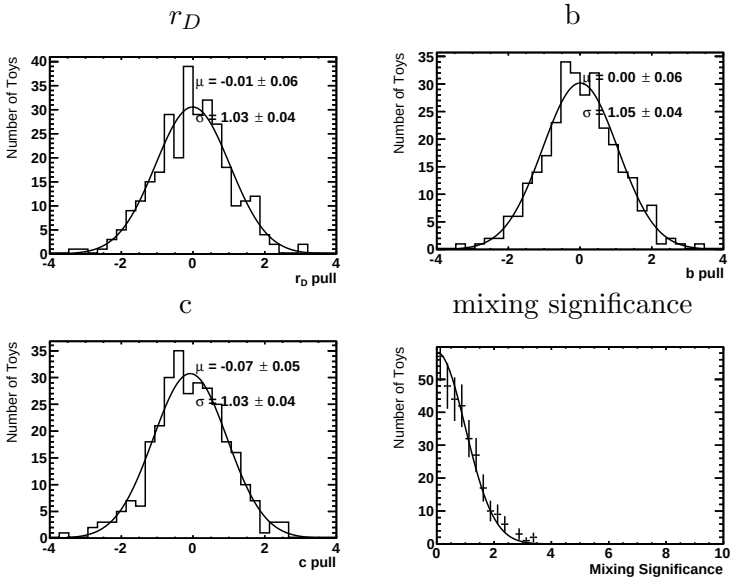

Figure 5.40: Results of the `'Mixing Constrained'` pull study with `NoMixing` input values. The fit parameters are defined in Section 5.7. The bottom right plot shows the mixing significance obtained from the simulated data samples.

5.9 Results

5.9.1 Mixing Unconstrained Fit

The corrected WS/RS ratio, $\mathbf{R}^{\mathrm{COR}}$, is shown in Figure 5.41 with the results of the `'Mixing Unconstrained'` and `'No Mixing'` fits (Equation 5.58 and Equation 5.57 respectively) superimposed. Also shown in Figure 5.41 is a table of the fit results, listing the central values and uncertainties of the fit parameters. Using the difference in χ^2 between the `'Mixing Unconstrained'` and `'No Mixing'` fits, $(\chi^2_{\mathrm{NULL}} - \chi^2)$, the probability of the result being a statistical fluctuation of the no mixing hypothesis is calculated to be 0.25×10^{-5} - this corresponds to a significance of 4.7σ. The validity of this method was tested on simulated data, and was found to give the correct coverage (Section 5.8.3).

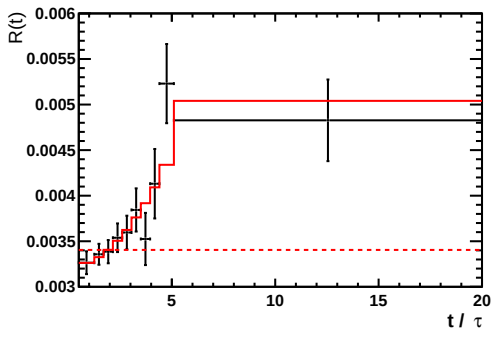

Fit Parameter	Result
r_D	0.0565 ± 0.0023
b	-0.0004 ± 0.0036
c	0.000048 ± 0.000033
χ^2	7.2
χ^2_{NULL}	33
σ_{MIX} (p-value)	4.7 (0.25×10^{-5})

Figure 5.41: (left) The corrected WS/RS ratio measured in data is shown by the black data points - the error bars include all systematic uncertainties. Superimposed is the `'Mixing Unconstrained'` fit Equation 5.58 (solid red line) and the `'No Mixing'` fit Equation 5.57 (dotted red line). The fit is aware of correlations between lifetime bins which are not shown in the figure (right) The fit results of the `'Mixing Unconstrained'` fit, and the χ^2 of the no mixing fit. Also shown is the mixing significance, calculated using the χ^2 difference between the two hypotheses.

Table 5.7 gives a breakdown of how the systematic uncertainties on the WS/RS ratio (described in Section 5.5) propagate to the uncertainty on a fit parameter (reported in Figure 5.41). In Figure 5.41, the uncertainty on a fit parameter encompasses both a statistical and a systematic component, and is therefore labelled $\sigma_{\mathrm{stat+sys}}$. A fit to the WS/RS ratio with no systematic uncertainties included gives a fit parameter uncertainty of σ_{stat} i.e. just the statistical uncertainty on a fit parameter. The systematic uncertainty on the fit parameter, σ_{sys}, can then be estimated by looking at the difference

in quadratures $\sigma^2_{\text{sys}} = \sigma^2_{\text{stat+sys}} - \sigma^2_{\text{stat}}$. For the fit parameters r_D, b and c the systematic uncertainty found using this technique is $\sim 50\%$ of the statistical uncertainty. The contribution of each individual systematic uncertainty (double mis-ID correction, efficiency correction, secondary correction, ghost systematic and shape systematic) is also evaluated using the same technique.

The systematic uncertainties listed in Table 5.7 suggest that the analysis will become systematics-dominated with $\sim$ 4 times the statistics. In reality this is not the case because many of the systematic uncertainties will also decrease with additional statistics.

	$\sigma(r_D)$ [%]	$\sigma(b)$ [%]	$\sigma(c)$ [%]
statistical	0.196	0.317	0.0031
systematic	0.114	0.175	0.0014
double mis-ID	0.064	0.088	0.0007
efficiency	0.032	0.026	0.0004
secondary	0.060	0.122	0.0010
ghost	0.024	0.017	0.0001
shape	0.018	0.019	0.0001
total	0.226	0.362	0.0033

Table 5.7: A breakdown of how the systematic uncertainties on the WS/RS ratio (described in Section 5.5) propagate to the uncertainty on the fit parameters r_D, b and c in the `'Mixing Unconstrained'` fit. The method used to estimate these is described in the text.

The observable $R_M = (x^2 + y^2)/2$ (equivalent to $2c$) has previously been measured by the BABAR experiment in the $D \to K\pi\pi\pi$ decay - they report a value of $0.019^{+0.016}_{-0.015} \pm 0.002$ % [78] where the first uncertainty is statistical, and the second is systematic. The parameter R_M is only dependent on the mixing parameters x and y, and is therefore independent of the final state of the D decay. Using the HFAG averages, shown in Equation 5.75, R_M is calculated to be 0.0038 ± 0.0011 %. The measurements of R_M from BABAR, LHCb, and the HFAG average are summarised in Figure 5.42. The uncertainty on R_M from the LHCb measurement is less than half of that from BABAR, although it is still much larger than the world average taken from HFAG.

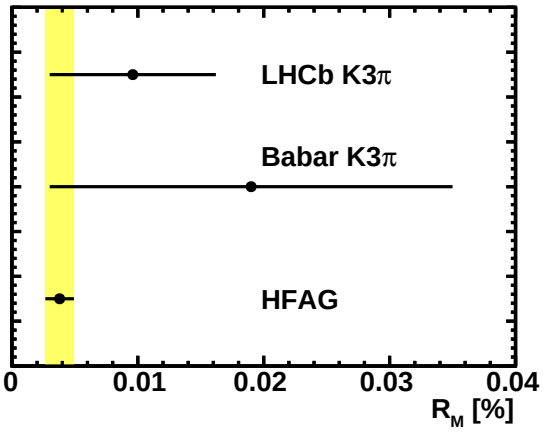

Figure 5.42: Experimental measurements of $R_M = (x^2 + y^2)/2$ from LHCb and BABAR [78] in $D^0 \to K^+\pi^-\pi^+\pi^-$ decays, and the world average measurement of R_M from HFAG [71] using several decay modes.

5.9.2 Mixing Constrained Fit

The corrected WS/RS ratio, $\mathbf{R}^{\mathrm{COR}}$, is shown in Figure 5.43 with the results of the `'Mixing Constrained'` fit (Equation 5.59) superimposed. In this fit the mixing parameters x and y have been constrained to their HFAG world averages (Equation 5.75). Also shown in Figure 5.41 is a table of the fit results, listing the central values and uncertainties of the fit parameters. The parameters r_D and b found from the `'Mixing Constrained'` fit are consistent with those from the `'Mixing Unconstrained'` fit, although have uncertainties $\sim 50\%$ of the size.

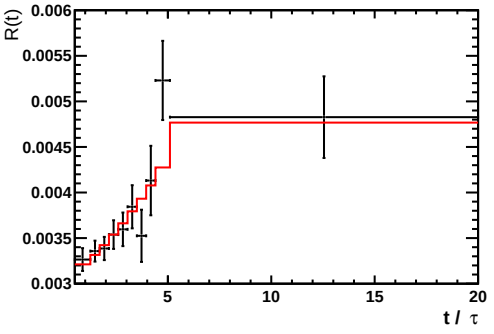

Fit Parameter	Result
r_D	0.0548 ± 0.0012
b	-0.0034 ± 0.0013
x	0.0055 ± 0.0016
y	0.00677 ± 0.00088
χ^2	8.0

Figure 5.43: (left) The corrected WS/RS ratio measured in data is shown by the black data points - the error bars include all systematic uncertainties. Superimposed with a solid red line is the `'Mixing Constrained'` fit Equation 5.59. The fit is aware of correlations between lifetime bins which are not shown in the figure (right) The fit results of the `'Mixing Constrained'` fit.

Table 5.8 gives a breakdown of how the systematic uncertainties on the WS/RS ratio (described in Section 5.5) propagate to the uncertainty on a fit parameter (reported in Figure 5.43). The process to obtain these uncertainties is described in Section 5.9.1. The systematic uncertainties on the fit parameters r_D and b are $\sim 50\%$ of the statistical uncertainties.

The constraint reported on r_D is the world's first direct measurement of this quantity. The BELLE experiment has previously performed a lifetime-integrated measurement of WS $D^0 \to K^+\pi^-\pi^+\pi^-$ decays, then used external input for x, y, $R^{K3\pi}$ and $\delta^{K3\pi}$ to indirectly obtain the currently most precise measurement of $r_D = 0.327^{+0.019}_{-0.016}$. In Figure 5.44 this is compared to the measurement from LHCb (from both the `'Mixing Constrained'` and `'Mixing Unconstrained'` fits). The LHCb and BELLE results are

	$\sigma(r_D)$ [%]	$\sigma(b)$ [%]
statistical	0.108	0.113
systematic	0.055	0.066
double mis-ID	0.039	0.039
efficiency	0.014	0.033
secondary	0.019	0.029
ghost	0.022	0.005
shape	0.023	0.029
total	0.121	0.130

Table 5.8: A breakdown of how the systematic uncertainties on the WS/RS ratio (described in Section 5.5) propagate to the uncertainty on the fit parameters r_D and b in the `'Mixing Constrained'` fit. The method used to estimate these is described in the text.

in good agreement, with the `'Mixing Constrained'` fit giving marginally better uncertainties than the BELLE result.

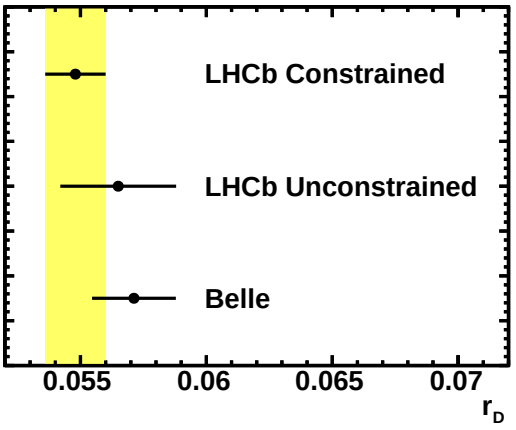

Figure 5.44: Experimental measurements of r_D from LHCb and BELLE [79] in $D^0 \to K^+\pi^-\pi^+\pi^-$ decays. The LHCb result is shown for both the `'Mixing Unconstrained'` and `'Mixing Constrained'` fits (results given in Figure 5.41 and Figure 5.43 respectively).

5.9.3 χ^2 Scans

Using the **'Mixing Constrained Scan'** parameterisation (Equation 5.61) a χ^2 scan is performed over the $D \to K\pi\pi\pi$ complex interference parameter $\mathcal{Z}^{K3\pi}$. This is done in both cartesian and polar coordinates, with the results presented in Figure 5.45. The $1, 2$ and 3σ regions are calculated using standard techniques based on χ^2 differences.

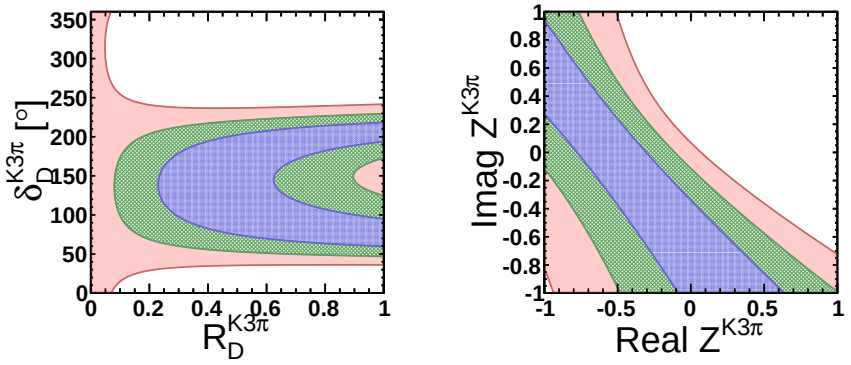

Figure 5.45: χ^2 scans over (left) $R_D^{K3\pi}$ and $\delta_D^{K3\pi}$ (right) Real $Z^{K3\pi}$ and Imag $Z^{K3\pi}$. These two parameterisations of the interference in $D \to K\pi\pi\pi$ decays are related by $Z^{K3\pi} = R_D^{K3\pi} e^{-\delta_D^{K3\pi}}$ (i.e. cartesian and polar co-ordinates). The figures show the 1, 2 and 3 sigma confidence regions found from standard χ^2 difference techniques - these regions are indicated by the blue, green, and red shaded regions respectively.

The $1, 2$ and 3σ confidence regions from the LHCb result are compared to those from CLEO-c [51] in Figure 5.46. The central value reported by CLEO-c is excluded by over 3σ, although the results are still compatible at the 2σ level.

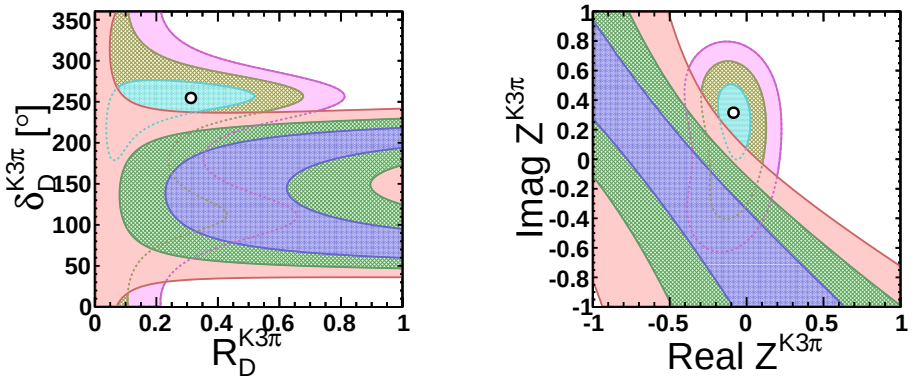

Figure 5.46: χ^2 scans over (left) $R_D^{K3\pi}$ and $\delta_D^{K3\pi}$ (right) Real $Z^{K3\pi}$ and Imag $Z^{K3\pi}$. A full description of the plots can be found in Figure 5.45. The LHCb contours are repeated from Figure 5.45 whereas the additional set of contours are taken from the CLEO-c result [51].

5.9.4 CLEO-c Combination

In this section the χ^2 scan over $\mathcal{Z}^{K3\pi}$ (Figure 5.45) is combined with the existing measurement from CLEO-c - to do this the 2D χ^2 scans from the two measurements are summed, and the confidence regions recalculated. The combined χ^2 scan is shown in Figure 5.47, and the resulting constraints on the charm interference parameters in Table 5.9. In terms of polar coordinates ($R^{K3\pi}$ and $\delta^{K3\pi}$) the combination is quite a significant improvement compared to the CLEO-c result alone - for both parameters the uncertainty is reduced by $\sim 40\%$. In terms of Cartesian coordinates ($\mathcal{Z}^{K3\pi}$) the uncertainty on $\mathcal{R}e\ \mathcal{Z}^{K3\pi}$ is almost unchanged, whereas the uncertainty on $\mathcal{I}m\ \mathcal{Z}^{K3\pi}$ is reduced by $\sim 30\%$.

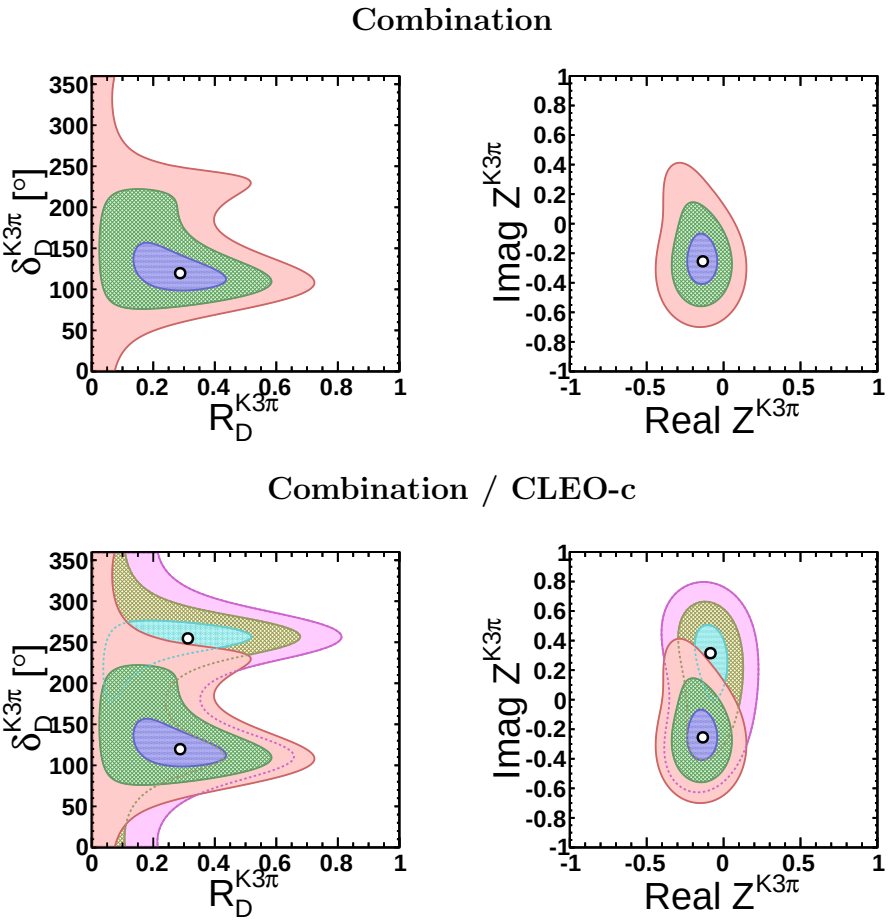

Figure 5.47: χ^2 scans over (left) $R_D^{K3\pi}$ and $\delta_D^{K3\pi}$ (right) Real $Z^{K3\pi}$ and Imag $Z^{K3\pi}$. A full description of the plots can be found in Figure 5.45. The top row shows the χ^2 scan from a combination of the LHCb and CLEO-c results. The bottom row repeats this result, but now overlaid on the CLEO-c result alone.

Parameter	CLEO-c	LHCb + CLEO-c
$R_D^{K3\pi}$	$0.31^{+0.21}_{-0.27}$	$0.29^{+0.15}_{-0.15}$
$\delta_D^{K3\pi}$	255^{+22}_{-76}	120^{+37}_{-21}
Real $Z^{K3\pi}$	$-0.08^{+0.10}_{-0.10}$	$-0.135^{+0.095}_{-0.105}$
Imag $Z^{K3\pi}$	$0.32^{+0.19}_{-0.32}$	$-0.26^{+0.19}_{-0.16}$

Table 5.9: The central values and uncertainies of $R_D^{K3\pi}$, $\delta_D^{K3\pi}$, Real $Z^{K3\pi}$ and Imag $Z^{K3\pi}$ found from the 1σ contours in Figure 5.47. The results are shown for CLEO-c alone, and the combination of CLEO-c and LHCb.

5.10 Conclusions

Following the formalism and method described in Chapter 4, an analysis of D-mixing in WS $D^0 \to K^+\pi^-\pi^+\pi^-$ decays has been performed using $1.0\,\text{fb}^{-1}$ of data collected by the LHCb experiment during 2011. The analysis has provided the first evidence (4.7σ) of D-mixing in this decay mode.

The ratio of DCS to CF amplitudes, $r_D^{K3\pi}$, is measured,

$$r_D^{K3\pi} = 0.0548 \pm 0.0012 \tag{5.79}$$

giving the world's first direct measurement of this quantity. The measurement is compatible with, and more precise than an indirect measurement of $r_D^{K3\pi}$ by BELLE [79].

Using external input for the charm mixing parameters x and y, it is possible to constrain a line of solutions in the complex $Z^{K3\pi}$ plane - such constraints provide vital information for a measurement of γ in $B \to DK$, $D \to K\pi\pi\pi$. The constraints on $Z^{K3\pi}$ using LHCb data alone do not provide point constraints in the complex plane, although when combined with current constraints from CLEO-c, one gets a significant improvement on the existing measurement. The combined constraints from LHCb and CLEO-c are,

$$\mathcal{R}e\mathcal{Z}^{K3\pi} = -0.135^{+0.095}_{-0.105}, \qquad \mathcal{I}m\mathcal{Z}^{K3\pi} = -0.26^{+0.19}_{-0.16}, \tag{5.80}$$

which for $\mathcal{I}m\ \mathcal{Z}^{K3\pi}$, is a reduction in the uncertainty by $\sim 30\%$ when compared to the measurement from CLEO-c alone. In terms of polar coordinates ($R^{K3\pi}$ and $\delta^{K3\pi}$) the combined constraints are:

$$R^{K3\pi} = 0.29^{+0.15}_{-0.15}, \qquad \delta^{K3\pi} = 119^{+37}_{-21}\,^\circ, \tag{5.81}$$

which is a reduction in the uncertainty, for both parameters, by $\sim 40\%$.

The results presented in this analysis are expected to improve significantly with the addition of LHCb data from 2012, which will give a 4 fold increase in statistics.

Chapter 6

Model-independent measurements of the CKM phase γ

6.1 Introduction

In Chapters 4 and 5 it was shown that input from charm mixing, when combined with constraints from threshold data, can substantially reduce the uncertainty on $\mathcal{Z}^f$ [1]. In this chapter a new method is presented for an amplitude model-independent measurement of γ based on input from charm mixing. In order to extract sufficient information for the measurement, it is required that that the D decay's phase space is divided into multiple bins. Such a measurement could be made with no input from the charm threshold. The feasibility of the method is verified using simulated data. Also studied is the performance of a binned analysis with charm input from the charm threshold, rather than mixing, as proposed in [8]. While both methods provide interesting constraints on γ and related parameters, it is found that a combined approach far outperforms each method individually. Applying this method to $B^- \to DK^-$, $D \to K\pi\pi\pi$, a substantially

better precision on γ and related parameters can be achieved than with previously considered methods for this decay mode, potentially making this one of the most precise individual measurements.

This chapter is organised as follows: Section 6.2 reviews the formalism for $B \to DK$ decays where the D subsequently decays to a multi-body final state. In Section 6.3 it is shown that, when the D decay's phase space is divided into multiple bins, it is possible to extract γ from a simultaneous analysis of $B \to DK$ and D-mixing without input from charm threshold data. Section 6.4 describes the CF and DCS $D \to K\pi\pi\pi$ amplitude models that are subsequently used in simulation studies. In Section 6.5 a method of dividing the five-dimensional phase space of $D \to K\pi\pi\pi$ into bins is discussed - this is done in a way that optimises the sensitivity to γ. In Section 6.6-Section 6.13 the results of a simulation study are presented for the decay mode $B^- \to DK^-$, $D \to K\pi\pi\pi$, using sample sizes corresponding to estimates of plausible current and future LHCb event yields. The precision on γ and related parameters is estimated for various data-taking scenarios and approaches, with and without input from the charm threshold. The key results of the simulation study are summarised in Section 6.14 (Table 6.2). The conclusions are presented in Section 6.15.

6.2 ADS phenomenology

The decay $B^- \to DK^-$, and related decays, provide a particularly clean way of measuring the CKM phase γ. The details of the analysis depend considerably on the final state f of the subsequent D decay, which must be accessible to both D^0 and $\overline{D}^0$ [9, 10, 23, 44–46]. The sensitivity to γ arises from the interference between the decay amplitudes for the intermediary states D^0K^- and $\overline{D}^0K^-$, which are expressed:

$$\begin{aligned} \mathcal{F}^+ &\equiv \langle \overline{D}^0 K^+ | \hat{H} | B^+ \rangle, \qquad \mathcal{S}^+ \equiv \langle D^0 K^+ | \hat{H} | B^+ \rangle, \\ \mathcal{F}^- &\equiv \langle D^0 K^- | \hat{H} | B^- \rangle, \qquad \mathcal{S}^- \equiv \langle \overline{D}^0 K^- | \hat{H} | B^- \rangle, \end{aligned} \tag{6.1}$$

where $\mathcal{F}$ denotes colour favoured amplitudes, while $\mathcal{S}$ denotes colour suppressed amplitudes. The Feynman diagrams for both amplitudes are pictured in Figure 6.1.

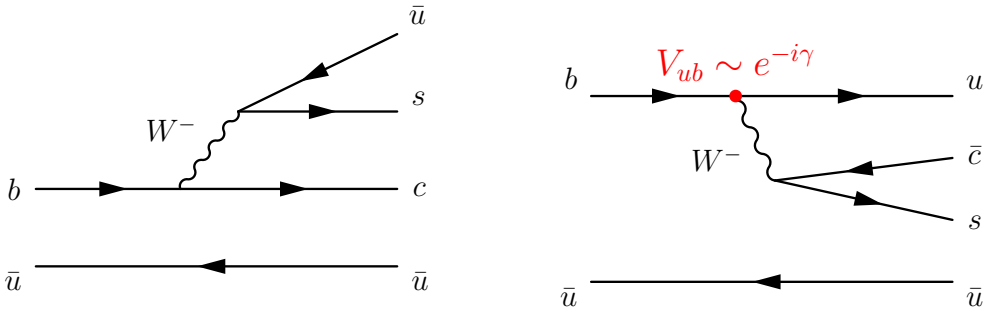

Figure 6.1: Feynman diagrams for (left) the colour favoured amplitude $B^- \to D^0 K^-$ (right) the colour suppressed amplitude $B^- \to \overline{D}^0 K^-$. Highlighted is the $u \to b$ transition which introduces a relative weak phase of -γ between the two amplitudes. In the CP conjugate amplitudes, this relative weak phase is reversed.

The ratios of the suppressed to favoured amplitudes are given by,

$$r_B e^{i(\delta_B - \gamma)} = \frac{\mathcal{S}^-}{\mathcal{F}^-}, \qquad r_B e^{i(\delta_B + \gamma)} = \frac{\mathcal{S}^+}{\mathcal{F}^+}, \tag{6.2}$$

where r_B is the magnitude of those ratios, while δ_B and $\mp\gamma$ are their strong and weak phase differences respectively.

Because r_B is small (~ 0.1 [80, 81]), the interference effects and thus the sensitivity to γ in $B^- \to DK^-, D \to f$, are enhanced if a final state is chosen such that $D^0 \to f$ is doubly Cabibbo suppressed, while $\overline{D}^0 \to f$ is Cabibbo favoured, at the cost of an overall low decay rate. Constraining γ using such decays is known as the 'ADS' method, named after the authors who introduced it (Atwood, Dunietz and Soni) [23]. The time and phase space-integrated decay rate for these suppressed $B^\mp$ decays is given by,

$$\Gamma\left(B^- \to DK^-, D \to f\right)_\Omega \simeq \mathcal{F}^2\mathcal{A}_\Omega^2 + \mathcal{S}^2\mathcal{B}_\Omega^2 + \mathcal{F}\mathcal{S}\mathcal{A}_\Omega\mathcal{B}_\Omega \left|\mathcal{Z}_\Omega^f\right| \cos(\delta_B - \delta_\Omega^f - \gamma) \tag{6.3}$$

$$\Gamma\left(B^+ \to DK^+, D \to \bar{f}\right)_{\bar{\Omega}} \simeq \mathcal{F}^2\mathcal{A}_\Omega^2 + \mathcal{S}^2\mathcal{B}_\Omega^2 + \mathcal{F}\mathcal{S}\mathcal{A}_\Omega\mathcal{B}_\Omega \left|\mathcal{Z}_\Omega^f\right| \cos(\delta_B - \delta_\Omega^f + \gamma) \tag{6.4}$$

Here the D decay amplitudes and interference parameters are those defined in Section 4.3. The corresponding favoured decay $B^- \to DK^-, D \to \bar{f}$ is completely dominated by the favoured decay amplitude with negligible interference effects and negligible sensitivity to γ, and has a much larger branching fraction. It therefore provides an ideal

normalisation or control mode. Its time and phase space-integrated rate is given by:

$$\Gamma(B^- \to DK^-, D \to \bar{f})_{\bar{\Omega}} \simeq \Gamma(B^+ \to DK^+, D \to f)_{\Omega} \simeq \mathcal{F}^2 \mathcal{B}^2_{\Omega} \tag{6.5}$$

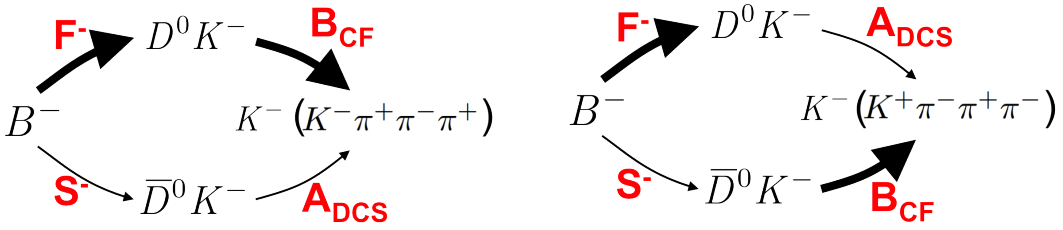

Figure 6.2: Diagram showing the two contributing amplitudes in (left) favoured $B^- \to DK^-, D \to K^-\pi^+\pi^-\pi^+$ decays (right) suppressed $B^- \to DK^-, D \to K^+\pi^-\pi^+\pi^-$ decays. The red labels indicate the contributing amplitudes that are defined in the text, and the weight of the corresponding arrow is proportional to its magnitude. The CF and DCS subscripts have been added to the D decay amplitudes for clarity.

Both favoured and suppressed decays are pictured in Figure 6.2, which illustrates the amplitudes contributing to each decay rate. The ratios of the favoured and suppressed rates are given by

$$\frac{\Gamma\left(B^- \to DK^-, D \to f\right)_{\Omega}}{\Gamma\left(B^- \to DK^-, D \to \bar{f}\right)_{\bar{\Omega}}} = r^2_{D,\Omega} + r^2_B + r_{D,\Omega} r_B \left|\mathcal{Z}^f_{\Omega}\right| \cos(\delta_B - \delta^f_{\Omega} - \gamma) \tag{6.6}$$

$$\frac{\Gamma\left(B^+ \to DK^+, D \to \bar{f}\right)_{\bar{\Omega}}}{\Gamma\left(B^+ \to DK^+, D \to f\right)_{\Omega}} = r^2_{D,\Omega} + r^2_B + r_{D,\Omega} r_B \left|\mathcal{Z}^f_{\Omega}\right| \cos(\delta_B - \delta^f_{\Omega} + \gamma). \tag{6.7}$$

These can also be expressed in terms of the Cartesian coordinates

$$x_{\pm} \equiv \mathcal{R}e\left(r_B e^{i(\delta_B \pm \gamma)}\right) \qquad y_{\pm} \equiv \mathcal{I}m\left(r_B e^{i(\delta_B \pm \gamma)}\right) \tag{6.8}$$

using the relations

$$r_B \left|\mathcal{Z}^f_{\Omega}\right| \cos(\delta_B - \delta^f_{\Omega} \pm \gamma) = x_{\pm} \mathcal{R}e \mathcal{Z}^f_{\Omega} + y_{\pm} \mathcal{I}m \mathcal{Z}^f_{\Omega} \quad \text{and} \qquad r^2_B = x^2_{\pm} + y^2_{\pm}. \tag{6.9}$$

Effects due to D-mixing have been ignored in the expressions for the $B^{\mp} \to DK^{\mp}$, $D \to f(\bar{f})$ decay rates, which is justified given the expected statistical precision. These effects can be included if required [82].

6.3 Parameter counting

6.3.1 Using ratios

Taking Γ_D, x, and y from external inputs, Equations 4.26, 6.6, 6.7 depend on three unknown parameters for each pair of *CP*-conjugate phase space bins (Ω, $\bar{\Omega}$): $r_{D,\Omega}$, $\mathcal{R}e\mathcal{Z}^f_\Omega$ and $\mathcal{I}m\mathcal{Z}^f_\Omega$; and three that are the same in all bins: γ, δ_B and r_B. The time-dependent fit to the tagged charm decay rates (Equation 4.26) provides two constraints on these parameters for each bin (the constant and the coefficient of the linear term). The $B \to DK$ decay rate ratios (Equations 6.6, 6.7) provide another two constraints. For N bin pairs, there are therefore $4N$ constraints and $3N+3$ unknown parameters. To extract all unknown parameters from the data therefore requires $4N \geq 3N+3 \Leftrightarrow N \geq 3$. If instead one wishes to measure $x_\pm, y_\pm$, then $N \geq 4$ is required.

6.3.2 Using rates

Taking again Γ_D, x, and y from external inputs, Equations 4.23, 4.24, 6.3, 6.4, 6.5 depend on four unknown parameters for each pair of *CP*-conjugate phase space bins: $\mathcal{A}^2_\Omega$, $\mathcal{B}^2_\Omega$, $\mathcal{R}e\mathcal{Z}^f_\Omega$, and $\mathcal{I}m\mathcal{Z}^f_\Omega$; and four that are the same in all bins: γ, δ_B, $r_B = \mathcal{S}/\mathcal{F}$, $\mathcal{F}^2$. Equations 4.23 - 4.24 provide three constraints for each bin, and Equations 6.3 - 6.5 another three. Hence, to extract all of these parameters, $6N \geq 4N + 4 \Leftrightarrow N \geq 2$ is required. A fit to extract $x_\pm, y_\pm$ requires $N \geq 3$.

6.4 Amplitude Model

Up to this point, the discussion has not been specific to any particular final state of the D decay. For the remainder of this chapter, a specific amplitude model is required to test the binning method (Section 6.5) and perform simulation studies (Section 6.6 onwards) - the case where the D meson decays to $K\pi\pi\pi$ has been chosen. The model chosen for the CF $\overline{D}^0 \to K^+\pi^-\pi^+\pi^-$ amplitude is based on that found by the MARK III experiment [83]. There is currently no model available for the DCS decay $D^0 \to K^+\pi^-\pi^+\pi^-$.

Any experiment in a position to use the method described here would have sufficient DCS decays to obtain such a model. For the purpose of this study, a series of plausible DCS models is created by randomly varying the magnitudes and phases of the amplitude components of MARK III's CF model. Amongst these a representative sample of 100 DCS models is chosen that give, together with the MARK III model for the CF decay, global complex coherence parameters $\mathcal{Z}^{K3\pi}$ distributed approximately according to the CLEO-c measurement [11]. Most studies are based on a default model, which is chosen based on its $\mathcal{Z}^{K3\pi}$ value of $0.26 + i0.24 = 0.36e^{i(42\pi/180)}$, which is consistent with the central value measured in [11].

6.5 Binning Multi-body phase space

The model-independent method for measuring γ described in Section 6.2 relies on dividing the $D^0 \to f$ phase space, which is five dimensional for $D^0 \to K\pi\pi\pi$, into several bins. In principle, any binning will work, for example the rectangular five dimensional binning used in [57]. However, to optimise the sensitivity of the approach, the ideas for a model-informed binning described in [54, 84] are followed. Because $\mathcal{Z}^f_\Omega$ is a factor in all γ-sensitive terms, the sensitivity to γ increases with larger values of $|\mathcal{Z}^f_\Omega|$ in each bin. A strategy that ensures large $|\mathcal{Z}^f_\Omega|$ is to split phase space into bins of similar phase difference $\delta^f_{\mathbf{p}}$. An amplitude model is used to assign a value of $\delta^f_{\mathbf{p}}$ to each event. The optimised binning is then achieved by splitting the one-dimensional $\delta^f_{\mathbf{p}}$ distribution into continuous intervals, as pictured in Figure 6.3, each of which constitutes one bin (which could in principle be discontinuous in 5-dimensional phase space). The size of the intervals is chosen so that there is a similar number of suppressed $B \to DK$ events in each bin. Figure 6.4 shows projections of the 5D phase space for events generated according to the default DCS model discussed in Section 6.4. The figure also indicates the fraction of events that fall into each phase space bin - one can see that the relative fraction of events falling into each phase space bins changes significantly when moving across a resonance.

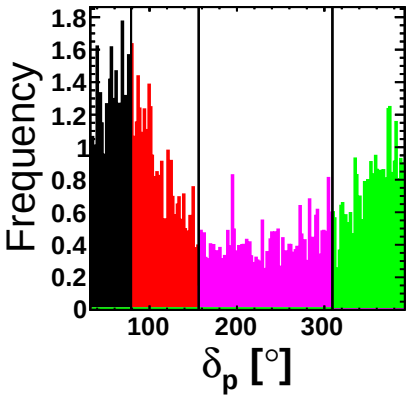

Figure 6.3: Events generated according to the default DCS model are plotted against strong phase difference $\delta_{\mathbf{p}}$. The distribution is split into four intervals, indicated by the colour coding, to give approximately the same number of events in each.

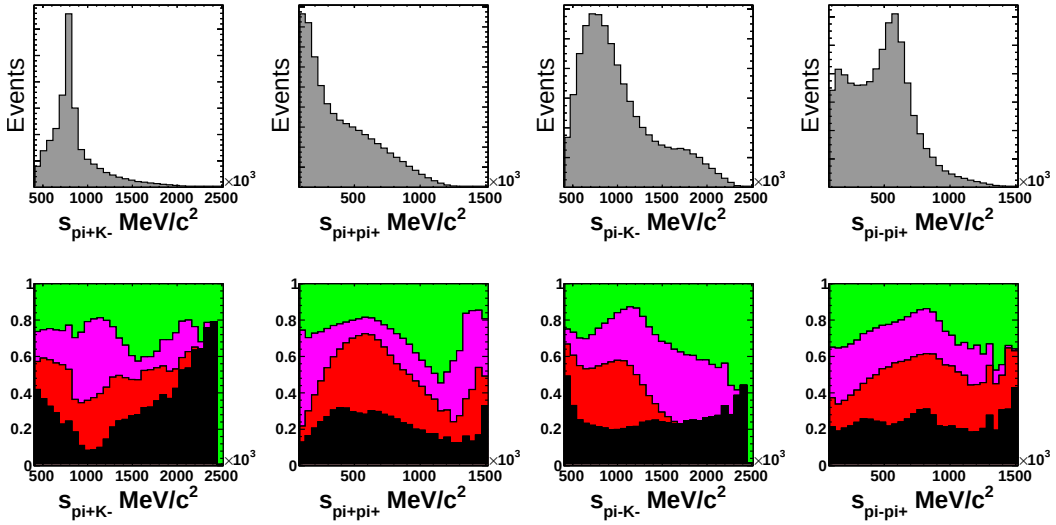

Figure 6.4: In all figures, events are generated according to the DCS model. The top row of figures shows the squared invariant mass of all 2-daughter combinations, where $s_{ij} = m^2_{ij}$. The bottom row shows the fraction of events that fall into each of the phase space bins, as defined in Figure 6.5

An incorrect model would result in a sub-optimal binning, leading to smaller, but still model-independently measured, $|\mathcal{Z}^f_\Omega|$ in each bin. While this would reduce the sensitivity, which would be evident from the statistical uncertainty estimated from the fit, it would not introduce a model-dependent bias.

Figure 6.5 shows the binned $\mathcal{Z}^{K3\pi}_\Omega$ obtained from the default model, in the centre for

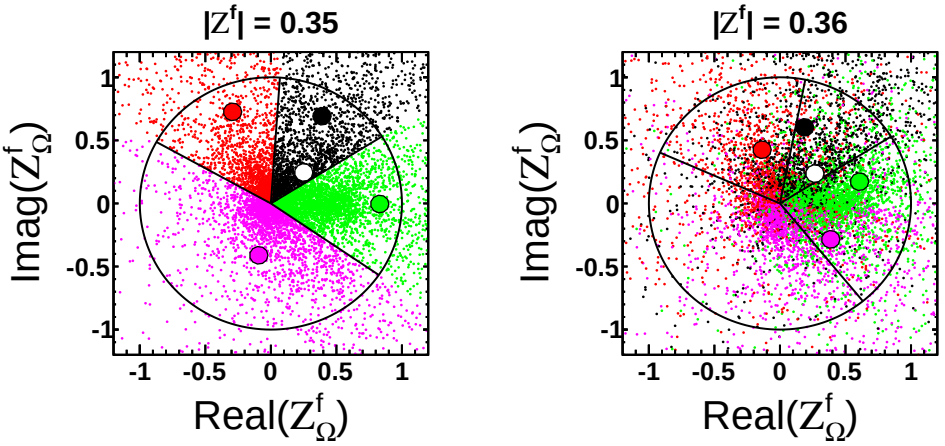

Figure 6.5: Simulated events (small dots), complex coherence parameters $\mathcal{Z}_\Omega^{K3\pi}$ (colour-filled circles) for each bin, and the global coherence parameters $\mathcal{Z}^{K3\pi}$ (white-filled circle), represented in the $\mathcal{R}e\mathcal{Z}^{K3\pi} - \mathcal{I}m\mathcal{Z}^{K3\pi}$ plane, with bin assignments based on (left) perfect knowledge of the amplitude model (right) imperfect knowledge of the amplitude model.

a binning based on a perfect model and on the right for a binning based on an imperfect model. The perfect model is identical to the one used for the event generation. The imperfect model is obtained from the perfect one by multiplying each amplitude component's magnitude by a random factor between 0.8 and 1.2 (corresponding to a fit fraction variation of 0.64-1.44), and by adding to each component a random phase between -0.3 and $+0.3$ radians. Figure 6.5 shows simulated events represented in the $\mathcal{R}e\mathcal{Z}^{K3\pi} - \mathcal{I}m\mathcal{Z}^{K3\pi}$ plane. The events are generated according to the phase space density of states. The position of the small dots represents the true value of $\frac{1}{\mathcal{A}_\Omega\mathcal{B}_\Omega}\langle f_\mathbf{p}|\hat{H}|D^0\rangle\langle f_\mathbf{p}|\hat{H}|\overline{D}^0\rangle^*$, while the colour-coding represents the bin they have been assigned to. For the left plot, this assignment is done with the perfect model, for the right hand plot with an imperfect model. The circular 'pie chart' represents the bins in $\delta_\mathbf{p}^f$ based on the model used for the binning. The $\mathcal{Z}_\Omega^{K3\pi}$ values extracted are the average over the true values of $\frac{1}{\mathcal{A}_\Omega\mathcal{B}_\Omega}\langle f_\mathbf{p}|\hat{H}|D^0\rangle\langle f_\mathbf{p}|\hat{H}|\overline{D}^0\rangle^*$ for the events in the bin they have been assigned to (which includes events beyond the plot boundaries). The model-independent method proposed above does of course not require the knowledge of $\frac{1}{\mathcal{A}_\Omega\mathcal{B}_\Omega}\langle f_\mathbf{p}|\hat{H}|D^0\rangle\langle f_\mathbf{p}|\hat{H}|\overline{D}^0\rangle^*$ to measure $\mathcal{Z}_\Omega^{K3\pi}$, this information is only used for this illustration. The $\mathcal{Z}_\Omega^{K3\pi}$ values are shown as colour-filled circles. The global complex coherence parameter $\mathcal{Z}^{K3\pi}$ is shown as a white-filled circle. While the imperfect model leads to smaller $|\mathcal{Z}_\Omega^{K3\pi}|$, they are still on average larger than the global $|\mathcal{Z}^{K3\pi}|$. In

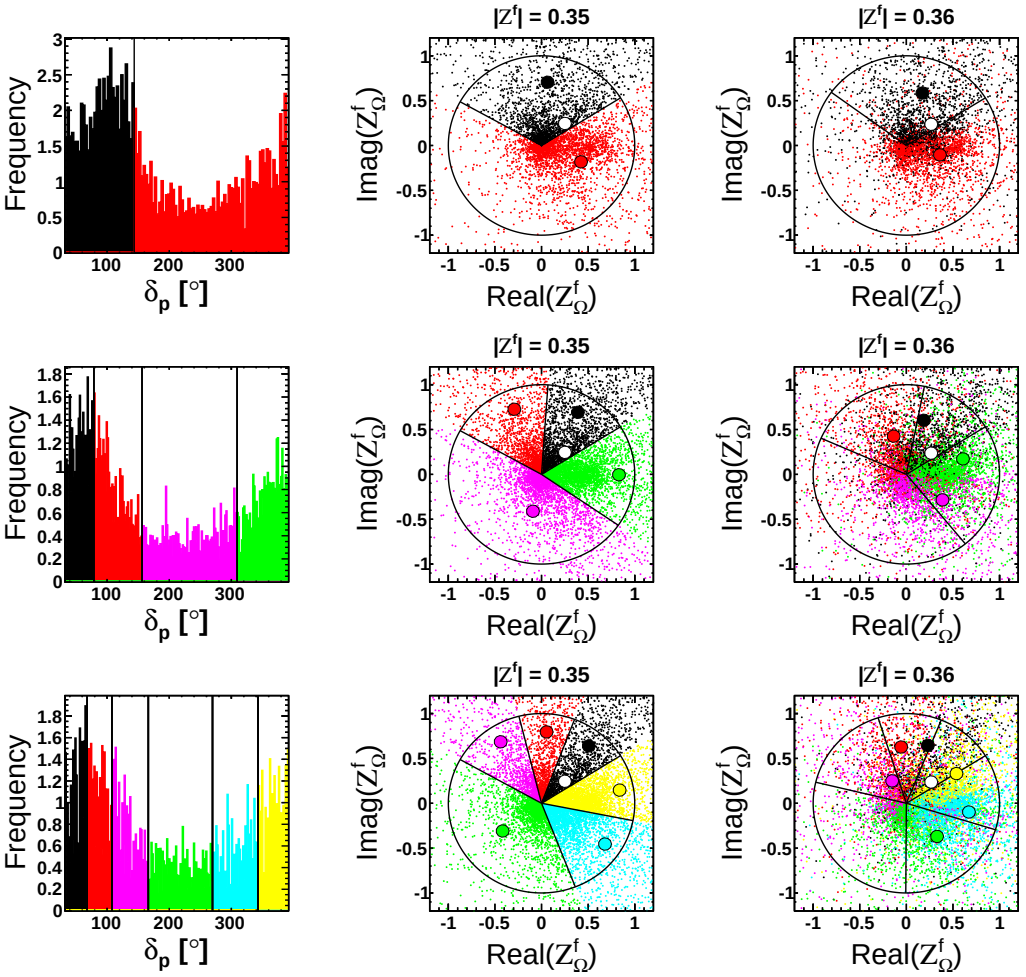

Figure 6.6: These plots illustrate the distribution of $\mathcal{Z}_\Omega^{K3\pi}$ using different numbers of phase space bins. The binning is based on a perfect model (centre column) and an imperfect amplitude model (right column). More detailed descriptions of the figures can be found in Figures 6.3 and 6.5.

Figure 6.6 this process has been repeated for 2, 4, and 6 bins, to demonstrate that the $|\mathcal{Z}_\Omega^{K3\pi}|$ increase as the phase space is further divided.

To quantify this observation, the study is repeated with the full set of 100 representative models (discussed in Section 6.4) and different numbers of bins. The results are summarised in Figure 6.7 which shows the average $|\mathcal{Z}_\Omega^{K3\pi}|$ as a function of the number of bins for the case where the binning is based on a perfect model, and for the case where the model used for binning is randomised as described above. The study shows that even a rather 'bad' model provides typical binned coherence factors that are substantially larger than the global coherence factor.

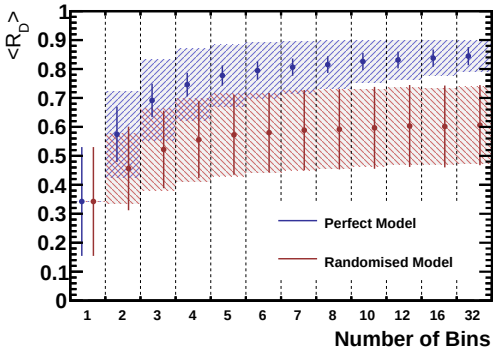

Figure 6.7: The average coherence factor with different number of bins in strong phase difference, for the set of 100 representative models, with perfect binning (blue, on top) and imperfect binning described in the text (red, lower). The error bars represent the standard deviation of the mean $\mathcal{Z}_\Omega^{K3\pi}$ of each model, i.e. they represent the 'between model scatter'. The shaded areas represent the average of the standard deviation of $\mathcal{Z}_\Omega^{K3\pi}$ within the models (i.e. the 'within model scatter').

6.6 Simulated data samples

In order to demonstrate the validity of the method, and to evaluate its sensitivity, fits are performed to simulated data.

The data are generated according to the CF amplitude model based on the MARK III analysis of $D^0 \to K^-\pi^+\pi^-\pi^+$ [83] . The DCS amplitude describing $D^0 \to K^+\pi^-\pi^+\pi^-$ was choosen from the large number of models generated (see Section 6.4). The one selected best reproduces the measured value of $\mathcal{Z}^{K3\pi}$ [11] when combined with the CF model. Other DCS models are also considered to evaluate the stability of the results.

	$B^\pm \to D(K3\pi)K^\pm$		$D^{*\pm} \to$
	suppressed	favoured	$D(K3\pi)\pi^\pm$
LHCb run I ($3\,\text{fb}^{-1}$ @ $7-8\,\text{TeV}$)	120	10k	8M
LHCb run II ($8\,\text{fb}^{-1}$ @ $13\,\text{TeV}$)	800	60k	50M
LHCb upgrade ($50\,\text{fb}^{-1}$ @ $13\,\text{TeV}$)	9000	700k	600M

Table 6.1: Event yields assumed in the simulation studies, based on reported event yields for $1\,\text{fb}^{-1}$ at LHCb [57, 85]. The event yields are inclusive, for example, LHCb run II yields includes those from LHCb run I. The fraction of WS events in $D^{*\pm} \to D(K3\pi)\pi^\pm$ depends on the input variables; typically it is 0.38%.

Three scenarios are studied with different event yields, based on plausible extrapolations of the yields reported for $1\,\text{fb}^{-1}$ at LHCb [57, 85]: 'LHCb run I', where event yields are extrapolated to LHCb's already recorded $3\,\text{fb}^{-1}$; 'LHCb run II', plausible event yields

at the end of the next LHC data-taking period with approximately twice the collision energy; and 'LHCb upgrade', estimated event yields for the LHCb upgrade. The increase in the heavy flavour cross section at higher collision energies is considered, as well as the expected improvement in trigger efficiency at the LHCb upgrade [86]. The sample sizes used in the simulation studies are given in Table 6.1. These extrapolations of course have large uncertainties.

Also taken into account is the time-dependent detection efficiency that is typical for hadronic heavy flavour decays at LHCb, where the trigger is based on detecting displaced vertices, disfavouring small decay times. The same efficiency function is used as in Section 4.4 as shown in Figure 4.8. All other detector effects and backgrounds are ignored. Given the clean data samples at LHCb even for the suppressed $B^{\mp} \to D(K3\pi)K^{\mp}$ modes [85], this is a reasonable simplification for the purpose of these feasibility studies. Simulated data are generated with the following parameter values: $\gamma = 69.7°$ $\delta_B = 112.0°$, $r_B = 0.0919$, and $r_D^2 = \frac{1}{300}$.

6.7 Fit method and parametrisation

The default approach is to perform a simultaneous χ^2 fit to the decay rates Equations 4.23, 4.24, 6.3, 6.4 and 6.5 in terms of the fit parameters $r_{D,\Omega}$, $\mathcal{R}e\mathcal{Z}_{\Omega}^{f}$, $\mathcal{I}m\mathcal{Z}_{\Omega}^{f}$, $\mathcal{B}_{\Omega}$, $\mathcal{F}$, γ, δ_B and r_B. As a cross check, binned likelihood fits are also performed where it was found that they lead to equivalent results, but take longer to converge.

As long as all phase space bins are well populated, it was seen that the fit results are not crucially dependent on the number of bins. In the default scenario the phase space is divided into 4 bins for Run I, 6 bins for Run II and 8 bins for the upgrade scenario.

As in Section 4.4, the charm mixing parameters x and y are allowed to vary in the fit, but their values are constrained with a two-dimensional Gaussian constraint to their world-average using, for the LHCb Run I scenario [71]:

$$x = 0.526 \pm 0.161\% \qquad y = 0.668 \pm 0.088\% \qquad \rho_{xy} = 0.188, \tag{6.10}$$

where ρ_{xy} is the correlation coefficient between x and y. It is expected that substantial improvements will be made on this measurement from LHCb, its upgrade, and BELLEII in the future. Lacking detailed forecasts, for the purpose of this study, it is assumed that the uncertainties on x and y scale with the inverse square-root of LHCb event yields of the relevant data-taking scenario, while the correlation coefficient remains constant. The well-measured average D lifetime is fixed to $\tau_D = 1/\Gamma_D = 410.1\,\text{fs}$ [13].

While the default approach is to fit the decay rates, in an experimental measurement it may be favourable to fit the decay rate ratios given in Equations 4.26, 6.6 and 6.7. In this case one loses sensitivity to the parameters $\mathcal{B}_\Omega$ and $\mathcal{F}$. Using both fit methods on the same simulated dataset, it was found that both approaches give the same results on the parameters they share. In Section 6.12 it is demonstrated how fitting the rates, as opposed to the ratios, allows additional constraints to be added to the fit.

6.8 Algorithms

In order to cope with the various local χ^2 minima that are present in addition to the four global minima, a two-stage fitting process is used. The first step is a fit with the GENEVA [87] package which is specifically designed to deal with multiple minima. GENEVA's parameter estimates are then used as starting values for MINUIT [88] which performs a second fit to refine these estimates. To further reduce the risk of converging on false minima, the fit procedure is repeated 75 times with many randomly chosen starting values for all fit parameters. Finally, the fit result that gives the smallest χ^2 is chosen as the central value. In order to avoid unphysical values of $\mathcal{Z}_\Omega^f$, which can also lead to further secondary minima, a term is added for each volume Ω that increases the χ^2 if $\mathcal{Z}_\Omega^f$ leaves the physical region:

$$\chi^2_{\text{constr }\mathcal{Z}_\Omega^f} = \left\{ \begin{array}{cc} \Big((|\mathcal{Z}_\Omega^f| - 1)/0.5\Big)^2 & \text{if } |\mathcal{Z}_\Omega^f| > 1 \\ 0 & \text{else} \end{array} \right\} \tag{6.11}$$

Figure 6.8 shows a simulated dataset for the LHCb Run II scenario with the fit result superimposed. In this example, the dataset was split into four phase space bins, and the fit was performed to the rates, rather than the ratios.

6.9 Coverage Test

When creating the confidence level scans in Section 6.10 it is assumed that the probability that the true value of the fit parameter is amongst those values with $\sigma < \sqrt{\Delta\chi^2}$ relative to the best parameter estimate is given by

$$\mathrm{CL} = \frac{1}{\sqrt{2\pi}} \int_{-\sigma}^{+\sigma} e^{-\frac{1}{2}y^2} dy = 1 - p \tag{6.12}$$

which also defines the p-value, $p = 1 - \mathrm{CL}$, used in Figure 6.10. The validity of this assumption is tested using a large number of simulated experiments. For each experiment and each fit parameter, $\Delta\chi^2$ is evaluated as the difference in χ^2 between the value obtained at the minimum, and the χ^2 obtained when repeating the fit, but fixing the relevant parameter to its true value. Figure 6.9 shows the difference between the fraction of experiments where with $\sigma < \sqrt{\Delta\chi^2}$ to the number expected from Equation 6.12. If this cumulative distribution from the simulated experiments lies above the expectation, the method of estimating CL's over-covers, if it lies below, it under-covers. Generally good behaviour was found for all fit parameters; importantly, for the main parameters of interest, r_B, δ_B and γ, shown in Figure 6.9, the scans show close to exact coverage. While the results shown in Figure 6.9 are for one single amplitude model and data-taking scenario, this general behaviour is also observed in other amplitude models studied and is consistent across event yields. Amongst the large number of amplitude models considered, there were however some where significant deviations from exact coverage was found (mostly over-coverage), suggesting that these studies ought to be repeated once an amplitude model has been obtained from data. In the meantime, these results are taken as confirmation that the method of estimating confidence regions is adequate for most potential amplitude models.

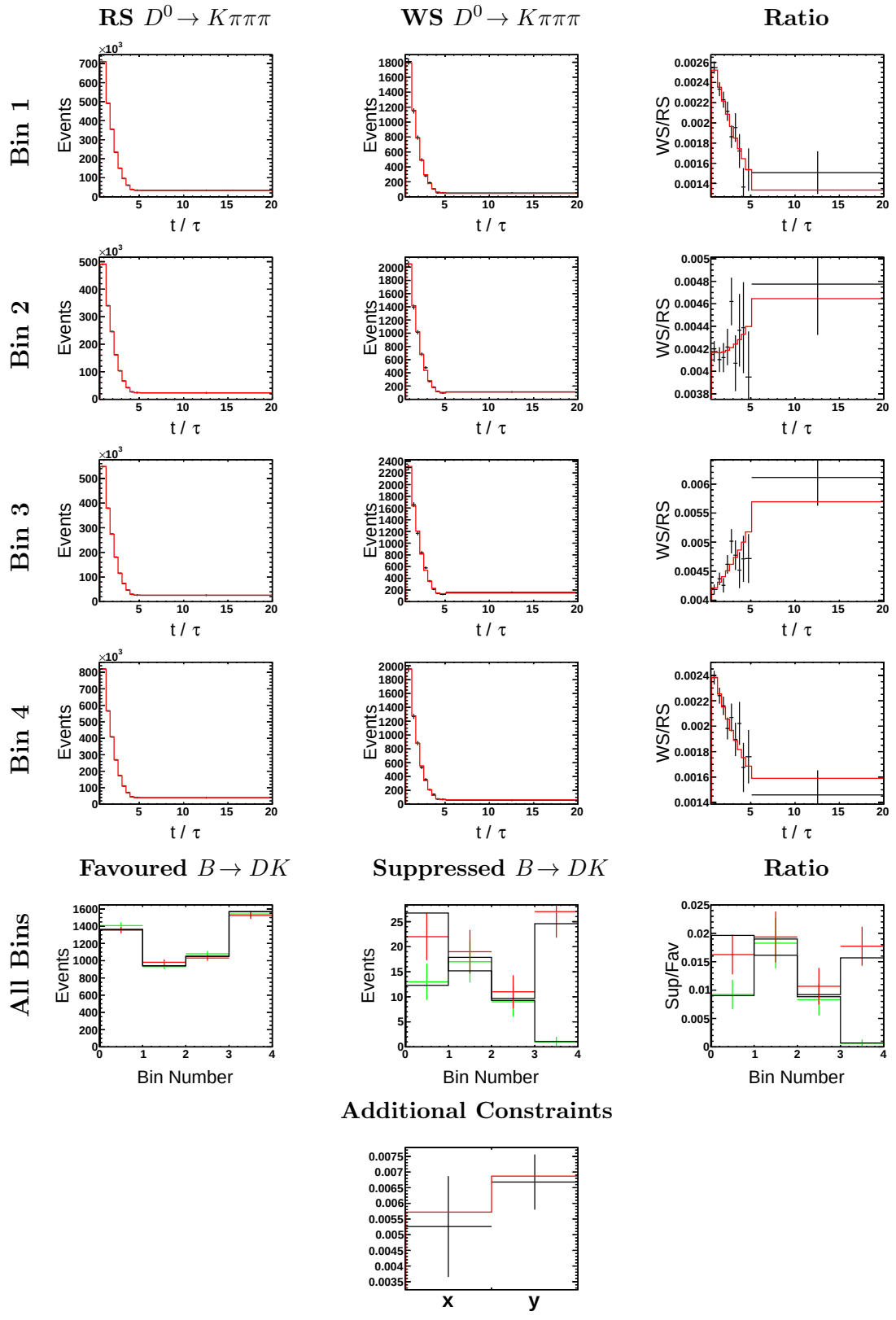

Figure 6.8: Simulated data generated with expected LHCb Run II statistics and divided into four phase space bins. The top four rows show the simulated $D^0 \to K\pi\pi\pi$ data (black markers), the fifth row shows the simulated $B \to DK$ data ($B^+ \to DK^+$ green markers, $B^- \to DK^-$ red markers), and the final row shows the external constraints for the mixing parameters x and y (black markers). The simulated data are shown in both 'rate' and 'ratio' form. For all figures in this paper the 'rate' plots are used to perform the fit, although fits to the 'ratios' gave consistent results. In all figures the fit results are superimposed.

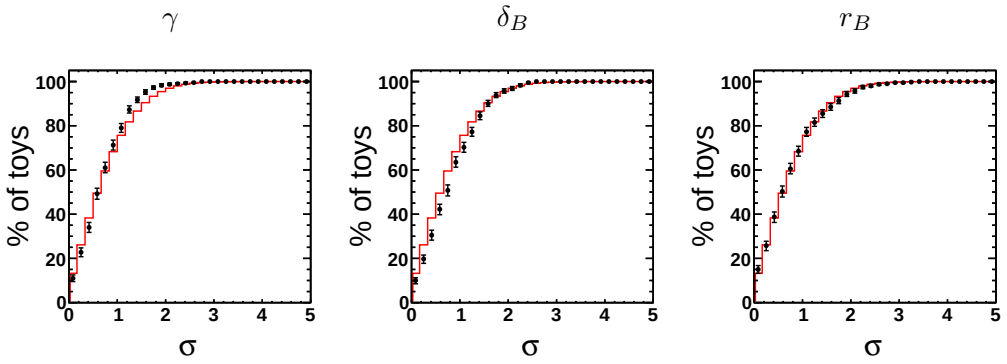

Figure 6.9: Coverage tests for γ, δ and r_B (Run II statistics, 8 phase space bins, default model). The red line represents the number of fits expected with $\sqrt{\Delta\chi^2} < \sigma$ (defined in the text), the black crosses with error bars represent the number found. Because this is a cumulative distribution, the uncertainties between the bins are highly correlated.

6.10 Confidence regions in γ, δ_B, r_B and $x_\pm$, $y_\pm$

Confidence regions are constructed in the parameters of interest based on the χ^2 difference, $\Delta\chi^2$, of the fit where the relevant parameters are fixed to the values to be probed, relative to the χ^2 of the best fit result when all parameters float.

Figure 6.10 shows 2-dimensional scans in terms of $1, 2, 3\sigma$ confidence regions for δ_B vs γ, r_B vs γ, and $y_\pm$ vs $x_\pm$ for each of the three data-taking scenarios. The results show that the precision on x_-, y_- (or $\delta - \gamma$) is much better than that on x_+, y_+ (or $\delta + \gamma$). This behaviour was observed in many of the D amplitude models studied (see Figure 6.12), and it appears to depend predominantly on the values for δ_B, and γ. One striking feature of the scans is the four fold ambiguity in δ_B, and γ - this is understood, and explained in Appendix B. In Section 6.12 it is shown that this can be reduced to a 2-fold ambiguity using external constraints.

6.10.1 Using the wrong model

To study the impact of an imperfect binning, the sensitivity study is repeated using the imperfect binning discussed in Section 6.5, and applied to the default Run II scenario. Comparing the results, shown in Figure 6.11, to those in Figure 6.10 shows that the imperfect binning results in a visible reduction in sensitivity especially at the 3σ level,

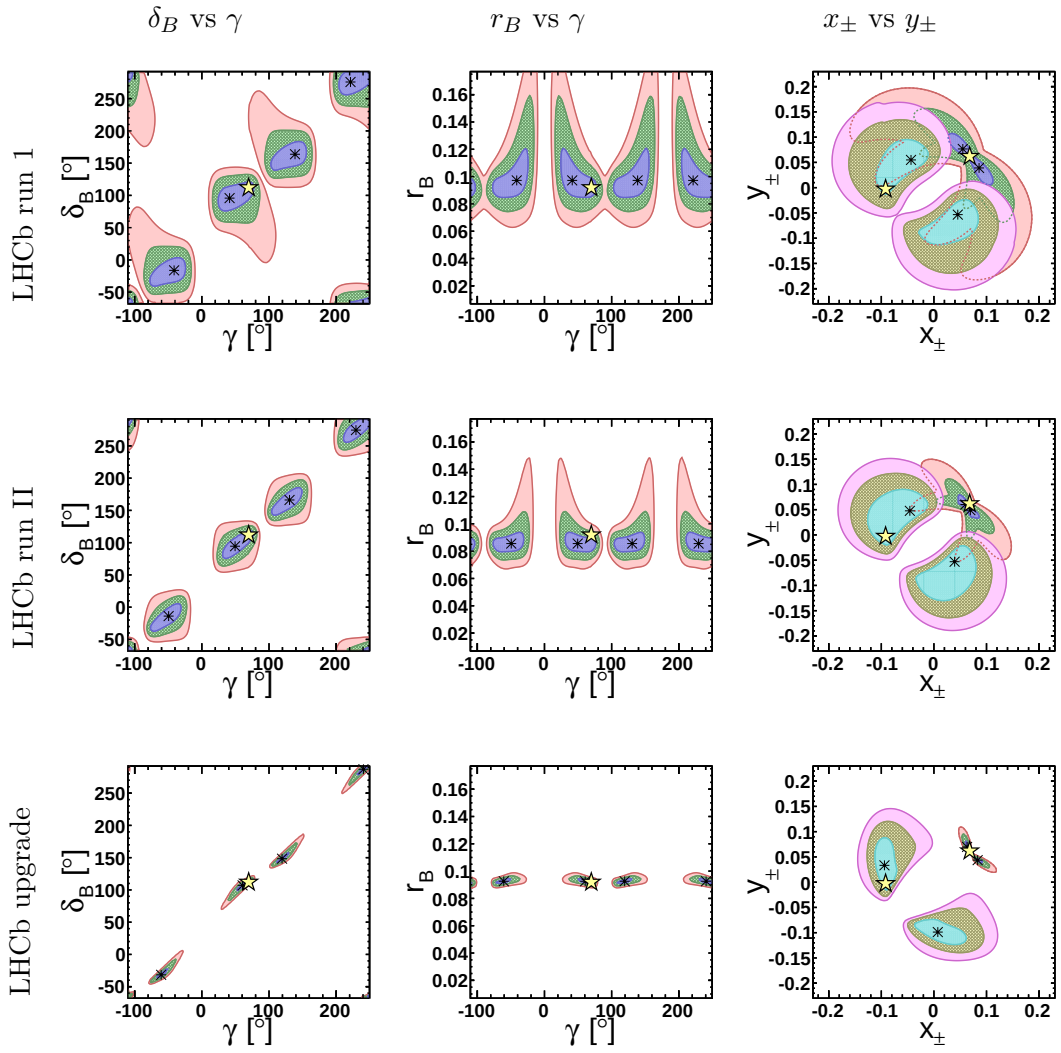

Figure 6.10: Confidence-level scans for γ, δ and r_B in the first two columns, and $x_\pm, y_\pm$ in the third column, for simulated events according to the different scenarios given in Table 6.1. The 2D plots show $\sqrt{\Delta\chi^2} = 1, 2, 3$ contours. The yellow star indicates the input value, the black stars the (multiple) χ^2 minima. When secondary local minima are present, as in Figure 6.11, their positions are indicated with black crosses. The plots in the last column show contours for x_+, y_+ (with minima in the second and fourth quadrant) and x_-, y_- (with two minima in the first quadrant).

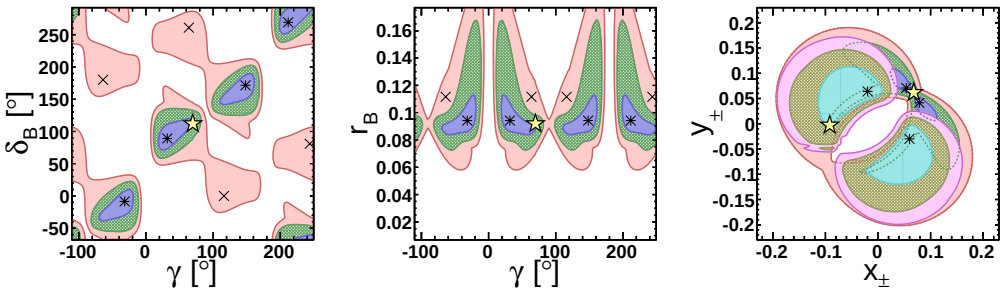

Figure 6.11: CL scans for simulated data generated with the default model, but binned based on the randomised model described in Section 6.5 (same format as in Figure 6.10).

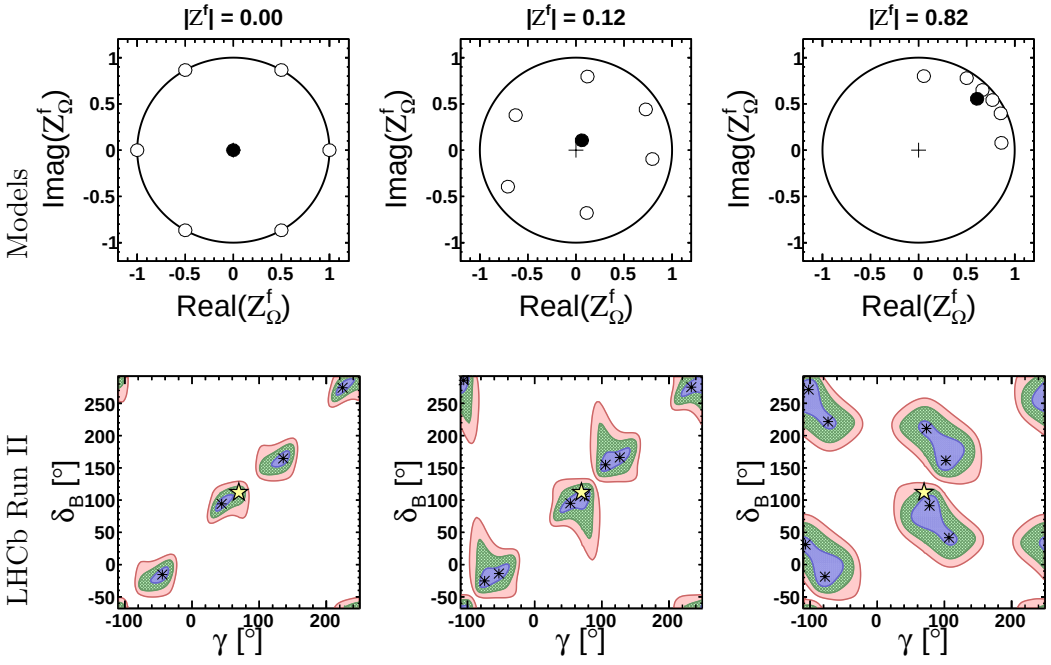

Figure 6.12: CL scans for three alternative models, for the LHCb Run II data taking scenario. The top row shows the $\mathcal{Z}_\Omega^{K3\pi}$ values and the central value of $\mathcal{Z}^{K3\pi}$ for each model. The second row shows the CL scans in the $\gamma - \delta_B$ plane, for the LHCb Run II scenario.

but it does not lead to a catastrophic deterioration of the fit, which retains a similar precision at the 1σ level.

6.11 Studies with other models

To study the dependence of the results on the particular amplitude model for the DCS $D^0 \to K^+\pi^-\pi^+\pi^-$ decay, the studies are repeated with a variety of amplitude models. CL scans in the γ-δ_B plane for three examples, for the LHCb Run II data-taking scenario, are shown in Figure 6.12.

The first column shows an artificial 'ideal' model, set up to have bins with evenly distributed δ_Ω^f, and $|\mathcal{Z}_\Omega^f| = 1$, $\mathcal{B}_\Omega = 1$, $\mathcal{A}_\Omega = r_D$ for all Ω; this also implies $|\mathcal{Z}^f| = 0$. The second and third column show models taken from the set of randomly generated models; one where $|\mathcal{Z}^{K3\pi}|$ is smaller than CLEO-c's central value, and another where it is larger. The results illustrate a general tendency observed, which is that the fit results improve

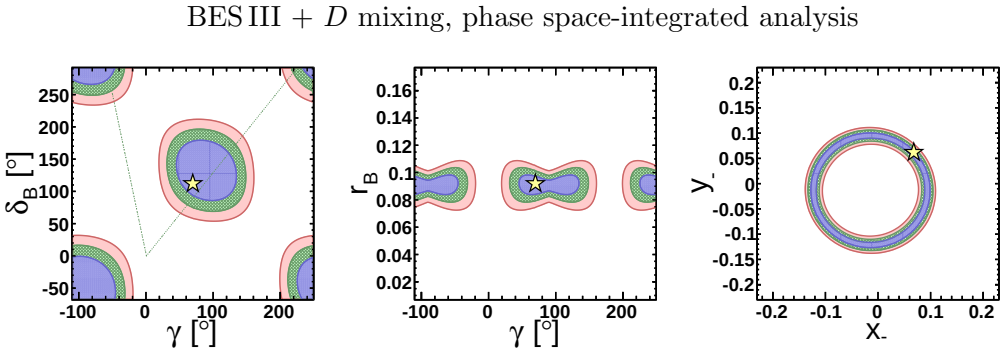

Figure 6.13: Constraints on r_B, δ_B, γ, x_-, y_- obtained using the phase space-integrated approach proposed in [8], with additional constraints from mixing as proposed in Section 4.4. In contrast to all other results shown in this chapter, neither D-mixing nor $B \to DK$ data are separated into multiple phase space bins. The study uses global constraints on $\mathcal{Z}^{K3\pi}$ extrapolated to BES III statistics [11], and the LHCb Run II data scenario.

for models with a fairly even spread of $\delta_{\mathbf{p}}^f$, while clustering of $\delta_{\mathbf{p}}^f$, a feature typical for models with large $|\mathcal{Z}^{K3\pi}|$, leads to reduced sensitivity.

6.12 Additional input from the charm threshold

Two ways of incorporating additional information from the charm threshold are considered. One is to incorporate constraints on the global coherence factor $\mathcal{Z}^f$. Such constraints are already available for $D^0 \to K\pi\pi\pi$ and a few other decay modes, based on CLEO-c data [11, 48, 52], and could significantly improve with input from BES III, who have collected 3.5 times as much integrated luminosity at the charm threshold. These constraints can be added either to a phase space-integrated analysis of D-mixing and $B \to DK$ as proposed in Section 4.4 or to the binned analysis introduced here. Alternatively, charm threshold data can be analysed in the same phase space bins as $B \to DK$ and charm mixing. This, as shown below, will add additional information that substantially improves the measurement. Below each method is discussed in turn.

6.12.1 Phase space-integrated analysis with input from the charm threshold

In contrast to all other results presented in this chapter, for this analysis, neither the charm mixing data, nor the $B \to DK$ data are divided into multiple phase space bins. Constraints on $\mathcal{Z}^{K3\pi}$ obtained from charm threshold data are incorporated following [8], and the fits are performed to simulated data with and without input from a phase space-integrated D-mixing analysis as proposed in [1]. With this approach there is not enough information to measure $x_\pm$ and $y_\pm$, or r_B, δ_B and γ. Figure 6.13 shows confidence regions obtained for such a phase space-integrated analysis based on the LHCb Run II scenario, with input from the charm threshold extrapolated to BES III statistics [11], including input from charm mixing. While no point-values can be obtained, 68% confidence regions can still be interpreted in terms of uncertainties on γ, δ_B and r_B, as described in Section 6.13. Averaging over 10 simulated experiments, $\sigma(\gamma) = 56^\circ$ (64°), $\sigma(\delta_B) = 53^\circ$ (66°) and $\sigma(r_B) = 0.92 \cdot 10^{-2}$ ($4.1 \cdot 10^{-2}$) with (without) input from D-mixing. While the constraints on γ and δ_B are rather weak, the precision on r_B is excellent. As [11] have shown, input from such an analysis would play an important role in a global fit to measure γ.

6.12.2 Global constraints from the charm threshold, with a binned $B \to DK$ and D-mixing analysis

Performing the fit on the absolute decay rates (see Sections 6.3.2 and 6.7) rather than the fractions, it is possible to incorporate constraints on the total coherence factor $\mathcal{Z}^f$ from the charm threshold while still performing the binned analysis of $B \to DK$ and charm mixing data as described above, using the relation

$$\sum_{\text{all } \Omega_\text{i}} \mathcal{A}_{\Omega_i} \mathcal{B}_{\Omega_i} \mathcal{Z}^f_{\Omega_i} = \mathcal{A}\mathcal{B}\mathcal{Z}^f. \tag{6.13}$$

In the above expressions, $\mathcal{A}, \mathcal{B}, \mathcal{Z}^f$ are the equivalent quantities to $\mathcal{A}_{\Omega_i}, \mathcal{B}_{\Omega_i}, \mathcal{Z}^f_{\Omega_i}$ for a volume that encompasses the entire phase space. Figure 6.14 illustrates the significant

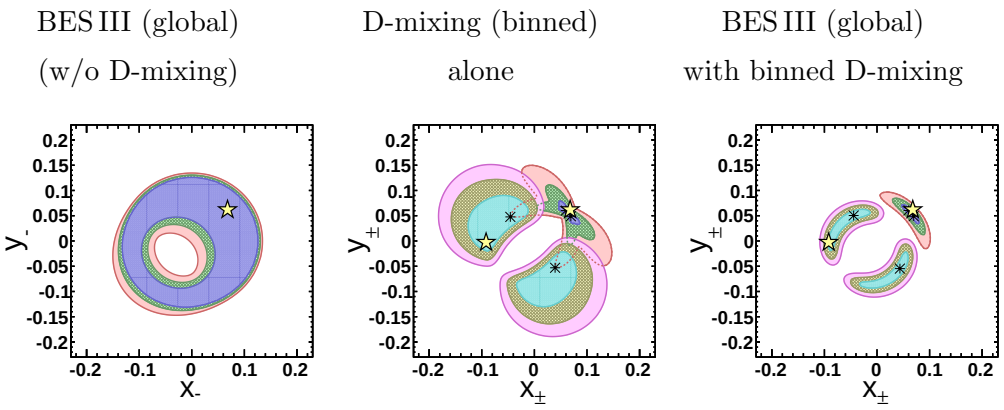

Figure 6.14: Constraints on $x_\pm$ and $y_\pm$, obtained by combining simulated $B \to DK$ data (LHCb Run II statistics) with different constraints from charm. Left: future (BES III) charm threshold constraints on $\mathcal{Z}^{K3\pi}$ (only the effect on x_-, y_- is shown, results for x_+, y_+ are similar). Centre: D-mixing constraints. Right: Both. (Same format as in Figure 6.10.)

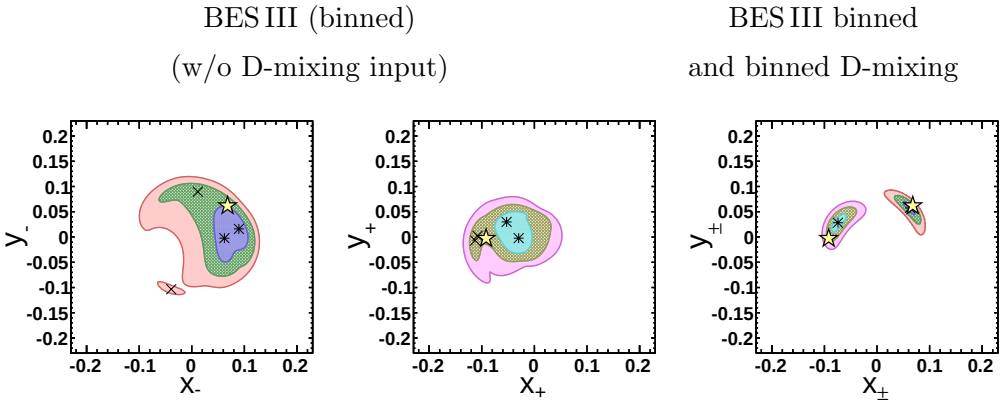

Figure 6.15: Constraints on $x_\pm$ and $y_\pm$, obtained by combining simulated $B \to DK$ data (LHCb Run II statistics) with different constraints from charm. Left: future (BES III) charm threshold constraints on binned $\mathcal{Z}_\Omega^{K3\pi}$. Right: that, combined with D-mixing. (Same format as in Figure 6.10.)

benefit of such additional constraints, numerical results can be found in Table 6.2. The predicted BES III uncertainties on $\mathcal{Z}^{K3\pi}$ are taken from [11].

6.12.3 Binned constraints from the charm threshold

This section presents a comparison of the performance of a binned analysis relying on charm threshold data for the charm interference parameter, as proposed in [8], with the novel method proposed in this section, and with a combined approach using binned threshold and charm mixing data. The charm threshold data are analysed in the same

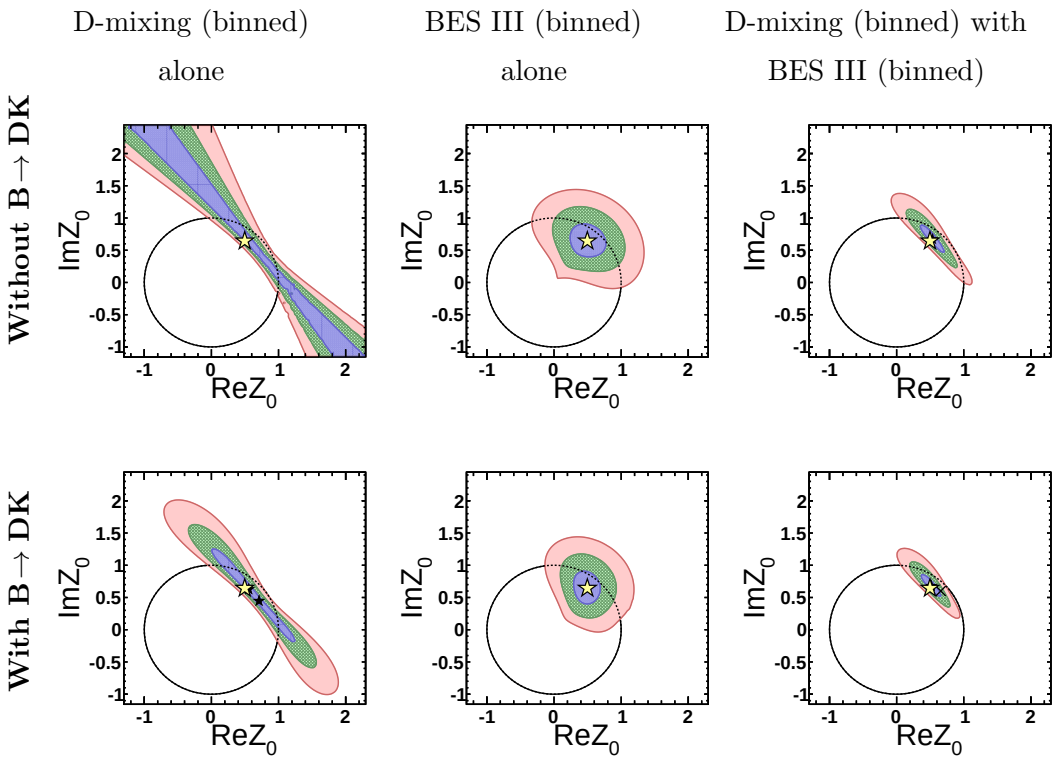

Figure 6.16: Constraints on $\mathcal{R}e\mathcal{Z}_0^f$ and $\mathcal{I}m\mathcal{Z}_0^f$ ($\mathcal{R}e\mathcal{Z}_\Omega^f$ and $\mathcal{I}m\mathcal{Z}_\Omega^f$ in the 0^{th} bin of phase space) for different charm inputs for estimated LHCb Run II statistics. The bottom row includes constraints from $B \to DK$ decays.

phase space bins as $B \to DK$ and charm mixing. This provides a constraint from threshold data on each individual $\mathcal{Z}_\Omega^{K3\pi}$, rather than only their weighted sum as in Section 6.12.2. To estimate the uncertainties on $\mathcal{Z}_\Omega^{K3\pi}$ from such an analysis, the results on $\mathcal{Z}^{K3\pi}$ from [11] are used, along with the assumption that uncertainties scale with the inverse square-root of the number of signal events used for the measurement. Given the fairly large uncertainty on $\mathcal{Z}^{K3\pi}$ from CLEO-c data, it is assumed that these data can be divided into at most three bins while still providing meaningful constraints on $\mathcal{Z}_\Omega^{K3\pi}$ in each bin. With BES III statistics, it is expected to be possible to match the binning schemes defined in Section 6.7, with up to eight bins. Figure 6.15 and Figure 6.16 illustrate in the $x_\pm - y_\pm$ and $\mathcal{R}e\mathcal{Z}_0^f$-$\mathcal{I}m\mathcal{Z}_0^f$ planes respectively, the dramatic effect that the combination of mixing constraints and binned $\mathcal{Z}_\Omega^{K3\pi}$ constraints from a future analysis of BES III threshold data could have. Not only are the uncertainties on $x_\pm, y_\pm$ much reduced compared to either constraint being applied individually (see Table 6.2 for numerical results), but the BES III input also removes the previously existing ambiguities in $x_\pm$ and $y_\pm$. Figure 6.17, described below, confirms this observation for 1-dimensional

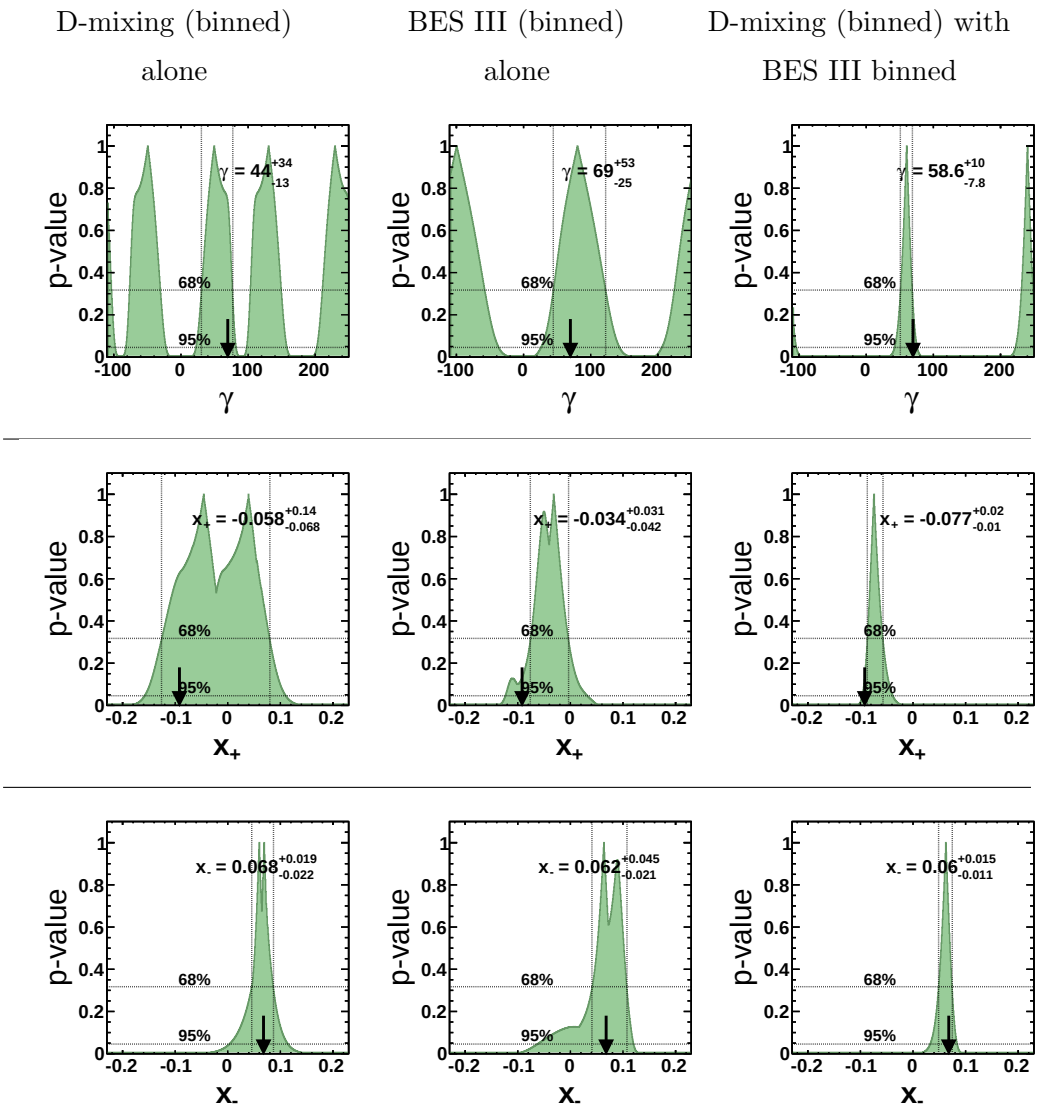

Figure 6.17: The p-value (see Equation 6.12) versus γ, x_+, and x_- for different charm inputs for estimated LHCb Run II statistics. The arrow indicates the input value with which the experiment was simulated. The numbers inside the scans represent the best fit value $\pm 1\sigma$, as described in the text.

parameter scans of $x_\pm$ and γ.

6.13 1-D scans and quantified uncertainties

One-dimensional p-value (see Equation 6.12) scans are performed for the parameters of interest. To translate a scan into a numerical result for the uncertainty σ on a given parameter, the peak which is nearest the input value (with which the data were generated) is chosen, and σ is taken to be half its width at $1 - p = 68\%$. Multiple

solutions are ignored unless two solutions merge at the 68% CL level, in which case the width of the merged double-peak is used to calculate σ. This is illustrated for a few examples in Figure 6.17.

6.14 Summary of results

Table 6.2 summarises the estimates of the uncertainties on the parameters describing *CP* violation in $B \to DK$, measured in $B \to DK$, $D \to K\pi\pi\pi$ for different charm inputs and data taking scenarios. These estimates are obtained from p-value scans as described above, averaged over 50 simulated experiments, generated using the default amplitude model.

The results indicate that an interesting precision on these parameters (especially x_- and y_-) can be achieved solely based on a combined analysis of $B \to DK$, $D \to K\pi\pi\pi$ and charm mixing data in several bins of the D decay's phase space. Such a result would not provide a competitive measurement of γ by itself, but would be expected to make a valuable contribution to a combined fit, such as the ones described in [11, 48, 80].

However, using both charm input from mixing and from threshold data transforms this into a precision measurement of γ. While precise predictions are impossible until there is a better understanding of the $D^0 \to K^+\pi^-\pi^+\pi^-$ amplitude structure, the above results suggest that, with the approach proposed here applied to LHCb Run 1 data, this channel can reach a similar precision as the combined analysis of $B \to DK$ with $D \to K_S\pi^+\pi^-$ and $D \to K_SK^+K^-$ on LHCb Run 1 data [89], currently the most precise individual measurement of γ in tree-level decays. Conversely, the inclusion of information from charm mixing leads to a vastly improved precision compared to that achievable based on charm input from threshold data alone, by about an order of magnitude for the upgrade scenario, emphasising the crucial role of the information from charm mixing.

Finally, the results indicate that the input from BES III has the potential to substantially improve the precision on γ over that achievable with CLEO-c's dataset alone, especially if a binned analysis were to be performed. Further improvements would be expected

LHCb scenario	D^0 mix?	charm threshold?	$\sigma(\gamma)$ [°]	$\sigma(\delta_B)$ [°]	$\sigma(r_B)$ $\times 10^2$	$\sigma(x_+)$ $\times 10^2$	$\sigma(y_+)$ $\times 10^2$	$\sigma(x_-)$ $\times 10^2$	$\sigma(y_-)$ $\times 10^2$
run I			26	47	1.6	8.7	9.1	8.8	8.2
run II	Y	none	22	29	1.4	7.6	6.9	4.5	4.0
upgr			15	14	0.17	4.7	5.2	0.56	0.98
run I			20	29	0.82	6.4	5.7	6.6	5.9
run II	Y	CLEO global	15	19	0.62	5.4	3.9	2.5	2.7
upgr			11	10	0.16	3.8	2.8	0.44	0.50
run I			19	25	0.78	6.4	5.5	6.5	5.8
run II	Y	BESIII global	14	18	0.57	5.4	3.9	2.4	2.7
upgr			9.0	8.2	0.15	3.7	2.7	0.43	0.48
run I			46	35	3.2	6.9	6.5	8.6	10
run II	N	CLEO binned	50	34	3.3	6.9	6.7	8.9	11
upgr			52	35	3.3	7.6	6.7	8.9	11
run I			40	24	2.6	4.1	5.0	5.7	6.2
run II	N	BESIII binned	34	17	2.5	3.6	4.1	5.0	5.1
upgr			39	14	2.9	3.9	4.1	4.3	5.6
run I			16	18	0.78	2.1	3.5	2.6	3.1
run II	Y	CLEO binned	12	13	0.53	1.7	3.1	1.7	2.0
upgr			7.8	7.2	0.15	1.1	2.6	0.40	0.46
run I			12	14	0.68	1.6	2.6	2.0	2.5
run II	Y	BESIII binned	8.6	9.6	0.47	0.90	2.1	1.5	1.5
upgr			4.1	3.9	0.14	0.53	1.3	0.35	0.38

Table 6.2: Uncertainties on key parameters, obtained based on the default amplitude model in different configurations, averaged over 50 simulated experiments. The typical uncertainty on these figures is $\sim 5\%$. All results are for the binned approach applied to $B \to DK$ and, where used, charm mixing data. The first column refers to the scenarios defined in Table 6.1. The second column defines whether charm mixing input was used (Y), or not (N). The third column describes additional input from the charm threshold. 'CLEO global' refers to the phase space-integrated input from [11]. 'BES III global' is the same, but uses the uncertainties predicted in [11] for a data sample 3.5 times as large as that collected by CLEO-c. 'CLEO binned' and 'BES III binned' extrapolate to a potential binned analysis of the charm threshold data described in Section 6.12.3.

from combining CLEO-c and BES III input, which, in this study, were only considered separately.

6.15 Conclusions

This chapter presents a new method for the amplitude model-independent measurement of the *CP* violation parameter γ using $B^{\pm} \to DK^{\pm}$ decays, based on a combined analysis of $B \to DK$ and charm mixing. When analysed in several bins of the D decay's phase space, γ can be measured without additional input from the charm threshold. The performance of the method is evaluated in a simulation study for the case where the D decays to $K\pi\pi\pi$, using sample sizes representing existing and plausible future datasets. The precision ultimately achievable depends on the $D^0 \to K^+\pi^-\pi^+\pi^-$ amplitude structure realised in nature, that is not currently known. The results suggest that the new method would, even without input from the charm threshold, provide valuable input to a global γ combination, although the precision would be insufficient to provide a competitive γ measurement in its own right.

The performance of this novel method is compared to that of a binned analysis with charm input from the threshold, as proposed in [8]. For the Run I scenario, with BES III statistics, both methods perform similarly well. Assuming no additional data from the threshold, the mixing-based method introduced here performs significantly better for the LHCb-upgrade scenario, benefiting from the vast number of D events expected.

For all data-taking scenarios studied, combining the two methods results in a far superior performance than either can achieve individually. This is already the case when threshold data enter in the form of a phase space-integrated constraint on $\mathcal{Z}^f$, but by far the best results are obtained if D-mixing, $B \to DK$ and charm threshold data are analysed in the same phase space bins. Such a combined approach transforms this into a highly competitive precision measurement of γ, on par with the best existing constraints from individual channels. Its precision keeps improving with charm mixing and $B \to DK$ event yields projected into the foreseeable future, even if no new data from the charm threshold become available.

Once a $D^0 \to K^+\pi^-\pi^+\pi^-$ amplitude model is available to inform the binning, the techniques introduced here can be used to significantly improve the precision on γ and related parameters that can be obtained from $B \to DK$, $D \to K\pi\pi\pi$. Such a measurement would benefit greatly from an update of the $\mathcal{Z}^{K3\pi} = R^{K3\pi}e^{-\delta^{K3\pi}}$ measurement [11, 48] with BES III's larger dataset, and, even more so, a binned $\mathcal{Z}_\Omega^{K3\pi}$ analysis. With all of the above ingredients in place, the methods introduced in this chapter, applied to $B \to DK$, $D \to K\pi\pi\pi$, could lead to one of the most precise individual γ measurements.

Chapter 7

Conclusions

The LHCb experiment is a specialised detector aimed towards precision measurements in flavour physics. The detector is placed at one of the LHC interaction points, which provides the largest production cross-section of c and b hadrons in the world. Of particular importance to this thesis are the unprecedented numbers of $D \to K\pi\pi\pi$ and $B^{\pm} \to DK^{\pm}, D \to K\pi\pi\pi$ decays that have been collected by LHCb during 2011 and 2012. The LHCb detector has several unique features that were essential in collecting these samples. The VELO sub-detector provides tracking within 8 mm of the beam line, allowing the secondary (and tertiary) decay vertices of B and D mesons to be distinguished from the PV. The LHCb trigger system allows the experiment to collect large, clean heavy flavour samples, even in all-hadronic final states. Two RICH detectors give excellent discrimination between pions, kaons and protons, allowing the suppressed decay $D^0 \to K^+\pi^-\pi^+\pi^-$ to be separated from the much more copious $D^0 \to K^-\pi^+\pi^-\pi^+$.

Constraining the parameters of the CKM matrix, which describes the relative probability of flavour-changing charged currents in the SM, is one of the major goals of flavour physics. The CKM phase γ is particularly interesting because it is currently the least constrained angle of the unitarity triangle, and additionally is the only angle that can be measured in tree-only decays.

The decay $B \to DK, D \to K\pi\pi\pi$ provides a theoretically clean (tree-only) method of measuring the CKM phase γ that is unlikely to be influenced by any new physics

contributions. However, this SM reference is crucial for the new physics sensitivity of the quark flavour sector. In order to constrain γ using $B \to DK, D \to f$ decays one needs external input to describe the interference between $D^0 \to f$ and $\overline{D}^0 \to f$ amplitudes - this interference can be parameterised by the complex interference parameter $\mathcal{Z}^f$. Previously, constraints on $\mathcal{Z}^f$ could only be obtained at the charm threshold from e^+e^- colliders - for example, the CLEO-c or BES III experiment. It is shown using simulation studies that constraints on $\mathcal{Z}^f$ can also be obtained from a measurement of D-mixing. While it is not possible to get a point constraint in the complex $\mathcal{Z}^f$ plane, it is possible to constrain a line of solutions.

A measurement of D-mixing in the suppressed $D^0 \to K^+\pi^-\pi^+\pi^-$ decay is made using $1.0\,\text{fb}^{-1}$ of data collected by the LHCb experiment at a centre of mass collision energy of $\sqrt{s} = 7\,\text{TeV}$. To reduce experimental uncertainties, the favoured $D^0 \to K^-\pi^+\pi^-\pi^+$ decay is used as a normalisation channel. The ratio of DCS to CF amplitudes is measured to be,

$$r_D^{K3\pi} = 0.0548 \pm 0.0012,$$

which is the first direct measurement of this parameter, shown to be compatible with, and improving upon indirect constraints from BELLE [79].

A combination of results from LHCb and CLEO-c gives the following constraints on $\mathcal{Z}^f$:

$$\mathcal{R}e\mathcal{Z}^{K3\pi} = -0.135^{+0.095}_{-0.105}, \qquad \mathcal{I}m\mathcal{Z}^{K3\pi} = -0.26^{+0.19}_{-0.16},$$

which for $\mathcal{I}m\ \mathcal{Z}^{K3\pi}$, is a reduction in the uncertainty by $\sim 30\%$ when compared to the measurement from CLEO-c alone.

The probability of the LHCb data being a statistical fluctuation of the no-mixing hypothesis is 2.5×10^{-6}, corresponding to a significance of 4.7σ.

Measuring γ from $B \to DK, D \to f$ decays requires prior constraints on $\mathcal{Z}^f$. It was previously thought that these constraints could only come from the charm threshold - D-mixing would not be sufficient alone because it can only provide a line of constraints in the complex $\mathcal{Z}^f$ plane. It is shown with a novel approach, that it is in fact possible to constrain γ using *only* input from charm mixing. Such a measurement is only

possible when the final state of the D decay is multi-body, so that the phase space of the decay can be divided into independent volumes. The performance of the method is evaluated using simulated data for the final state $K\pi\pi\pi$. This is done for two scenarios: using input from charm mixing, and using input from the charm threshold. While both methods give useful constraints on γ, using the combination of both sets of constraints far outperforms each individually. Doing so makes the measurement highly competitive with γ constraints from other decay modes. With assumptions about the resonant substructure of the $D^0 \to K^+\pi^-\pi^+\pi^-$ DCS amplitude, it is estimated that γ can be measured to within 12° using existing data and 4° degrees for the LHCb-upgrade.

Appendix A

Phase Conventions

There are two different definitions of the *CP* operator in use. The Heavy Flavour Averaging Group (HFAG) [71] uses

$$CP_{\mathrm{HFAG}}|D^0\rangle = -|\bar{D}^0\rangle, \tag{A.1}$$

which is the convention usually adopted for charm analyses. In the context of extracting γ from $B \to DK$ decays, it is usual practice to follow the "ADS" convention [23],

$$CP_{\mathrm{ADS}}|D^0\rangle = +|\bar{D}^0\rangle. \tag{A.2}$$

This difference affects several relevant parameters, and needs to be taken into account when providing charm input to the measurement of γ. The choice of convention decides how the mass eigenstates $|D_1\rangle$ and $|D_2\rangle$ defined in Equation 4.3 relate to the *CP* even and odd eigenstates, $|D_+\rangle$ and $|D_-\rangle$. In the HFAG convention $|D_1\rangle \approx |D_-\rangle$ and $|D_2\rangle \approx |D_+\rangle$ (these relations become exact in the absence of CPV). In the ADS convention it is the other way around. The mixing variables x and y are defined in terms of (approximate) *CP* eigenstates, $x = \frac{M_+ - M_-}{\Gamma}, y = \frac{\Gamma_+ - \Gamma_-}{\Gamma}$, where the subscripts + and − label the masses and widths of the predominantly *CP*-even and *CP*-odd mass eigenstates, respectively. The formalism detailed above, with the mixing parameters defined in Equation 4.5, follows the HFAG convention. Changing this to the ADS convention implies a simultaneous change $x \to -x$ and $y \to -y$.

The choice of convention also affects the complex interference parameter $\mathcal{Z}_\Omega^f$. To ensure that the same physical *CP* even or *CP* odd state corresponds to the same wave function (up to a phase), the $|D^0\rangle$ and $|\overline{D}^0\rangle$ wavefunctions between the two conventions must be related by

$$\begin{aligned} |D^0\rangle_{\mathrm{ADS}} &= e^{i\xi}|D^0\rangle_{\mathrm{HFAG}}, \\ |\overline{D}^0\rangle_{\mathrm{ADS}} &= -e^{i\xi}|\overline{D}^0\rangle_{\mathrm{HFAG}}, \end{aligned} \tag{A.3}$$

where ξ is an arbitrary phase. As $\mathcal{Z}^f_\Omega \propto \int_\Omega \langle f_\mathbf{p}|\hat{H}|D^0\rangle\langle f_\mathbf{p}|\hat{H}|\overline{D}^0\rangle^* \frac{d\Phi}{d\mathbf{p}}\mathrm{d}\mathbf{p}$, this implies

$$\mathcal{Z}^f_{\Omega\ \mathrm{ADS}} = -\mathcal{Z}^f_{\Omega\ \mathrm{HFAG}}, \tag{A.4}$$

which is equivalent to

$$\begin{aligned} R^f_{D\ \mathrm{ADS}} &= R^f_{D\ \mathrm{HFAG}} & c_i^{\mathrm{ADS}} &= -c_i^{\mathrm{HFAG}} \\ \delta^f_{D\ \mathrm{ADS}} &= \delta^f_{D\ \mathrm{HFAG}} + \pi & s_i^{\mathrm{ADS}} &= -s_i^{\mathrm{HFAG}}. \end{aligned} \tag{A.5}$$

Appendix B

Phase Ambiguities

As described in [1], the charm mixing input constrains each $\mathcal{Z}_\Omega^f = R_\Omega^f e^{-i\delta_\Omega^f}$ to a line of slope $-y/x$ in the $\mathcal{R}e\mathcal{Z}_\Omega^f - \mathcal{I}m\mathcal{Z}_\Omega^f$ plane. The input from the $B \to DK$ adds information on the magnitude of $\mathcal{Z}_\Omega^f$, leaving two possible solutions for each $\mathcal{Z}_\Omega^f$, which have the same magnitude but different phases: $-\delta_{\Omega\,1}^f$ and $-\delta_{\Omega\,2}^f$, as illustrated in Figure B.1. These solutions are symmetric with respect to a line of symmetry that is perpendicular to the constraint from charm mixing. Their sum is always along this line of symmetry and has the phase $\alpha = -\frac{1}{2}(\delta_{\Omega\,1}^f + \delta_{\Omega\,2}^f)$. Because α depends only on the charm mixing parameters (with $\tan\alpha = x/y$) it is the same for all phase-space bins. It is easy to show that, as a consequence of this relationship, the system of equations remains invariant under the

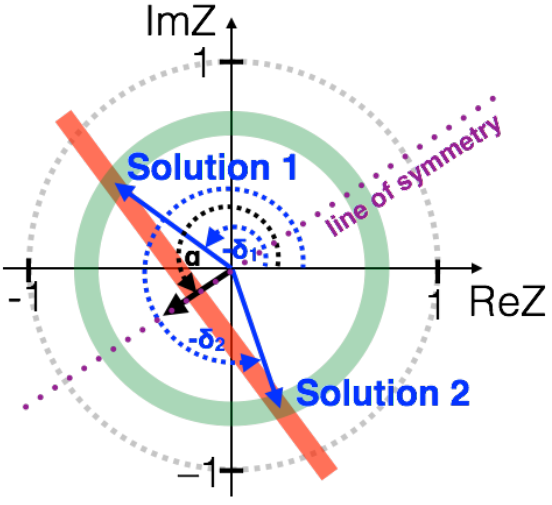

Figure B.1: The combined constraints on $\mathcal{Z}_\Omega^f = R_\Omega^f e^{-i\delta_\Omega^f}$ from charm mixing (red line with slope -y/x) and $B \to DK$ (green solid circle) lead to two possible solutions, whose sum (short black arrow) is always perpendicular to the charm constraint. (In the figure, the subscript Ω and superscript f are omitted for clarity.) The grey broken circular line indicates the boundary of the physically allowed region.

following operation:

$$\left(\left\{\delta_\Omega^f\right\}, \delta_B, \gamma\right) \to \left(\left\{-2\alpha - \delta_\Omega^f\right\}, -2\alpha - \delta_B, -\gamma\right). \tag{B.1}$$

There is also the more obvious invariance under the simultaneous shift by π of δ_B and γ:

$$\left(\left\{\delta_\Omega^f\right\}, \delta_B, \gamma\right) \to \left(\left\{\delta_\Omega^f\right\}, \delta_B + \pi, \gamma + \pi\right), \tag{B.2}$$

leading to an overall four-fold ambiguity in γ and δ_B. In Section 6.12 it is shown how external input from the charm threshold [11, 48] can be used to reduce this to a 2-fold ambiguity.

Appendix C

Efficiency Corrections

Figures C.1 - C.5 show a comparison of generator level MC (GEN) and LHCb MC that has been passed through detector simulation and event reconstruction (MC). The generator level MC has additionally been reweighted by the acceptance parameterisation, $\varepsilon_{K\pi\pi\pi}(\mathbf{p})$, described in Section 5.6. Projections of the two data samples are compared in the 5 variables that are used (in this thesis) to parameterise the 5D phase space of the $D^0 \to K\pi\pi\pi$ decay (m_{12}, m_{23}, m_{34}, m_{123} and m_{234}). Additionally, 4 slices (defined to have approximately the same number of events) are taken in each of these variables, then projections are shown over the remaining 4 i.e. slicing in 1 variable, then projecting over the other 4. If the acceptance parameterisation is working, one would expect each pair of projections to be compatible - this is observed to be the case.

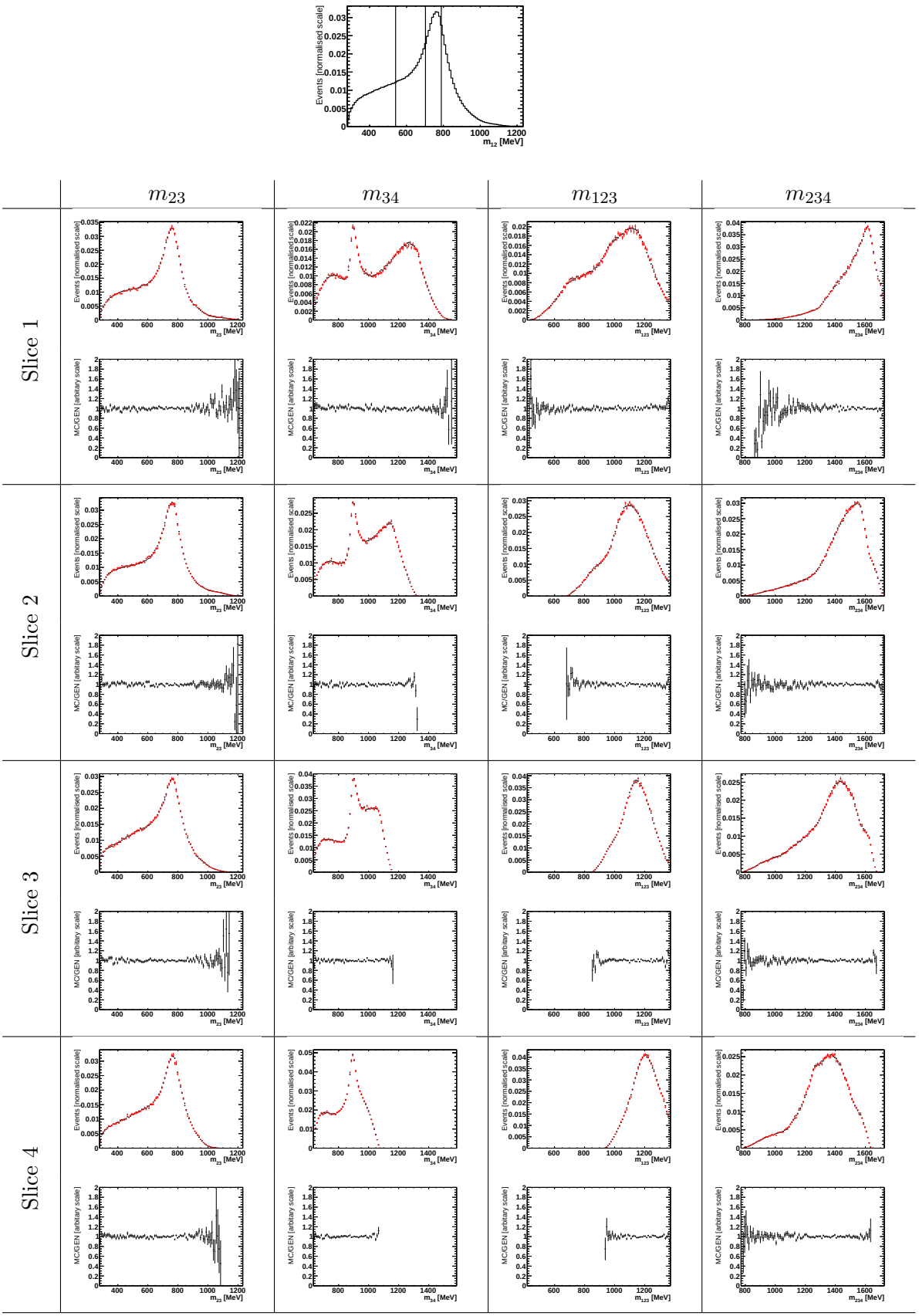

Figure C.1: Projections of MC (black) and GEN weighted by $\varepsilon_{K\pi\pi\pi}(\mathbf{p})$ (red) in 4 of the 5 variables chosen to parameterise phase space $(m_{23}, m_{34}, m_{123}, m_{234})$. The datasets MC and GEN, and the efficiency parameterisation, $\varepsilon_{K\pi\pi\pi}(\mathbf{p})$, are defined in Section 5.6. The projections are shown in 4 slices of m_{12}, which are defined by the uppermost plot (slices are defined by the black vertical lines, and labeled 1-4 from left to right). The ratio plots show the ratio of MC to GEN projections.

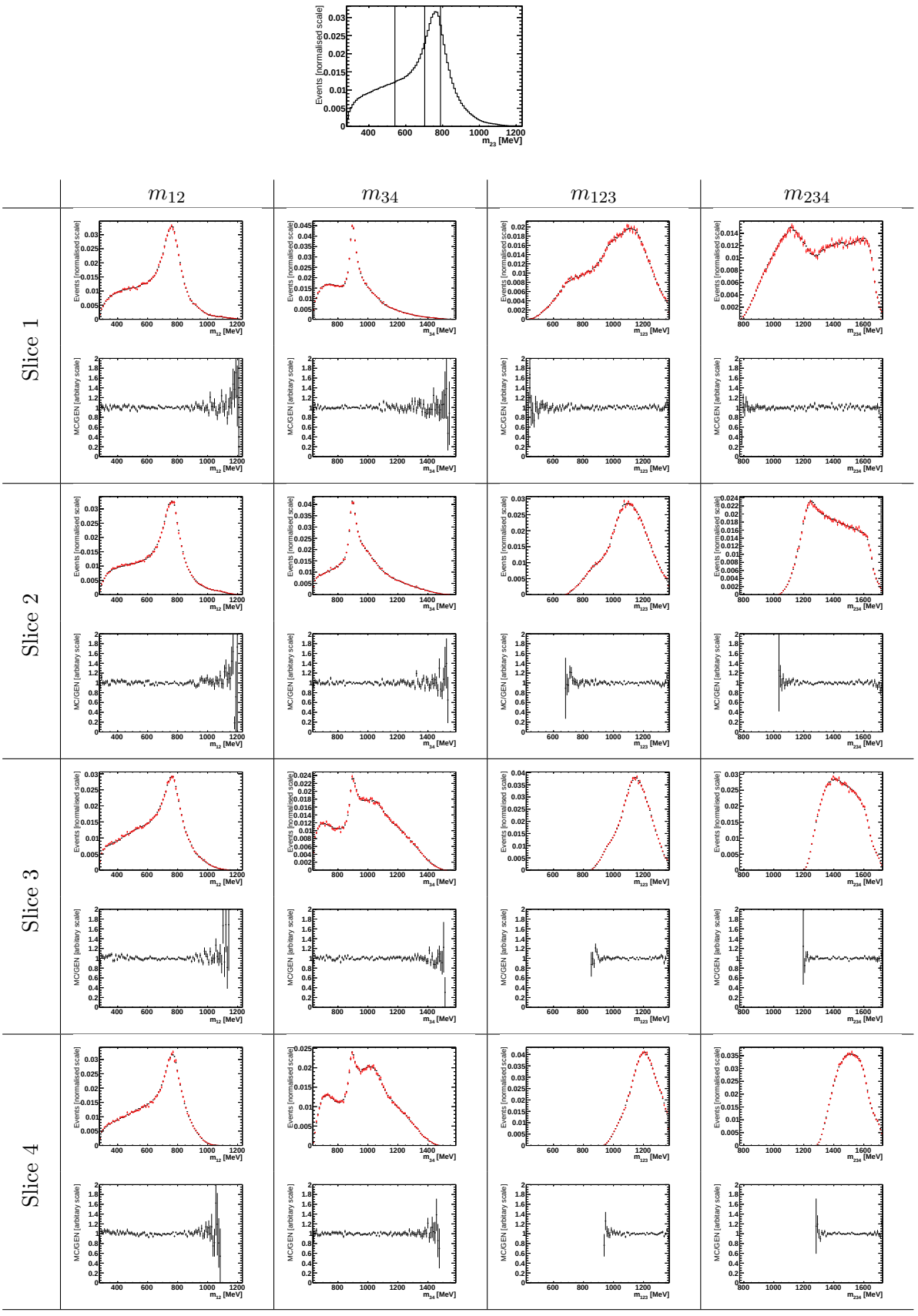

Figure C.2: Projections of MC (black) and GEN weighted by $\varepsilon_{K\pi\pi\pi}(\mathbf{p})$ (red) in 4 of the 5 variables chosen to parameterise phase space $(m_{12}, m_{34}, m_{123}, m_{234})$. The datasets MC and GEN, and the efficiency parameterisation, $\varepsilon_{K\pi\pi\pi}(\mathbf{p})$, are defined in Section 5.6. The projections are shown in 4 slices of m_{23}, which are defined by the uppermost plot (slices are defined by the black vertical lines, and labeled 1-4 from left to right). The ratio plots show the ratio of MC to GEN projections.

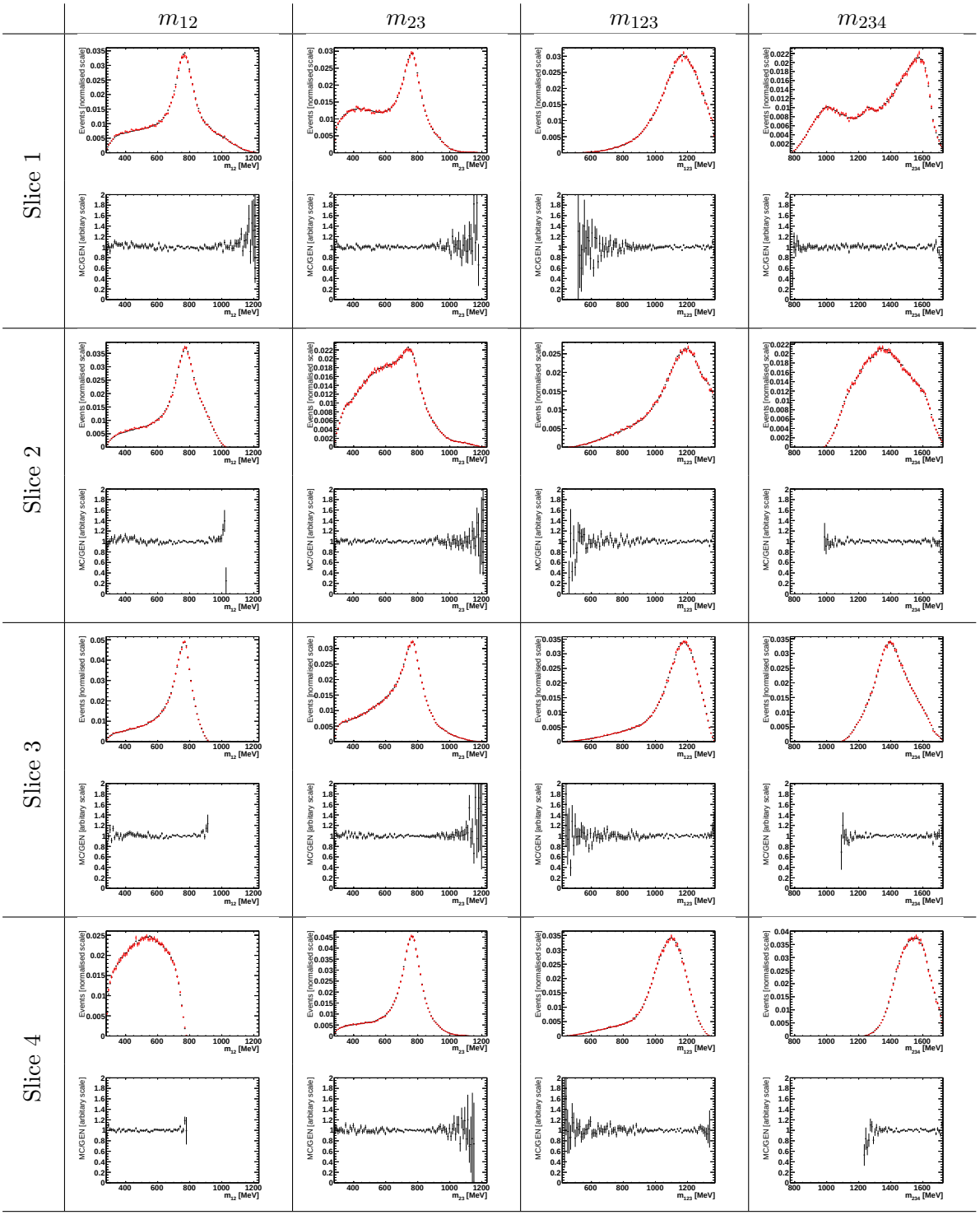

Figure C.3: Projections of MC (black) and GEN weighted by $\varepsilon_{K\pi\pi\pi}(\mathbf{p})$ (red) in 4 of the 5 variables chosen to parameterise phase space $(m_{12}, m_{23}, m_{123}, m_{234})$. The datasets MC and GEN, and the efficiency parameterisation, $\varepsilon_{K\pi\pi\pi}(\mathbf{p})$, are defined in Section 5.6. The projections are shown in 4 slices of m_{34}, which are defined by the uppermost plot (slices are defined by the black vertical lines, and labeled 1-4 from left to right). The ratio plots show the ratio of MC to GEN projections.

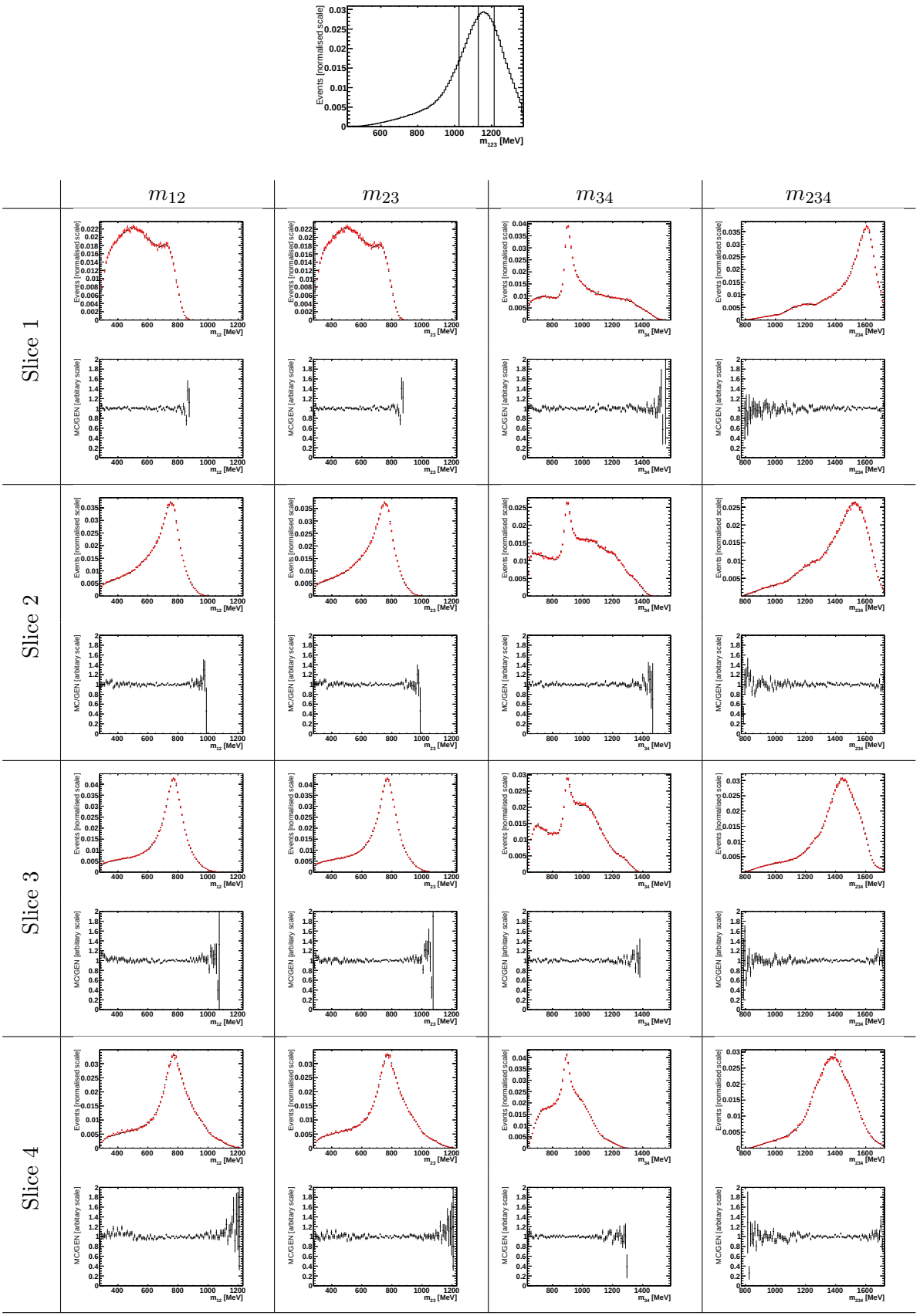

Figure C.4: Projections of MC (black) and GEN weighted by $\varepsilon_{K\pi\pi\pi}(\mathbf{p})$ (red) in 4 of the 5 variables chosen to parameterise phase space ($m_{12}, m_{23}, m_{34}, m_{234}$). The datasets MC and GEN, and the efficiency parameterisation, $\varepsilon_{K\pi\pi\pi}(\mathbf{p})$, are defined in Section 5.6. The projections are shown in 4 slices of m_{123}, which are defined by the uppermost plot (slices are defined by the black vertical lines, and labeled 1-4 from left to right). The ratio plots show the ratio of MC to GEN projections.

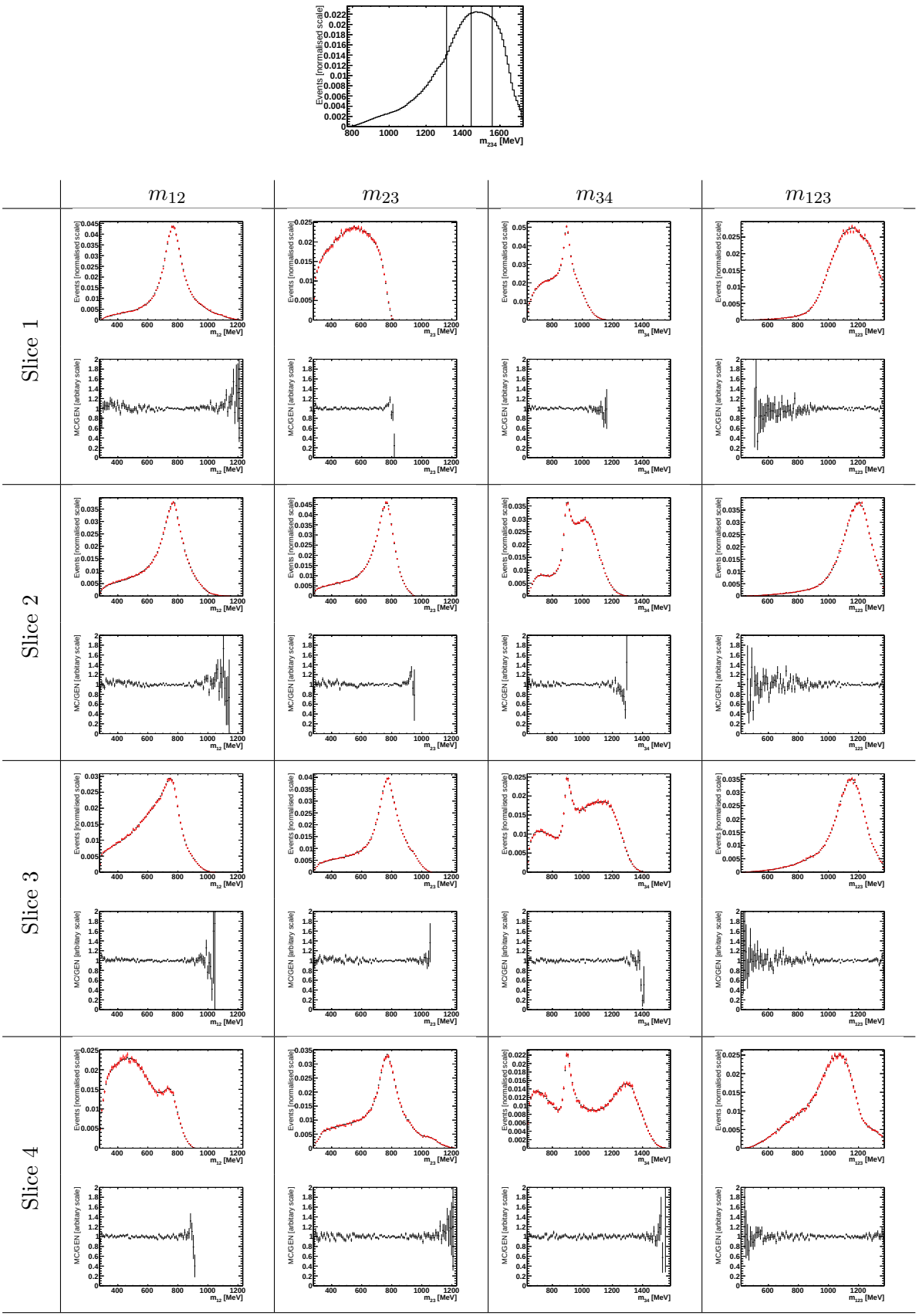

Figure C.5: Projections of MC (black) and GEN weighted by $\varepsilon_{K\pi\pi\pi}(\mathbf{p})$ (red) in 4 of the 5 variables chosen to parameterise phase space $(m_{12}, m_{23}, m_{34}, m_{123})$. The datasets MC and GEN, and the efficiency parameterisation, $\varepsilon_{K\pi\pi\pi}(\mathbf{p})$, are defined in Section 5.6. The projections are shown in 4 slices of m_{234}, which are defined by the uppermost plot (slices are defined by the black vertical lines, and labeled 1-4 from left to right). The ratio plots show the ratio of MC to GEN projections.

Bibliography

[1] S. Harnew and J. Rademacker, "Charm mixing as input for model-independent determinations of the CKM phase γ," *Phys.Lett.* **B728** (2014) 296–302, arXiv:1309.0134 [hep-ph].

[2] S. Harnew and J. Rademacker, "Model independent determination of the CKM phase γ using input from $D^0 - \bar{D}^0$ mixing," *JHEP* **1503** (2015) 169, arXiv:1412.7254 [hep-ph].

[3] L. Evans and P. Bryant, "LHC machine," *JINST* **3** (2008) S08001.

[4] **LHCb** Collaboration, A. A. Alves *et al.*, "The LHCb Detector at the LHC," *JINST* **3** (2008) S08005.

[5] **LHCb** Collaboration, B. Adeva *et al.*, "Roadmap for selected key measurements of LHCb," arXiv:0912.4179 [hep-ex].

[6] N. Cabibbo, "Unitary Symmetry and Leptonic Decays," *Phys.Rev.Lett.* **10** (1963) 531–533.

[7] M. Kobayashi and T. Maskawa, "CP Violation in the Renormalizable Theory of Weak Interaction," *Prog.Theor.Phys.* **49** (1973) 652–657.

[8] D. Atwood and A. Soni, "Role of a charm factory in extracting CKM-phase information via $B \to DK$," *Phys. Rev.* **D68** (2003) 033003.

[9] M. Gronau and D. Wyler, "On determining a weak phase from CP asymmetries in charged B decays," *Phys.Lett.* **B265** (1991) 172–176.

[10] M. Gronau and D. London, "How to determine all the angles of the unitarity triangle from $B_d \to DK_s$ and $B_s^0 \to D\phi$," *Phys.Lett.* **B253** (1991) 483–488.

[11] J. Libby, S. Malde, A. Powell, G. Wilkinson, D. Asner, *et al.*, "New determination of the $D^0 \to K^-\pi^+\pi^0$ and $D^0 \to K^-\pi^+\pi^+\pi^-$ coherence factors and average strong-phase differences," *Phys.Lett.* **B731** (2014) 197–203, arXiv:1401.1904 [hep-ex].

[12] B. Odom, D. Hanneke, B. D'Urso, and G. Gabrielse, "New measurement of the electron magnetic moment using a one-electron quantum cyclotron," *Phys. Rev. Lett.* **97** (Jul, 2006) 030801. http://link.aps.org/doi/10.1103/PhysRevLett.97.030801.

[13] **Particle Data Group** Collaboration, J. A. Olive *et al.*, "Review of Particle Physics," *Chin.Phys.* **C38** (2014) 090001. http://dx.doi.org/10.1088/1674-1137/38/9/090001.

[14] **CMS** Collaboration, S. Chatrchyan *et al.*, "Observation of a new boson at a mass of 125 GeV with the CMS experiment at the LHC," *Phys. Lett.* **B716** (2012) 30–61, arXiv:1207.7235 [hep-ex].

[15] **ATLAS** Collaboration, G. Aad *et al.*, "Observation of a new particle in the search for the Standard Model Higgs boson with the ATLAS detector at the LHC," *Phys. Lett.* **B716** (2012) 1 – 29, arXiv:1207.7214 [hep-ex].

[16] E. Noether, "Invariant variation problems," *Transport Theory and Statistical Physics* **1** (1971) no. 3, 186–207, http://dx.doi.org/10.1080/00411457108231446.

[17] C. S. Wu, E. Ambler, R. W. Hayward, D. D. Hoppes, and R. P. Hudson, "Experimental test of parity conservation in beta decay," *Phys. Rev.* **105** (Feb, 1957) 1413–1415. http://link.aps.org/doi/10.1103/PhysRev.105.1413.

[18] S. Weinberg, "General theory of broken local symmetries," *Phys. Rev.* **D7** (1973) 1068–1082.

[19] J. Goldstone, "Field theories with superconductor solutions," *Il Nuovo Cimento* **19** (1961) no. 1, 154–164.

[20] L.-L. Chau and W.-Y. Keung, "Comments on the parametrization of the kobayashi-maskawa matrix," *Phys. Rev. Lett.* **53** (Nov, 1984) 1802–1805. http://link.aps.org/doi/10.1103/PhysRevLett.53.1802.

[21] L. Wolfenstein, "Parametrization of the Kobayashi-Maskawa matrix," *Phys. Rev. Lett.* **51** (1983) 1945–1947.

[22] **CKMfitter Group** Collaboration, J. Charles *et al.*, "CP violation and the CKM matrix: Assessing the impact of the asymmetric B factories," *Eur. Phys. J.* **C41** (2005) 1–131.

[23] D. Atwood, I. Dunietz, and A. Soni, "Enhanced CP violation with $B \to \mathrm{KD}^0(\overline{\mathrm{D}}^0)$ modes and extraction of the Cabibbo-Kobayashi-Maskawa Angle γ," *Phys.Rev.Lett.* **78** (1997) 3257–3260, arXiv:hep-ph/9612433 [hep-ph].

[24] **ATLAS** Collaboration, G. Aad *et al.*, "The ATLAS experiment at the CERN Large Hadron Collider," *JINST* **3** (2008) S08003.

[25] **CMS** Collaboration, S. Chatrchyan *et al.*, "The CMS experiment at the CERN LHC," *JINST* **3** (2008) S08004.

[26] **ALICE** Collaboration, K. Aamodt *et al.*, "The ALICE experiment at the CERN LHC," *JINST* **3** (2008) S08002.

[27] **LHCb** Collaboration, *LHCb VELO (VErtex LOcator): Technical Design Report.* CERN, Geneva, 2001.

[28] **LHCb** Collaboration, *LHCb inner tracker: Technical Design Report.* CERN, Geneva, 2002.

[29] **LHCb** Collaboration, *LHCb outer tracker: Technical Design Report.* CERN, Geneva, 2001.

[30] **LHCb** Collaboration, R. Aaij *et al.*, "LHCb Detector Performance," *Int.J.Mod.Phys.* **A30** (2015) 1530022, `arXiv:1412.6352 [hep-ex]`.

[31] **LHCb** Collaboration, *LHCb magnet: Technical Design Report.* CERN, Geneva, 2000.

[32] **LHCb** Collaboration, *LHCb RICH: Technical Design Report.* CERN, Geneva, 2000.

[33] **LHCb** Collaboration, *LHCb calorimeters: Technical Design Report.* CERN, Geneva, 2000.

[34] **LHCb** Collaboration, *LHCb muon system: Technical Design Report.* CERN, Geneva, 2001.

[35] **LHCb** Collaboration, *LHCb trigger system: Technical Design Report.* CERN, Geneva, 2003.

[36] T. Sjostrand, S. Mrenna, and P. Z. Skands, "PYTHIA 6.4 Physics and Manual," *JHEP* **0605** (2006) 026, `arXiv:hep-ph/0603175 [hep-ph]`.

[37] T. Sjostrand, S. Mrenna, and P. Z. Skands, "A Brief Introduction to PYTHIA 8.1," *Comput.Phys.Commun.* **178** (2008) 852–867, `arXiv:0710.3820 [hep-ph]`.

[38] D. Lange, "The EvtGen particle decay simulation package," *Nucl. Instrum. Meth.* **A462** (2001) 152–155.

[39] **GEANT4** Collaboration, S. Agostinelli *et al.*, "GEANT4 - a simulation toolkit," *Nucl. Instrum. Meth.* **A506** (2003) no. 3, 250 – 303.

[40] **LHCb VELO Group** Collaboration, R. "Aaij and others", "Performance of the LHCb Vertex Locator," *J. Instrum.* **9** (May, 2014) P09007. 61 p. `https://cds.cern.ch/record/1707015`. Comments: 61 pages, 33 figures.

[41] **LHCb RICH group** Collaboration, M. "Adinolfi and others", "Performance of the LHCb RICH detector at the LHC," *Eur. Phys. J. C* **73** (Nov, 2012) 2431. 25 p. https://cds.cern.ch/record/1495721.

[42] **LHCb Outer Tracker group** Collaboration, R. "Arink and others", "Performance of the LHCb Outer Tracker," *J. Instrum.* **9** (Nov, 2013) P01002. 30 p. https://cds.cern.ch/record/1629476. Comments: 30 pages, 20 figures.

[43] R. Aaij *et al.*, "The LHCb Trigger and its Performance in 2011," *J. Instrum.* **8** (Nov, 2012) P04022. 31 p. https://cds.cern.ch/record/1493820.

[44] A. Giri, Y. Grossman, A. Soffer, and J. Zupan, "Determining γ using $B^{\pm} \to \mathrm{DK}^{\pm}$ with multibody D decays," *Phys. Rev. D* **68** (2003) 054018.

[45] **Belle** Collaboration, A. Poluektov *et al.*, "Measurement of ϕ_3 with dalitz plot analysis of $B^{\pm} \to D^{(*)}K^{\pm}$ decays," *Phys. Rev. D* **70** (2004) 072003.

[46] J. Rademacker and G. Wilkinson, "Determining the unitarity triangle gamma with a four-body amplitude analysis of $B^+ \to (K^+K^-\pi^+\pi^-)_D K^{\pm}$ decays," *Phys.Lett.* **B647** (2007) 400–404, arXiv:hep-ph/0611272 [hep-ph].

[47] A. Giri, Y. Grossman, A. Soffer, and J. Zupan, "Determining gamma using $B^{\pm} \to DK^{\pm}$ with multibody D decays," *Phys.Rev.* **D68** (2003) 054018, arXiv:hep-ph/0303187 [hep-ph].

[48] **CLEO** Collaboration, N. Lowrey *et al.*, "Determination of the $D^0 \to K^-\pi^+\pi^0$ and $D^0 \to K^-\pi^+\pi^-\pi^+$ coherence factors and average strong-phase differences using quantum-correlated measurements," *Phys. Rev.* **D80** (2009) 031105.

[49] **CLEO** Collaboration, J. Libby *et al.*, "Model-independent determination of the strong-phase difference between D^0 and $\bar{D}^0 \to K^0_{S,L}h^+h^-$ ($h = \pi, K$) and its impact on the measurement of the CKM angle γ/ϕ_3," *Phys.Rev.* **D82** (2010) 112006, arXiv:1010.2817 [hep-ex].

[50] **CLEO** Collaboration, R. A. Briere *et al.*, "First model-independent determination of the relative strong phase between D^0 and $\bar{D}^0 \to K^0_s\pi^+\pi^-$ and its impact on the CKM Angle γ/ϕ_3 measurement," *Phys.Rev.* **D80** (2009) 032002, arXiv:0903.1681 [hep-ex].

[51] **CLEO** Collaboration, D. M. Asner *et al.*, "Determination of the $D^0 \to K^+\pi^-$ Relative Strong Phase Using Quantum-Correlated Measurements in $e^+e^- \to D^0\bar{D}^0$ at CLEO," *Phys.Rev.* **D78** (2008) 012001, arXiv:0802.2268 [hep-ex].

[52] **CLEO** Collaboration, J. Insler *et al.*, "Studies of the decays $D^0 \to K^0_S K^-\pi^+$ and $D^0 \to K^0_S K^+\pi^-$," *Phys.Rev.* **D85** (2012) 092016, arXiv:1203.3804 [hep-ex].

[53] S. Malde and G. Wilkinson, "$D^0 - \bar{D}^0$ mixing studies with the decays $D^0 \to K^0_S K^{\mp}\pi^{\pm}$," *Phys.Lett.* **B701** (2011) 353–356, arXiv:1104.2731 [hep-ph].

[54] A. Bondar, A. Poluektov, and V. Vorobiev, "Charm mixing in the model-independent analysis of correlated D^0 $\bar{D}^0$ decays," *Phys.Rev.* **D82** (2010) 034033, arXiv:1004.2350 [hep-ph].

[55] R. Dalitz, "Cxii. on the analysis of -meson data and the nature of the -meson," *The London, Edinburgh, and Dublin Philosophical Magazine and Journal of Science* **44** (1953) no. 357, 1068–1080. http://dx.doi.org/10.1080/14786441008520365.

[56] R. "Aaij and others", "Search for cp violation in $D^+ \to K^-K^+\pi^+$ decays," *Phys. Rev. D* **84** (2011) 112008.

[57] **LHCb** Collaboration, R. Aaij *et al.*, "Model-independent search for CP violation in $D^0 \to K^-K^+\pi^-\pi^+$ and $D^0 \to \pi^-\pi^+\pi^-\pi^+$ decays," arXiv:1308.3189 [hep-ex].

[58] **ARGUS** Collaboration, H. Albrecht *et al.*, "Observation of $B^0 - \overline{B}^0$ mixing," *Phys. Lett.* **B192** (1987) no. 1-2, 245 – 252.

[59] **CDF** Collaboration, A. Abulencia *et al.*, "Observation of $B^0_s - \overline{B}^0_s$ oscillations," *Phys. Rev. Lett.* **97** (2006) 242003.

[60] K. Lande, E. T. Booth, J. Impeduglia, L. M. Lederman, and W. Chinowsky, "Observation of long-lived neutral V particles," *Phys. Rev.* **103** (1956) 1901–1904.

[61] C. A. Chavez, R. F. Cowan, and W. Lockman, "Charm meson mixing: An experimental review," *Int.J.Mod.Phys.* **A27** (2012) 1230019, arXiv:1209.5806 [hep-ex].

[62] **Belle** Collaboration, I. Adachi *et al.*, "First measurement of ϕ_3 with a binned model-independent Dalitz plot analysis of $B^{+-} \to DK^{+-}, D \to K^0_s\pi^+\pi^-$ decay," arXiv:1106.4046 [hep-ex].

[63] **LHCb** Collaboration, R. Aaij *et al.*, "A model-independent Dalitz plot analysis of $B^{\pm} \to DK^{\pm}$ with $D \to K^0_S h^+h^-$ $(h = \pi, K)$ decays and constraints on the CKM angle γ," *Phys. Lett.* **B718** (2012) 43–55, arXiv:1209.5869 [hep-ex].

[64] C. Thomas and G. Wilkinson, "Model-independent $D^0 - \bar{D}^0$ mixing and CP violation studies with $D^0 \to K^0_S\pi^+\pi^-$ and $D^0 \to K^0_S K^+K^-$," *JHEP* **1210** (2012) 185, arXiv:1209.0172 [hep-ex].

[65] **CDF** Collaboration, T. Aaltonen *et al.*, "Evidence for $D^0 - \bar{D}^0$ mixing using the CDF II Detector," *Phys.Rev.Lett.* **100** (2008) 121802, arXiv:0712.1567 [hep-ex].

[66] **Belle** Collaboration, M. Staric *et al.*, "Evidence for D^0 - $\bar{D}^0$ Mixing," *Phys.Rev.Lett.* **98** (2007) 211803, arXiv:hep-ex/0703036 [hep-ex].

[67] **BaBar** Collaboration, B. Aubert *et al.*, "Evidence for D^0 - $\bar{D}^0$ Mixing," *Phys.Rev.Lett.* **98** (2007) 211802, arXiv:hep-ex/0703020 [HEP-EX].

[68] **BaBar** Collaboration, B. Aubert *et al.*, "Measurement of $D^0 - \bar{D}^0$ mixing from a time-dependent amplitude analysis of $D^0 \to K^+\pi^-\pi^0$ decays," *Phys.Rev.Lett.* **103** (2009) 211801, arXiv:0807.4544 [hep-ex].

[69] **BaBar** Collaboration, B. Aubert *et al.*, "Measurement of $D^0 - \bar{D}^0$ Mixing using the Ratio of Lifetimes for the Decays $D^0 \to K^-\pi^+$ and K^+K^-," *Phys.Rev.* **D80** (2009) 071103, arXiv:0908.0761 [hep-ex].

[70] **LHCb** Collaboration, R. Aaij *et al.*, "Observation of D^0–$\overline{D}^0$ oscillations," *Phys. Rev. Lett.* **110** (2013) 101802, arXiv:1211.1230 [hep-ex].

[71] **Heavy Flavor Averaging Group** Collaboration, Y. Amhis *et al.*, "Averages of B-Hadron, C-Hadron, and tau-lepton properties as of early 2012," arXiv:1207.1158 [hep-ex].

[72] **LHCb** Collaboration, R. Aaij *et al.*, "Measurement of mixing and CP violation parameters in two-body charm decays," *JHEP* **04** (2012) 129, arXiv:1112.4698 [hep-ex].

[73] **BaBar** Collaboration, J. Lees *et al.*, "Search for $b \to u$ Transitions in $B^\pm \to [K^\mp\pi^\pm\pi^0]_D K^\pm$ Decays," *Phys.Rev.* **D84** (2011) 012002, arXiv:1104.4472 [hep-ex].

[74] W. D. Hulsbergen, "Decay chain fitting with a kalman filter," *Nucl. Instrum. Meth.* **552** (2005) no. 3, 566 – 575.

[75] N. L. Johnson, "Systems of frequency curves generated by methods of translation," *Biometrika* **36** (1949) 149 – 176.

[76] M. Pivk and F. R. Le Diberder, "sPlot: a statistical tool to unfold data distributions," *Nucl. Instrum. Meth.* **A555** (2005) 356–369, arXiv:physics/0402083.

[77] J. Brehmer, J. Albrecht, and P. Seyfert, "Ghost probability: an efficient tool to remove background tracks," Tech. Rep. CERN-LHCb-INT-2012-025, CERN, Geneva, 2012.

[78] **BABAR** Collaboration, B. Aubert *et al.*, "Search for $D^0 - \overline{D}^0$ mixing in the decays $D^0 \to K^+\pi^-\pi^+\pi^-$," arXiv:hep-ex/0607090 [hep-ex].

[79] **Belle** Collaboration, E. White *et al.*, "Measurement of the wrong-sign decay $D^0 \to K^+\pi^-\pi^+\pi^-$," *Phys.Rev.* **D88** (2013) no. 5, 051101, arXiv:1307.5935 [hep-ex].

[80] **LHCb** Collaboration, R. Aaij *et al.*, "Measurement of the CKM angle γ from a combination of $B^\pm \to Dh^\pm$ analyses," *Phys.Lett.* **B726** (2013) 151–163, arXiv:1305.2050 [hep-ex].

[81] **LHCb** Collaboration, R. Aaij *et al.*, "Improved constraints on γ from $B^\pm \to DK^\pm$ decays including first results on 2012 data," *LHCb-CONF-2013-006* (2013) . http://inspirehep.net/record/1258302/files/LHCb-CONF-2013-006.pdf.

[82] M. Rama, "Effect of D-Dbar mixing in the extraction of gamma with $B^- \to D^0K^-$ and $B^- \to D^0\pi^-$ decays," *Phys.Rev.* **D89** (2014) 014021, arXiv:1307.4384 [hep-ex].

[83] **Mark III** Collaboration, D. Coffman *et al.*, "Resonant substructure in $\overline{K}\pi\pi\pi$ decays of d mesons," *Phys. Rev. D* **45** (1992) 2196–2211. http://link.aps.org/doi/10.1103/PhysRevD.45.2196.

[84] A. Bondar and A. Poluektov, "On model-independent measurement of the angle phi(3) using Dalitz plot analysis," arXiv:hep-ph/0703267 [HEP-PH].

[85] **LHCb** Collaboration, R. Aaij *et al.*, "Observation of the suppressed ADS modes $B^\pm \to [\pi^\pm K^\mp\pi^+\pi^-]_D K^\pm$ and $B^\pm \to [\pi^\pm K^\mp\pi^+\pi^-]_D \pi^\pm$," *Phys. Lett.* **B723** (2013) 44, arXiv:1303.4646 [hep-ex].

[86] **LHCb** Collaboration, I. Bediaga *et al.*, "Framework TDR for the LHCb Upgrade: Technical Design Report," Tech. Rep. CERN-LHCC-2012-007. LHCb-TDR-12, CERN, Geneva, 2012.

[87] D. M. Kunze, D. S. Gabriel, and D. A. Garcia, "Distributed parametric optimization with the Geneva library," in *Data Driven e-Science*, S. Lin and E. Yen, eds., p. 303. Springer, 2011.

[88] F. James, "MINUIT Function Minimization and Error Analysis: Reference Manual Version 94.1," *CERN-D-506* (1994) .

[89] **LHCb** Collaboration, R. Aaij *et al.*, "Measurement of the CKM angle γ using $B^\pm \to DK^\pm$ with $D \to K^0_S\pi^+\pi^-, K^0_S K^+K^-$ decays," *JHEP* **1410** (2014) 97, arXiv:1408.2748 [hep-ex].